PHONON SENSOR DYNAMICS FOR CRYOGENIC DARK MATTER SEARCH EXPERIMENT: A STUDY OF QUASIPARTICLE TRANSPORT IN ALUMINUM COUPLED TO TUNGSTEN TRANSITION EDGE SENSORS

A DISSERTATION
SUBMITTED TO THE DEPARTMENT OF PHYSICS
AND THE COMMITTEE ON GRADUATE STUDIES
OF STANFORD UNIVERSITY
IN PARTIAL FULFILLMENT OF THE REQUIREMENTS
FOR THE DEGREE OF
DOCTOR OF PHILOSOPHY

Jeffrey Jyh-Chung Yen

December 2015

This dissertation is online at: http://purl.stanford.edu/tp321kn3285

I certify that I have read this dissertation and that, in my opinion, it is fully adequate in scope and quality as a dissertation for the degree of Doctor of Philosophy.

Blas Cabrera, Primary Adviser

I certify that I have read this dissertation and that, in my opinion, it is fully adequate in scope and quality as a dissertation for the degree of Doctor of Philosophy.

Peter Graham

I certify that I have read this dissertation and that, in my opinion, it is fully adequate in scope and quality as a dissertation for the degree of Doctor of Philosophy.

Chao-Lin Kuo

Approved for the Stanford University Committee on Graduate Studies.

Patricia J. Gumport, Vice Provost for Graduate Education

This signature page was generated electronically upon submission of this dissertation in electronic format. An original signed hard copy of the signature page is on file in University Archives.

Preface

Understanding the quasiparticle diffusion process inside sputtered aluminum (Al thin films ($\sim$ 0.1-1 μm is critical for the Cryogenic Dark Matter Search (CDMS experiment to further optimize its detectors to directly search for dark matter. An initial study with Al films was undertaken by our group $\sim$ 20 years ago, but some important questions were not answered at the time. This thesis can be considered a continuation of that critical study.

The CDMS experiment utilizes high purity silicon and germanium crystals to simultaneously measure ionization and phonons created by particle interactions. In addition to describing some of the rich physics involved in simultaneously detecting ionization and phonons with a CDMS detector, this thesis focuses on the detailed physics of the phonon sensors themselves, which are patterned onto CDMS detector surfaces. CDMS detectors use thin sputtered Al films to collect phonon energy when it propagates to the surfaces of the detector crystals. The phonon energy breaks Cooper pairs and creates quasiparticles (qps . These qps diffuse until they get trapped in an proximitized "overlap" region where lower-T_c tungsten films connect to the Al film. These tungsten films are the transition edge sensors (W-TESs CDMS uses to readout phonon signals.

We performed a wide range of experiments using several sets of test devices designed and fabricated specifically for this work. The devices were used mostly to study quasiparticle (qp transport in Al films and qp transmission through Al/W interfaces. The results of this work are being used to optimize the design of detectors for SuperCDMS SNOLAB.

This thesis is intended for CDMS collaborators who are interested in knowing more

about the detailed fundamentals of how our phonon sensors work so they can take full advantage of their benefits. However, this work can also be read by general readers who are interested in particle detection using TES technology. This thesis contains eight chapters. The first chapter gives basic background information about dark matter and searches for it. We then describe the basic CDMS detector technology in Chapter two. Chapter three focuses on superconductivity and explains some of the solid state physic most relevant to our Al and W film studies. We then turn our attention to the fabrication processes used to make test devices, and describe some of the studies done to characterize our W and Al film properties. Chapter five explains the experimental setup including how a ^{3}He/^{4}He dilution refrigerator works, and how our electronics were configured. We then get to chapter six where we present key experimental results. Chapter seven covers the TES model we used for our test devices to simulate the data pulse shapes and reconstruct the pulse energies. We also describe the diffusion models used to fit our data. Finally, we end with a short summary of our findings and provide a few suggestions for future studies.

Acknowledgements

The completion of this thesis work consists of the collective efforts of many people. I would like to thank my advisor, Blas Cabrera, for taking me into his group and providing and sharing his invaluable wisdoms and experiences. Not only do did I gain a tremendous amount of physics knowledge in and insights into physics from him, I also learn acquired his positive attitudes toward life. I would also like to thank Betty Young, for her unconditional tireless efforts in to help and to assisting me with this project. We spent many endless long nights together fixing and cooling down our dilution refrigerator system. She also spent many days and nights working with me editing my published papers and presentations. Her unlimited passion and energy excitement toward science truly inspired me. To my fellow graduate students: Ben Shank, Kristi Schneck and Robert Moffatt,. I will always remember the endless physics discussions we had for over the past six years, especially the sleepless late night conversation we had when we were altogether at Soudan Shift Leader's house. To the CDMS SLAC fabrication team,: Paul Brink, Astrid Tomada, Matt Cherry and John Mark Kreikebaum,. If it was not for them, all the test devices could not have been fabricated and improved upon for me to test. It was a truly a valuable experience to learn the complex fabrication process from them and to work with them in the clean room. I thank Peter Redl for helping and teaching me data analysis skills for both CDMS data and the quasiparticle experiments data. We spent many great times together, with Jasmine Hasi, for eating, drinking and laughing. I want to thank Steve Yellin for our useful insightful discussions. I am was very fortunate to have the assistance of Connor Brooks, Teddy Tortorici, Devin Wesenberg, Trevor Howarth and Roger Romani for their efforts in improving lab equipments, and maintaining the lab

in a good condition.

I thank Bernard Sadoulet for taking me into the CDMS group at Berkeley, and supported supporting my decision to pursue my graduate school at a different institution. I want to thank Nader Mirabolfathi for being the first person to train me in handling cryogenic equipments, including how to operate a ^{3}He/^{4}He dilution refrigerator. It requires a lot of patience and time, and I am truly grateful for that. He is also a great mentor and a friend. I had a great time interacting with every member in the CDMS Berkeley group, and I will never forget about it.

Lastly, I thank my family members who provided me their unconditional love and support. I am especially grateful for my parents, they have given me the freedom to pursue whatever I like in my chose, but also provided me the necessary guidance when I needed one. I would have never become who I am if it were not for them.

Contents

List of Tables

List of Figures

Chapter 1

Introduction - Dark Matter Basics

Since the beginning of civilization, humans have been curious about the natural world around them. The evolution of the human race, the origin of the Earth and Solar formation, the beginning of the Universe and its ultimate fate are some of the most fundamental questions we have asked for thousands of years. Advances in theoretical and experimental physics research have allowed us to understand most of the phenomena we experience everyday. The recent discovery of the Higgs boson completed the foundational work on the Standard Model of particle physics[1], and we can now explain all the detectable particles known to exist. Yet, this is merely the start of our space voyage to understand the Universe. Based on the most recent cosmological survey of the energy density in the Universe[2], the Standard Model explains only $\sim$ 5 % of the mass-energy density. About $\sim$ 70% of the energy density of the Universe that is responsible for the accelerating expansion of the Universe we call "dark energy" and its ultimate origin and properties remain a mystery. In addition, the properties of the remaining $\sim$ 25 % missing mass in our Universe ("dark matter" is also unclear. However, for the past few decades there have been many research efforts focused on decoding the nature of the dark matter. The work presented in this thesis represents one contribution to these efforts, primarily in the area of detector technology advancement for the Cryogenic Dark Matter Search (CDMS experiment. CDMS is a direct detection dark matter experiment.

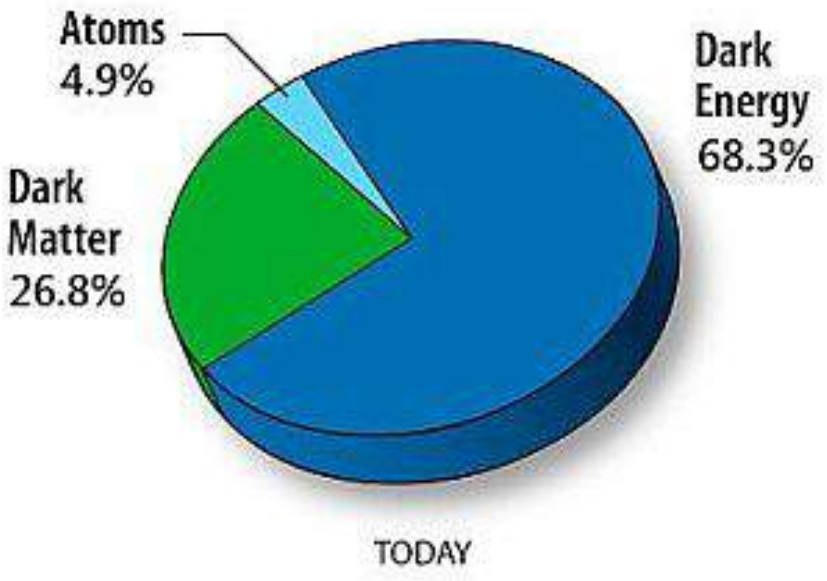

Figure 1.1: Energy density distribution in the Universe. The ordinary matter known to us comprises just $\sim$ 5% of the Universe, where the remaining $\sim$ 95 % is still unknown to date.

1.1 Evidence for Dark Matter

Substantial indirect evidence and astrophysical observations indicate our Universe contains a significant amount of invisible "dark" matter. This section summarizes some of the standard evidence that supports the modern dark matter hypothesis.

1.1.1 Galactic Rotation Curves

Simple Newtonian dynamics can be used to calculate the expected relationship between the orbital speed of a test mass object, v, as a function of the distance, r, between it and some source mass, M, by setting the gravitational force equal to ma_c for the orbiting object:

$$F_c = G\frac{Mm}{r^2} = \frac{mv^2}{r} \tag{1.1}$$

$$v = \sqrt{\frac{GM}{r}} \propto r^{-1/2} \tag{1.2}$$

The test mass object, m, can be anything: a star, a galaxy, or a cluster. The speed in Equation 1.1 can be replaced by $\langle v \rangle$ for a non-circular orbit, and the relation still holds. However, Figure 1.2 shows one of many examples of rational speed versus distance from the center of the galaxy that indicates either Equation 1.2 is incorrect or there is a mass distribution that is not visible. In Figure 1.2, the rotational curve of the galaxy M33 is shown and the data points (in blue were measured by using 21 cm hydrogen line after 20,000 light years away from the center of the galaxy[3]. So far, no compelling experiments show that Newtonian physics should be altered, so it is now commonly believed that a dark matter halo must surround our galaxy (among others! .

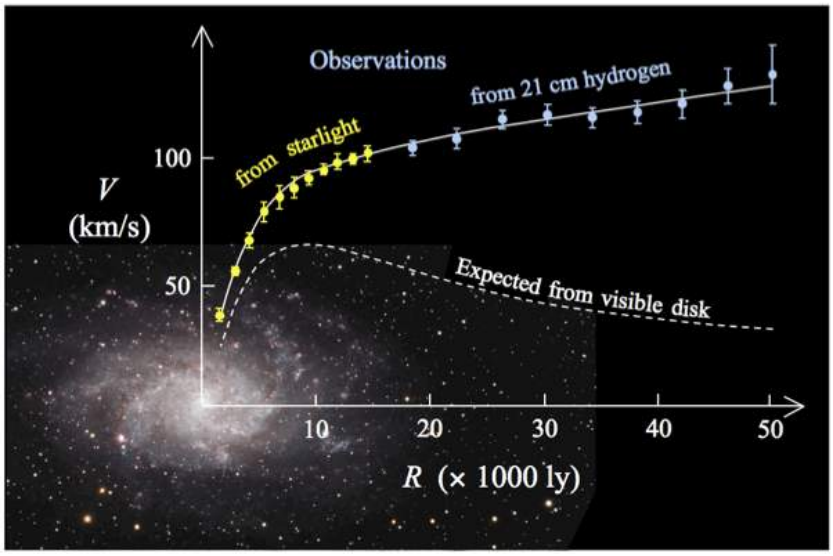

Figure 1.2: Orbital velocity (km/s versus distance (in units of lightyears from the center of the galaxy M33. The dashed-line is the predicted velocity based on Equation 1.2; the observed results are indicated by the yellow and blue data points.

1.1.2 The Cosmic Microwave Background Radiation

The measurement of anisotropies in the cosmic microwave background provides detailed constraints on the density and evolution of the matter in the Universe. Approximately 380,000 years after the Big Bang, the Universe has expanded and cooled

enough that photons and matter became decoupled. Hence, the CMB radiation is the earliest light we can "see" today, and it provides excellent constraints on baryonic and dark matter densities in this epoch. Figure 1.3[left] shows an all-sky map for temperature anisotropies in galactic coordinates from the Planck Space Telescope. The temperature fluctuations range from -300 μK to 300 μK, where the zero shown on the color bar corresponds to $\sim$ 2.73 Kelvin[2]. The power spectrum of the primary temperature anisotropies in the CMB determined from this plot is shown in Figure 1.3[right]. The various peaks shown correspond to acoustic oscillations resulting from interactions between baryons and photons prior to the recombination time[4]. In addition, the relative heights of the even and odd acoustic peaks constrain the ratio of baryonic matter to dark matter. These measurements were used to make the energy density "pie" of the Universe shown in Figure 1.1.

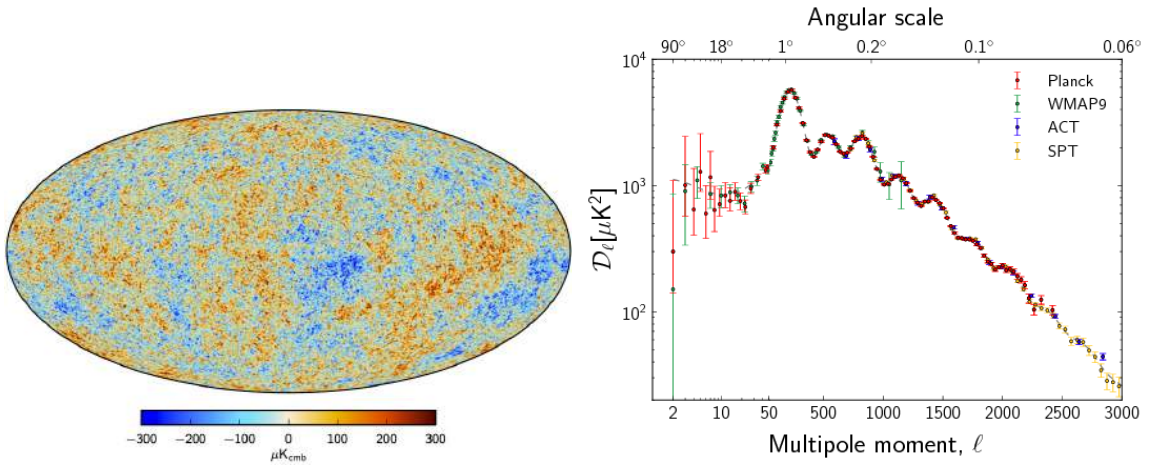

Figure 1.3: *Left*: All-sky map of the cosmic microwave background temperature fluctuation. *Right*: Angular power spectrum plotted from four recent observational astronomy experiments.

1.1.3 Bullet Cluster Collision

Recent images showing the collision of two clusters[5] also provides compelling hints to the existence of an unknown matter distribution in the Universe. Figure 1.4 shows

an optical image (yellow taken from the Hubble Telescope overlaying both an x-ray emission image (pink from the Chandra X-ray Observatory and a mass-distribution reconstruction (blue provided by gravitational lensing data. This composite image shows that the majority of the mass present is not visible.

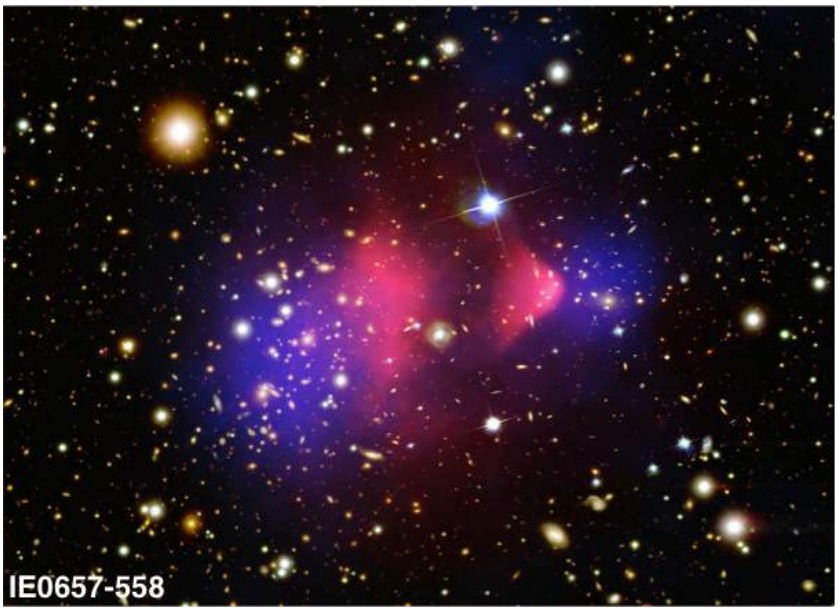

Figure 1.4: The collision of the Bullet Cluster. Composite optical (yellow and x-ray image (pink of the Bullet cluster (IE0657-558 . The blue image in the mass distribution reconstructed from lensing.

1.1.4 Dark Metter Candidate: Weakly Interacting Massive Particles

Basic dark matter candidates should satisfy certain criteria:

- They should be abundant: Of the $\sim$ 30 % of the Universe that is matter, astronomical measurements indicate $\sim$ 85 % of this mass is dark matter.
- They should be stable: Since the dark matter still exists today, dark matter particles should be stable or have lifetimes close to the age of the Universe.

- They should be "cold": Although relativistic "hot" particles like neutrinos could contribute a few percent of the dark matter density, the CMB acoustic peaks indicate the majority of dark matter should be non-relativistic, or "cold".

- They should be collisionless and dissipationless: The current direct search experiments indicate that dark matter interacts with baryons at the weak scale ($< 10^{-45}$ cm^2 at 100 GeV/c^2 . In addition, the size of dark matter halos indicates that dark matter doesn't cool efficiently by radiating photons, nor does it collapse to form dense structures like baryonic matter.

- They should be non-baryonic: From the CMB measurements, the dark matter needs to be non-baryonic as it should decouple from photons or light nuclei prior to the cosmological recombination time. In addition, big-bang nucleosynthesis (BBN puts a very tight constraint on the baryonic density.

A few dark matter candidates have been purposed based on different theories. However, one of the most well-motivated candidates that fits all the criteria above is called the Weakly Interacting Massive Particle (WIMP . This dark matter candidate is the focus of the CDMS experiment.

1.2 Dark Matter Detection Methods

Figure 1.5 shows a qualitative diagram connecting three general dark matter detection methods to fundamental physics, via the same basic set of Feynman diagrams shown at the center of the figure. Indirect searches (green arrow look for evidence of dark matter annihilation. A leading indirect detection experiment is operated using the Fermi Gamma-ray Space Telescope, a large-array space telescope looking at the center of the Milky Way, where the density of dark matter is expected to be high. The signature of dark matter annihilation may be found in the extragalactic gamma-ray background (EGB . A significant gamma-ray emission excess from our galaxy cannot be explained by the known point-source populations detected by the Fermi telescope. This excess may provide important clues to the existence of dark matter.

Another active area of dark matter search uses high-power, high-energy particle colliders such as the Large Hadron Collider (LHC to decode the fundamental properties of dark matter. This approach (blue arrow is complementary to indirect or direct-detection methods because the accelerator based approach can only reasonably probe a small mass range. In addition, since WIMPs or other dark matter candidates can easily escape from accelerator detector arrays, their existence can only be deduced by looking for missing mass or missing energy during event reconstruction. This limits the type of information that accelerator-based experiments can provide[6]. Nevertheless, accelerators are still important tools to use in the overall search for dark matter.

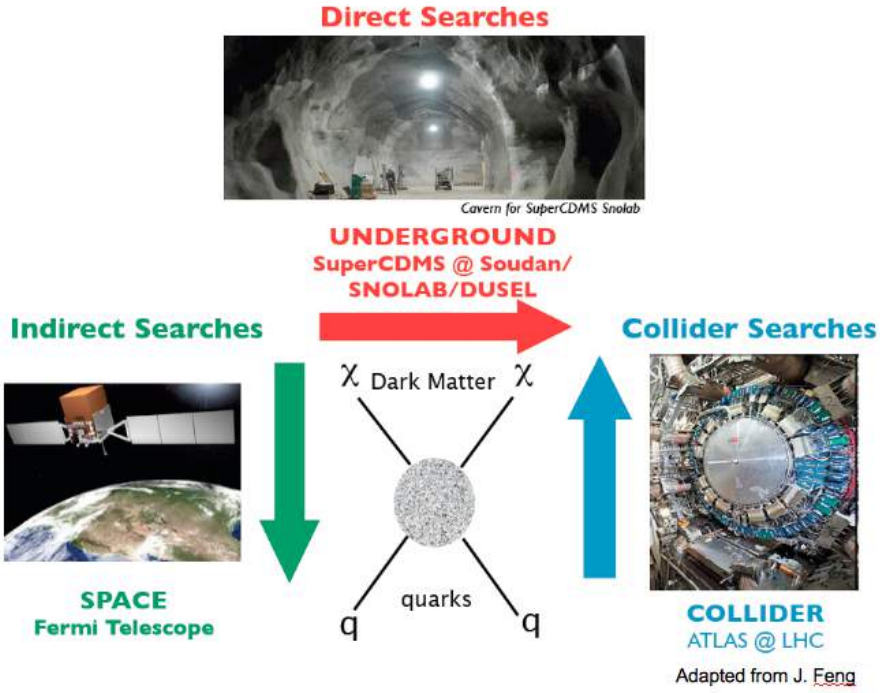

Figure 1.5: Qualitative diagram showing the complementarity between direct detection (in red , indirect detection (in green , and collider probes (in blue of dark matter. Each technique corresponds to the same basic set of Feynman diagrams, with χ denoting the dark matter particle, and q denoting some set of target particle nuclei. The arrows indicate the direction of time.

Perhaps the most straightforward way to search for dark matter is through direct interaction, where the dark matter particle, denoted as χ in Figure 1.5, interacts with

ordinary matter. Direct detection dark matter experiments typically rely on collecting scintillation and/or ionization and/or phonons to sense particle interactions in a target material. To effectively discriminate WIMPs from other types of background particles, many experiments utilize two of the three methods to discriminate between electron and nuclear recoils[7, 8, 9]. The CDMS experiment measures ionization and phonons in its direct detection WIMP search.

Chapter 2

The Cryogenic Dark Matter Search Experiment

The Cryogenic Dark Matter Search (CDMS Experiment is operated deep underground in the Soudan Mine State Park in northern Minnesota. The deep site ($\sim$ 2300 ft, 2100 m.w.e shields our experiment from the vast majority of cosmic rays. With careful lab design and choice of cryostat materials, plus extensive shielding, we have achieved a background event rate $<$ 1/ sec[10]. The current SuperCDMS Soudan experiment utilities a sophisticated cryogenic setup[11, 12] and we have been operating the detector payload at $\sim$ 50 mK continuously for the past two years. Since its initial installation, much effort has gone into optimizing all aspects of the experiment, including detector fabrication and testing, background rejection, electronics, cryogenics, and data acquisition and analysis software. What we have learned is being fed into the next generation SuperCDMS SNOLAB experiment. In this chapter, I focus on CDMS detector physics and operating principles. At the end of the chapter, I motivate the rationale for this thesis study on quasiparticle dynamics in superconducting films.

2.1 Direct Detection

In our direct detection dark matter experiment, we use high-purity Si and Ge crystals as detector targets to simultaneously measure ionization and phonon energy created by particle interactions. When an event occurs in a CDMS detector, electron-hole pairs and phonons are created. A small electric field (∼1V/cm is used to drift the e-/h+ pairs through the bulk of the crystal so charge can be collected at the detector surfaces (see Figure 2.1[left] . At the same time, athermal phonons produced by the initial event make their way to the detector surfaces where they are absorbed by phonon sensors (see Figure 2.1[right] . These phonon sensors consist of photolithographically pattered aluminum and tungsten films. The athermal phonons break Cooper pairs in the Al films and create quasiparticles. The quasiparticles diffuse randomly in the Al until they get trapped in a region where the Al and W films overlap, and where the superconducting energy gap is smaller than in the Al film alone[13]. This trapped energy ultimately gets absorbed by the W film, providing the detector's phonon signal for that event. We call these phonon sensors Al/W **Q**uasiparticle-trap-assisted-**E**lectrothermal-feedback **T**ransition-edge-sensors (QETs [14]. These sensors are at the heart of the experiments described in this thesis.

2.1.1 Ionization Yield Discrimination

A particle interacts with our detectors via either electron or nuclear scattering, depending on target material, particle mass, charge and kinetic energy. A low mass particle will deposit most of its energy in the detector electron system, creating a relatively large population of e^-/h^+ pairs. A heavy and/or slow particle will generally transfer a more significant fraction of its energy to the atomic cores of the target material, resulting in lower ionization yield. We can define ionization yield by:

$$y \equiv \frac{E_Q}{E_r} = \frac{E_Q}{E_P - \frac{eV_b}{\epsilon} E_Q} \qquad (2.1$$

Here, E_Q is the collected ionization energy and is normalized in our analysis so that $y = 1$ for electron recoils. E_P is the collected phonon energy. The second term in the

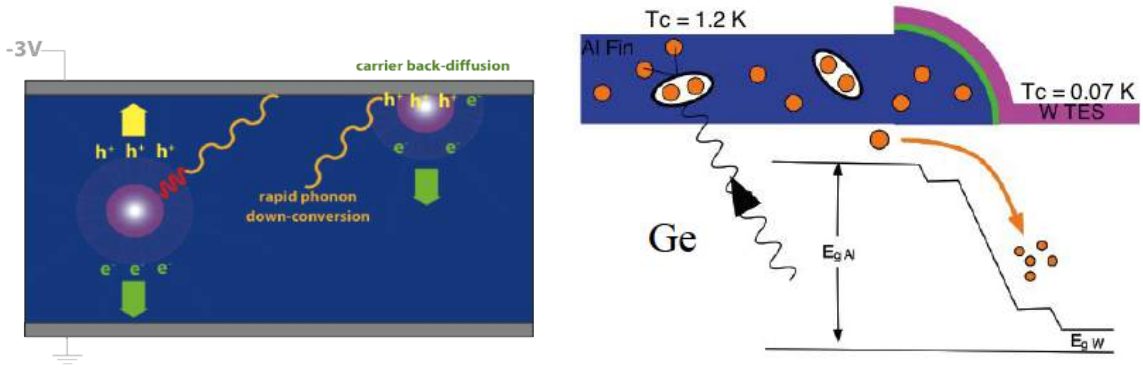

Figure 2.1: When a particle interacts with our detector crystal, it generates electron-hole pairs as well as phonons. *Left*: Detector operation principle. A ~ 1 V bias applied through the detector crystal sends electrons and holes to opposite sides of the detector, where they get collected at the surfaces. *Right*: When the athermal phonons reach the detector surfaces, they are absorbed by photolithographically pattered Al/W QETs. This requires breaking Cooper pairs and generating quasiparticles (qps in the Al film. The qps diffuse and get trapped in an W/Al overlap region where the superconducting band-gap has lower energy. Finally, the qps get absorbed by W-TESs, producing our phonon signals.

denominator represents Neganov-Luke phonons[15] created by the electron-hole pairs as they drift through the detector crystal under the influence of the applied electric field. ϵ represents the average energy required to generate an electron-hole pair in the Si or Ge detector crystal. Lastly, V_b is the voltage bias applied across the crystal.

Figure 2.2 shows a yield plot for a CDMS detector exposed to a ^{133}Ba calibration source (356 keV gamma . The majority of events appear in the electron recoil band (red as expected. A population of events with incomplete charge collection can appear below the electron recoil band and droop into the nuclear recoil band (blue . These events have been identified as surface events. Our new detector technology and analysis tools allow us to dramatically discriminate against these events. The presence of these surface events has driven the CDMS detector technology and data analysis development for the past several years.

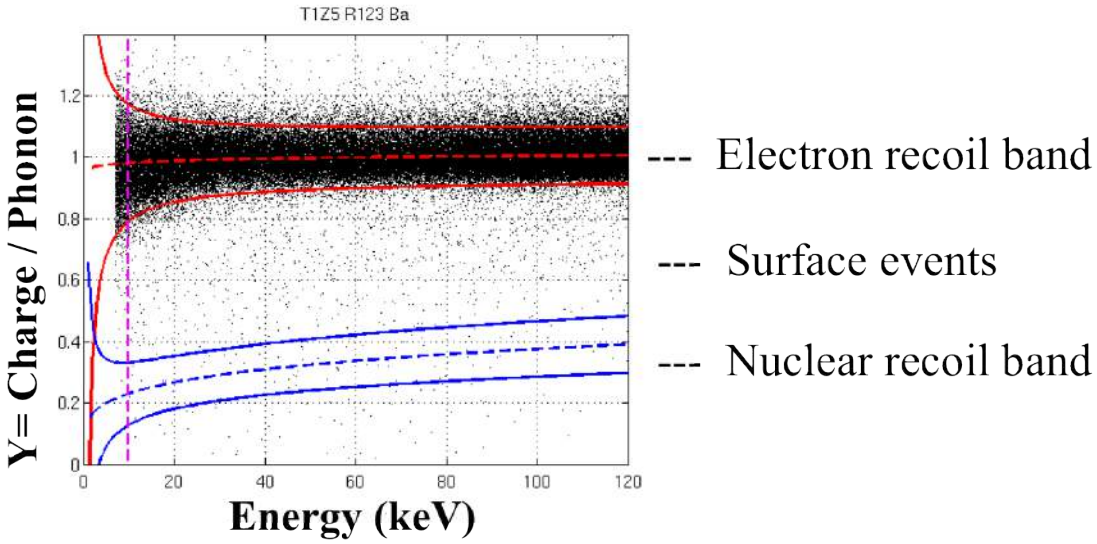

Figure 2.2: A typical yield plot that shows both the nuclear recoil (blue and electron recoil (red bands, clearly separated by their ($\sim$ x3 different ionization yields. Potential WIMP events would appear in the nuclear recoil band. These data show leakage of gamma events from the strong ^{133}Ba calibration source into the nuclear recoil band. Such events can be identified and discriminated against using our advanced detector and analysis technologies described below.

2.1.2 Detector Technology: Charge and Phonon

The CDMS detector technology has undergone constant improvement over the past two decades. Many significant studies have been performed to improve our detailed understanding of charge transport in crystalline, high-purity Si and Ge. Most recently, we studied the oblique propagation of electrons and holes in semiconductors both theoretically and experimentally[16]. By utilizing CDMS Detector Monte Carlo (DMC techniques, we were able to identify the cause of excess background signals present in one of our CDMS dark matter detectors (T5Z3 - the detector had a shorted outer electric charge line[17].

The CDMS phonon sensor design has also undergone continuous improvement[18]. A constant theme has been to use QETs for the phonon sensors. In the early years of CDMS, arrays of QETs were pattered on only one side of each detector crystal. The other side of the detector was reserved for two concentric ionization collection

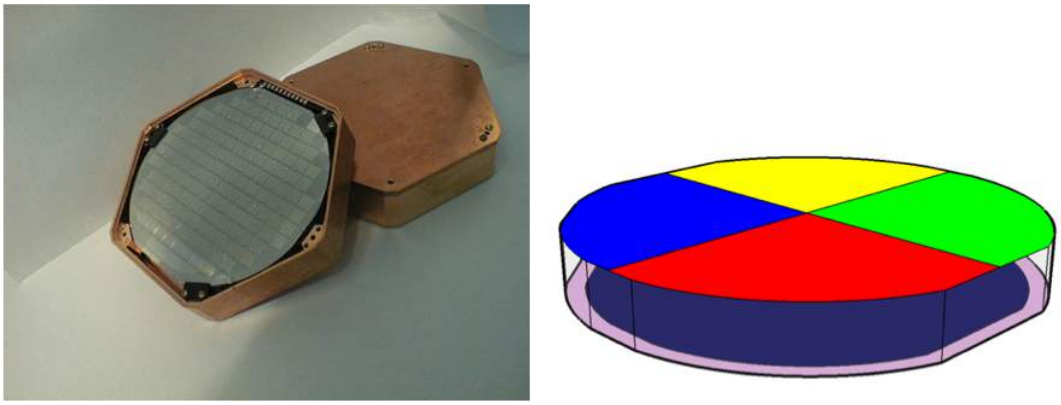

Figure 2.3: *Left*: Picture of a Z-dependent Ionization and Phonon (ZIP detector. The detecter shown is a CDMS II Si detector, 3" in diameter × 1 cm-thick. The top surface is covered with 4 QET channels, each with ∼ 1000 TESs. *Right* Schematic sensor configuration of a ZIP detector: the top face contains four phonon sensor quadrants, the bottom face is divided into two concentric charge collection electrodes.

electrodes. The ionization electrodes were used to define a detector fiducial volume. These detectors, which we called "Z-dependent" Ionization and Phonon (ZIP detectors, provided event location information in all three dimensions (x, y and z . They had their QET phonon sensor arrays divided into four quadrants (see Figure 2.3 . By comparing the phonon signal amplitudes and rise-times for the different QET quadrants, we got information about the x, y and z location of each event[19].

The detector technology was improved even further for the SuperCDMS Soudan experiment. An interleaved-ZIP (iZIP detector design was developed with interleaved phonon and charge channels on both sides. These new detectors offered dramatically improved surface event rejection capability. In this design, the phonon channels are "grounded", while the interleaved charge electrodes are held at +2 V (top surface and -2 V (bottom surface . As shown in Figure 2.4, the electric field is quite uniform in the bulk of the detector. This leads to largely symmetric ionization signals for electrons and holes for events occur at the bulk of the crystal. However, for surface events, non-uniform E fields close to the surface prevent electrons or holes from propagating through the crystal to the far electrode. The iZIPs, 3" diameter × 1" thick (see Figure 2.5[left] , are larger than all previous CDMS detectors and naturally

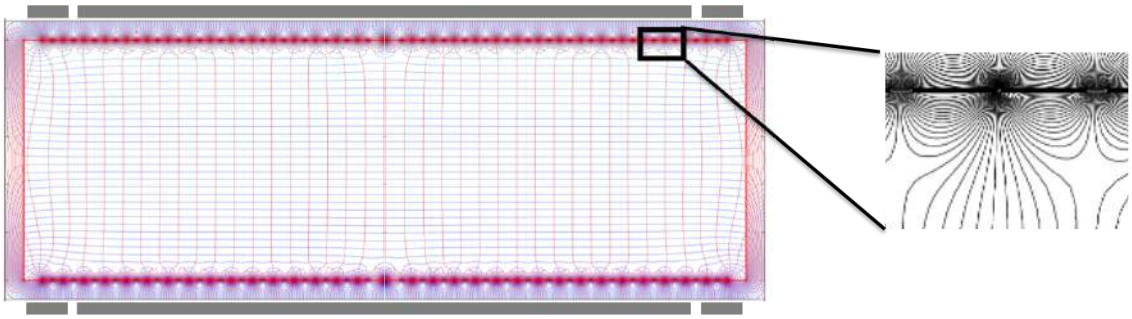

Figure 2.4: Simulated electric filed lines (red and equipotentials (blue for an Interleaved ZIP detector (iZIP . Uniform electric field lines in the bulk of the detector provide excellent separation of electron-hole pairs for events occurring in the bulk of the detector. The local high density of electric field lines that bend back toward the electrodes is useful for vetoing surface events. These surface events can be identified by the asymmetry in the charge collected at the two detector surfaces.

provide more target mass for our WIMP search. The phonon channel geometry on these iZIPs is shown in Figure 2.5[right].

A prototype SuperCDMS SNOLAB detector (100 mm diameter × 33.3 mm-thick is shown in Figure 2.6[left]. Both high-purity Si and Ge substrates will be used. The charge and phonon channel layout is shown in Figure 2.6[right]. There are six phonon channels per detector face, with a 45° rotation between the two detector faces.

2.2 Phonon Detection: Optimizing Collection Efficiency

An absolute phonon collection efficiency study for early CDMS detectors by Walter Ogburn (Figure 2.7 showed a much lower energy collection efficiency than expected. The low efficiency was largely attributed to poor connectivity between the W and Al films of the QETs. In this thesis, I will present results from x-ray experiments with several W/Al test devices that were designed and fabricated specifically to better understand energy collection in CDMS-style phonon sensors.

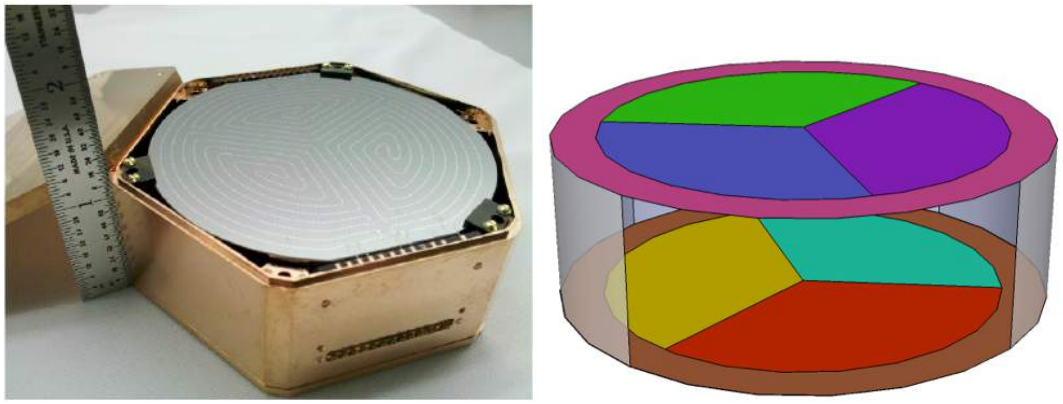

Figure 2.5: *Left*: The Ge iZIP detector shown is 3" diameter × 1" thick. Thousands of QETs are connected in parallel and interleaved with the charge electrodes. *Right*: Schematic sensor configuration of an iZIP detector: top detector face is divided into three inner and one outer QET channels with the "Mercedes" shape shown. The bottom face has a similar phonon channel design, but rotated by 60°.

To effectively collect phonon energy without degrading energy resolution, a SuperCDMS detector should have a large fraction of its surface covered with active superconducting Al films that efficiently couple quasiparticles into relatively small tungsten TESs. Considerable work has been done (and is continuing to optimize the Al and W film geometries of our detectors (see, e.g.[18] .

In the simplest form, a W-TES is a sensitive thermometer that can detect small energy depositions according to:

$$\Delta E = c_s \, \mathcal{V} \, \Delta T, \tag{2.2}$$

where c_s is the specific heat (per volume of tungsten, $\mathcal{V}$ is volume of the W film, and ΔT is the change in temperature of the W-TES. The basic idea is to have a relatively large temperature increase for a small energy deposition. According to Equation 2.2, this can be accomplished by using small TESs. Thus, for large-area CDMS detectors with small W-TESs, the only way to effectively collect energy is to couple the W-TESs to larger structures. Our W/Al QETs are designed with this in mind.

The trade-off for the Al films in the QETs is that we want the Al films to be large

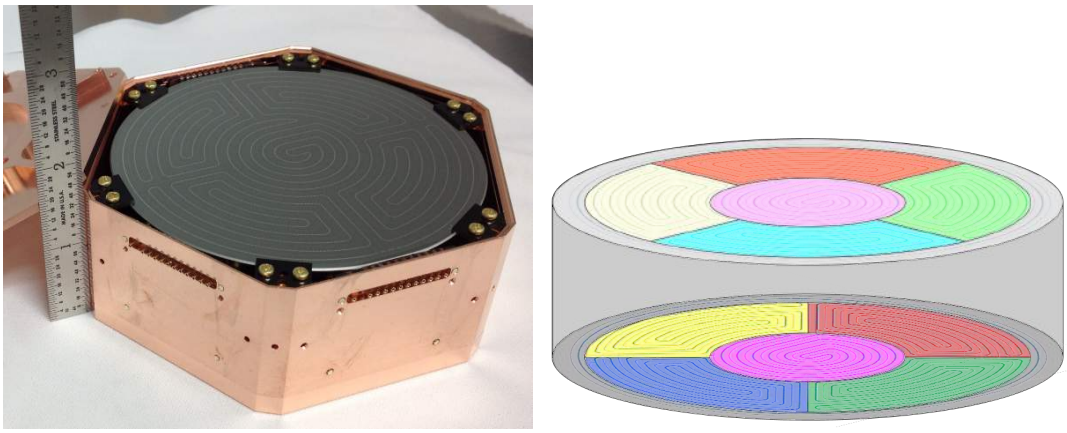

Figure 2.6: *Left*: A Ge SuperCDMS SNOLAB detector, 100 mm diameter × 33.3 mm-thick. *Right*: Schematic of interleaved phonon sensor and charge electrode design for the new iZIP detectors. There are six phonon channels per detector face; one outer channel surrounding five inner channels. The bottom detector face is identical in design but rotated by 45°.

in area to collect phonon energy from the substrate, but the films can't be too large, or energy will be lost back to the substrate as qps diffuse through the Al on their way to the W-TESs. We can reduce energy loss to the substrate by increasing the Al film thickness. However, until recently, our Al film thickness was limited by step-coverage limitations where the W-TESs overlap the Al films. We address all of these issues in this thesis.

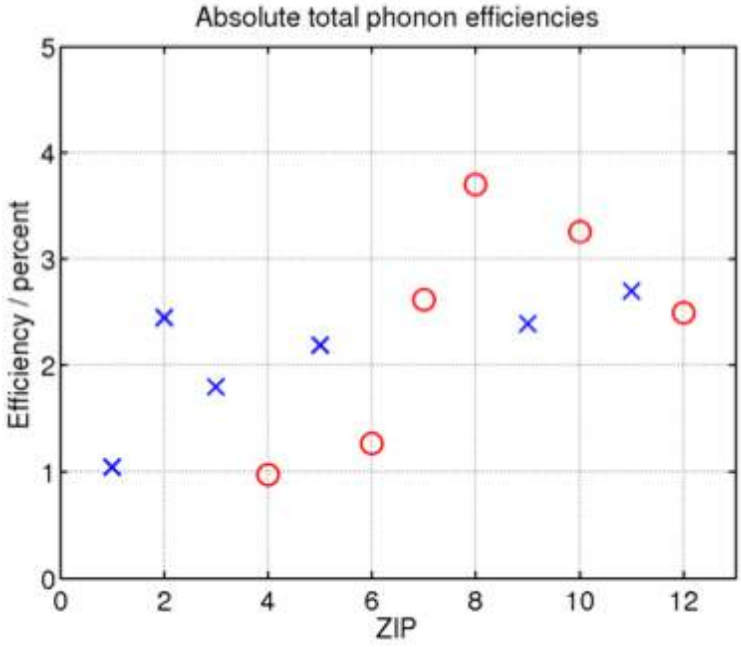

Figure 2.7: Total phonon collection efficiency for 12 CDMS II detectors (Runs 118-119 . Crosses correspond to Ge detectors and circles represent Si detectors. The observed total phonon collection efficiency was only 1% - 4%. Analysis by W. Ogburn.

Chapter 3

Superconducting Sensor Physics

A particle detector or energy sensor relies on efficient interactions with the external energy source. In superconducting low temperature particle detection techniques, two main approaches are taken: in the first, the event energy is detected by measuring the number of quasiparticles generated from broken Cooper pairs. The other approach relies on measuring the temperature change of an absorber. Because the energy bandgap of a superconductor is $\sim$1000 $\times$ less than the bandgap of a traditional semiconductor ($\sim$ eV , these detectors can provide considerably better energy sensitivity than conventional semiconductor detectors.

A Superconducting Tunnel Junction (STJ detector is one example of a device that measures energy depositions by measuring the number of quasiparticles passing through an insulating junction layer ($\sim$ nm coupling two superconducting films to each other[20, 21, 22]. A Kinetic Inductance Detector (KID measures the energy deposited in a detector by sensing a shift in the resonant frequency of a superconducting LC circuit. This shift in resonant frequency is caused by the change in qp density resulting from the event[23]. A Transition-Edge Sensor (TES [14] measures event energy by detecting changes in detector temperature. In a TES calorimetric measurement, the event energy is measured directly by monitoring the resistance of a superconducting film. In a TES bolometric measurement, the TES monitors thermal power absorbed by the sensor.

Each of these superconducting sensor types has a wide range of applications. With

careful design, these sensors can be used to detect a large fraction of the electromagnetic spectrum, ranging from millimeter waves to gamma rays. The devices also can be used for single particle detection in the $\sim$ eV to $\sim$ MeV range. Many other innovative low temperature detectors such as roton detectors, Magnetic Penetration Thermometers (MPTs , and others are not mentioned here[24, 25].

The CDMS experiment uses the TES technology. In our configuration, Al thin films are patterned on top of high purity Ge and Si crystals (Section 2.2 . An event ultimately creates qps in the Al that diffuse to intimately connected superconducting tungsten TES where they are absorbed and contribute to a signal. We call this integrated sensor design **Q**uasiparticle-trap-assisted **E**lectrothermal feedback **T**ransition-edge sensors (QETs .

In this chapter, we review basic theories of superconductivity before transitioning into a discussion of quasiparticle down-conversion dynamics in superconductors.

3.1 Superconductivity

After the first discovery of superconducting mercury in 1911, the microscopic theory of superconductivity (BCS wasn't fully established until 1957 by J. Bardeen, L. N. Cooper, and J. R. Schrieffer[26]. Previously, V. L. Ginzburg and L. D. Landau had already described superconductivity in a phenomenological manner using a macroscopic free energy approach [27]. In this section, we summarize some key components of superconductivity. More information can be found in the works of M. Tinkham[22] and C. G. deGennes[28].

3.1.1 BCS Theory: Cooper Pairs

Qualitatively speaking, a *Cooper pair* forms when two electrons on opposite side of the Fermi surface, and close to the Fermi surface, experience an attractive potential in addition to Coulomb repulsion. An electron traveling through a metal with a periodic lattice potential feels an attractive force from the positive ion cores. This Coulomb force distorts the local potential. A second electron that interacts with

this modified potential experiences an attraction force that effectively binds the two electrons together into a Cooper pair. The separation between electrons in a Cooper pair is ~ 100 nm, which is much greater than the lattice spacing in the host material.

To be more quantitative, let us consider that the one-electron states below the Fermi level are all occupied at $T = 0$. Thus if two additional electrons ($\mathbf{k_1}, E_1$ and ($\mathbf{k_2}, E_2$ are added to the system, we can describe them via a two-particle spatial wavefunction:

$$\psi(\mathbf{r_1}, \mathbf{r_2} \ = \sum_{\mathbf{k_1}} \sum_{\mathbf{k_2}} g_{\mathbf{k_1}} e^{i\mathbf{k_1}\cdot\mathbf{r_1}} g_{\mathbf{k_2}} e^{i\mathbf{k_2}\cdot\mathbf{r_2}} \tag{3.1}$$

To conserve momentum, we set $\mathbf{k_1} = -\mathbf{k_2}$. In Equation 3.1, $g_{\mathbf{k_1}}$ and $g_{\mathbf{k_2}}$ are the probability amplitudes of finding one electron with plane wave momentum $\hbar\mathbf{k_1}$ and $\hbar\mathbf{k_2}$. Transforming into the center of mass frame, and considering only the spin singlet state (which is lower energy than the triplet states , the full two-electron wavefunction then becomes:

$$\psi(\mathbf{r_1} - \mathbf{r_2} \ = \left[\sum_{k>k_F} g_{\mathbf{k}} \cos \mathbf{k} \cdot (\mathbf{r_1} - \mathbf{r_2} \right] (| \uparrow_1> | \downarrow_2> - | \downarrow_1> | \uparrow_2> \tag{3.2}$$

By plugging-in Equation 3.2 to Schrödinger's equation, we get:

$$\frac{\hbar^2}{m} k^2 g_{\mathbf{k}} + \sum_{k'} g_{\mathbf{k'}} V_{kk'} = (E + 2E_F \ g_{\mathbf{k}} \tag{3.3}$$

$$V_{kk'} = \frac{1}{L^3} \int V(\mathbf{r} \ e^{-i(\mathbf{k}-\mathbf{k'} \cdot \mathbf{r}} \ d\mathbf{r} \tag{3.4}$$

where the volume L^3 is included for normalization. Cooper[29] simplified the matrix elements for this interaction by setting $V_{kk'} = -V$ within a thin spherical shell in $\mathbf{k}$-space, where both $E_F < \hbar^2 k^2/2m < E_F + \hbar\omega_c$ and $E_F < \hbar^2 k'^2/2m < E_F + \hbar\omega_c$. $V_{kk'} = 0$ for $\omega > \omega_c$, where ω_c is the cutoff frequency. The negative value of $V_{kk'}$ indicates an attractive potential. A self-consistency condition can be found using above condition and Equation 3.3:

$$1 = \frac{V}{L^3} \sum_{k'} \frac{1}{2(\hbar^2 k'^2/2m - E_F \ - E} \tag{3.5}$$

By changing variables, $\eta' = \hbar^2 k'^2/2m - E_F$, and introducing the density of states, N(η' , we can rewrite Equation 3.5 as:

$$1 = V \int_0^{\hbar\omega_c} N(\eta' \ \frac{1}{2\eta' - E} \ d\eta'. \tag{3.6}$$

Assuming $\hbar\omega_c << E_F$, $N(\eta'$ can be considered to be a constant and $N(\eta' \approx N(0$, the single spin electronic density of states at the Fermi level. We can then perform the integral in Equation 3.6 using a weak-coupling approximation, $N(0 \ V \ll 1$, yielding:

$$E = -2\hbar\omega_c \ e^{-2/N(0 \ V} \tag{3.7}$$

This equation shows that a two-electron bound state with energy $E < 0$ alway exists, no matter how small V is. This is the origin of the Cooper pairs. For aluminum, $N(0 \ V = 0.18$ [Table 3.1].

The full BCS theory takes this model a step further and includes all the valence electrons, N, in the system and groups them into pairs. The total wavefunction becomes:

$$\phi_N = A\phi(\mathbf{r_1} - \mathbf{r_2} \ \cdots \phi(\mathbf{r_{N-1}} - \mathbf{r_N} \ (\uparrow_1 \ (\downarrow_2 \ \cdots (\uparrow_{N-1} \ (\downarrow_N \tag{3.8}$$

where A is an anti-symmetrization operator. This equation can be simplified further by introducing Wigner-Jordan notation and using creation (a_k^+ and annihilation (a_k operators that act on the vacuum state, ϕ_0[26]:

$$\tilde{\phi} = \prod_k \left(u_k + v_k a_{k\uparrow}^+ a_{-k\downarrow}^+\right) \phi_0 \tag{3.9}$$

with

$$u_k^2 + v_k^2 = 1 \tag{3.10}$$

Minimizing

$$< \tilde{\phi}|H|\tilde{\phi} > -E_F < \tilde{\phi}|N|\tilde{\phi} > \tag{3.11}$$

where H is the pairing hamiltonian of the interacting electron system, can be used

to define the superconducting energy bandgap Δ [28] as:

$$\Delta = N(0\ V \int_{-\hbar\omega_D}^{\hbar\omega_D} \Delta \frac{d\eta}{2\sqrt{\eta^2+\Delta^2}} = \frac{\hbar\omega_D}{\sinh[1/N(0\ V]}. \quad (3.12$$

Here we assume $V_{kk\prime} = -V$ and $\eta = \hbar^2k^2/2m - E_F$, just as before. The energy limits of the integral are set using $\hbar\omega_c = \hbar\omega_D$, where ω_D is defined as the Debye frequency. In the dilute limit, $N(0\ V \ll 1$, and the superconducting bandgap becomes:

$$\Delta \approx 2\hbar\omega_D e^{-1/N(0\ V} \quad (3.13$$

The superconducting gap energy as a function of temperature can be found by solving:

$$1 = N(0\ V \int_0^{\hbar\omega_D} \frac{d\eta}{\sqrt{\eta^2+\Delta^2}}[1 - 2f(\eta^2+\Delta^2\ ], \quad (3.14$$

where f(E is the Fermi-Dirac distribution, $f = 1/1 + e^{\epsilon/k_BT}$. The resulting bandgap at zero temperature is:

$$\Delta(0\ \ = 1.76\ k_BT_C \quad (3.15$$

and has an asymptotic form near $T = T_C$ (the superconducting critical temperature [22]:

$$\frac{\Delta(T}{\Delta(0} \approx 1.74\sqrt{1 - \left(\frac{T}{T_C}\right)} \quad (3.16$$

Notice Equation 3.16 only works when $T \sim T_C$ and is not applicable when $T \ll T_C$. For the Al films described in this thesis (T_C = 1.2 K , Equation 3.15 is relevant ($T \sim 35$ mK and $\Delta_{\rm Al} = \Delta_{\rm Al}(0\ \ = 0.18$ meV. The W films used in our studies were operated in their superconducting transition ($T \sim T_C$, and thus we assume $\Delta_{\rm W} \approx 0$.

Another important parameter that can be derived from the BCS theory is the coherence length of a pure superconductor, ξ_0^{BCS}:

$$\xi_0^{BCS} = \frac{\hbar v_F}{\pi\Delta(0} \quad (3.17$$

The coherence length corresponds to the characteristic distance over which the superconducting electron concentration does not change appreciably in the superconductor. Table 3.1 lists the calculated coherence length.

	$[N(0\ V]_{exp}$	$\Delta(0$ (meV	v_F (m/s	ξ_0^{BCS} (nm	ξ_0 (nm	τ_0 (ns	τ_{273} (fs
Al	0.18	0.18	2.03×10^6	2100	1600	110	8

Table 3.1: Commonly accepted values of the density of states, energy bandgap, Fermi velocity, theoretical and experimental values of coherence length, and characteristic time scales for qps in Al.

3.1.2 Ginzburg-Landau Theory

The Ginzburg-Landau (GL theory is a macroscopic treatment of superconductivity that introduces a pseudowavefunction $\psi(\mathbf{r}$ as a complex order parameter. The GL theory can be derived from microscopic BCS theory [30], although historically the GL theory came before BCS theory. The theory is valid near the critical temperature T_c, and when ψ is small and varies slowly in space, and the vector potential $\mathbf{A}(\mathbf{r}$ is nearly constant. In the GL theory, $|\psi(\mathbf{r}\ |^2$ is the density of superconducting electrons, $n_s(\mathbf{r}$, and the free energy density F of a superconductor can be written:

$$F = F_{n0} + \alpha|\psi|^2 + \frac{\beta}{2}|\psi|^4 + \frac{1}{2m^*}\left|\left(\frac{\hbar}{i}\nabla - \frac{e^*}{c}\mathbf{A}\right)\psi\right|^2 + \frac{h^2}{8\pi}, \qquad (3.18$$

where $F_{n0} + h^2/8\pi = F_n$ is the free energy of the normal state with $m^* = 2m_e$ and $e^* = 2e$. Minimizing Equation 3.18 by varying $\psi(\mathbf{r}$ by $\delta\psi(\mathbf{r}$ and $\mathbf{A}(\mathbf{r}$ by $\delta\mathbf{A}(\mathbf{r}$, and setting $\delta F = 0$, yields:

$$\alpha\psi + \beta|\psi|^2\psi + \frac{1}{2m^*}\left(\frac{\hbar}{i}\nabla - \frac{2e^*\mathbf{A}}{c}\right)^2\psi = 0 \qquad (3.19$$

This equation can be further simplified by assuming no external magnetic field is present ($\mathbf{A} = 0$, and by introducing a normalized wavefunction, $f = \psi/\psi_\infty$, where

$\psi_\infty = -\alpha/\beta$. Equation 3.19 then becomes:

$$\xi^2(T \ \frac{d^2 f}{dx^2} + f - f^3 = 0 \qquad (3.20$$

where

$$\xi^2(T \ = \frac{\hbar^2}{2m^*|\alpha|} \qquad (3.21$$

is the GL coherence length, and $\xi(T \ \approx \xi_0$ for pure materials. Additional calculations within the GL theory show that[22]:

$$\xi(T \quad = \quad 0.74\frac{\xi_0}{(1-\frac{T}{T_C} \ ^{1/2}} \quad \text{pure} \qquad (3.22$$

$$\xi(T \quad = \quad 0.855\frac{(\xi_0 l \ ^{1/2}}{(1-\frac{T}{T_C} \ ^{1/2}} \quad \text{dirty} \qquad (3.23$$

A superconducting material is considered to be in the "dirty limit" when its qp mean-free-path, $\Lambda \ll \xi_0$. Our 300 nm-thick Al films have a measured mean-free-path of:

$$\Lambda = \text{RRR} \cdot \tau_{273} \cdot v_F = 11 \cdot 8 \times 10^{-15}[s] \cdot 2.03 \times 10^6[m/s] \approx 0.179 \ \mu m \qquad (3.24$$

where RRR is the measured residual-resistivity ratio (R_{300K}/R_{4K} . Thus, $\Lambda \ll \xi_0$ (Table 3.1 , so our Al films are in the "dirty limit" regime.

3.1.3 Quasiparticles in Equilibrium

Quasiparticles are created when Cooper pairs are broken. Quasiparticles are intrinsically unstable and they decay by emitting phonons or recombining with other qps. At a given equilibrium film temperature, the rate of pair breaking by thermal excitation equals the qp recombination rate such that the total density of quasiparticles, $N'(T$, is:

$$N'(T \ = 4N(0 \ \int_0^\infty \frac{\eta}{\sqrt{\eta^2 - \Delta^2}} f(\eta \ \ d\eta \qquad (3.25$$

The factor of four comes from two electrons (each with two possible spin states , and $f(\eta$ is the Fermi distribution function. When $T \ll T_c$, this equation can be solved

analytically[31],

$$N'(T \ = 4N(0 \ \Delta(T \ \sqrt{\frac{\pi}{2}\frac{k_B T}{\Delta(T}} \cdot e^{-\Delta(T \ /k_B T} \quad (3.26$$

or equivalently,

$$N'(T \ = N(0 \ \sqrt{8\pi\Delta(T \ k_B T} \cdot e^{-\Delta(T \ /k_B T} \quad (3.27$$

In our experiments, the base temperature $T \sim 35$ mK, so $N'(T \ \ll 1$. Thus we assume zero equilibrium qps are present.

3.1.4 Quasiparticles Out of Equilibrium: Energy Down Conversion

The energy downconversion process for non-equilibrium qps created when an x-ray is absorbed by a thin film can be described in terms of three sequential stages. The overview below is based on P.L. Brink's thesis [32] and publications from A. Kozorezov [33, 34, 35, 36]. An overview diagram shown in Figure 3.1 was provided by A. Kozorezov with slight modifications.

Stage I: Photoelectron to Electron Cloud

When a low energy x-ray with energy E_γ is absorbed by a superconducting Al film, it produces a photoelectron with energy $\Omega_{init} = E_\gamma$. Within tens of femtoseconds, the photoelectron shares its energy with neighboring electrons until the average energy $E_1 = \Omega_{init}/\langle n \rangle$ is reached. Here, $\langle n \rangle$ is the average number of quasiparticles produced through electron-electron interactions. The physical size, R (in nm , of this secondary cloud is empirically given by[32, 37] for x-ray energies ranging from 2 keV to 20 keV:

$$R = \frac{57}{\rho} E^{5/3} \quad (3.28$$

Here, ρ is the material density (g/cm^3 , and E is the energy of the primary electrons and Auger electrons. For the 2.6 keV x-rays used in our studies, Equation 3.28 indicates an electron cloud of radius $R \sim 10$ nm, which is small compared to our Al film dimensions (250 μm-wide $\times$ 350 μm-long $\times$ 300 nm-thick . We can treat the

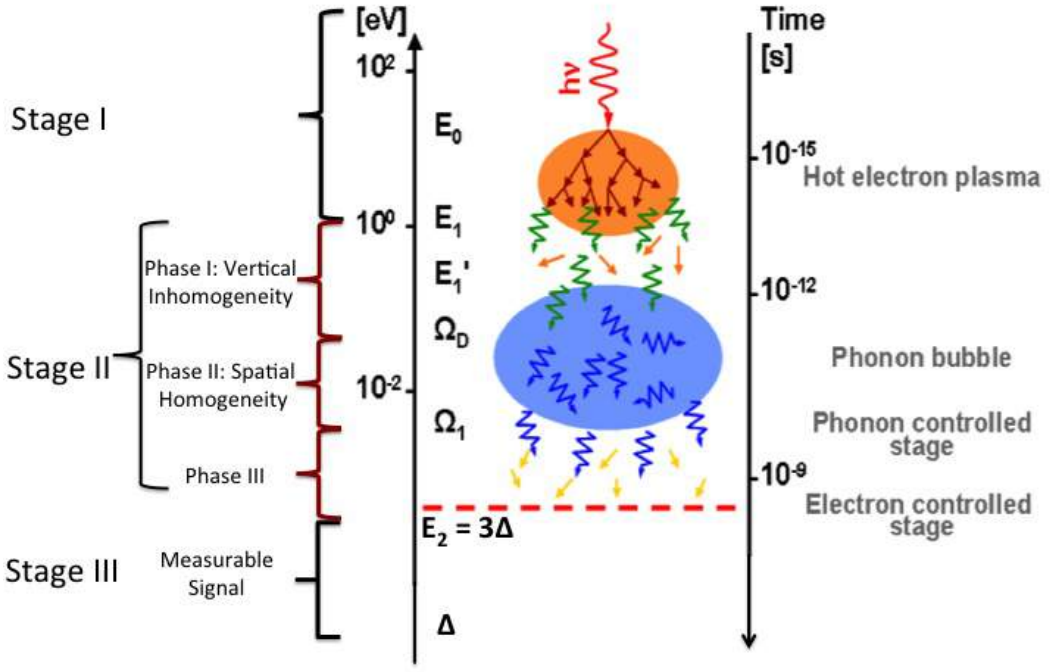

Figure 3.1: Quasiparticle (qp energy down conversion stages: Stage I is dominated by electron-electron interaction where an energetic photoelectron distributes energy ($\sim$ 1 fs to surrounding electrons and creates an electron cloud. Stage II begins when electron-phonon interactions play a significant role. In this stage, some portion of athermal phonon energy leaks into substrate and contributes to energy loss in our TES signals. Stage III begins when the average electronic energy reaching $\sim 3\Delta$, and the number of qps becomes constant as the subgap phonons don't have enough energy to break more Cooper pairs. Section 7.2.2 has a in-depth discussion about this stage.

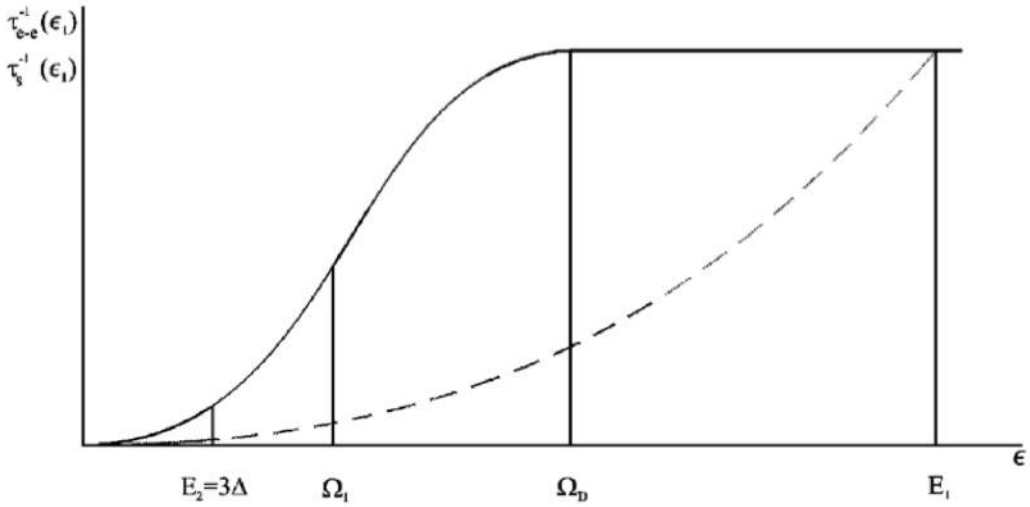

Figure 3.2: Electron-electron scattering rate, Γ_{ee} (dashed-line , and electron-phonon scattering rate, $\Gamma_{e\phi}$ (solide-line plotted against quasiparticle energy, ϵ. Stage II expands from $E_2 < \epsilon < E_1$.

position of the initial interaction in our Al film as a delta function. At the end of Stage I, the electron energies are $E_1 \sim 1$ eV. It is worth mentioning that $E_1 \gg \Omega_D$, the Debye energy. At this stage, electron-phonon interactions haven't yet played a significant role yet.

Stage II: From Electron Cloud to Phonon Bubble

Within tens of femtoseconds of the initial x-ray absorption (see Figure 3.1 , Stage II begins. At this time, the non-equilibrium electrons have energies $\sim E_1$, and the electron-phonon scattering rate, $\Gamma_{e\phi}(\epsilon = \tau_{e\phi}^{-1}(\epsilon$, is equal to the electron-electron scattering rate $\Gamma_{ee}(\epsilon = \tau_{ee}^{-1}(\epsilon$. Moreover, a portion of athermal phonons created in this stage can leak into the substrate, thereby contributing to energy loss in our W-TES signals.

In Figure 3.2, $\Gamma_{e\phi}$ and Γ_{ee} are plotted as a function of quasiparticle energy, ϵ. The dashed line corresponds to the electron-electron scattering rate while the solid line corresponds to the electron-phonon scattering rate. Stage II extends from energy

scale E_1 to E_2 (see Figure 3.1 . Experimentally, it has been shown[38], that the scattering rates depend on temperature according to:

$$\Gamma_{eeAl}(T \quad \propto \quad T^2 \tag{3.29}$$

$$\Gamma_{e\phi Al}(T \quad \propto \quad T^3 \tag{3.30}$$

Figure 3.2 shows the scattering rates in terms of the qp energy, ϵ, which depends directly on the electron cloud temperature, T. We can subdivide Stage II into three phases[33], where the end of each phase is marked by a characteristic energy (Ω_D, Ω_1 or E_2 .

As noted in Figure 3.1, from energy E_1 to Ω_D (vertical inhomogeneity phase , the energy lost to the substrate can depend strongly on the event location, z (i.e. proximity to the film-substrate boundary . Here $z = -d/2$ at the film-substrate boundary and $z = +d/2$ at the top surface of the film (of thickness d . Following Kozorezov's calculation, the energy lost to the substrate through phonon emission in this phase is given by[36]:

$$E_{loss,E_1\to\Omega_D}(z_0 \ = 4E\bar{\eta}p(1+\xi_c \ \sum_0^\infty \kappa(m^2\zeta^2 \ \times\cos\left[m\pi\left(\frac{1}{2}+\frac{z_0}{d}\right)\right] Y(m,\beta,1 \ , \tag{3.31}$$

where

$$\begin{aligned} Y(m,\beta,\xi \ =&\frac{\beta}{3}\Big\{1-3m^2\pi^2\beta^2\xi^2-3\beta^3\xi^3(-1 \ ^m(2-m^2\pi^2 \\ &+3m^3\pi^3\beta^3\xi^3\Big[\arctan\left(\frac{1}{m\pi\beta\xi}\right) \\ &+\mathrm{Si}(m\pi \ -\frac{\pi}{2}\Big]\Big\} \end{aligned} \tag{3.32}$$

and Si(x is the integral sine function. Appendix J includes the Matlab scripts and physical parameters used to compute the energy loss for our Al and W films during this phase. In Figure 3.3 we show the percentage of energy lost to the substrate for our 40 nm-thick W film (left and 300 nm-thick Al film (right .

For $\Omega_1 < \epsilon < \Omega_D$ (spatial homogeneity phase , more energy is lost to the substrate compared to the previous phase because phonons have longer mean-free-paths

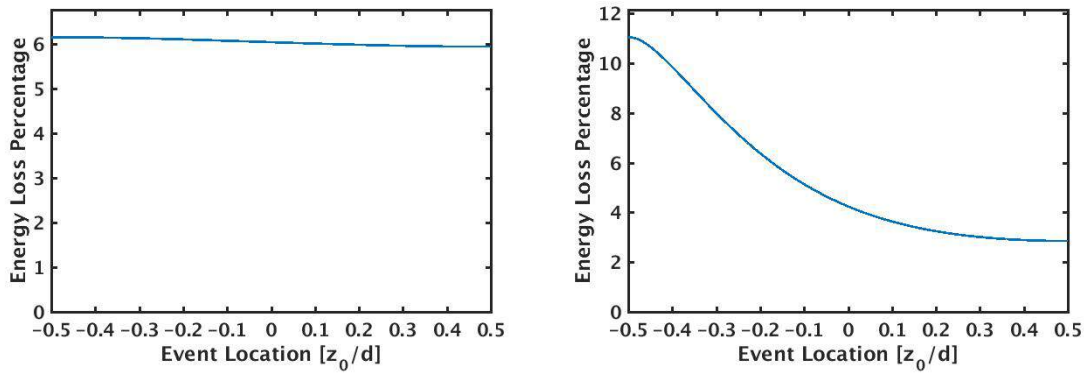

Figure 3.3: Percentage energy loss to the substrate for W and Al films calculated using Equation 3.31. The x-axis is the dimensionless distance from event location to the film-substrate boundary. $z_0/d = 0$ corresponds to the center of the film. *Left*: W film (40 nm-thick shows $\sim 6\%$ energy loss in this phase and is fairly independent of thickness. *Right*: Al film (300 nm-thick shows a larger variation of energy loss as function of event location.

and lifetimes. The energy loss to the substrate during this phase can be written in dimensionless form as follows:

$$E_{\text{loss},\Omega_{\text{D}}\to\Omega_1} = E\eta p\frac{1+\xi_c}{2}\frac{12Z(0}{11Z(0\ +3}\beta g\left(\frac{\Omega_{\text{D}}}{\Omega_1}\right), \tag{3.33}$$

where

$$\begin{aligned} g(x\ &= x\int_{1/x}^{1}\frac{dz}{z}f(z\ \Big\{\text{Ei}(1,z(x-1\ \ -\text{Ei}(1,1-z \\ &+\exp(z\ [\text{Ei}(1,1\ \ -\text{Ei}(1,xz\ ]+\ln\frac{x-1}{x(1-z}\Big\} \end{aligned} \tag{3.34}$$

Again, see Appendix J and Refs[33, 34] for details.

The third phase ($\Omega_1 \to E_2$ is characterized by $\Gamma_{ee} \ll \Gamma_{e\phi}$ and is dominated by electron down conversion. In this phase, electronic excitations can be considered long-lived, and no significant energy is lost to the substrate via phonons.

Combining Equation 3.31 and 3.33, the total loss of phonon energy to the substrate is therefore:

$$E_{loss} = E_{loss,E_1\to\Omega_D}(z_0\ \ + E_{\text{loss},\Omega_{\text{D}}\to\Omega_1} \tag{3.35}$$

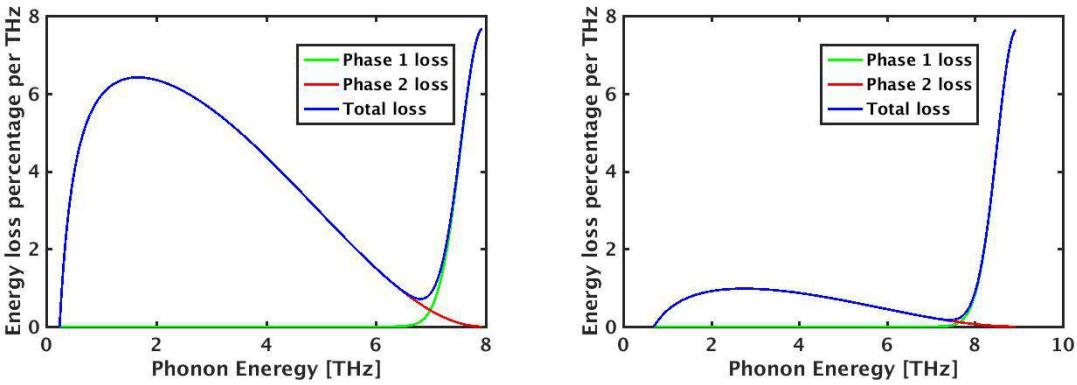

Figure 3.4: Percentage energy loss as function of the phonon energy up to the Debye energies. The sum over frequencies ranging from Ω_1 to Debye energy gives total energy loss. Both phase I and phase II distribution are shown. *Left*: Energy loss distribution for 40 nm-thick W film. The total energy loss came out to be 49 %. *Right*: Energy loss distribution for 300 nm-thick Al film. The total energy loss came out to be 11 %.

The results are shown in Figure 3.4 where we plot the phonon energy loss distribution as a function of phonon energy. The total energy loss was computed for $\Omega_1 < \hbar\omega < \Omega_D$. In our qp experiments, the W film thickness was fixed at 40 nm, but different Al film thicknesses were used (300 nm to 900 nm . The predicted energy loss percentages using this calculation for our Al film thicknesses are shown in Table 3.2.

	300 nm	500 nm	600 nm	900 nm
Al	11.0 %	6.6 %	5.5 %	3.7 %

Table 3.2: Percentage energy loss to substrate for Al with different thicknesses.

Stage III : Subgap Phonon & QP Trapping

Stage III ($\epsilon < E_2 = 3\Delta$ begins within $\sim$ 1 ns of the initial event, and this is the stage our measurements directly sense. It is in this stage when the qp number density becomes roughly constant and the phonons presents no longer have enough energy to break more Cooper paris. The qps start to diffuse from the event location inside

the Al. In our qp experiments, we treat this as a one dimensional process because we detect signals with W-TESs only at the ends of our Al films. While these qps diffuse randomly toward the W-TESs, they shed subgap phonons and provide additional energy loss to our signals. Moreover, depending on the film quality (i.e. purity, granary size , additional energy loss may also occur due to local gap variations in the Al that can trap qps, resulting in additional energy loss. Chapter 7 includes an in-depth description of this stage.

3.1.5 Another Approach to Substrate Energy Loss

Langenberg and Kaplan,*et. al.* used an acoustic mismatch model to calculate the phonon energy lost at the boundary between a superconducting film and an insulating substrate. Langenberg defined a dimensionless phonon trapping (loss factor, F_ω[39]:

$$F_\omega = 1 + \frac{\Gamma_{pb}(\Omega = 2\Delta}{\Gamma_{esc}} = 1 + \frac{4d}{\eta_t c_t \tau_0^{ph}} \quad (3.36$$

where, Γ_{pb} is the pair-breaking rate, Γ_{esc} is the phonon transmission rate into the substrate, d is still the film thickness, η_t is the transverse phonon transmission coefficient, and c_t is the transverse phonon velocity. Taking $\eta_t = 0.34$ and $c_t = 3.26 \times 10^3$ m/s[40], and $1/\tau_o^{ph} = \Gamma_{pb} = 134$ ps[32], we can compute the phonon escape probabilities $P_{esc}(\Omega = 2\Delta \ = F_\omega^{-1}$ as shown in Table 3.3:

	$300nm$	500 nm	600 nm	900 nm
Al	11.0 %	6.9 %	5.8 %	4.0 %

Table 3.3: Percentage energy loss to substrate for Al films with different thicknesses using acoustic mismatch model.

Notice the results shown in Table 3.3 are closed to the results shown in Table 3.2. Our experimental analyses incorporate the values shown in Table 3.2.

3.2 Quasiparticle-Trap-Assisted Electrothermal Feedback Transition Edge Sensors (QETs

As discussed in Section 2.2, the CDMS experiment uses QETs to absorb phonon energy that propagates to the surface of the detector crystals. The phonon energy breaks Cooper pairs in superconducting Al films and creates quasiparticles. These quasiparticles diffuse randomly until they reach a lower energy gap region at the W/Al interface, where they get trapped, relax in energy and get absorbed by the W-TES. This provides our phonon signals. To improve phonon energy collection from our detector substrates, we designed different QET geometries over the years to both increase surface coverage and boost signal sensitivity. In this section, we introduce voltage-biased TES physics first. We then discuss quasiparticle diffusion in Al films coupled to W-TESs, and present a new analysis of data first taken in 1997.

3.2.1 Transition Edge Sensor Physics

At temperatures less than the Debye temperature θ_D, the heat capacity of a metal in the normal state can be written as:

$$C = \gamma T + AT^3, \tag{3.37}$$

where γ is the coefficient for the electron system, and A is the coefficient for the phonon system. Their values are material specific. In a superconducting metal at low temperature, the electrons are weakly coupled to the phonons via a thermal conductance,G. Hence, when an external energy source disturbs the electron system, it takes finite amount of time for the film to cool back to its initial state. This weak coupling is critically important to the operation of a TES. A voltage-biased TES relies on the power balance between Joule heating created by the electron system, and cooling provided by the phonon system. Denoting R as the TES resistance and

R_l as a load resistance in series with the TES, this power balance can be modeled by:

$$C\frac{dT}{dt} = P_J - P_{cool} = \left(\frac{V}{R+R_l}\right)^2 R - \Sigma(T^n - T_b^n \ , \qquad (3.38$$

where T is the electron temperature and T_b is the phonon (or substrate temperature. $\Sigma = \kappa\mathcal{V}$ depends on the electron-phonon coupling constant, κ, and the TES volume $\mathcal{V}$. The exponent n is an integer ($n = 5$ for our tungsten electron-phonon system . When the TES is biased within its superconducting to normal transition, $dT/dt \approx 0$, and thus equilibrium power, P_0, can be set equal to the right hand side of Equation 3.38:

$$P_0 \equiv \left(\frac{V}{R+R_l}\right)^2 R = \Sigma(T^n - T_b^n \ . \qquad (3.39$$

These two equations can be used to define an "electro-thermal" feedback regime in which the film will be maintained at a constant temperature as any increase in T caused by an increase in R will lead to a decrease in Joule heating, P_J. A decrease in temperature (causing a decrease in R will have the opposite effect. This is described in more detail below.

Using a simple Thevenin equivalent circuit with voltage V and load resistance R_l, we can relate the TES current (I to the TES resistance ($R = R(T, I$:

$$\begin{aligned} I &= \frac{V}{R+R_l} \\ \frac{dI}{dR} &= -\frac{V}{(R+R_l\ ^2} \\ \frac{d\ \ln I}{d\ \ln R} &= \frac{R}{I}\frac{dI}{dR} = -\frac{R}{R+R_l} \end{aligned} \qquad (3.40$$

By setting $r = R_l/R$, Equation 3.40 becomes:

$$d\ \ln I = -\left(\frac{1}{1+r}\right) d\ \ln R \qquad (3.41$$

Thus:

$$\begin{aligned} d\ \ln R &= \alpha\ d\ \ln T + \beta\ d\ \ln I \\ &= \alpha\ d\ \ln T - \beta\ \left(\frac{1}{1+r}\right) d\ \ln R \\ \left(1+\frac{\beta}{1+r}\right) d\ \ln R &= \alpha\ d\ \ln T \end{aligned} \tag{3.42}$$

where we use the conventional dimensionless parameters

$$\alpha \equiv \frac{T_0}{R_0}\frac{\partial R}{\partial T} = \frac{\partial\ \ln R}{\partial \ln T} \tag{3.43}$$

$$\beta \equiv \frac{I_0}{R_0}\frac{\partial R}{\partial I} = \frac{\partial\ \ln R}{\partial \ln I} \tag{3.44}$$

This allows us to define a dimensionless quantity Γ where:

$$\gamma \equiv \frac{d\ \ln R}{d\ \ln T} = \frac{\alpha(1+r}{1+r+\beta} \tag{3.45}$$

The basic dynamics of a TES system can be described by considering the power terms P_J and P_{cool}[16]. First, consider the Joule heating term, P_J, and its derivative:

$$\frac{dP_J}{dR} = -2\frac{V^2}{(R+R_l\ ^3}R + \frac{V^2}{(R+R_l\ ^2} = \frac{P_J}{R}\left(1-2\frac{R}{R+R_l}\right) = -\rho\frac{P_J}{R}, \tag{3.46}$$

where

$$\rho \equiv \frac{R-R_l}{R+R_l} = \frac{1-r}{1+r}. \tag{3.47}$$

In equilibrium ($P_J \approx P_0$, and the first-order correction term to P_J is:

$$\delta P_J = -\rho P_0 \frac{\delta R}{R} = -\gamma\rho P_0 \frac{\delta T}{T_0} \tag{3.48}$$

Similarly, for the P_{cool} term, we can write:

$$\delta P_{cool} = n\kappa\ T_0^{n-1}\delta T = G\delta T \tag{3.49}$$

Combing Equations 3.38, 3.48 and 3.49 leads to:

$$\begin{aligned} C\frac{d}{dt}(\delta T &= -\left(\gamma\rho\frac{P_0}{T_0}+G\right)\delta T \\ \frac{d}{dt}(\delta T &= -\frac{G}{C}\left(\frac{\gamma\rho P_0}{GT_0}+1\right)\delta T \\ &= -\frac{G}{C}(L+1\ \ \delta T \end{aligned} \tag{3.50}$$

where we used the notation of M. Pyle[18] to define L:

$$L \equiv \frac{\gamma\rho P_0}{GT_0} = \frac{\gamma\rho\kappa(T_0^n - T_b^n}{n\kappa T_0^n} = \frac{\gamma\rho}{n}\left(1-\frac{T_b^n}{T_0^n}\right) \tag{3.51}$$

The solution to this first order differential equation (Equation 3.50 is:

$$\delta T(t\ = \frac{E}{C}e^{-t/\tau_{etf}} \tag{3.52}$$

where we have used $P_{ext} = E\delta(t$ to represent the initial energy deposition, and the electro-thermal feedback time constant, τ_{etf}, is defined by:

$$\tau_{etf} = \frac{C}{G}\frac{1}{L+1} \tag{3.53}$$

One of the advantages of the voltage-biased TES technology ($L \gg 1$ is its faster pulse recovery time compared to C/G ($L \ll 1$. We can write Equation 3.51 in terms of α, β and r to get:

$$L = \frac{\gamma\rho}{n}\left(1-\frac{T_b^n}{T_o^n}\right) = \frac{1}{n}\frac{\alpha(1-r}{1+r+\beta}\left(1-\frac{T_b^n}{T_o^n}\right) \tag{3.54}$$

If we assume $\beta \ll 1$, r $\ll 1$ and $T_b/T_o \ll 1$, we find that:

$$\tau_{etf} = \frac{C}{G}\frac{1}{1+\alpha/n} \tag{3.55}$$

To give some sense of our experimental values: $\alpha \sim 150$, $\beta \sim 0.3$, $n = 5$, $r \sim 0.02$, $T_b \sim 35$ mK and $T_0 = T_c \sim 80$ mK, and $L \approx 22$.

3.2.2 A Quasiparticle Trapping Primer

Quasiparticle transport dynamics have been studied experimentally by several groups[41, 42] using different materials, fabrication processes, and readout schemes. Our group studied qp transport in Al films many years ago using TESs. The results provided insightful information that contributed to the design of CDMS phonon sensors. However, some qp data from 1997 showed abnormal TES pulse shapes that we did not fully understand, and thus we did not publish those results in full. Fortunately, with our recently developed TES model (Section 7.1 we are now able to explain the abnormal pulse shapes seen in 1997. This new model is a powerful analysis tool that is being used to help define next-generation SuperCDMS QET sensors.

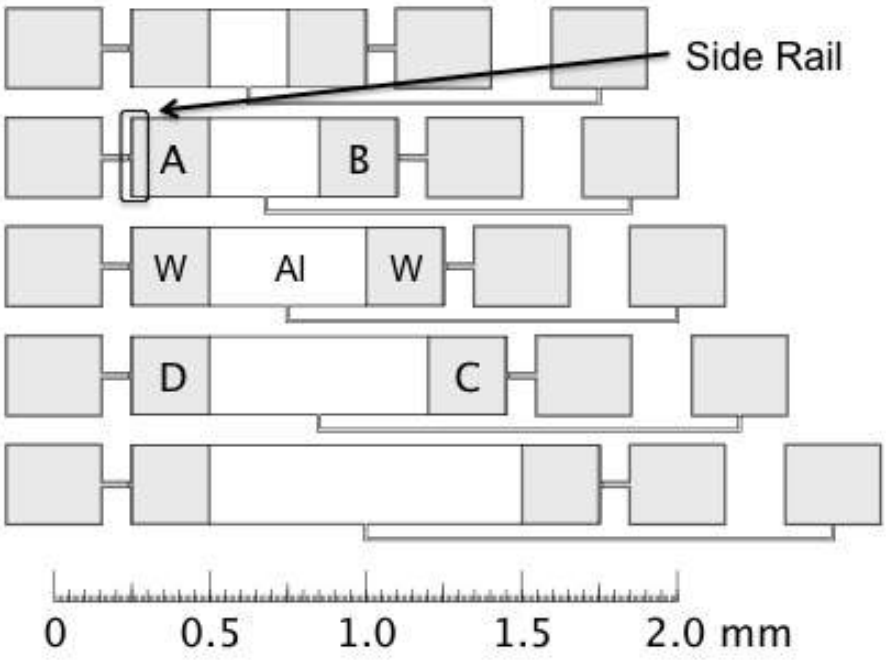

Figure 3.5: Quasiparticle test device geometries studied in 1997. Five different Al film lengths are shown here, but only two were studied (350 and 700 μm . In each 1997 device, the central Al film is connected to W-TESs (250 μm by 250 μm at its ends.

The qp test devices studied in 1997 are shown schematically in Figure 3.5. Devices with five different Al film lengths were fabricated, but only two device styles (350 and

700 μm-long Al were tested. Each device consisted of a 300 nm-thick Al film with W-TESs (250 μm $\times$ 250 μm $\times$ 40 nm-thick at each end. The two TESs (A & B, or C & D were individually biased but shared a common return through the Al film. The devices were exposed to low-energy fluorescence x-rays using an ^{55}Fe source.

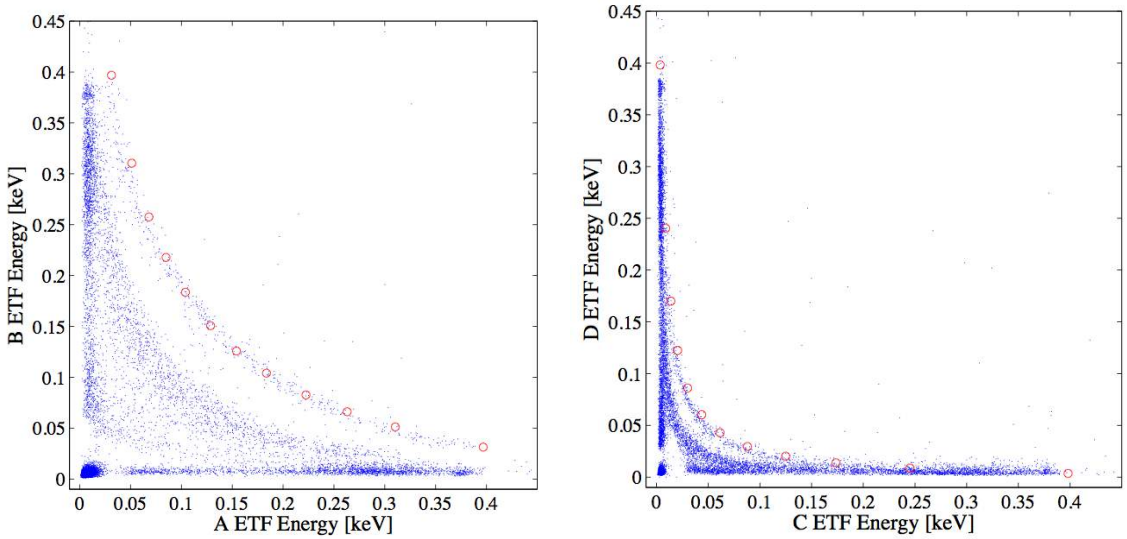

Figure 3.6: The old 1997 energy distribution data (blue dots for x-ray induced qp studies. The two axes correspond to the energy collected by the W-TESs on each end of a 300 nm-thick Al film. The red circles correspond to simulated events generated using a 1D diffusion model with a linear loss term. *Left*: Results from 350 μm-long $\times$ 250 μm-wide Al film. *Right*: Result from 700 μm-long $\times$ 250 μm-wide Al film.

Figure 3.6 shows results from x-ray experiments performed with the 350 μm-long Al device (left and the 700 μm-long Al device (right . The x-axis corresponds to the energy collected at one end of the Al film (TES A or TES C and the y-axis corresponds to the energy collected at the other end (TES B or TES D . The events of interest are those where the x-ray energy was directly absorbed in the Al film. These events appear underneath the red circles in Figure 3.6. The curvature present in the plots represents energy lost to the substrate. Thus, the longer Al film shows more energy loss (more band curvature than the shorter Al film. This is expected because qps generated in an x-ray event had to travel a greater distance to the W-TESs for the longer Al film. The red circles represent simulated events obtained

using a 1D diffusion model with proper boundary conditions. The data indicate a quasiparticle diffusion length L_{d} ~180 μm. Additional details can be found in M. Pyle's thesis[18].

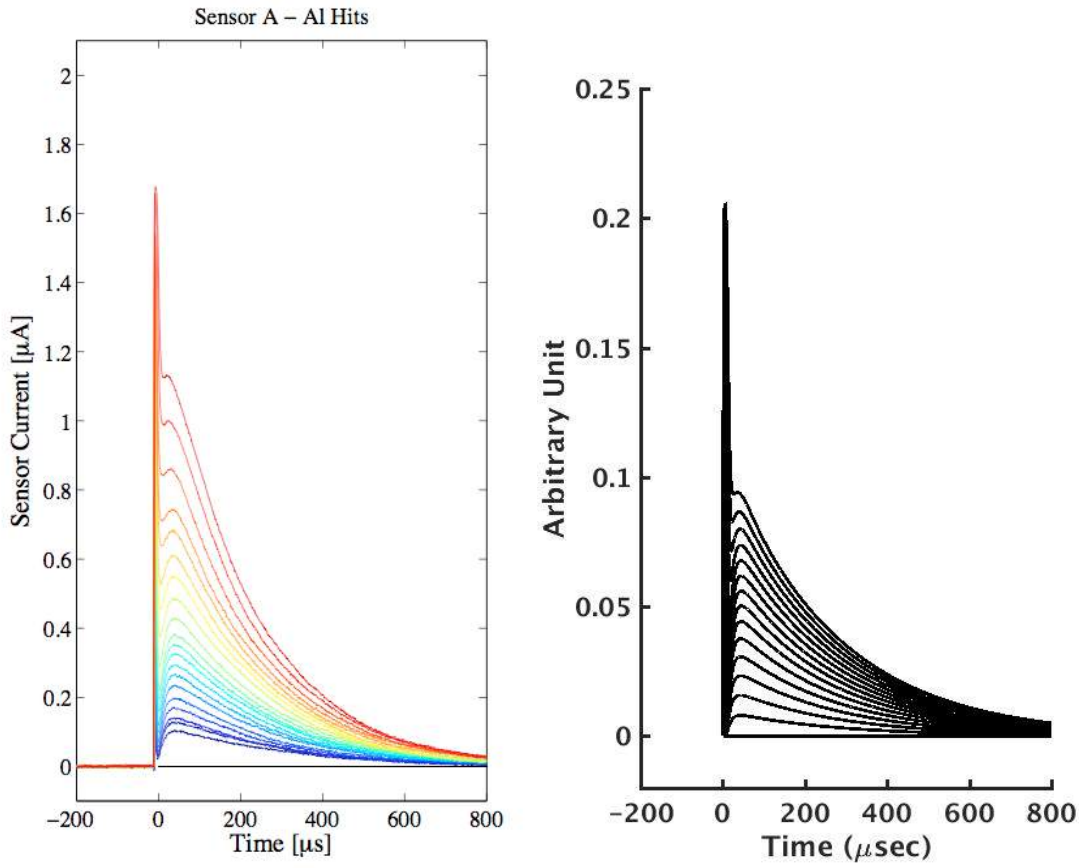

Figure 3.7: *left*: A series of real pulses from 1997 data that showed a double-peaked structure. The second peak can be explained by considering imperfections in the W/Al overlap region at the side rail. *Right*: Simulated pulses using our new model. (Model described in Chapter 7

Several pulse shapes were observed for TES A, as shown in Figure 3.7(left . A double-peaked structure is evident. By contrast, the pulses seen for TES B did not show such structure. The second peak observed with TES A we now understand was due to an imperfect connection between the W-TES and its Al/W side rail (as

indicated in Figure 3.5 . Simulated pulses from our new model are shown in Figure 3.7(right . These pulses have energies ranging from 0 keV to 2.2 keV. It is clear that our new model can reproduce the observed pulse shapes well. The model is described in detail in Chapter 7.

Chapter 4

Sample Preparation and Characterization

In the previous chapter we described some of the fundamental physics of quasiparticle (qp transport in Al films, and motivated its importance to the sensitivity of the CDMS detector phonon sensors. In this chapter we describe how the actual test devices used in our qp experiments were designed and fabricated. Although the present CDMS detector fabrication methods are mature and robust, new fabrication approaches that were used for our qp studies yielded results that are already feeding into the design of next-generation SuperCDMS SNOLAB detectors.

4.1 Device Geometry for Quasiparticle Study

Based on results of early qp experiments done by our group and reported in 1997 (Sec. 3.2.2 , we designed a new set of test devices that added a third, distributed, TES channel to veto substrate events. Figure 4.1 shows a portion of one 1 × 1 cm Si chip, where three full qp test devices are shown (along with two separate W diagnostic pads . The three main test devices each include a central Al film (250 μm-wide × 300 nm-thick × 250, 350, or 500 μm-long , with W-TESs (250 μm × 250 μm × 40 nm-thick at each end. The width of the interface (overlap region coupling each Al film to its W-TESs is 5 μm. All three TES channels on a device are separately

voltage-biased and read-out. The two main TESs share a common return through the central Al film. More subtle details about the test devices will be discussed in a later chapter when we show experimental results. Not shown here but included on each die are otherwise identical devices but with smaller W-TESs and a smaller Al film width (180 μm scale . Ref [43] and Appendix B gives the details of the die and device layouts.

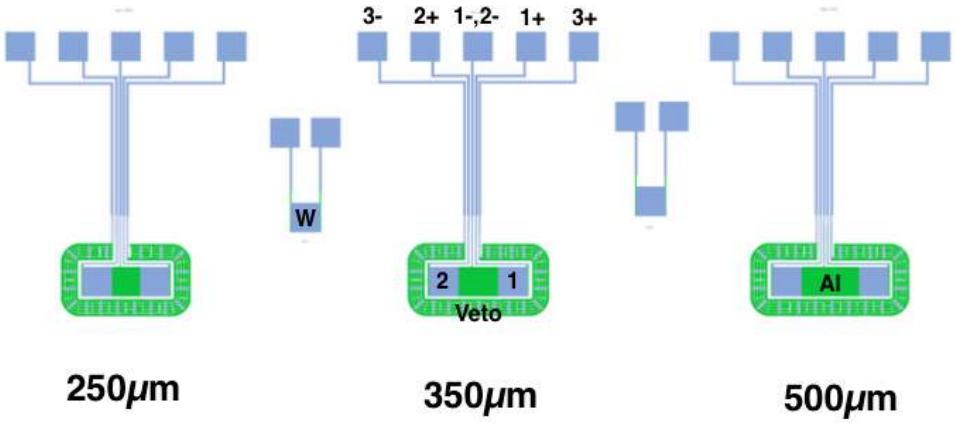

Figure 4.1: Top view of three test devices. Each includes two 250 μm $\times$ 250 μm by 40 nm-thick W-TESs at the ends of a 250 μm-wide by 300 nm-thick Al film (250 μm, 350 μm or 500 μm-long . Different Al thickness were also used. The two main TESs and the veto channels are separately voltage-biased and read-out via superconducting Al(Si wire bonds. (Bonding pads shown at top of die. W-TES1 and W-TES2 share a common return through the central Al film. Also shown are two square, isolated W-TESs used for T_c and R_n diagnostics.

4.2 Fabrication

The qp test devices shown in Figure 4.1 were photolithographically pattered on 100 mm diameter <100> silicon wafers. Compared to a more complex photolithography process, our devices are rather simple. They require just two masks: one for the W layer, and one for the Al layer. Our masks were designed using L-Edit software. Substrates were prepared and photolithography was performed in the Stanford

Nanofabrication Facility (SNF on the Stanford campus. All metal films (and an underlying 40 nm-thick sputtered Si layer were deposited using an AJA International ATC-2200 confocal DC/RF magnetron sputtering system (see Figure 4.2 located in the physics building. In our confocal sputtering system, the step coverage quality depends on wafer orientation and distance from the center of the extended wafer. In this thesis, we focus on two device topologies. The first we refer to as "non-inverted" (traditional CDMS style , where the W film is pattered on top of the Al film in the overlap region. The second topology, the "inverted" design, has the Al film pattered after the W-TESs are defined. Details about our fabrication process have been published[44], and are also described below.

4.2.1 High-Quality W and Al Superconducting Films

The W sputtering targets used for fabricating our qp test devices were supplied by VEM, Inc. and had purities of 99.960% (at. . The T_C of a W film depends critically on its crystal structure. Our films consist of an admixture of α-phase (bcc, T_C = 15 mK and β-phase (A15, T_C = 1 - 4 K . We and others have shown that the T_c of as-deposited W films can be adjusted by varying sputtering chamber parameters including target power, chamber pressure and substrate bias [45]. The presence of ferromagnetic materials such as iron in our W films also can significantly affect their T_C. In general, the higher the Fe content, the lower the W T_c. Most of the qp test devices studied in our work were made using a W target that contained 3.2 ppm (at. of Fe.

Our Al target was supplied by AJA Intl., Inc. and had a purity of 99.9998% (at. . Despite its high purity, our films are still considered to be in the "dirty limit" (Sec. 3.1.1 because the measured mean-free-path, Λ, of qps in the films is shorter than the superconducting Al coherence length ξ_0 (Section 3.1.2 . Both the grain size and film thickness can limit this mean-free-path (Section 4.3 .

Figure 4.2: AJA International ATC-2200 confocal DC/RF magnetron sputtering system used for the deposition of W and Al films in this work. The system allows us to vary Ar pressure, sputtering target power, and substrate bias voltage to adjust properties of our films, including W Tc.

4.2.2 "Non-Inverted" (Traditional CDMS style QP Devices

The non-inverted device fabrication process used was similar to that developed by CDMS for full scale detectors. An overview of the process is shown in Figure 4.3. To make a qp test device wafer, we first put the Si wafer through a traditional "diffusion-clean" procedure before loading it into our AJA sputtering machine (using a load-lock chamber . The base pressure of the system was $<$ 8.0E-8 torr. After loading the cleaned wafer in the chamber, the substrate was lightly RF-etched for 15 mins (substrate power 100 Watts at 3 mT Ar pressure . Next, a 40 nm-thick sputtered-Si

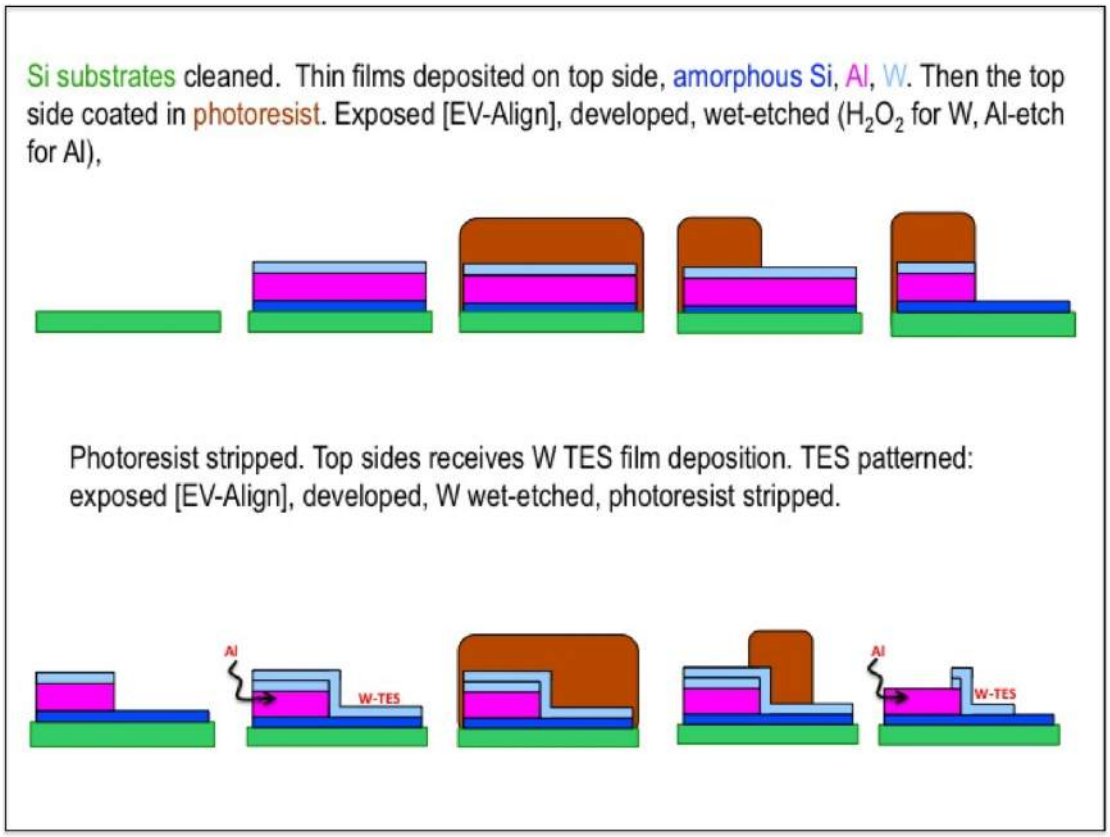

Figure 4.3: Side view of the fabrication process used for non-inverted qp devices. Current CDMS detectors used the same process except that both sides of the substrate are patterned and the αSi (dark blue layer is etched away to electrically isolate charge lines form phonon sensors.

layer (480 sec., 400 Watts, 5.5 mT Ar was deposited, followed by a 300 nm-thick Al deposition (1007 sec., 700 Watts, 2 mT Ar . Lastly, and still without breaking vacuum, a 30 nm-thick W "capping" layer was deposited (226 sec., 400 Watts, 3 mT Ar, -150 V DC substrate bias . This W layer was included to prevent formation of an Al oxide. After the trilayer deposition (αSi, Al, W was completed, the Si wafer was removed from the chamber and photolithography was performed. The W was etched using 30% H_2O_2 at 25°C (300 sec. for the initial trilayer 30 nm-thick film . The Al film was etched using KMG Al etchant 80:3:15 NP (H_3PO_4:HNO_3:CH_3COOH . Al

film etch rates depend strongly on temperature (roughly four times faster at 40°C compared to 25°C [44], and the process is exothermic. It was important not to over-etch the Al film. Doing so would comprise later fabrication steps (see Section 4.3 . After stripping the photoresist on the etched wafer, the wafer was brought back to the AJA to receive a final 40 nm-thick W deposition. This W layer was then pattered and etched to define the W-TESs on the finished qp devices (see Figure 4.1 .

A few points on the device geometry merit special comment. In this qp design, the uniformity of the second W deposition is critical because the W-TES film (40 nm-thick is dramatically thinner than the Al film (300 nm-thick . An imperfect connection between the W and Al films will severely limit qp energy collection. The interface region between the two films consists of two parts: an overlap region where the W lies fully on top of the Al, and a more problematic "waterfall" region (see next Section , whose quality is directly limited by the difference between the two film thicknesses.

4.2.3 "Inverted" QP Devices

The need to develop a fabrication process for an inverted Al/W QET geometry was not exactly new to us. In fact, one attempt to fabricate inverted devices (Al over W was made years ago when QETs were initially developed at Stanford. However, the resulting devices showed elevated T_c (> 100 mK and had broader transition widths ($\Delta T \gg 1$ mK , compared to devices made at the same time using the traditional geometry (W over Al . The exact cause was never determined but we believe the W was proximitized to higher T_c by residual Al that remained after Al etching. We re-visited the inverted device geometry when CDMS started using the new AJA sputtering machine and had direct access to SEM machine at both Santa Clara University and Stanford.

In particular, J.M. Kreikebaum dedicated significant time and effort to successfully develop a working recipe for making inverted qp devices. Figure 4.4 outlines the main process steps for the new inverted devices. The full process and fabrication recipe is attached in Appendix D. According to that recipe, after normal wafer cleaning, a

40 nm-thick αSi layer is sputtered onto the substrate, followed by a 40 nm-thick film of tungsten. The W film is then patterned and etched to define the W-TESs. The wafers are then put back into the sputtering chamber and the Al film is deposited. Because there is no waterfall issue with this inverted geometry, we can make devices with arbitrarily thick films of Al. Our first devices with this new recipe had Al film thicknesses from 300 nm to 900 nm.

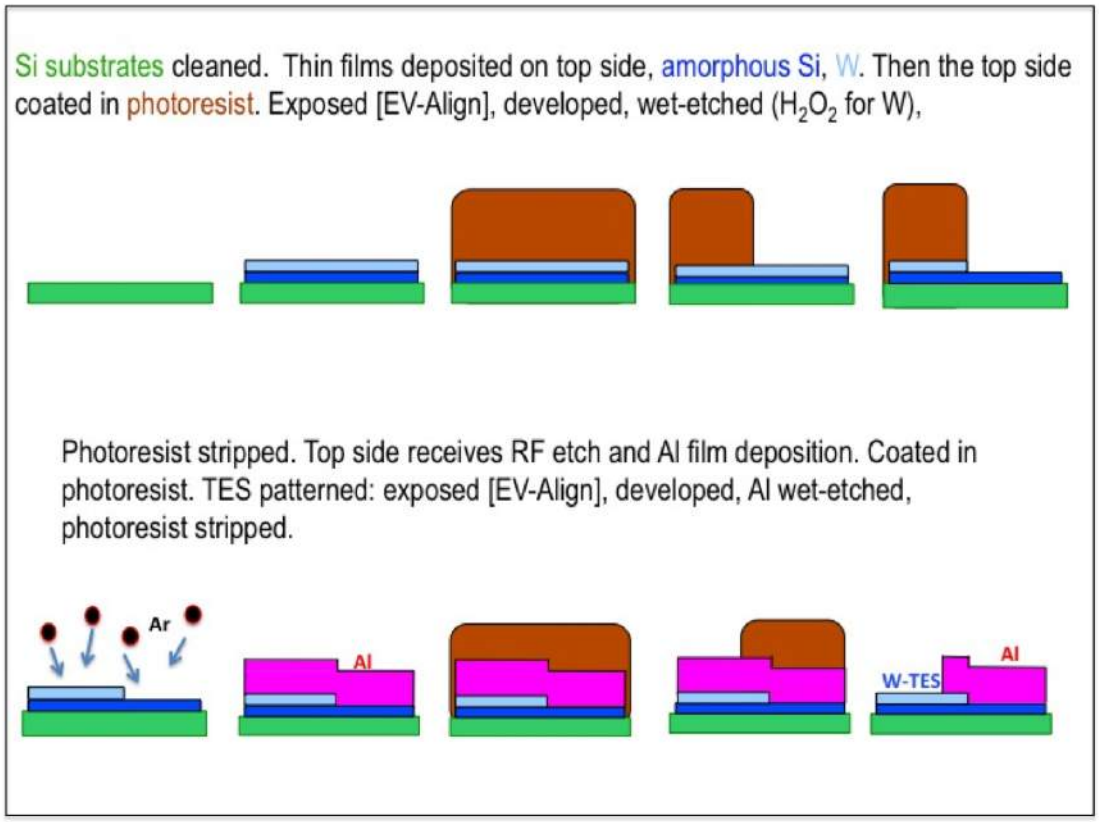

Figure 4.4: Side view for the "inverted" fabrication process that gives us freedom to vary the Al film thickness. The detailed process recipe is attached in Appendix D.

4.3 Film Characterization

The Stanford/SLAC CDMS group has established robust ways to tune W film Tc and achieve Tc uniformity across a wafer. For the SuperCDMS SNOLAB experiment we aim to have $T_c \sim 60$ mK. This should allow for even better detector energy resolution and energy thresholds compared to what was possible with CDMS Soudan detectors. We have also performed detailed studies to optimize the wet-etch processes used to define our Al/W QETs. In this section, we first show results of room temperature film characterization studies done with our qp devices using scanning electron microscopy (SEM , atomic force microscopy (AFM and focused ion beam (FIB imaging. We then summarize the basic physics of the residual-resistivity ratio (RRR test for metal films and show how the RRR value obtained relates to the microscopic properties of the measured film.

4.3.1 Room Temperature Studies

Scanning Electron Microscope (SEM : Step-Coverage Study

A HITACHI Model S-4800 Field Emission Scanning Electron Microscope was used to study the step-coverage integrity of Al/W interfaces on several non-inverted qp devices. In the SEM method, a beam of focused electrons strikes a specimen, ejecting primary backscattered electrons, secondary electrons, Auger electrons and x-rays. Different detectors in the SEM tool collect the different types of signal and the information is used to reconstruct a high-resolution ($\sim$ few nm image of the sample surface.

Figure 4.5 shows SEM images of QET wet-etch test samples used to study step-coverage issues originally present for 40 nm-thick W films patterned over 600 nm-thick Al steps. The arrow shown in Figure 4.5(a points to the location where SEM images were taken. Initially, a horizontal W overhang is created when Al etchant undercuts the W-capped Al base layer on these devices. The overhang gets bent towards the wafer surface when the active W-TES film is later deposited (Figure

4.5(b . Ultimately, the undercut allows for a tenuous connection between the W-TES and the Al film below. Figure 4.5 (c-e shows a side view of 300 nm-thick Al films that were etched using KMG 16:1:1:2 NP Al etchant at room temperature: (c An uninterrupted 300 sec. etch dip leaves rough sidewalls with pronounced cavities $\sim$ 200-300 nm in diameter. (d Results from a series of 17 x 30 sec. etch dips interspersed with DI quench dips. (e Results from a series of 59 x 10 sec. etch dips with DI quenches showing that sidewall roughness is reduced even further. Cavities only $\sim$10 nm in diameter remain. Finally, Figure 4.5 (f shows a QET device where a 40 nm-thick W film achieves continuous step coverage over patterned 600 nm-thick Al features.

Figure 4.6 shows the overlap region of a new "inverted" (Al over W fabrication approach that yields excellent devices with arbitrarily thick Al energy-collection films coupled to W-TESs. Figure 4.6 (b and (c shows before and after an additional Al etch was performed to remove residual Al from the top of the W film. As the result of the additional etching, Figure 4.6 (d shows the etch-back of the thick Al side walls (etch-back extends $\sim 1.5 \times$ the Al film thickness relative to the W-TES edges. We can easily compensate for this in the future by editing one mask. Overall, we showed that our inverted QET fabrication method is robust, it can be used with arbitrarily thick Al energy-collection films, and it yields excellent devices with W-TES Tc unaffected by the process changes.

Atomic Force Microscope (AFM : Film Granularity Study

We used atomic force microscopy[1][46, 47] to investigate the crystallite sizes in our sputtered Al and W films. An AFM has a cantilever with a sharp tip that scans across a sample surface to detect vertical and lateral deflections. The deflections are monitored by reflecting a laser beam off the back of the cantilever and the data is recored for further analysis. Figure 4.7 shows AFM images for Al films deposited in two different sputtering system: the CDMS Soudan Balzers system (left and our new AJA system (right . The AJA film appears smoother than the Balzers film in the AFM images. We also compared the bulk granularity of AJA and Balzers films

[1]AFM work performed at Santa Clara University CNS

using SEM and found that the AJA films also appear more uniform throughout the full thickness of the film. Work is underway to better quantify the structure of our films because film granularity and/or irregularities in grain structure can significantly limit qp transport. As we will see in Chapter 6, smoother Al films allow better qp diffusion (but not by much , which improves overall energy collection in Al/W QETs.

Focused Ion Beam (FIB : Step-Coverage Study

A focused ion beam (FIB instrument operates in a similar fashion to an SEM but it typically uses a beam of gallium ions rather than electrons. It is also inherently destructive to the specimen (even more so than SEM, due in part to the size and mass of Ga ions . We partnered with Evans Analytical Group (EAG to obtain FIB images of our samples. Figure 4.8 (center shows a "top view" SEM image of one qp test device we imaged using FIB. This particular device had 180 μm-wide $\times$ 180 μm-long $\times$ 40 nm-thick W-TESs at the ends of a 500 μm-long $\times$ 180 μm-wide $\times$ 300 nm-thick Al film. The tiny slip in the left (right of the central image corresponds to the left (right side view image. As mentioned earlier, the Al etching is an exothermic process and the etch rate is heavily dependent on temperature performed during fabrication. The images shown correspond to a sample that underwent two 15 sec. Al etches (DI quench , with agitation. We believe the pocket (or void seen in the images was produced during the etch process by trapped Al etchant, caused in part by temperature variations at the film surface present during the exothermic etch. Figure 4.9 compares results for two different etch times (15 sec. per dip or 20 sec. per dip . Using FIB and SEM we were able to show[] that by using a series of short Al etch dips rather than just a few long dips we can reduce local temperature gradients at the surface(s of the Al film. This ultimately provides a more reproducible and more uniform etch, yields smoother Al sidewalls, and results in better connectivity of the W-TES to the main Al film of our QET devices (Figure 4.10 .

4.3.2 RRR Measurements

We learned a lot about our Al films using the room temperature techniques described in the previous section. However, to draw more quantitive conclusions, we needed to cool our samples to 4K and measure the residual-resistivity-ratio (RRR of the films (RRR= ρ_{300}/ρ_{4K} . It is well known that RRR values can be affected by the presence of impurities and grain boundaries; both cause excess electron scattering that reduces conduction within the film. Generally speaking, larger the RRR value, the better the film quality. We can also deduce the diffusivity constant, D, of our films using their measured RRR values. To show this simply, we start with the DC electric conductivity of a metal[48]:

$$\sigma = \frac{ne^2\tau}{m} \tag{4.1}$$

where n is the number density of the mobile electrons; e is the electric charge; m is the electron mass, and τ is the electron scattering relaxation time. Equivalently, we can write

$$\tau = \frac{m}{\rho n e^2} \tag{4.2}$$

Here, $\rho = 1/\sigma$ is the resistivity. Therefore, the ratio of the electron scattering time (and thus the ratio of the mean-free-path, λ at room temperature vs. 4K can be well approximated by measuring the resistance of the sample at both room temperature and 4K. At 273K, the scattering time in high-purity Al is $\tau = 8\ f$s (Ref. [48] Table 1.3 . Using the mean-free-path, $l = \lambda = v_0\tau$, with v_0 being the average electron speed, the RRR measurement can be written as:

$$\text{RRR} = \frac{\rho_{273K}}{\rho_{4K}} = \frac{\tau_{4K}}{\tau_{273K}} = \frac{\lambda_{4K}/v_F}{\lambda_{273K}/v_F} \tag{4.3}$$

We can treat $v_0 \sim v_F = 2.03 \times 10^6$ m/s for both 273 K and 4 K since the Fermi temperature for Al is 13.6×10^4 K $\gg$ 300 K $>$ 4 K (Ref.[48] Table 2.1 . Therefore,

the mean-free-path at 4 K simply:

$$\Lambda = v_F \times (RRR \times \tau_{273K} \tag{4.4}$$

Finally, the diffusivity becomes

$$D = \frac{1}{3}\Lambda v_F = \frac{1}{3}\ \tau_{273K}\ v_F^2 \times RRR \tag{4.5}$$

The CDMS films made in the AJA had RRR ∼10 for 300 nm-thick films and RRR ∼20 for 600 nm-thick films, indicating we were thickness limited. We believe surface roughness dominates the scattering process in these films. In Appendix E we show additional data for a much thicker film (2100 nm with RRR ∼30; it appears bulk scattering effects dominate in that case. Applying Equation 4.5 to our AJA Al films at 4K gives $D \sim 0.11 m^2/s$ for the 300 nm-thick films and $D \sim 0.22\ m^2/s$ for the 600 nm-thick films. Since $D \propto \sqrt{T/T_c}$, we found $D = 0.019\ m^2/s$ for 300 nm-thick film and $D = 0.037\ m^2/s$ for 600 nm-thick film at 35 mK.

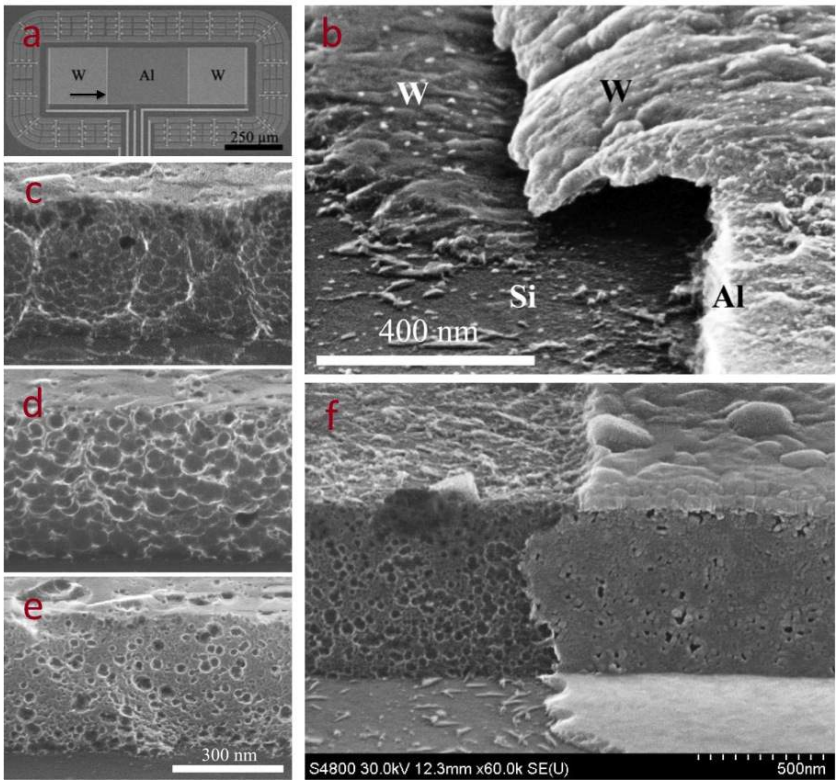

Figure 4.5: "Non-inverted" device. (a The arrow points to the region where SEM images were taken. (b W-TES overhang after final etching of a finished device. The horizontal W overhang is created when Al etchant undercuts the W-capped Al base layer of these devices before the active W-TES film is deposited and gets bent down toward the wafer surface. (c-e shows etched 300 nm-thick sputtered Al films using KMG 16:1:1:2 NP Al etchant at room temperature: (c An uninterrupted 300 sec. etch dip. (d Results of 17 x 30 sec. etch dips (interspersed with DI quenches , and (e Results from a series of 59 x 10 sec. etch dips (also interspersed DI quenches . (f A QET device showing continuous step-coverage for a 40 nm-thick film patterned over a 600 nm-thick Al film.

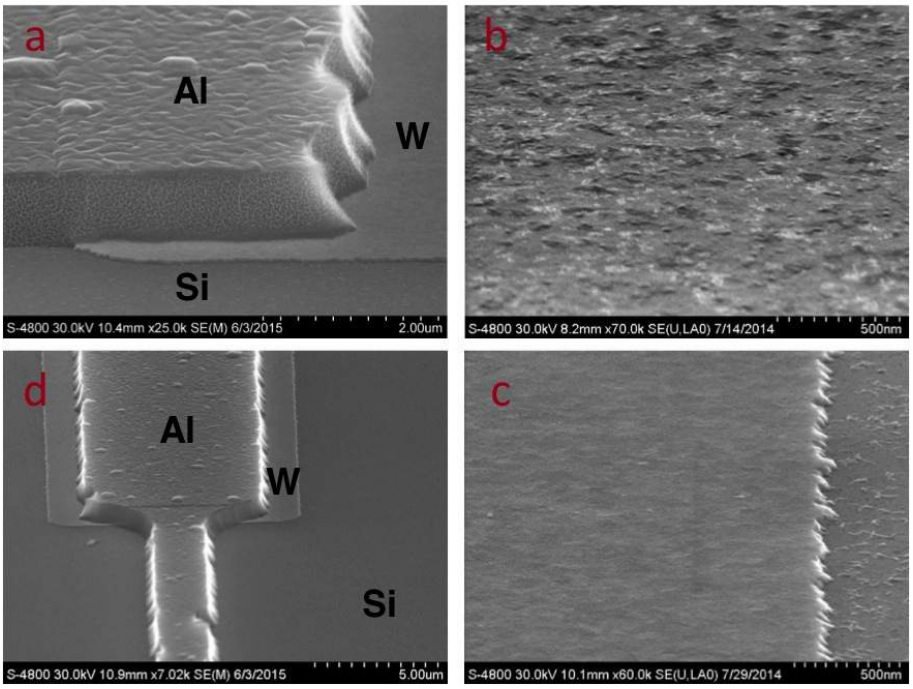

Figure 4.6: (a Inverted QET device with 600 nm-think Al film deposited and etched after 40 nm-thick W-TESs were patterned on Si. (b Residual Al left on the W-TES after patterning and etching the Al film. (c Residual Al was easily removed with additional etching. (d For this test the same masks were used as for our traditional non-inverted QET device geometry. This caused the observed etch-back of the thick Al side walls (∼150% of the thickness of the film relative to the W-TES edges. We can easily compensate for this in the future by editing one mask.

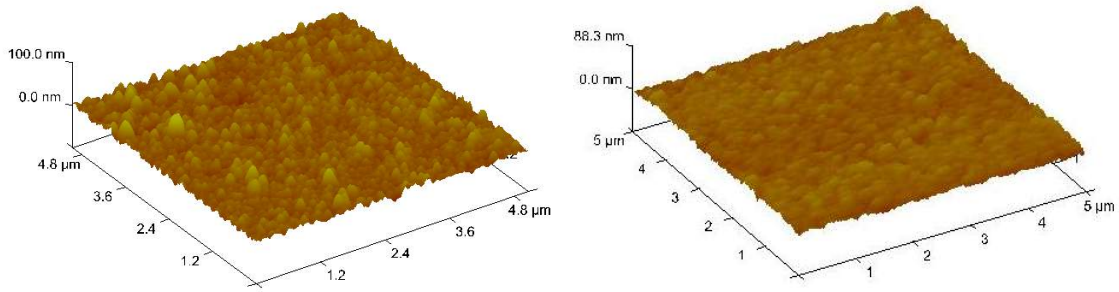

Figure 4.7: *Left*: Sputtered Al film surface produced by Balzers machine. Granular structures seen on the surface are $\sim$ 200 nm-wide $\times \sim$ 40 nm high. *Right*: Sputtered Al film surface produced by the AJA machine. We believe the detailed grain structure within each film plays a large role in their efficiency as energy collectors in our QET devices.

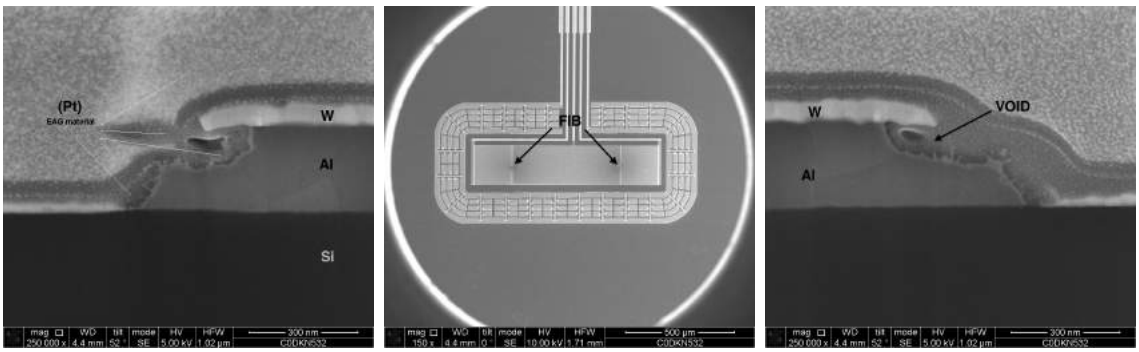

Figure 4.8: Center: Top view (SEM of qp test device consisting of a 180 μm-wide, 500 μm-long Al thin film (300 nm coupled to two 180 μm by 180 μm W-TESs (40 nm-thick . The small left (right slip in the Al/W overlap region was imaged to provide results shown above on the left and right images. Platinum was used to protect the materials being imaged while gallium ions bombarded the specimen.The images shown are for a 300 nm-thick Al device that was etched using two 15 sec. (agitated dips separated by a DI quench. The void is likely due to uneven etching caused by local temperature gradients at the Al surface during the etch.

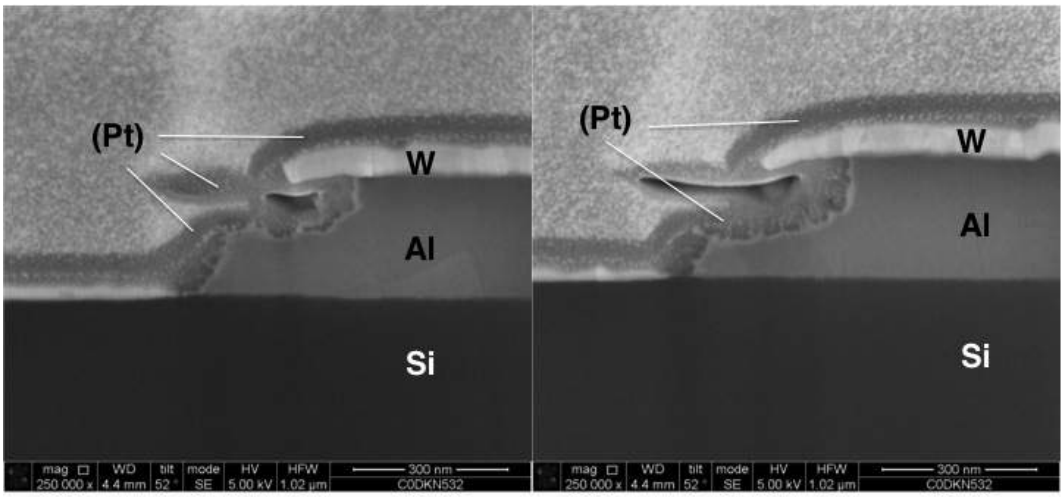

Figure 4.9: FIB images showing the W/Al overlap region for two qp test devices that had the Al etch performed slightly differently. *Left*: Results after two 15 sec. Al etch dips (with DI quench and agitation . *Right*: Results after two 20 sec. Al etch dips (with DI quench and agitation . Note the more pronounced undercut of the W film as the Al etched in the sample on the right.

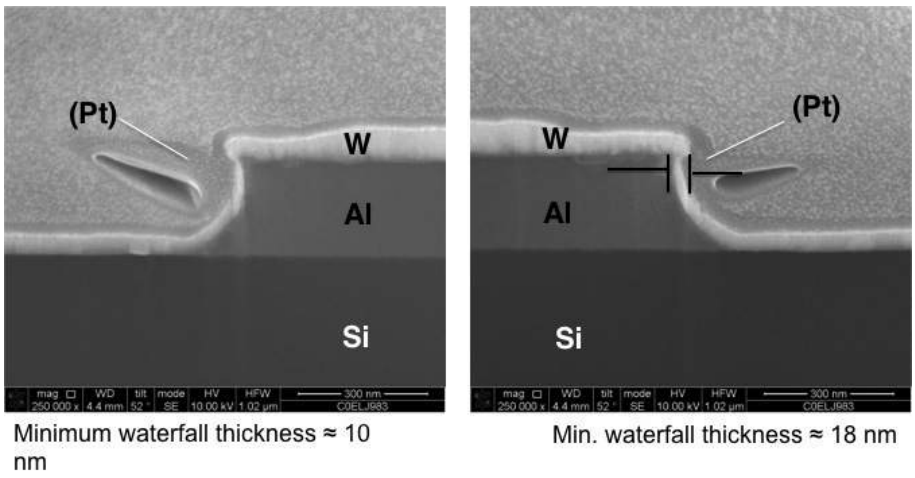

Figure 4.10: With repeatedly short agitation in the Al etching solution we can reduce local temperature gradients and achieve a more uniform etch. This also improves W film connectivity along the Al sidewall, and thus yields better energy collection in the TESs.

Chapter 5

Experimental Setup

All of the quasiparticle experiments and majority of AJA Tc sample measurements described in this thesis were conducted in a Kelvinox-15 ^{3}He/^{4}He dilution refrigerator that operates $\sim$ 35 mK and is housed in Varian 029. We designed, and Physics Machine Shop staff machined, the sample and source holders that made these studies possible. The wiring from the room temperature stage down to the mixing chamber stage included manganin wire twisted pairs (4-wire Tc measurements , constantine wires (thermometer sensors , copper wire (biasing lines , and niobium titanium (superconducting wires . Figure 5.1 shows the schematic circuitry setup, where the TES bias boxes, SQUID bias boxes and feedback amplifiers are at room temperature (in red , (20 mΩ shunt resistor, input and pick-up coils and SQUIDs are heat sunk to the 1K pot stage (in blue and the QET test devices are at the mixing chamber stage (in green . Analog DC SQUID preamplifier and feedback boxes were used to amplify W-TES signals, and these signals were further amplified by SRS560 with bandwidth (0.2 Hz to 1 MHz . The trigger was done by summing the W-TES1 and W-TES2 signals using SR560. The NI-PCI 6115 DAQ along with BNC-2110 were used to simultaneously record all three W-TES channels with 5 MHz sampling rate. Events were typically stored in .mat files (500-event per file the further data processing.

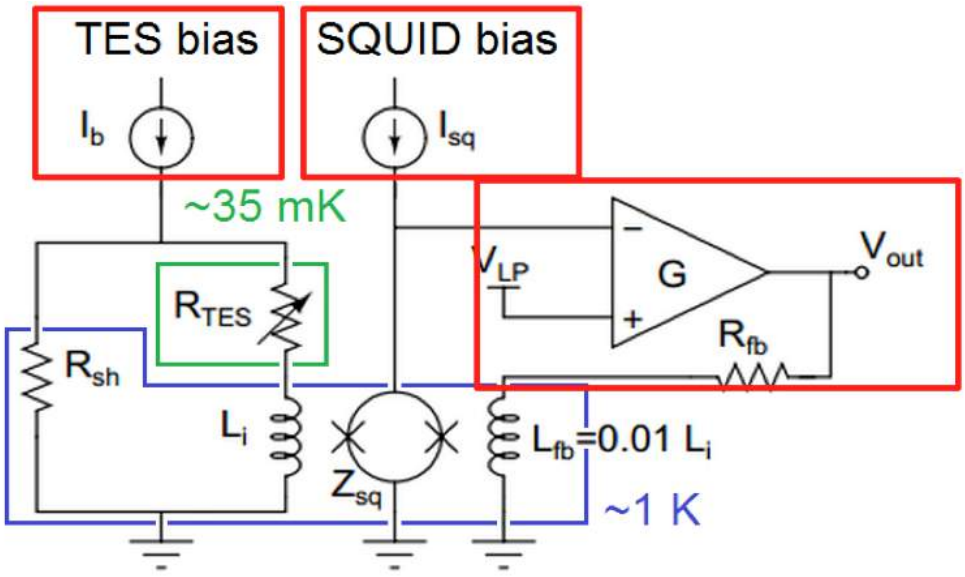

Figure 5.1: Simplified schematic circuit diagram used for the QP studies. The fundamental operation principles are identical to those used for CDMS phonon readout. The test devices are located at the coldest stage of the fridge (∼ 35 mK in green . The shunt resistors and SQUID preamplifiers are coupled to the 1K pot stage (blue , and are connected by wires to room temperature electronics (red .

5.1 Kelvinox-15: ^{3}He/^{4}He Dilution Refrigerator

An Oxford Kelvinox-15 ^{3}He/^{4}He dilution refrigerator was used to provide a stable operation temperatures below 100 mK continuously. The fundamental principle of a ^{3}He/^{4}He dilution refrigerator (DR is to utilize the finite solubility of ^{3}He in ^{4}He, and the enthalpy change of ^{3}He atoms moving from one phase (^{3}He rich to another (^{3}He dilute to cool a ^{3}He/^{4}He mixture to tens of mK. The physics is summarized below.

Let's denote the concentration of ^{3}He in the DR mixture by:

$$x = x_3 = \frac{n_3}{n_3 + n_4}, \tag{5.1}$$

where n_3 (n_4 is the number of ^{3}He (^{4}He atoms or moles. The x-T phase diagram at constant pressure of such a mixture is shown in Figure 5.2 [49]. The temperature that

turns ^{4}He from normal fluid to superfluid decreases from 2.177 K to 0.867K as the concentration of x increases from 0 to 67.5 % (the Lambda line . The superfluidity of ^{4}He ceases to exist as $x > 67.5\%$. The shaded two-phase region is where the DR operates. Here the mixture is separated into two phases as shown in Figure 5.3: a ^{3}He rich phase and a ^{3}He dilute phase (relative to ^{4}He . Since at zero temperature there is still a finite solubility of ^{3}He in ^{4}He (6.6% , this means a DR can theoretically produce arbitrary low temperature. The "right" percentage of the ^{3}He: ^{4}He mix ratio to operate a DR varies with DR. For example, the KO-15 has $^3\text{He} - ^4\text{He}$ mix ratio $\sim$ 20% while the mix ratio is $\sim$ 16% for the Soudan CDMS DR. These variations on the concentration depends on various parameters such as the physical sizes/dimensions of the mixing chamber and/or the volume of piping to connect various parts of the system (cryostat, pumps, etc.

In the two-phase region, the lighter, ^{3}He rich phase will float on top of the ^{3}He dilute phase. Cooling power is provided when the higher enthalpy ^{3}He atoms in the concentrated phase, $H_C(T$, diffuse to the dilute phase, $H_D(T$, with lower enthalpy. The enthalpy change of mixing at constant pressure is written by[50]:

$$H_D - H_C = T(S_D - S_C \ = T(106T - 22T \ = 84\ T^2 \text{ J/mol}, \qquad (5.2$$

where S_D (S_C is the entropy in the ^{3}He dilute (concentrated phase:

$$S = \int_0^T \frac{C_3(T'}{T'} dT' = 106(22\ T \qquad (5.3$$

Therefore the cooling power, $dQ(T\ /dt$, provide by the mixture is then

$$\frac{dQ}{dt} = \frac{dn_3}{dt}\Delta H = \frac{dn_3}{dt}(H_D(T\ - H_C(T\ = 84\ \frac{dn_3}{dt}\ T^2 \propto T^2. \qquad (5.4$$

In Figure 5.3 we show a schematic of a generic DR, alongside a photo of our KO-15 unit, with corresponding parts indicated. In the operation mode, the ^{3}He atoms enter the main impedance after getting cold-trap cleaned from the condenser side and pre-cooled to $\sim$1 K. After going through series of heat exchanges, the ^{3}He atoms dissolve in the the ^{3}He rich phase in the mixing chamber. These ^{3}He atoms diffuse

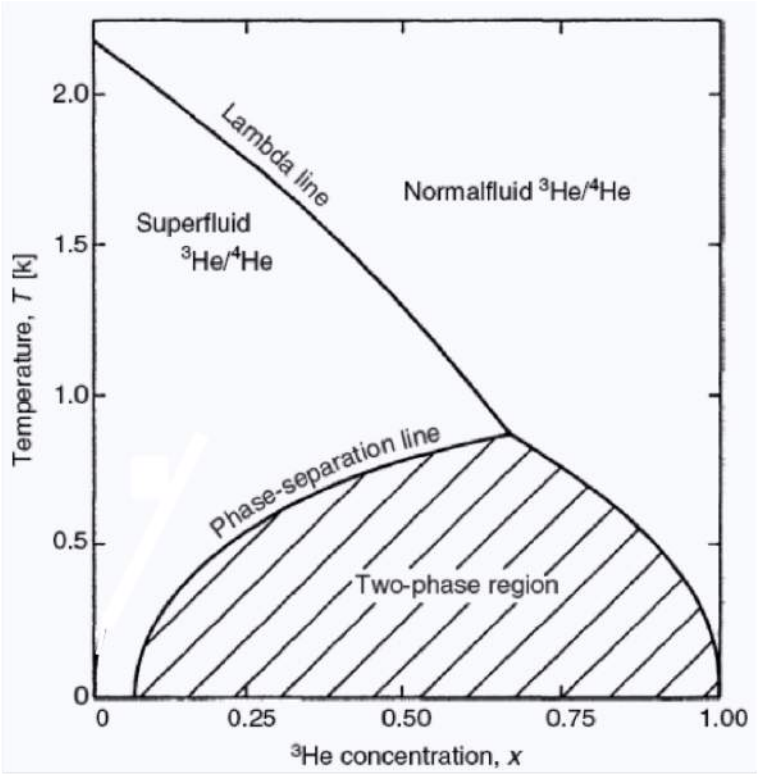

Figure 5.2: Phase diagram of ^{3}He and ^{4}He mixture with temperature versus ^{3}He concentration. Lambda line is shown, below which is the superfluid phase until the phase-separation line. The dilution refrigerator is operated at the two-phase region. The finite solubility of ^{3}He even at zero temperature provides the advantage of this cooling technology.

through the phase boundary and carry the heat with them to provide the cooling of the system. On their way to "still", the "cold" ^{3}He atoms exchange heat with the incoming "warm" ^{3}He to reduce heat load to the mixing chamber. In the still, the dilute phase of the mixture gets pumped out using a sealed circulation pump. Since the vapor pressure of ^{3}He is $\sim$1000 times higher than ^{4}He, the reduction in concentration of ^{3}He causing the ^{3}He in rich phase diffuse through the boundary in the mixing chamber. This osmotic pressure[50] is how the ^{3}He atoms get pushed through the phase boundary.

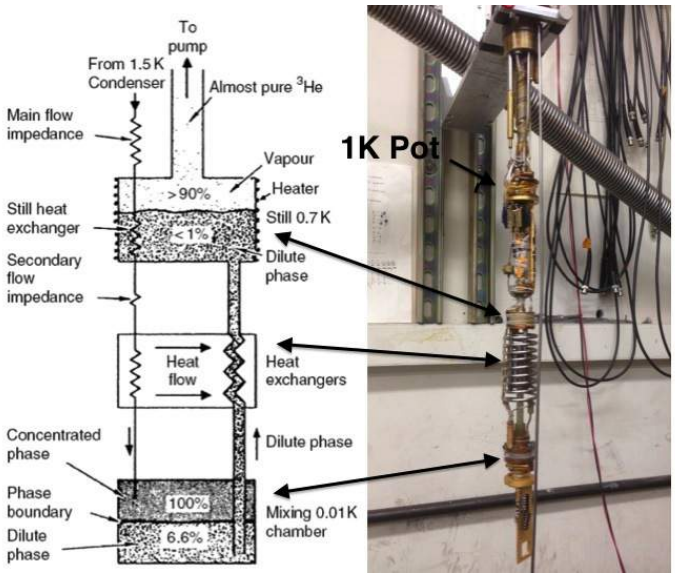

Figure 5.3: *Left*: A schematic representation of a dilution refrigerator. In operation mode, the ^{3}He gas entering the main impedance after getting cold-trap cleaned from the condenser side and pre-cooled to $\sim$1 K. After going through series of heat exchanges, the ^{3}He will dissolve in the the ^{3}He rich phase in the mixing chamber. These ^{3}He molecules diffuse through the phase boundary and carry the heat with them to provide the cooling of the system. After another heat exchange stage, the ^{3}He atoms got evaporated in the still and leave the fridge unit. Right: The physical dilution unit used with the corresponding parts to each stage shown in arrows. 1K pot is also shown in this picture.

5.2 Temperature Readouts

Three thermometers are installed in the KO-15 at three locations: one each at the 1K pot, still and mixing chamber. Unfortunately the still thermometer has one of the four wires broken inside the fridge, so only a two wire measurement can be done. Hence, to avoid excess heating of the still, we only read out the still thermometer value when we are troubleshooting fridge problems. The original 1K pot thermometer was replaced with an uncalibrated one by Oxford Instrument, Inc. last time when we sent it back for major still leak repair. Therefore, we only know the nominal 1K-pot working resistance values without knowing exact temperatures. This thermometer was read out using a Fluke 8842A multimeter in the 4-wire resistance measurement mode. At

the mixing chamber, we use a RuOx thermometer, and its resistance is measured using a LR-700 AC resistance bridge. This thermometer was cross calibrated with another nuclear-orientation[51] calibrated RuOx in AST dilution refrigerator. The current study of the W film Tc for SuperCDMS SNOLAB are quoted based on thermometer in KO-15 mixing chamber. We have long observed temperature discrepancy from fridge to fridge, test facility to test facility. In general KO-15 readings are higher than AST by $\sim$ 10 mK, and higher than Berkeley 75-fridge by 20-25 mK. We are still in the process of understanding these temperature difference. (This requires understanding noise performance and heat loading model in each system.

5.3 Cold Electronics

For our studies, the current going through a voltage-biased TES is $\sim$10 μA. When an energy is absorbed by a TES, its resistance increases and current decreases. This change in current induces a change in magnetic flux in the superconducting input coil (labeled L_i in Fig.5.1 that is in series with the TES. We use **S**uperconducting **QU**antum **I**nterference **D**evice (SQUID arrays as a pre-amplifier to convert the current signals to voltage signals. The voltage signals ($V_{\rm out}$ get further amplified in the room temperature stage.

5.3.1 SQUID Chips

The **S**uperconducting **QU**antum **I**nterference **D**evice (SQUID [52, 53] acts as transresistance pre-amplifier that converting current signals from the input coil to the voltage signals for the next stage amplifier. Our SQUID chips (Figure 5.4 (a were fabricated and tested by the National Institutes of Standards and Technology (NIST (See Appendix F . They were GE-varnished to the SQUID holders and connected to the circuit with superconducting wire bonds (initially Al(Si ; later in PbInAu . Figure 5.4 (b shows the back side of the four-channel SQUID chip holder that was gold-plated and heat sunk to the 1K pot. Four thin Nb foils located in the back the SQUID chips were used to shield the external magnetic field. Each SQUID chip

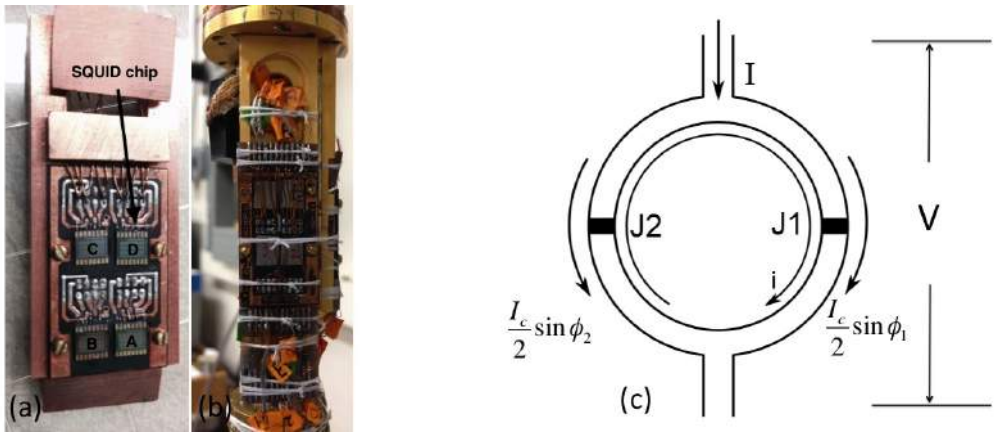

Figure 5.4: (a Four Nb-based SQUID chips along with shunt resistors (20 mΩ and 10 mΩ were fabricated and tested at NIST. Each chip consists of ∼100 SQUIDs in series. The chips shown were GE-varnished on CDMS-style SQUID holders and connected to the holder by superconducting wire bonds. (b The back side of the SQUID holder is shown. Four pieces of Nb foil functioned as external magnetic field shield. The SQUID chips/holder were heat sunk to the 1K pot. (c Current flows through junction J_1(J_2 is $\frac{I_c}{2}\sin\phi_1$($\frac{I_c}{2}\sin\phi_2$. The phase difference, $\Delta\phi = \phi_2 - \phi_1$, gives the sinusoidal dependent of the maximum current.

consists of one hundred Nb-based thin-film loop array. Collectively it acts as a two-junction DC-SQUID. A DC-SQUID is a highly sensitive quantum magnetometer. It utilizes the fact that magnetic flux in a superconducting loop is quantized in increments of the flux quantum, $\Phi_0 = h/2e$. The maximum critical current go through the device can be shown to be [22]

$$I_{tot} = I_c \left| \cos\left(\pi \frac{\Phi}{\Phi_0}\right) \right|, \qquad (5.5$$

where I_c is the critical current that can go through the device. The phase difference, $\Delta\phi$, between junction *J1* and junction *J2* (see Figure 5.4 (c is related by

$$\Delta\phi = 2n\pi - 2\pi \frac{\Phi}{\Phi_0}, \qquad (5.6$$

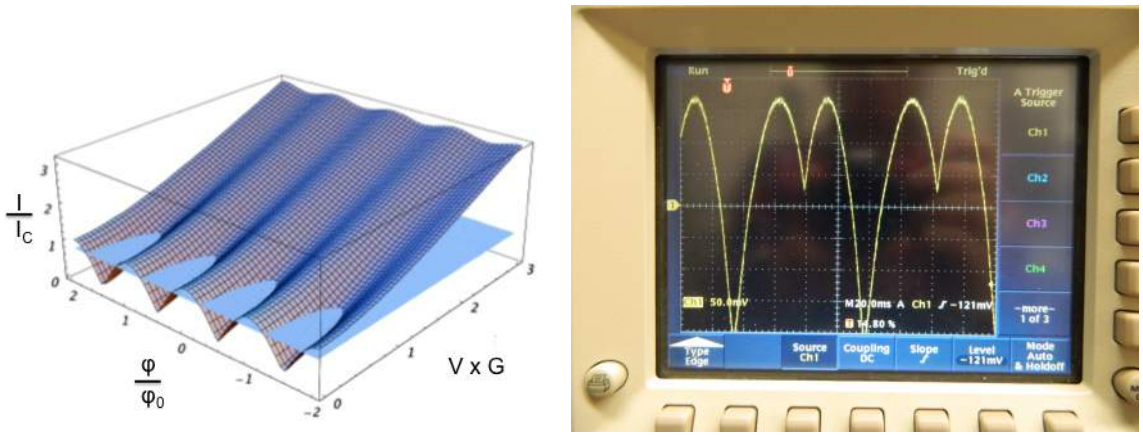

Figure 5.5: *Left*: The ideal relation between $V(\phi$, $I(\phi$ and ϕ for a SQUID. In CDMS and QP study operation, a constant current biased was used. This draw a constant V-ϕ plane as shown here. *Right*: We operate SQUID at its most sensitive regime where the slope of the projected V-ϕ curve the sharpest.

where n = integer. The voltage, V, across the single SQUID junction also depends on flux.

$$V = 0 \quad \text{for } I < I_c \tag{5.7}$$

$$V = \frac{I_c}{G}\sqrt{(I/I_c{}^2 - 1} \quad \text{for } I > I_c, \tag{5.8}$$

where G is conductance of the junction. Combing Eq.5.5 and Eq.5.8, the SQUID I-V relation is then [54]

$$V(\Phi = \frac{I_c}{G}\sqrt{(I/I_c{}^2 - \cos(\pi\frac{\Phi}{\Phi_0}} \tag{5.9}$$

$$I(\Phi = \sqrt{V^2G^2 + I_c^2\cos^2(\pi\frac{\Phi}{\Phi_0}} \tag{5.10}$$

Figure 5.5 shows the relationship, between $I(\phi$, $V(\phi$, and ϕ for an ideal SQUID. In the case of a current-biased SQUID, this draws a constant V-ϕ plane as shown. In our experiment, we locked each SQUID channel at its maximum sensitivities (the sharpest slope in V-ϕ plane shown in Figure 5.5 .

5.4 Warm Electronics

The warm electronics components in our experiments consist of the SQUID bias and feedback box for each SQUID channel. The variable power supplies that gave stable DC voltage to bias the TESs, and NI-PCI 6115 DAQ with BNC-2110 to record the raw pulses in the computer.

5.4.1 SQUID Bias/Preamp and SQUID Feedback Boxes

The twenty years old analog SQUID bias/preamplifier and SQUID feedback boxes are used in our experiments. They were designed by John Martinis, formally at NIST. T. J. Bay wrote a very nice summary page on how to debug and fix these analog boxes. We used gold-plated BNC/FME connectors and Al foils to shield the high frequency ambient (Figure 5.6 [left] .

Figure 5.6 [right] shows the schematic diagram of the SQUID feedback circuit. The output voltage, V_{out} is

$$V_{out} = \alpha(V_{in} - \beta V_{out} \ , \tag{5.11}$$

and the transfer function can be derived as

$$H = \frac{V_{out}}{V_{in}} = \frac{\alpha}{1+\alpha\beta}. \tag{5.12}$$

Here, α is the overall open-loop gain and $\beta = M_{fb}/R_{fb}$ is the closed-loop gain. The detailed analysis can been found in K. Sundqvist 's thesis [54]. One can find the transfer function of the system with frequency dependent $s = \sigma + i\omega$, to be

$$H(s \ = R_{fb}\frac{M_{in}}{M_{fb}}\left(\frac{1}{1+\frac{M_{in}R_{fb}(s+\omega_{int}}{M_{fb}Z_{SQ}A_{VG}A_{int}\omega_{int}}}\right) \tag{5.13}$$

We have already simplified the transfer function by assuming feedback inductance of the pick up coil, $L_{fb} \sim 25$ nH to be 0. M_{fb} is the mutual inductance of the pick-up coil to the SQUID, and ω_{int} is the cut-off frequency of the *integrator*. Plugging in some real values we can find the bandwidth by the -3 dB point of our SQUID is ~ 1

MHz.

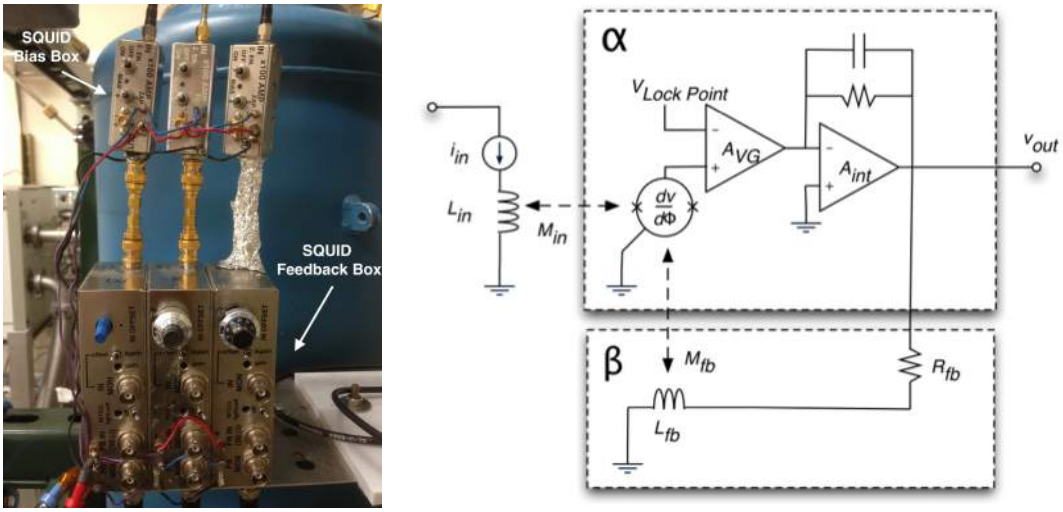

Figure 5.6: *Left*: Three sets of SQUID bias/preamp and SQUID feedback boxes shown here used for each of three TES channels. *Right*: Schematic diagram of SQUID amplifier feedback system. Box labeled α is the open-loop gain where it consists of SQUID amplifier, the variable gain amplifier, A_{VG} and the *integrator*, A_{int}. The β is the closed-loop gain configuration, where the negative feedback is provided.

5.4.2 Battery Bias Boxes

To provide a steady output DC voltage to properly bias TESs, two rechargeable lead acid batteries, designed and built by Teddy Tortorici (Figure 5.7 [left] , were used to provide both positive and negative voltages ranging from ~ -1 V to $\sim +1$ V. In normal operation the bias voltage is $\sim$ -100 mV with some exceptions depending on the Tc of the W-TESs. Figure 5.7 [right] shows one of such battery boxes with open lid.

5.4.3 Readout and DAQ

We used a NI-PCI 6115 DAQ with a BNC-2110 from the National Instruments to simultaneously record three TES/SQUID channels of. Matlab scripts used to record

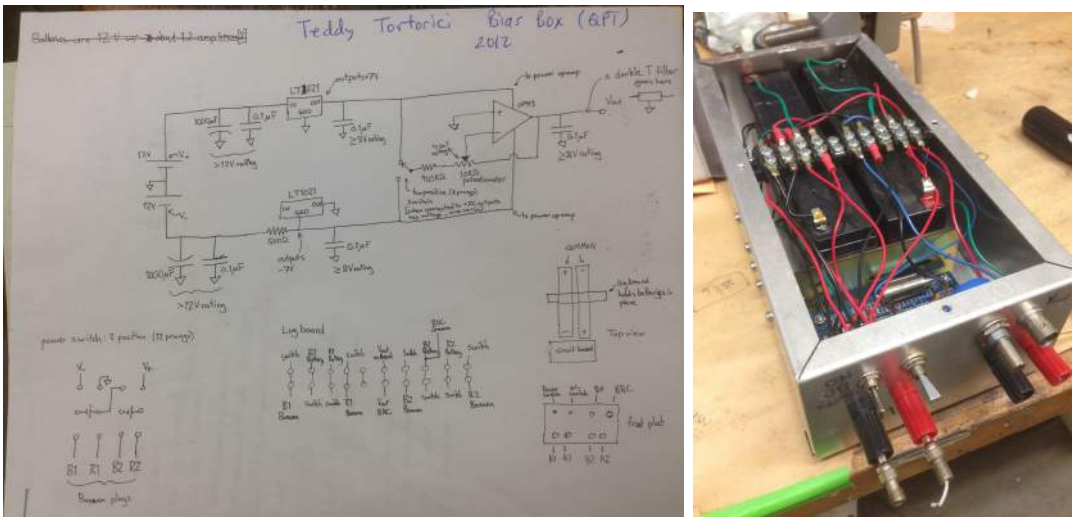

Figure 5.7: *Left*: Circuit schematic for regulating DC bias of the TESs. A potentiometer was used to control the output voltage from ~ -1V to $\sim +1$V with 1 mV precision. *Right*: One TES bias box is shown here. Two lead acid rechargeable batteries were used to provide stable and clean DC voltage. In normal operation, the voltage bias was provided $\sim$ -100 mV.

raw traces were adopted from S. Leman's previous Ph.D work [55] with slight modifications. There were two parts of triggering: the hardware triggering and the software triggering. Although we called it the "hardware" triggering, what we actually did was setting a voltage threshold such that only the signal (hopefully not the noise exceeded the set value will be recording in the buffer and passing through the software triggering. We chose the sum of W-TES1 and W-TES2 signals (channel 4 as our hardware triggering so we don't preferential particular TES to skew the statistics on one channel over another. We did, however, sometimes triggering on just one TES channel to quickly check if a test device working properly. The DAQ was set to recored 4096 bins, with each bin usually corresponding to 200 ns. When a signal hardware triggered, the DAQ would record the traces from the buffer 500 bins prior to the triggering bin. This is also typical recording scheme for CDMS DAQ setup

Once the summed signal (channel 4 passed the hardware triggering, the software triggering imposed three criteria to reject a particular signal, and the signal (event

which passes these criteria would get recored.

- **Preliminary substrate event cut:** the "energy" of the W-TES 3 veto channel (see Fig. 5.8 [right] was compared to some threshold "energy" to avoid substrate events. The "energy" is the computed averaged voltage in the W-TES 3 signal [bins 500 to 2000] . We then empirically selected a threshold voltage to which we only accepted events that was smaller than the threshold.

- **Low frequency noise cut:** The pulse-fall time is of order $\sim$ 100 μs in our devices. The low frequency noises would distort the based line noise and made accidental hardware triggered. We mitigated this problem by averaging the first and last 500 bins of W-TES 1 and W-TES 2 channels and keep the threshold voltage as close to based line noise as possible.

- **Glitch event cut:** Occasional glitch events could happen just due to the environmental change and unknown noise sources. The glitch events looks like a delta function with positive amplitude. We can easily discard them as we negatively biased our TESs and hence the pulses were negatively going pulses.

All three software trigger criteria had to be satisfied in order to have an event recored for all three channels, and these pulses would then go to the next stage processing.

5.5 X-ray Fluorescence Source and Sample Holder

The isotope ^{55}Fe is radioactive emit 5.90 keV (K-α with 24.4% and 6.50 keV (K-β with 2.85% x-rays with a half-life of 2.74 years [56]. The majority of emission by rate ($\sim$ 60% is via Auger electron with 5.19 keV and remaining 12% is accounted for Auger electrons with lower energy excitation. For our experimental purpose, we stopped the unwanted Auger electrons from reach our samples by putting a thin (0.0075" sheet of Kapton covering our collimator holes. A 30 mCi (2009 ^{55}Fe source was used to excite a home-made sodium chloride (NaCl reflector, 1.04 keV (Na and 2.6 keV (Cl x-rays via fluorescence. These secondary x-rays passed through a 1.27 mm thick Al collimator (Gold-plated (1.6 mm diameter hole before striking a test

device as shown in Figure.5.8. The NaCl reflector was designed with a hollow hole at its center (see Figure 5.8(a to let excess 6 keV x-rays going through instead of Bragg reflected to produce more substrate events in our test devices. Table 5.1 shows the x-ray attenuation from our sources inside different relevant materials[57]. It is worth noticed that at the lowest energy (2.62 keV , the attenuation is 0.2 μm for W. However, our typical W-TES films were only 0.04 μm. In addition, the Al films vary from 0.3-0.9 μm while the attenuation depth is 3.29 μm. This indicates the majority of the x-ray events will go through these films and get absorbed in the substrate Si.

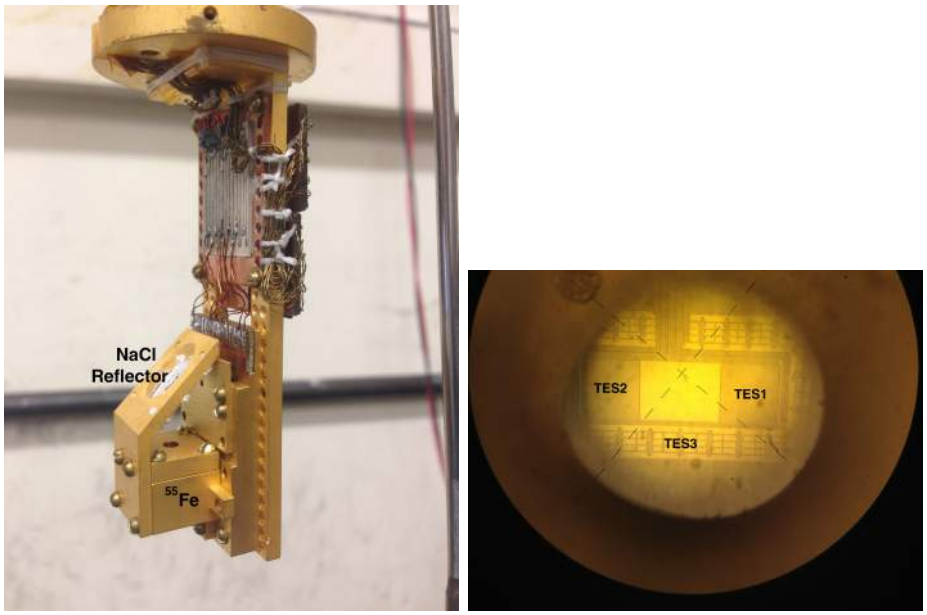

Figure 5.8: *Left*: 6 keV x-rays excites NaCl producing lower energy excitation x-rays (2.6keV that passes through the collimator hole providing uniform illumination on top of the test device shown on the right. *Right*: A microscope image of one test device as seen through the x-ray collimator. Samples with different Al film lengths and thicknesses were tested in the same set-up. The device shown has 250 μm $\times$ 250 μm $\times$ 40 nm-thick W-TESs patterned at the ends of a 250 μm-wide $\times$ 350 μm-long Al film.

Appendix G summarizes the calibration that was done using a Si(Li detector. We are primary interested in 2.62 keV (K_α and 2.81 keV (K_β emitted from Cl ion as our source of x-rays. These x-rays have about 100:1 probability of emission.

	(Cl-Kα 2.620 keV	(Cl-Kβ 2.820 keV	(Mn-Kα 5.899 keV	(Mn-Kβ 6.490 keV
Kapton	39.78 μm	48.75 μm	455.4 μm	605.8 μm
W	0.200 μm	0.230 μm	1.425 μm	1.817 μm
Al	3.290 μm	4.011 μm	31.99 μm	42.18 μm
Si	3.062 μm	3.716 μm	28.86 μm	37.98 μm

Table 5.1: X-ray attenuation length (1/e values in different materials most relevant to qp experiments. ^{55}Fe source (Mn-K$_\alpha$, Mn-K$_\beta$ and NaCl reflector (Cl-K$_\alpha$, Cl-K$_\beta$. Tabulated values from the NIST X-Ray Mass Attenuation Coefficients.

Appendix H shows the drawing specifications for both source and sample holders shown in Figure 5.8[left].

Chapter 6

Experimental Results

In this chapter, we present results of our precision quasiparticle studies using Al/W QETs. We begin with a description of I-V characterization measurements and sensor and circuit resistance studies, and then focus on qp dynamics, electron-phonon coupling, and energy collection efficiency. We then discuss event pulse shapes and energy reconstruction approaches, leading to energy distribution plots that ultimately give us fundamental information about qp diffusion and energy collection in our devices. We defer a detailed discussion about energy reconstruction methods to the next chapter.

In the second part of this chapter, we compare results obtained with a modified device fabrication recipe that dramatically improved step coverage at the Al/W overlap region. This discussion ties back to the SEM images shown in Section 4.3.1. The results of qp diffusion experiments using "non-inverted" (W over Al and "inverted" (Al over W device geometries are then compared. We demonstrate that the inverted devices show comparable performance to that of standard non-inverted devices. Finally, we focus our attention on devices made in the inverted geometry, and compare results obtained with various Al film lengths and thicknesses.

6.1 I-V Characterization

Figure 6.1 shows the electrical circuit central to our studies. The QET (TES device circuit shown on the left consist of a shunt resistor, R_{sh} (to set the voltage bias ,

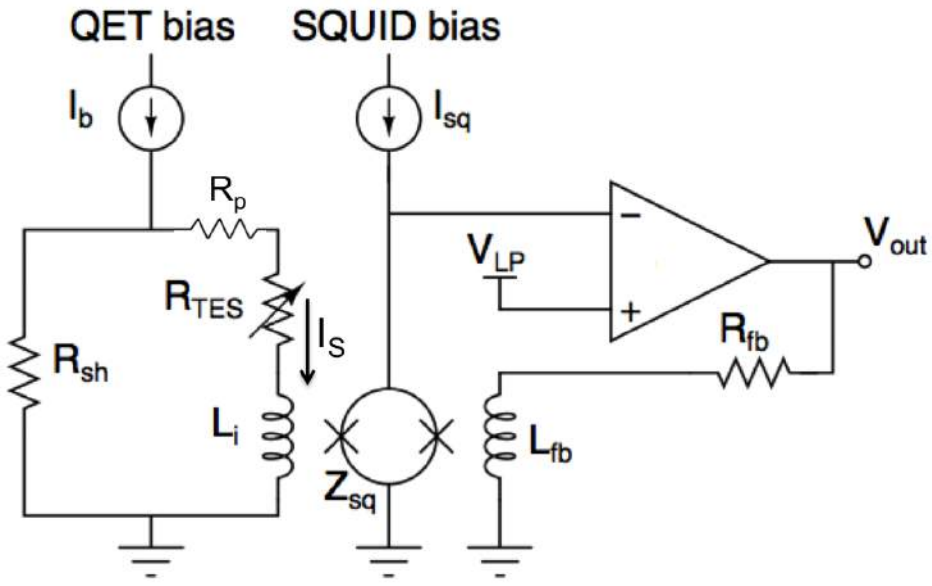

Figure 6.1: Schematic for a voltage-biased TES with SQUID feedback. R_{TES} is kept at constant voltage by placing a shunt resistor, R_{sh}, in parallel with the W-TES branch of the circuit. We denote the parasitic resistance in the circuit as $R_p (\approx 2 - 6\ m\Omega$. The superconducting input coil ($L_i \approx 250$ nH contributes no resistance. $R_{TES} \approx 3\ \Omega$ (normal ; $R_{sh} \approx 20\ m\Omega$; $R_{fb} \approx 1$ kΩ. Changes in W-TES resistance are measured using a constant current-biased SQUID with the amplifier stage described in Section 5.4.1.

a pick up coil, L_i, and a generic parasitic resistance, R_p, in series with the TES. A current source, I_b, is used to provide a voltage-bias to our W-TES. The current through the W-TES branch we denote as I_s. By equating the voltages across the two parallel branches of the circuit we get

$$(I_b - I_s\ R_{sh} = I_s(R_p + R_{TES} \tag{6.1}$$

where we have assumed $L_i(dI_s/dt$ is much smaller than the voltage drops across the resistors. The sensor resistance, R_{TES}, can then be written

$$R_{TES} = \left(\frac{I_b}{I_s} - 1\right) R_{sh} - R_p \tag{6.2}$$

If the W-TES is in its superconducting state, $R_{TES} = 0$, and the parasitic resistance is given by,

$$R_p = (I_b/I_s - 1\ R_{sh} \tag{6.3}$$

Therefore, for a given value of R_{sh}, we can determine the parasitic resistance of the circuit by measuring the W-TES current (I_s as a function of QET bias (I_b , assuming $I_s << I_c$ of the sensor. The slope of an I_s vs. I_b graph (effectively an I -V curve in this superconducting regime yields the parasitic resistance value, R_p. The same I_b-I_s data can also be used to determine the normal state W-TES resistance, R_n (see Equation 6.2 .

In these measurements, the value of I_s is determined from

$$I_s = \frac{V_{out}}{\epsilon g R_{fb}} \tag{6.4}$$

via the SQUID feedback circuit shown schematically in Figure 6.1. In Equation 6.4, the inductor turns-ratio, $\epsilon = L_i/L_{fb} \approx 10$, represents the SQUID gain, $g = 10$ is the external amplifier gain (SRS Model 560 , and $R_{fb} \approx 1$ kΩ.

Figure 6.2(a shows I_s vs. I_b data obtained using a low frequency (~ 2 Hz triangle wave for I_b. The slope (in green in the low bias regime corresponds to the parasitic circuit resistance, R_p. The high bias data yield the TES normal state resistance, R_n. The superconducting critical current, I_c, is heavily dependent on the temperature difference between T_c of the W-TES and the substrate temperature, T_b. It also depends on the quality of the W/Al overlap region. The poorer the connection, the lower the critical current. The data shown in Figure 6.2(a correspond to a device with critical current $I_c \sim 15$ μA. Typical values of I_c for our devices range from $\sim$ 5-50 μA.

Figure 6.2(b shows a plot of W-TES resistance, $R_{\rm TES}$ vs. I_b. For this plot, we used an effective $R_{sh} = 30$ mΩ to calculate R_p and R_n. The effective R_{sh} includes a 20 mΩ discrete resistor plus stray resistance ≈ 10 mΩ. We deduced the total 30 mΩ value using a precision 4-wire resistance measurement of a 5 mΩ Vishay metal thin film resistor.

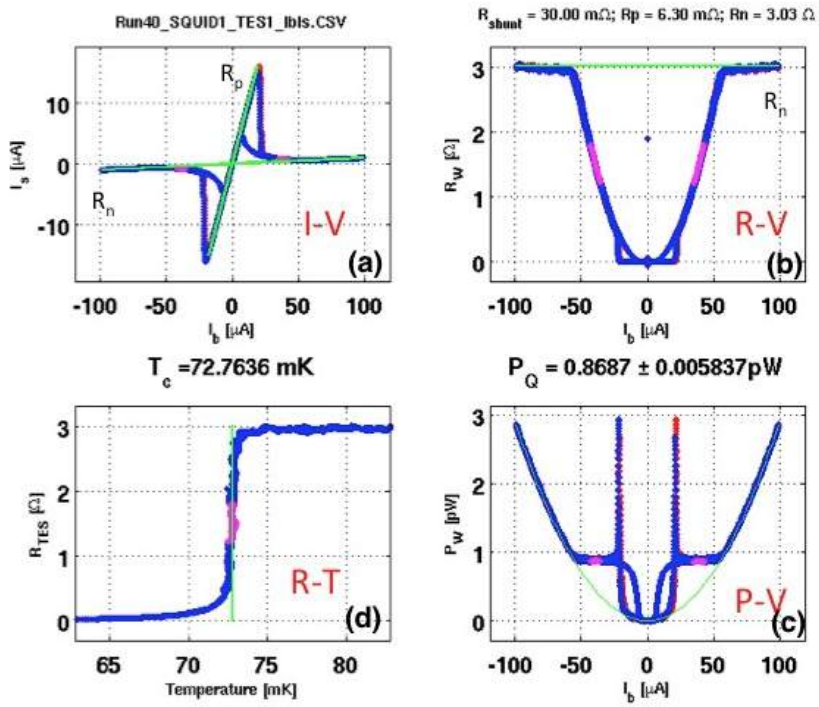

Figure 6.2: (a "I-V" response of a W-TES measured with the circuit shown in Figure 6.1. Two slopes (green can be used to deduce the parasitic and normal state resistances. (b W-TES resistance vs. bias current computed from (a using an "effective" shunt resistance of 30 mΩ. (c Power dissipation in the W-TES. The green curve corresponds to a normal state power dissipation $\propto I_b^2$. We bias our W-TESs in the flat region. (d W-TES resistance as a function of temperature. T_c is calculated from the middle of the sharp transition (purple line .

The power, P_W, dissipated by one of our W-TESs was calculated using

$$P_W = I_s^2 \; R_{TES} = \left(\frac{I_b R_{sh}}{R_{TES} + R_p + R_{sh}} \right)^2 \; R_{TES} \qquad (6.5$$

The results are shown in Figure 6.2(c , where the dissipated power (pW in the W-TES is plotted as a function of bias current, I_b. There are three relevant regions in this graph. At the lowest bias values, $R_{TES} = 0$ and therefore $P_W = 0$. At high bias, the power curve looks like that of a standard resistor. At intermediate biases, the power curve is flat: this is the quiescent state. This is the so-called electro-thermal

feedback regime [**?**, **?**], which we characterize by

$$P_W = \kappa \mathcal{V}(T^5 - T_b^5 \ , \tag{6.6}$$

where κ is the measured electron-phonon coupling constant, $\mathcal{V} = 250\ \mu\text{m} \times 250\ \mu\text{m} \times 40$ nm, is the volume of the W film, and T_b is the substrate temperature. Rearranging Equation 6.6 yields the W-TES temperature in terms of the known parameters

$$T = \left[\left(\frac{P_W}{\kappa \mathcal{V}} \right) + T_b^5 \right]^{1/5} \tag{6.7}$$

Finally, in Figure 6.2(d we show the calculated W-TES resistance vs. W-TES temperature, obtained using the I_b-I_s data shown in Figure 6.2(a . The sharp rise in resistance corresponds to $T = T_c$.

6.1.1 Electron-Phonon Coupling

The electron-phonon coupling constant, κ, is determined by measuring the quiescent power, P_Q, of a W-TES at different sample stage temperatures. Figure 6.3 [left] shows the resulting power curves for one device ($T_c \sim 90$ mK operated from 36 mK to 85 mK. We then fit our data using Equation 6.7. As expected, the quiescent power decreases as the temperature approaches the device T_c (here 89.5 mK , indicating that less external energy can be absorbed if the sensor is to remain in its quiescent state. This data, combined with empirical results that showed the dominant thermal impedance of our system is between the electrons and phonons within the W-TES (see Appendix K , was used to produce Figure 6.3[right]. A fit to this data yields $\kappa \sim 2.5 \cdot 10^5$ pW/K^5 for this device. Typical values of κ for other qp test devices show $\kappa \sim 2 \cdot 10^5$ pW/K^5. This value is roughly a factor of four smaller than that measured in similar studies performed by our group at UC Berkeley [58]. The discrepancy can be explained by different thermometer calibrations in the two cryostats (Stanford KO-15 reads $\sim 20 - 25$ mK higher than the Berkeley KO-75 fridge . The difference in thermometer readings has not yet been resolved.

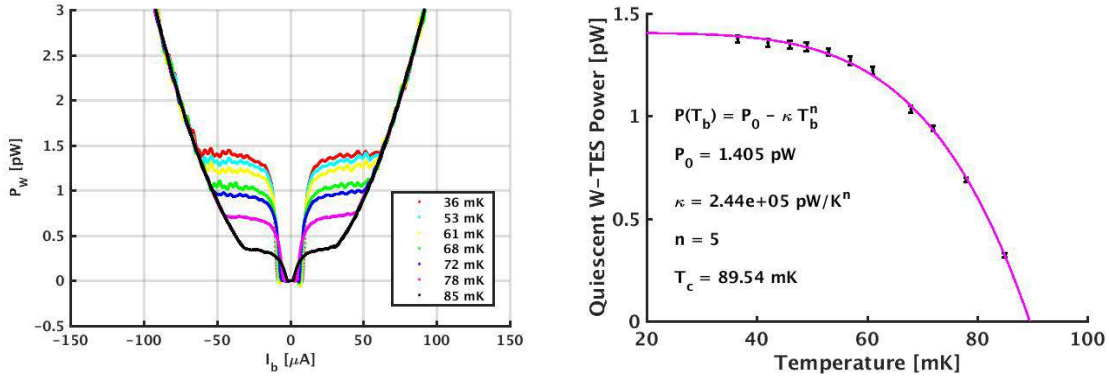

Figure 6.3: *Left*: Power dissipation in W-TES film as a function of bias current for various operating temperatures. The quiescent power (the flat region of each curve decreases as the fridge temperature approaches T_c. *Right*: Data points taken from the quiescent power curves shown on the left. The electron-phonon coupling, κ is deduced from a fit to Equation 6.7. We assumed n= 5.

6.2 X-ray Studies

As described in Section 5.5 and shown in Figure 5.8, we use an ^{55}Fe source to excite a NaCl reflector, yielding 2.6 keV (and other x-rays via fluorescence. The x-rays were used to perform detailed studies of W-TES energy collection and signal dynamics.

6.2.1 Raw Pulses

The total change in internal energy of a voltage-biased TES is well approximated by:

$$\Delta U = \Delta U_{ext} + \Delta U_J + \Delta U_{e-ph} = 0 \qquad (6.8$$

where ΔU_{ext} represents the deposited x-ray energy, ΔU_J corresponds to the Joule heating $\sim V^2/R$ of the biased TES, and ΔU_{e-ph} is an energy loss term arising from electron-phonon coupling within the TES. This latter term accounts for the thermal relaxation of the TES (Section 3.2.1 . It is relatively small when the TES is operated in the linear, non-saturated region of its $R(T, I$ curve, and only small energy inputs are considered. When in this linear, low energy regime, the first two terms in the

energy balance equation dominate the physics, and essentially cancel each other. Therefore, the energy of an x-ray event can be defined in terms of the approximate Joule power that would have been present without the pulse.

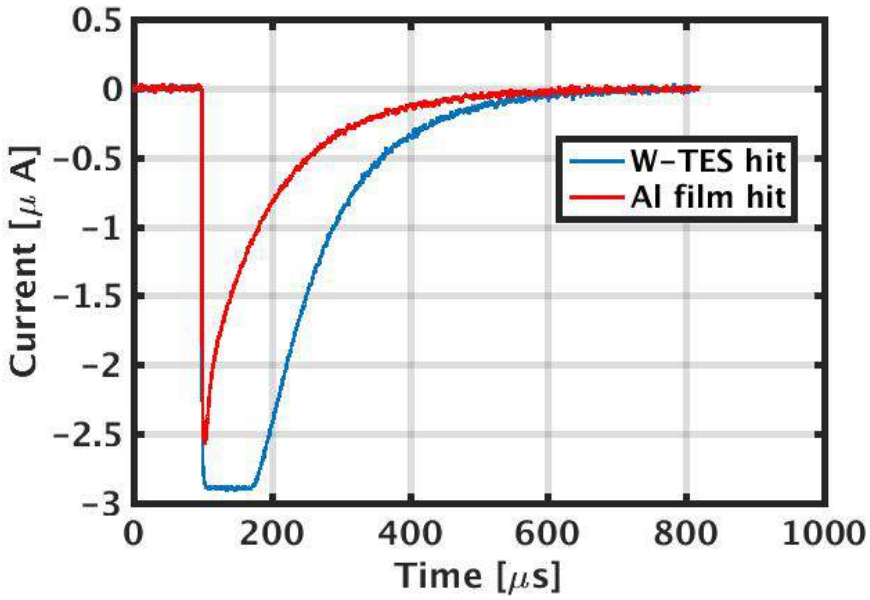

Figure 6.4: Typical raw pulses seen for x-ray events directly hitting W-TES (blue and Al film (red . The characteristic fall-time seen, $\tau_{etf} \sim 200\ \mu$s is due to electro-thermal feedback within W-TES. More subtle effect within the film create more complicated pulse dynamics as described in Chapter 7. The saturation seen in blue corresponds to an x-ray event with sufficient energy to drive the W-TES normal.

$$\begin{aligned} \Delta U_{ext} &= -\Delta U_J \\ &= -\int_0^t [(V_s \cdot I_{s\ f} - (V_s \cdot I_{s\ q}]dt' \\ &= \int_0^t [(I_b R_{sh} - (R_s + R_p\ I_s\ I_s]_q dt' - [(I_b R_{sh} - (R_s + R_p\ I_s\ I_s]_f dt' \end{aligned} \quad (6.9$$

Here, V_s and I_s are voltage and current associated with R_{TES}. The subscript q corresponds to the sensor when it is in the quiescent state. Equation 6.9 gives the integrated pulse energy associated with an x-ray event.

Figure 6.4 shows typical x-ray pulses for events occurring directly in a W-TES

(blue and the Al film (red . The characteristic fall-time, $\tau_{etf} \sim 200$ μs is essentially the same for both event types. Pulse saturation occurs when the x-ray energy is sufficiently large that it drives the TES fully normal. In this case, Equation 6.9 can no longer be used to calculate the event energy, as ΔU_{e-ph} in Equation 6.8 cannot be ignored.

Figure 6.5 shows three saturated W-TES pulses for 2.6 keV x-ray with the sensor operated at three different temperatures. Considering these pulses are the result of the same incident x-ray energy, the inconsistent integrated energy values shown in the legend indicate that the pulse integral method described above cannot be used for accurate energy reconstruction. Thus, for the rest of this chapter, we present results using an optimal filter analysis approach rather than an integrated energy approach.

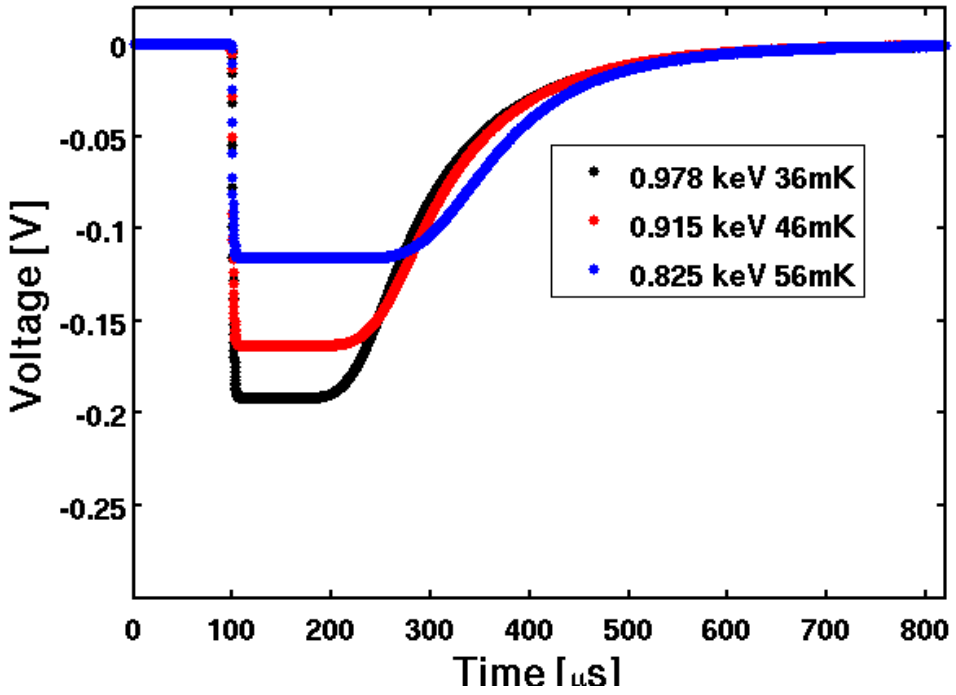

Figure 6.5: Pulse shapes of a W-TES (T_c = 73 mK operated at three different temperatures. Considering these pulses are the results of the same incident x-ray energy, the integrated energy values shown in the legend indicate the pulse integral method alone is not ideal for event energy reconstruction.

6.2.2 Coincidence Events

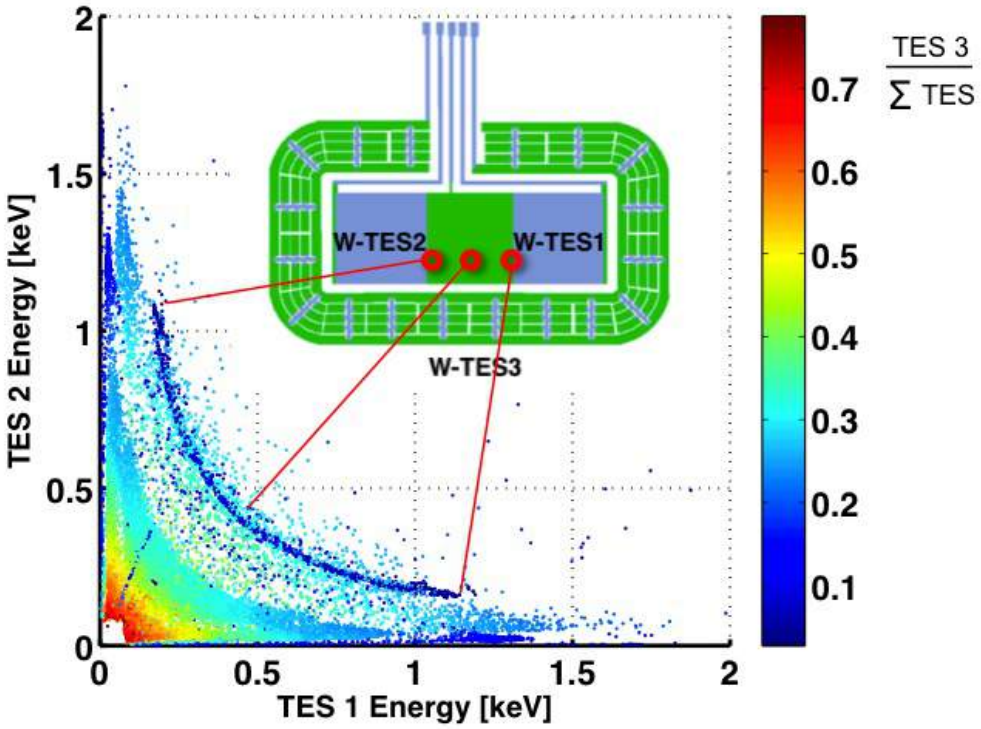

Figure 6.6: Energy distribution plot: x and y axis are energy collected in the two main W-TESs, while the color represents the total energy fraction that collected in the guard ring (W-TES 3 . The inset shows a 250 μm-long Al film device under study. The there red pointers indicates where the x-ray events would appear on the energy distribution plot.

In Figure 6.6 we show the energy detected by each of the three W-TESs (inset figure on a single QP non-inverted (W on top of Al device exposed for $\sim$ 48 hours to a NaCl fluorescence source. The data were obtained with a 250 μm-long Al film device. Event energies were determined using a non-linear optimal filter template fitting approach [59]. The x- and y-axis show the energy collected in the two W-TESs at the ends of the central Al film. A third TES channel around the whole device was used as a guard ring to veto events that occured in the silicon substrate. The color represents the fraction of event energy absorbed in W-TES 3 compared

to the sum of all three W-TES channels. Each data point corresponds to a single x-ray event. The majority of events occurred in the silicon substrate because the penetration depth for 2.6 keV photons in Al is ~ 3 μm (Table 5.1 , and Al film used for this particular experiment was only 0.3 μm-thick. The points shown in dark blue corresponds to events that occur directly in the main W-TESs (W-TES1, W-TES2 or Al film. For each of these events, $< 15\%$ of the total energy was absorbed in guard ring channel (W-TES3 .

The Al direct-hit events appear as the dark blue band with "banana" shape. If there were no qp energy loss within the Al, this band would look like a straight line declining at 45 degrees. In addition, if there was negligible impedance at the Al/W interfaces, the two ends of this band would touch x- and y-axes. Any observed curvature in this band, therefore informs us about qp losses in the Al. The distance between the band edges and the axes similarly tells us about the Al/W interface impedance.

We can turn Figure 6.6 into a 3-dimensional plot as shown in Figure 6.7. Here, the x and y-axes still show the energy collected in the two main W-TES channels, and the z-axis represents the energy collected in the guard ring. Four basic classes of events are evident: (1 x-rays absorbed directly in W-TES1 or W-TES2, (2 x-rays absorbed in the central Al film, (3 x-rays absorbed in one of the four main W/Al overlap regions of the device (one at each end of both W-TES1 and W-TES2 , and most commonly (4 x-rays absorbed in the Si substrate (large W-TES3 signal . The relative count rates observed for the various event types were consistent with the source-collimator geometry and the known penetration depths for 2.62 keV x-rays in Al (3.3 μm and W (0.2 μm . The films were 300 nm-thick (Al and 40 nm-thick (W .

6.2.3 W-TES Direct Hit

The population of direct-hit events can be seen more clearly in Figure 6.8 [left], where we have plotted the detected guard ring W-TES3 energy vs. W-TES1 energy. These data were obtained with an inverted QP device geometry. The results presented

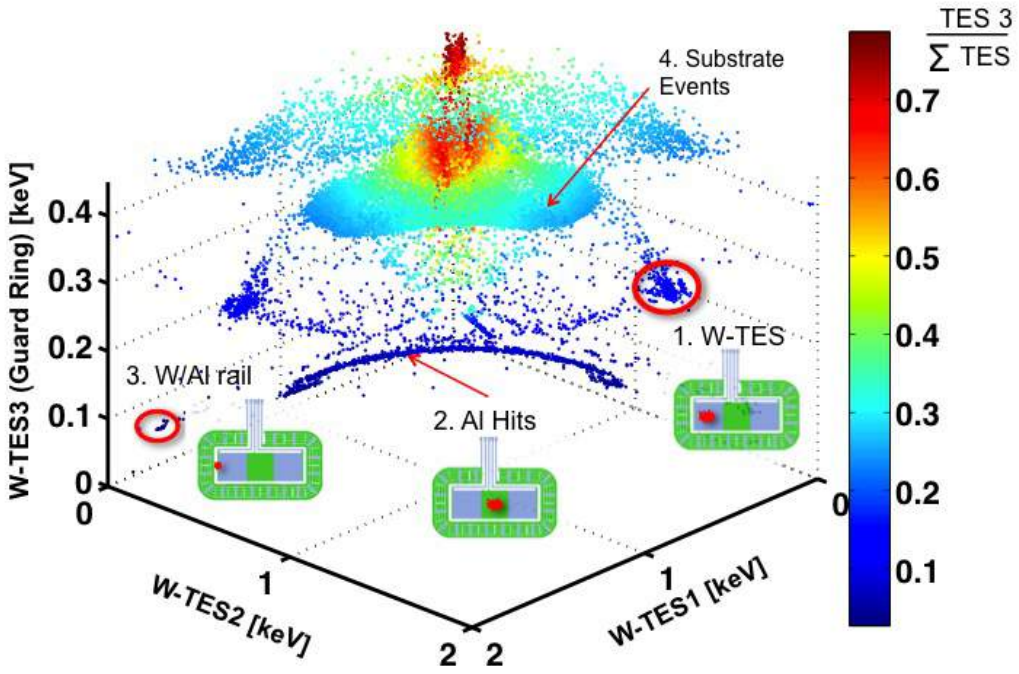

Figure 6.7: X-ray event energy collected in each of the three W-TESs of a 250 μm-long central Al film device. Four distinct x-ray interaction locations are noted: W-TES, central Al, Al/W overlap regions, and the substrate. The color bar indicates the fraction of the total detected energy appearing in the substrate channel (W-TES3 . The energy collected by W-TES1 and W-TES2 for x-ray hits along the central Al film (the banana-shaped cluster of points shown is consistent with the known device geometry.

here are general since the physical dimensions of W-TES1 (250 μm x 250 μm x 40 nm-thick is identical for all test devices. In the figure, we can clearly see Cl Kα (2.62 keV and Cl Kβ (2.82 keV populations, with the number of Kα and Kβ events in a 10:1 ratio, as expected. Since the W-TES is only 40 nm-thick, a significant fraction ($\sim$ 50 % of the deposited energy is loss to the Si substrate via phonons. As described in Section 3.1.4, the much thicker Al film (300 nm-thick here , produces less energy loss to the substrate ($\sim$ 11 % . Figure 6.8 [right] shows a histogram of W-TES direct-hit events using 5 eV binning. Assuming a gaussian distribution, the FWHM $= 2\sqrt{2\ \ln 2}\ \sigma = 17$ eV at 1.7 keV, or 26 eV at 2.6 keV.

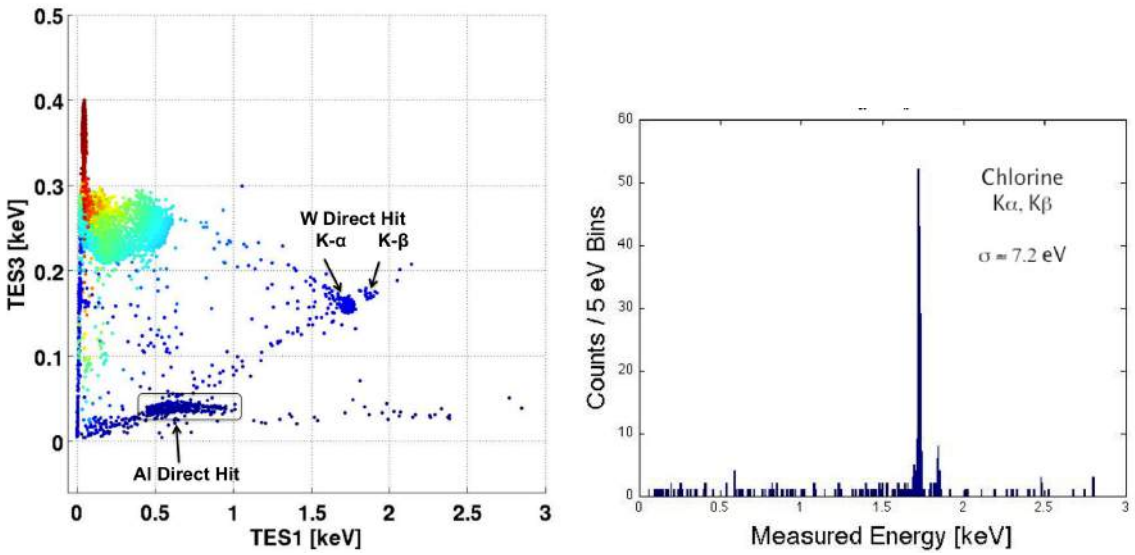

Figure 6.8: *Left*: Energy distribution plot for guard ring events (W-TES3 . The Cl Kα (2.62 keV and Cl Kβ (2.82 keV event populations can be seen with the expected 10:1 ratio. The energy collected by the guard ring for direct-hit W-TES1 or the Al film comes from phonon leakage for these events. In general, such phonon losses are greater for thicker films; this explains the rather large difference in W-TES3 energy collection for the W-TES1 direct-hit events compare to the Al film direct-hit events shown. *Right*: W-TES1 direct-hit energy histogram. The FWHM energy resolution is 17 eV at 1.7 keV collected energy, corresponding to 26 eV at 2.6 keV. The measured separation between Kα and Kβ peaks is 7.6 %, consistent with the energy separation between the known x-ray incident energies (2.62 keV and 2.82 keV .

All of the inverted test devices measured showed an absolute energy collection of $\sim$ 1.7 keV energy collection on both W-TES 1 and W-TES 2 for 2.62 keV x-rays. Non-inverted test devices evaluated previously yielded total energy collection of 1.4 keV. Both of these values are slightly higher than theoretical predictions ($\sim$ 1.3 keV, see Section 3.1.4 for the given W film thickness. We surmise that some of the energetic phonons that initially leak out of the W film and into the Si substrate get scattered back into the W-TES while it is still in its energy down conversion phase.

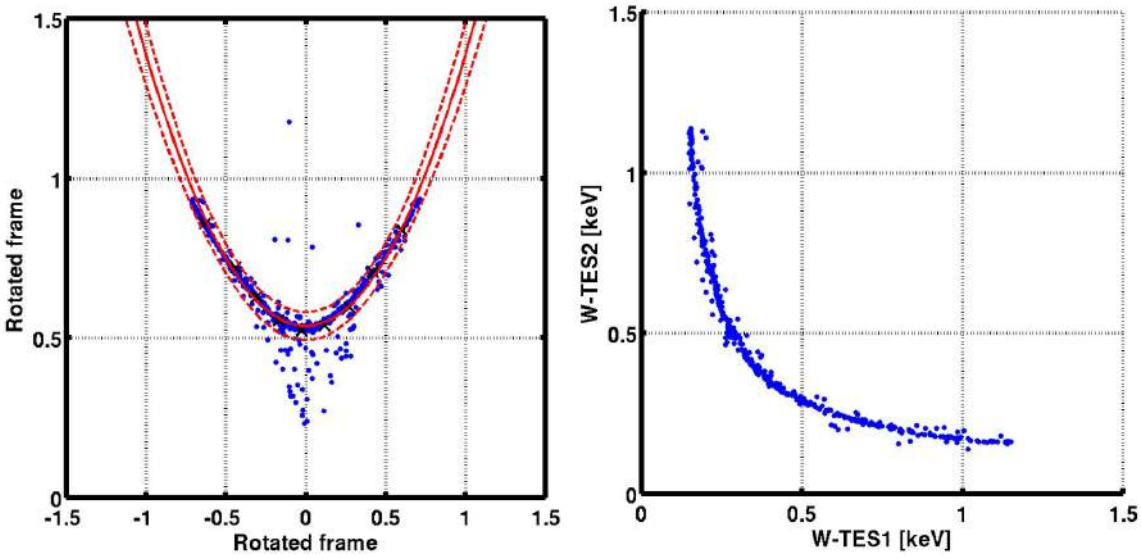

Figure 6.9: *Left*: After a preliminary offline cut to remove substrate events and W-TESs direct-hit events, we rotated the energy distribution plot by 45°. Using a MATLAB function to find the best fit in quadratic, we can find 95% C.L. of events that are Al direct-hit. *Right*: This shows result of selecting only Al direct-hit events. We use the same method repeatedly for all the qp test devices.

6.2.4 Al Events Direct Hit

To carefully select Al film direct-hit events in offline analysis, we first remove the substrate events by selecting events that are $\sim < 15\%$ of the total collected energy. We then remove W-TESs direct-hit events that are very close to the two axes. After that, we rotate the energy distribution plot by 45° like the one shown in Figure 6.9 [left]. Next, using the MATLAB function Kmeans, we identified clusters of data points along the banana-like band and minimized the sum of the squares of energy distance from each point to the cluster centroids. Finally, we fit a quadratic curve to these data, and calculated the 95 % C.L. The event selection result for this particular dataset is shown (after rotating back to the original frame in Figure 6.9 [right].

6.2.5 Poor Al/W Interfaces

The Al/W interface quality plays an important role in the energy collection efficiency of our devices. For a non-inverted device (W on top of Al , there are two major obstacles qps encounter (in addition to potential film quality and impurity issues : The first is the effectiveness of qp trapping in the lower energy band-gap region, where the W and Al overlap ($\sim$ 5 μm-wide region . The formation of an Al oxide within the W/Al interface can seriously degrade the effectiveness of qp trapping, and it also decreases the probability for qp transmission into the W-TES. To mitigate this problem, we deposit αSi, Al and W without breaking vacuum (Section 4.3 to avoid the oxidation formation between Al and W. For the inverted devices, since the Al film is the last step in the fabrication process, the oxidation doesn't affect the overlap region. The second major concern is achieving good connectivity in the "waterfall" region (see Figure 6.10 where the 40 nm-thick W film meets the $\geq$ 300 nm-thick Al film. But no matter how perfect the W/Al overlap region is, and no matter in what order the films are deposited, the impedance mismatch between the W and Al layers always exists, and therefore no perfect transmission of qps from the Al to the W-TES is possible.

Figure 6.10 shows Al film direct-hit x-ray data for two non-inverted test devices with the same film geometry (W over Al but with very different quality Al/W waterfall regions. Data from a good (bad waterfall device is shown in black (red . Both devices had a 350 μm-long and 300 nm-thick Al film. In the figure, the total energy (W-TES1 + W-TES2 is reduced in the device with the poor waterfall. In addition, this poor waterfall connection makes the reflection probability of qps at the Al/W boundary higher, leading the ends of the Al direct-hit band pull away form the x- and y-axes. This indicates that the qps spend more time in the Al film bouncing around before being absorbed by W-TES1 or W-TES2. This causes the energy collection in both W-TESs to be similar regardless of the initial event location in the Al film.The general quality of the waterfall region can often be deduced by a room temperature continuity check, since the normal state is typically much higher ($\sim$ 100 Ω - 1000 Ω for a device with poor film connectivity compare to one with a good waterfall connection ($\sim$ 10 Ω . A detailed study by J. M. Kreikebaum et. al. [44] helped

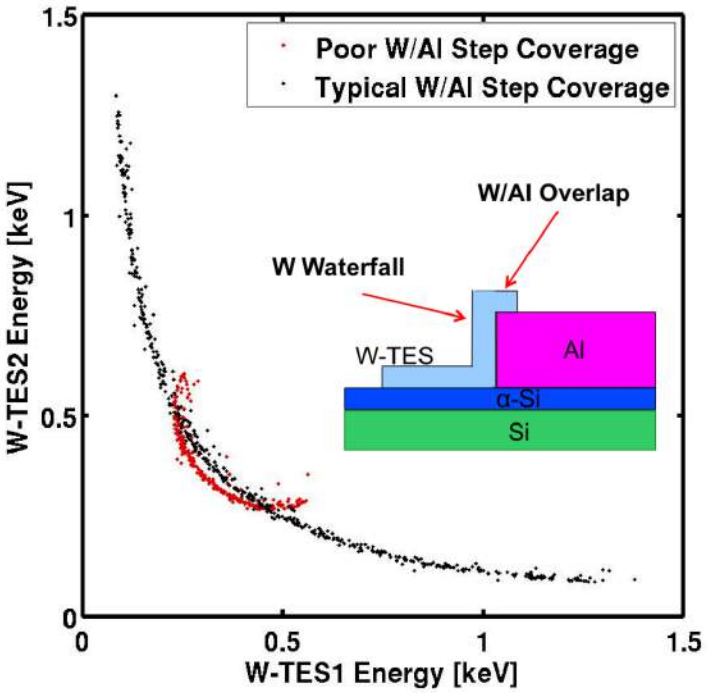

Figure 6.10: Results of a diagnostic 2.62 keV x-ray fluorescence experiment performed at $\sim$ 35 mK to quantitatively evaluate the quality of W/Al interfaces. A device with good W/Al interfaces produces a band of events such as that shown in black. A device with poor filamentary W/Al step coverage (a poor waterfall region yields a band of events such as that shown in red. More total energy (W-TES1 + W-TES2 is collected in devices with uniform W step coverage.

us resolve the step converge problem in the fabrication process. The W-TES energy collection for Al direct-hit events is now limited by the quality of the $\sim$ 5 μm-long W/Al overlap region.

6.2.6 Substrate Events

Although our primary interest is in studying Al and W x-ray direct-hit events, substrate events merit a short discussion as they represent $>$ 50% of the total number of events in our datasets even after the hardware and software triggering applied (Section 5.4.3 . The substrate events shown in Figure 6.6 occurred just a few microns

below either the Al or W films. If events occurred somewhere deep inside the Si wafer, the energy collected by W-TES1 and W-TES2 would be approximately equal. These events appear in a 45° diagonal band in the energy distribution plot, with very high guard ring collection fraction (Figure 6.11 .

In addition, we occasionally observe the substrate events with collected energy shifted in the same device operated in different fridge runs. We suspect this was due to settling into different neutralization states of the impure Si wafer upon cooling.

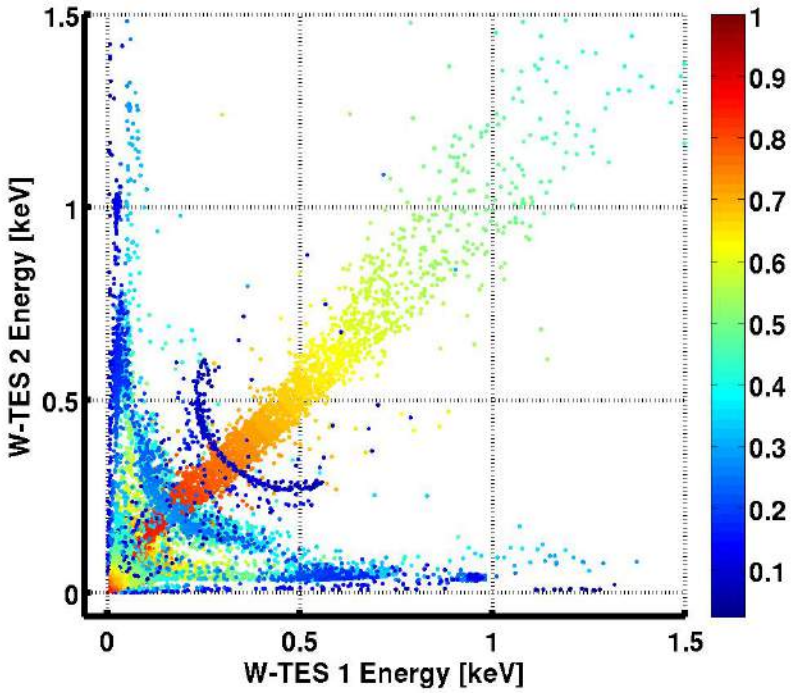

Figure 6.11: The 45° diagonal band with equal W-TES1 and W-TES2 energy collection correspond to x-ray events occur deep in the Si substrate. The energy fraction collected by the guard ring for these events are high (> 50 % . The data shown here were obtained with a "poor waterfall" W connection device. These excess substrate events shown can be easily removed from datasets using online & offline cuts.

6.3 Energy Collection Efficiency

6.3.1 Dependance on Geometry: Non-Inverted vs. Inverted

Data from experiments with devices in the non-inverted (W over Al and inverted (Al over W geometry exposed to the same x-rays source are shown in Figure 6.12a (non-inverted device and Figure 6.12b (inverted device . Note the striking similarity between the two results. Both plots shown correspond to 250 μm x 250 μm x 40 nm-thick W-TESs (TES 1 and TES 2 coupled to a central 500 μm-long x 250 μm-wide x 300 nm-thick Al film. Curvature in the data is due to qp energy loss during

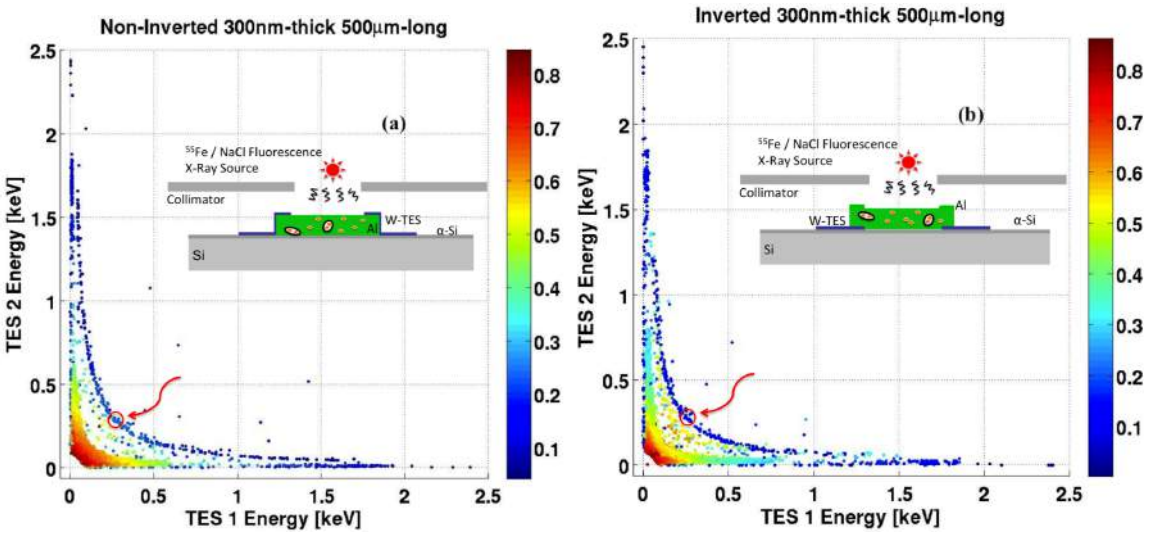

Figure 6.12: Quasiparticle (qp energy collected in W-TESs at opposite ends of a qp test device (500 μm-long x 300 nm-thick Al film fabricated in the (a non-inverted (W-TES over Al and (b inverted (Al over W-TES geometry. The overall curvatures of the Al direct-hit events indicate the same intrinsic Al film properties. In addition, in both cases the events occur at the center of the Al film (shown in red arrows have the total energy collection $\sim$ 0.5 keV for both device geometries, indicating $\sim$ 20 % collection efficiency.

diffusion in the Al film. Looking at the combined energy collection (W-TES1 + W-TES2 for events located at the center of the Al film, we find qp energy collections of 0.50 keV for 2.6 keV Cl x-rays striking inverted devices, and 0.48 keV for 2.6 keV

x-rays striking non-inverted devices. The results indicate that the new inverted device geometry provides just as good qp collection efficiency as our standard non-inverted design ($\sim$ 20% in 500 μm-long Al film , but utilizes a more robust fabrication process. In addition, the "inverted" devices allow us to increase the Al film thickness without having to worry about losing connectivity between Al and W in the critical waterfall region of the device.

6.3.2 Inverted Devices

With the inverted device geometry, we are able to vary the Al film thickness without jeopardizing the Al/W connectivity since the step coverage (waterfall issue no longer exists. To probe the Al qp diffusion process, we evaluated the performance of devices made in the inverted geometry as a function of both Al film thickness and length. Results from these experiments are shown in Table 6.1. Each row in Table 6.1 corresponds to a specific Al film thickness (300, 500 or 900 nm and each column corresponds to an Al film length (250, 350 or 500 μm . All nine devices yielded comparable results for x-rays that directly hit W-TES 1 or W-TES 2 (see dark blue data points close to the x- or y-axis in Table 6.1 , despite slight differences in W T_c, TES bias voltage, and fridge temperature. Differences in the total number of events resulted in slight difference in density of the data points shown in each plot. However, for each plot, the total number for different event populations are consistent with device geometry. The devices also have similar energy resolutions for direct-hit events in the W-TESs ($\sim$10 eV for 2.62 keV x-rays . As expected, the total energy collected by W-TES 1 and W-TES 2 combined is greater (data more diagonal, less loss to the Si substrate for central x-ray events in the shorter Al films (horizontal trend and thicker Al films (vertical trend . Notice the more visible Kβ bands in the 900 nm-thick Al film data, since the x-ray stopping power of thicker films is stronger. The slight hint of 5.9 keV band shows up for the 250 μm-long and 900 nm-thick device. These events are due to primary x-rays from our ^{55}Fe source.

Dependance on Al Film Length

For a given Al film thickness (horizontal trend in Table 6.1 , total energy collected by W-TES1 and W-TES2 is greater (data more diagonal, less loss to substrate for central x-ray events in the shorter Al films. The effect is most pronounced for the thinnest (300 nm-thick films. In Figure 6.13, we combine the Al direct-hit events for three different Al film lengths in a single plot, one for each of the Al film studied.

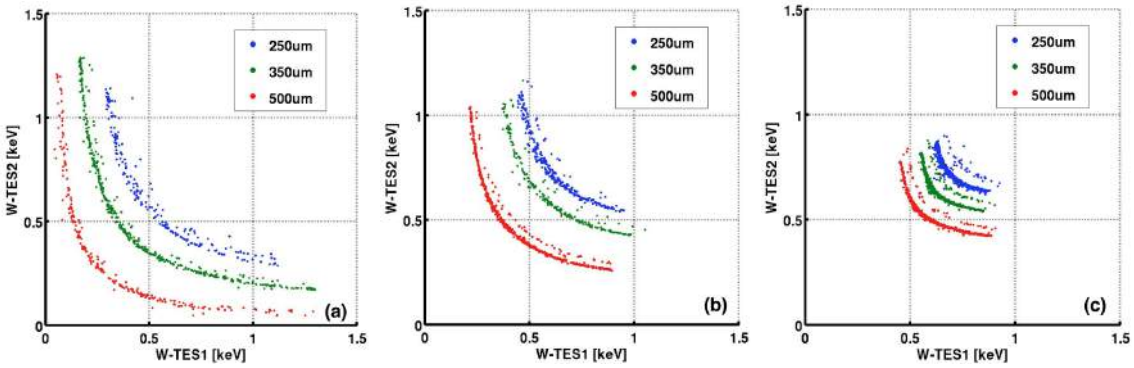

Figure 6.13: Composite graphs showing energy absorbed in W-TES1 and W-TES2 for 2.62 keV & 2.82 keV Cl x-rays striking Al film with three different Al film lengths (250, 350, 500 μm . For a given film thickness, the longer film length requests qps to travel further to the W-TESs and therefore more energy loss is expected. (a 300 nm-thick Al films. (b 500 nm-thick Al films. (c 900 nm-thick Al films.

Dependance on Al Film Thickness

For a given Al film length (vertical trend in Table 6.1 , the total energy collected by W-TES1 and W-TES2 is greater for central x-ray events in the thicker Al films. This indicates we are still in the thickness-limited regime where the qp mean-free-path, l, depends on film thickness, z. There is less position dependence in the Al direct-hit events for the thickest (900 nm-thick films; most notably, W-TES1 and W-TES2 collect comparable energy for each direct-hit Al event in the shortest, thickest film.

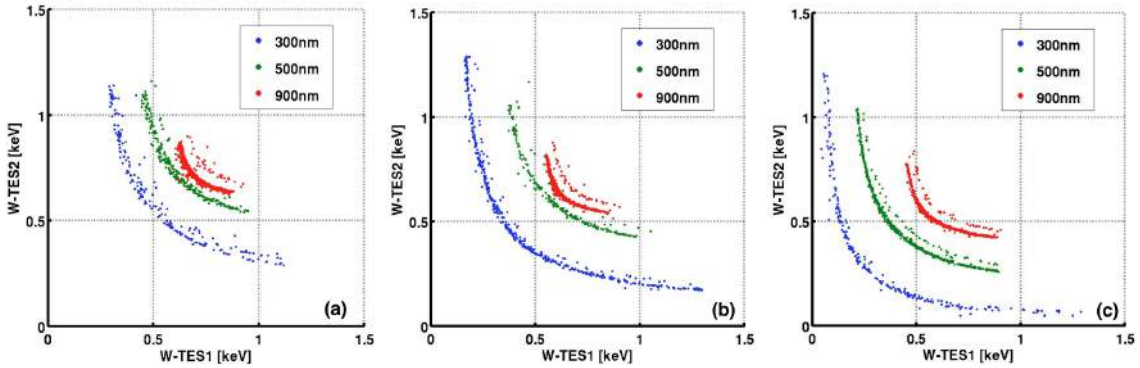

Figure 6.14: Composite graphs showing energy absorbed in W-TES1 and W-TES2 for 2.62 keV & 2.82 keV Cl x-rays striking Al film with three different Al film thicknesses (300, 500, 900 nm . (a Results of 250 μm-long Al films. (b Results of 350 μm Al films. (c Results of 500 μm Al films.

6.4 Summary

We have shown that the inverted and non-inverted device geometries provide comparable energy collection. This largely reduces the complication between W/Al connectivity, and allows us probing intrinsic Al film properties as function of its thickness in a more systemic way. In the next chapter, we show non-linear optimal filtering method for W-TES pulses and reconstruct the event energies resulting in the energy distribution plots seen in this chapter. We also show the qp diffusion model that allows us to draw more quantities conclusion for qp transport in the Al films.

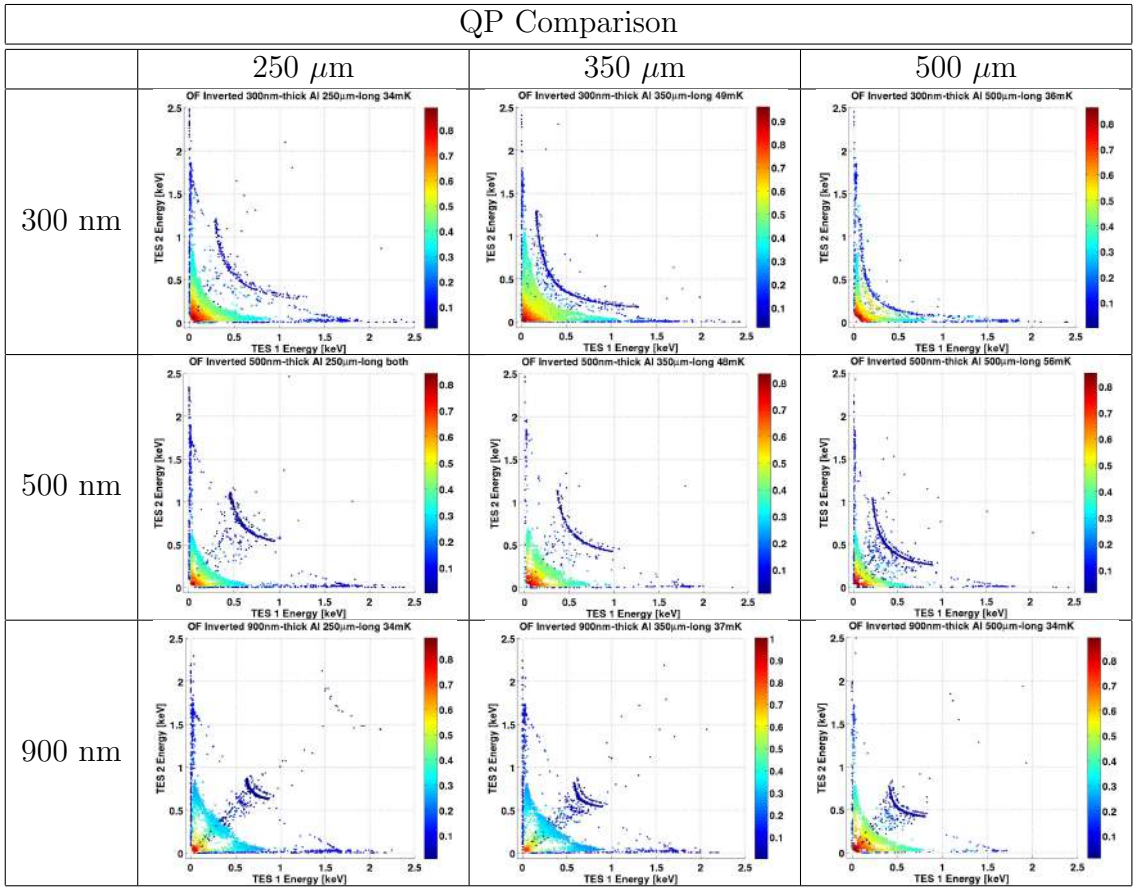

Table 6.1: 2-D energy distribution plots for inverted QP test devices for three different Al-film lengths (250 μm, 350 μm and 500 μm with three different Al-film thickness (300 nm, 500 nm and 900 nm . For a given Al film thickness (horizontal trend , total energy collected by TES 1 and TES 2 is greater (data more diagonal, less loss to substrate for central x-ray events in the shorter Al films. For a given Al film length (vertical trend , the total energy collected by W-TES1 and W-TES2 is greater for central x-ray events in the thicker Al films

Chapter 7

Modeling and Simulation

In this chapter, we describe a TES model specifically designed for our device geometry. We then use this model to reconstruct x-ray event energies using a non-linear optimal template method which takes into account energy lost to phonons. We then continue the chapter by modeling the quasiparticle diffusion process in our Al films using two different approaches. The first is a macroscopic approach that treats the qp population as a whole and uses the diffusion equation to model the spatial evolution of this population. The other approach incorporates physical qp parameters and energy decay dynamics as the qps propagate to Al/W boundaries and get absorbed by a W-TES. This latter model closely follows the energy down conversion theory discussed in Section 3.1.4. More specifically, the microscopic model we describe below starts from Stage III of Figure 3.1 where the mean qp energy $E_2 = 3\Delta$, and qps are no longer generated through their interactions with phonons. We end this chapter with a discussion of our experimentally observed thickness dependent of qp diffusion and absorption in Al films. Finally, we connect our results to future QET designs for a SuperCDMS SNOLAB high voltage experiment.

7.1 W-TES Modeling And Simulation

When an incident x-ray has sufficient energy to drive a TES fully normal, the integrated quantities (Equation 6.9 can no longer be used to accurately reconstruct the

event energy. This is because the longer a TES stays saturated in the normal regime, the greater the energy loss to phonons. We have developed a TES model for qp test devices that takes into account these losses. As shown in Figure 7.1 (bottom , we first divide each square TES into ten equal-size strips, and then add short stubs in series with each TES to mimic the W/Al interfaces. In the model, the stub length (joining the Al to the W-TES is fixed at 25 μm, but we vary the stub width from 5 μm to 250 μm to represent the quality of the interface.

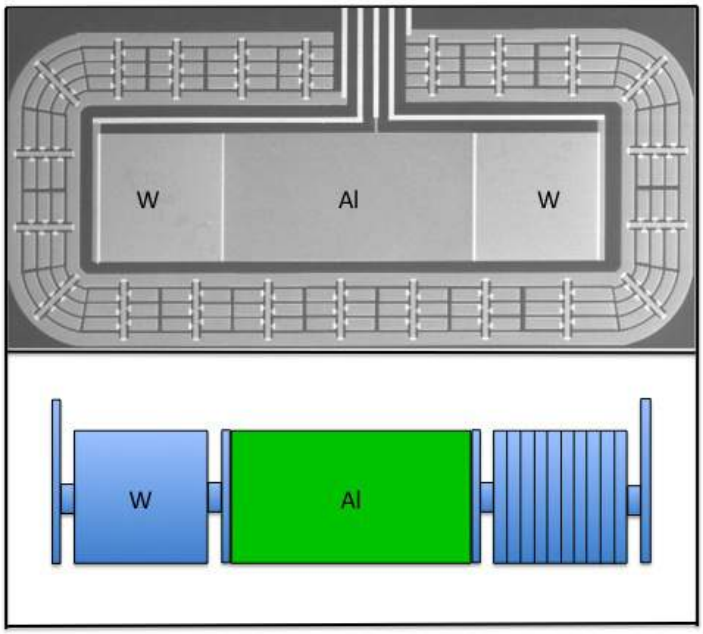

Figure 7.1: *Top*: An SEM image of a 500 μm-long $\times$ 250 μm-wide Al film qp device. *Bottom*: A schematic diagram of the "waterfall" model used to reconstruct x-ray pulse shape for this device. We divide each square TES into ten equal-sized strips and add short stubs on both ends to represent the imperfect connections the TES makes to its neighboring films. Dividing the W-TES into equal-sized strips allows us to track the thermal response of each strip, and calculate the time for thermal conduction along the full TES sensor.

To see how well this model simulates our pulses, we start by treating each W-TES square as a single lumped element. When energy flows from the Al into the W-TES, the temperature of W-TES increases. In this (simplest model, the heat pulse decays with the characteristic time constant given in Section 3.2.1:

$$\tau_{etf} = \frac{C}{G}\,\frac{1}{1+\alpha/n} \qquad (7.1$$

A fit to our data using this single exponential decay is shown in Figure 7.2(a , where

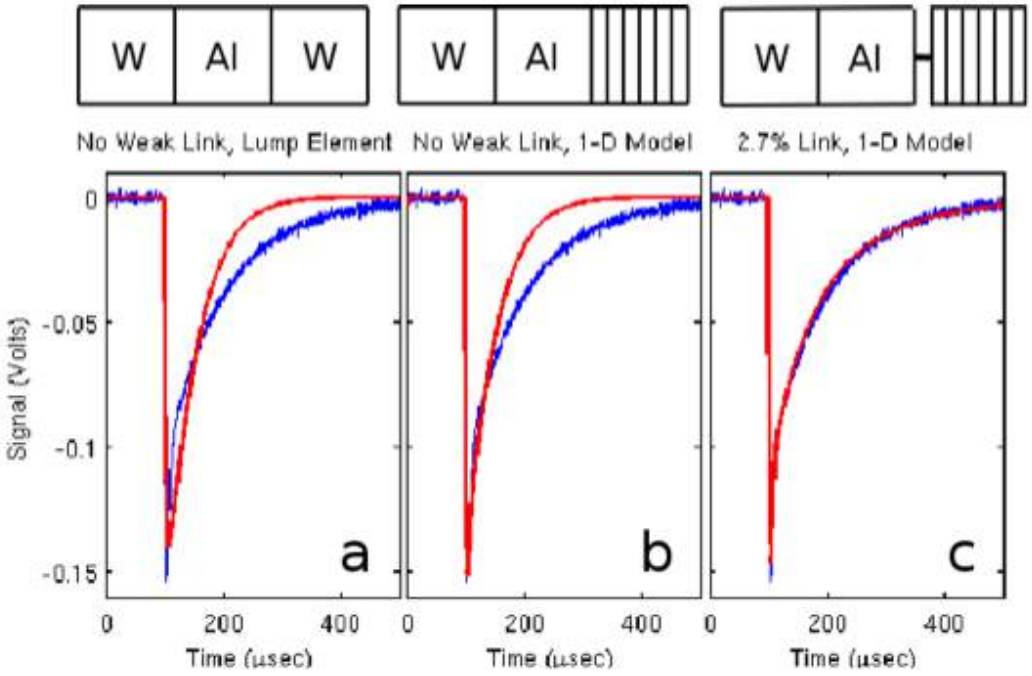

Figure 7.2: Simulated pulse shape (red plotted on top of a real data pulse (blue . (a A simple lumped element model predicts a single fall-time. (b Partitioning the TES into 10 equal strips yields a good match to the initial sharp peak observed in the data. (c Incorporating small W stubs in series with the TES to mimic boundary impedance at the W/Al interfaces accurately reproduces the longer fall-time seen in the tail of real pulses.

the simulated pulse (red is plotted on top of the real data pulse (blue . The simulated pulse does not math the real data but does show the general pulse shape. Note: in

this simulation, the heat capacity for tungsten in its transition, C_{TES}, is computed by adopting the G-L two fluid model, where the heat capacity is treated as a sum of normal-state (C$_n$ and superconducting (C$_s$ terms:

$$C_{TES}(T = f_n C_n(T + (1 - f_n C_s(T \quad (7.2$$

Here, the resistance parameter, $f_n = R_{TES}/R_n$ varies between 0 (W film completely superconducting and 1 (W film completely normal .

For real devices, when the flux of event energy flows from the Al film into the W-TES, it takes a finite amount of time for the heat energy to propagate through the TES from one end to the other [60]. To account for this, we modify the lumped element model by dividing each square W-TES into equal-sized strips (see Figure 7.2[b] . We then track (in time steps the heat conduction from one strip to the next and apply the Weidemann-Franz Law:

$$\frac{\kappa}{\sigma} = LT \quad (7.3$$

where κ is the thermal conductivity and σ is the electrical conductivity at a given temperature, T. The Lorentz number, L, is theoretically derived to be $L_0 = 2.44 \times 10^{-8}$ $[\frac{\mathrm{W}\cdot\Omega}{K^2}]$ [61], but experimentally its value can vary by up to a factor of two for different metals. In our simulations, the Lorentz number was found to be $\sim 50-150\%$ of the theoretical value. This revised model shown in Figure 7.2(b recreates the sharp initial peak seen in the real pulses.

The third piece of our simplified geometric model accounts for losses at the W/Al overlap region. For a non-inverted device geometry, we model the imperfect step coverage (waterfall using a short stub to join the Al and W films together[62]. We later discovered that this model also works well for the inverted device geometry where, by design, no step coverage issues are present. This indicates that our dominant boundary impedance is in the overlap region between the W and Al films (rather than in the waterfall region . The critical current in the stub is smaller than that in a full-sized strip, resulting in local heating of the W-TES. This drives the quiescent state of the TES beyond the steepest part of the TES transition, thereby reducing electro-thermal

feedback effects and increasing the pulse fall-times. By explicitly incorporating this "waterfall" effect into our model, we have obtained excellent agreement between pulse data and our simulations (Figure 7.2(c . Out pulse simulation scripts are shown in Appendix L.

Figure 7.3 shows simulated TES pulses assuming different percentages of W/Al connectivity, while holding other parameters fixed. In the legend, 0.02 corresponds to a 2 % effective W/Al connection (1.0 corresponds to a 100 % connection . The simulated pulse shapes shown vary considerably as a function of W/Al connectivity, but become similar and show the same characteristic fall-time for $\geq 10\%$ connectivity. A careful fit to our data show that the percentage of connectivity in real devices is $\sim 2-3\%$ for non-inverted devices and $\sim 4-5\%$ for inverted devices. Thus, poor waterfall connectivity at the W/Al boundaries of non-inverted devices is not the limiting factor of their performance.

7.1.1 Revisit 1997 Pulses

One triumph of the waterfall model decribed above is that it also explains some mysterious double-peaked pulses first observed by the Cabrera group in 1997. Figure 7.4 shows the simulated pulses (black dashed line plotted over W-TES pulses seen with a 1997 qp test device (350 μm-long $\times$ 250 μm-wide $\times$ 300 nm-thick Al film as described in Section 3.2.2. The double-peaked pulse structure seen in Figure 7.4[left] can now be explained by modeling the (poor W/Al connection at the far end of each W-TES where the W attached to the Al bias rail. The particular pulse shown was well fit by assuming a 15% connection at the main Al/W interface, and a 3.6 % connection at the Al bias rail. Figure 7.4[right] shows a pulse from the second W-TES of the same device. Again, two distinct fall-times are evident. The first sharp peak corresponds to heat conduction along the W-TES. The second decay time is well modeled by assuming imperfect connectivity at the W/Al boundaries.

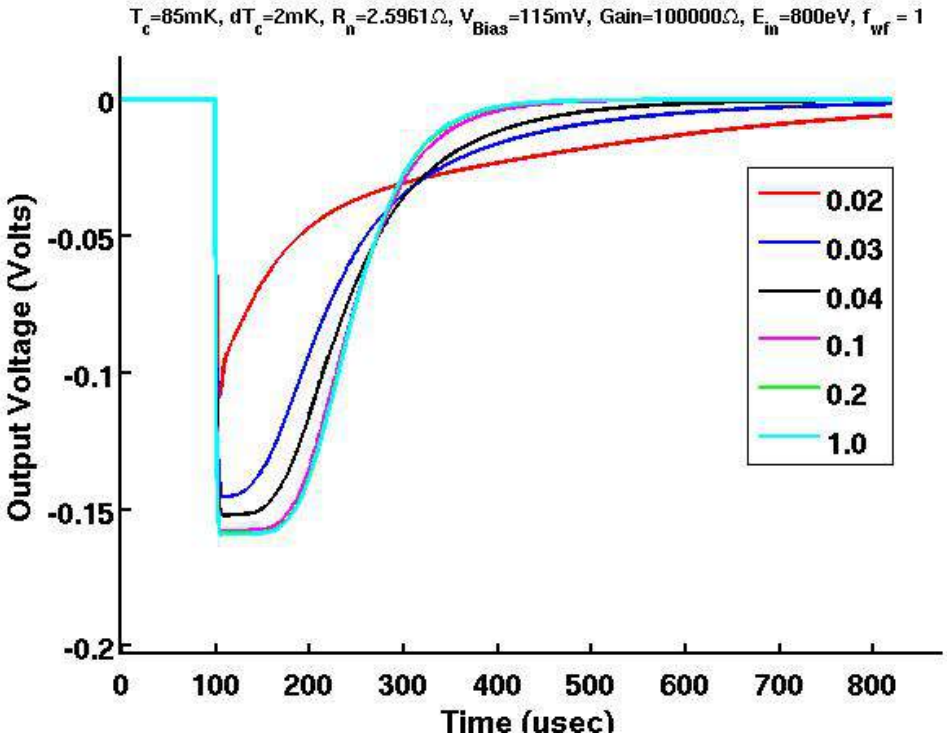

Figure 7.3: Six simulated pulses, each assuming a different percentage (2%- 100% of W/Al connectivity. The smallest pulse shown corresponds to the 2% case. For connectivities $\geq$ 10%, the pulse shapes become similar and have comparable fall-times.

7.1.2 Template Matching

Figure 7.5 shows a series of simulated pulse templates ranging from 100 eV to 1800 eV in 100 eV increments. These templates are based on the model shown in Figure 7.1 and are used to reconstruct the x-ray event energy in our experiments. In a TES, two major noise sources exist: Johnson noise (V_{rms} , given by:

$$V_{rms} = \sqrt{4k_B T R f} \qquad (7.4$$

and thermal power fluctuation noise between the electron and phonon systems:

$$P_{rms} = \sqrt{4k_B T^2 g f} \qquad (7.5$$

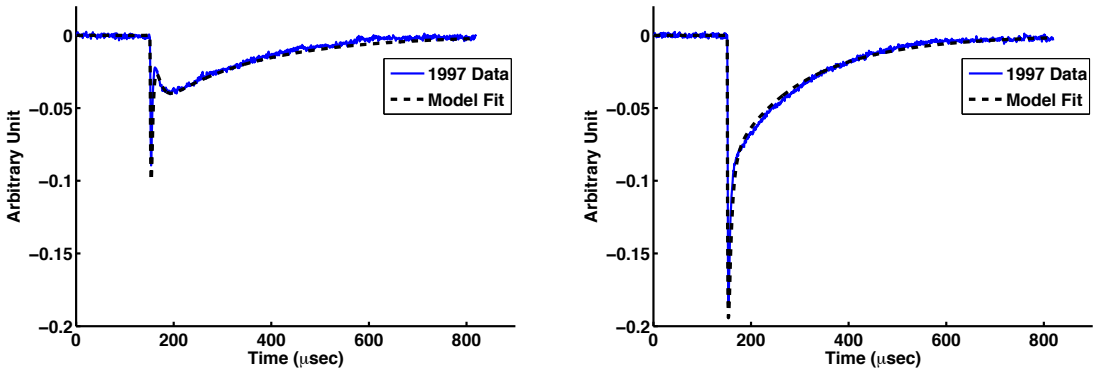

Figure 7.4: Simulated pulses (dashed black lines and real pulses (blue from TESs at opposite ends of the 1997 qp test device. *Left*: The double-peaked pulse shape can be simulated by adding an impedance to the W/A interface at the Al bias rail. *Right*: Typical pulse for opposing TES channel on the same device. The pulse shape looks similar to modern device results. This is well modeled using only one stub at the main Al film/ W-TES boundary.

where

$$g = \frac{dP}{dT} = \frac{d}{dT}(\Sigma(T^5 - T_b^5 \quad = 5\Sigma T^4 \tag{7.6}$$

Since these power fluctuations dissipate energy on a time scale comparable to the recovery time, τ_{etf}, of the device [62], we cannot treat the noise in each time bin independently. Hence, a standard χ^2 minimization technique is no longer appropriate. In the standard signal analysis, the χ^2:

$$\chi_j^2 = \sum_i \left(\frac{S_i - T_{i,j}}{\sigma_{i,j}} \right)^2 \tag{7.7}$$

is the sum over bins of signal deviation from the templates divided by expected noise variance. S_i corresponds to i^{th} bin of the signal, S. $T_{i,j}$ corresponds to i^{th} bin of the j^{th} template, and $\sigma_{i,j}$ is the expected root-mean-square (rms noise at the i^{th} bin of the j^{th} template. The template with the lowest deviation is the best fit.

Since we cannot treat each time bin independently, we need to construct a correlated covariance matrix, Σ, where each time bin is dependent on other time bins.

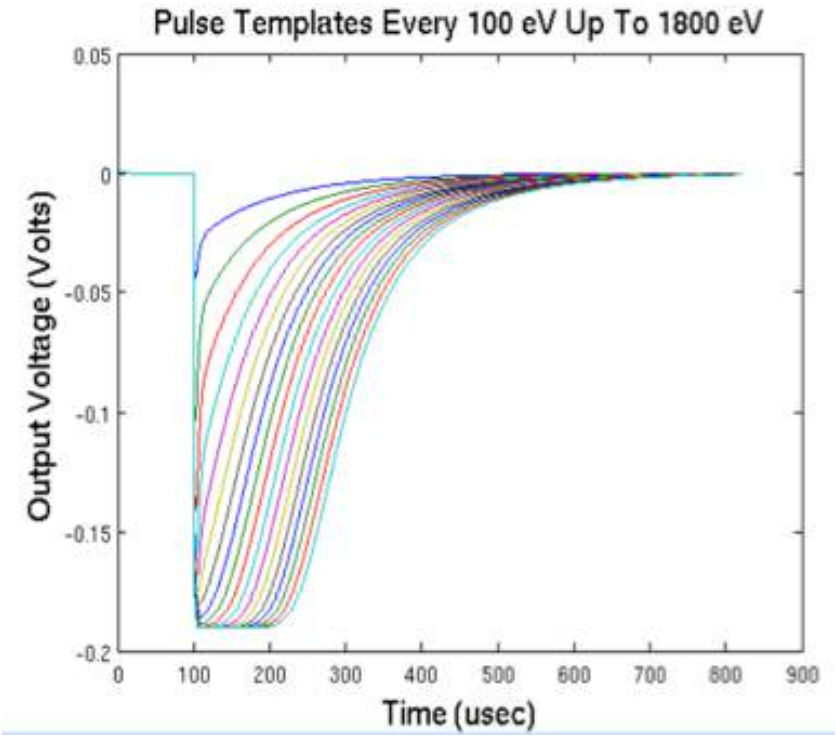

Figure 7.5: Simulated pulse templates with energy ranging from 100 eV to 1800 eV, 100 eV increment. These templates are generated to fit the real event pulses to reconstruct the x-ray event energy.

Notice Σ here is an $n \times n$ matrix and is different from the electron-phonon coupling constant. The χ^2 equation then becomes:

$$\chi^2 = (S - T\ ^T(\Sigma^2\ ^{-1}(S - T \qquad (7.8$$

A more in-depth discussion can be found in B. Shank's thesis [62]. Key points of the analytic approach are presented in Appendix M. Using a series of templates like those shown in Figure 7.5, combined with a χ^2 minimization described by Equation 7.8, we can accurately reconstruct x-ray event energies for both saturated and unsaturated pulses observed in real devices (Figure 7.6 .

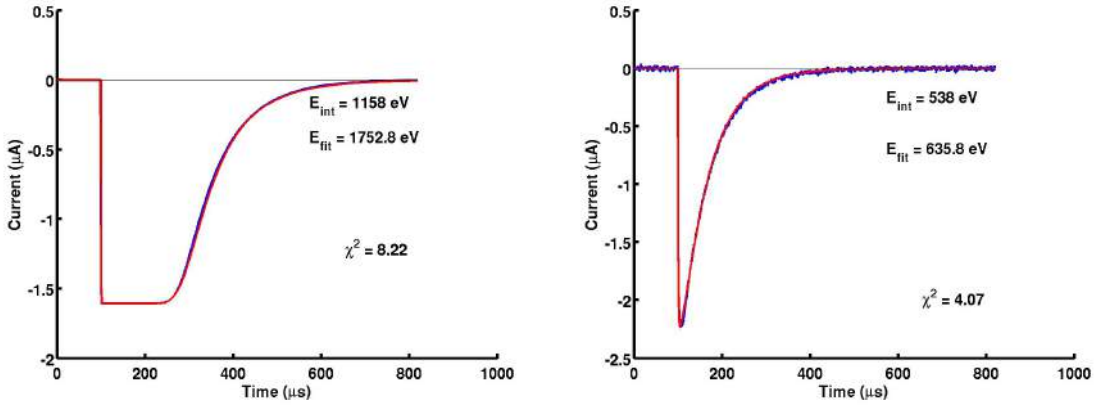

Figure 7.6: Real event pulses (blue and template-matched simulated pulses (red for both saturated [left] and non-saturated [right] pulses.

7.1.3 Comparison of Pulse Integration and Template Matching Methods for Energy Reconstruction

Figure 7.7[a] shows a histogram of W-TEs direct-hit events, where the event energies were determined using the pulse integral method (Equation 6.9 . Figure 7.7[b] shows the same W-TES direct-hit events. Here, the event energies were determined using the waterfall model to simulate TES pulses that were then compared to the data using our template matching technique. As the histograms show, the template matching technique correctly reconstructs the known (7.6 % energy separation between Cl K_α and Cl K_β lines while the integral method underestimates the energy separation. Perhaps this is not a surprise, since the integral method is inherently non-linear in the saturation regime.

In Figure 7.8 we show energy distribution plots for events in a single, inverted qp device (500 μm-long $\times$ 500 nm-thick Al film . The dataset shown was taken at 56 mK, with a W-TES voltage bias of -125 mV. The figure on the left was generated using the pulse integral method (see Equation 6.9 while the figure on the right was analyzed using our optimal filter technique. Since the energy accuracy of the pulse integral technique worsens as a W-TES gets into its saturated regime, it is not surprising that the two analysis methods yield different results for the energies of direct-hit events.

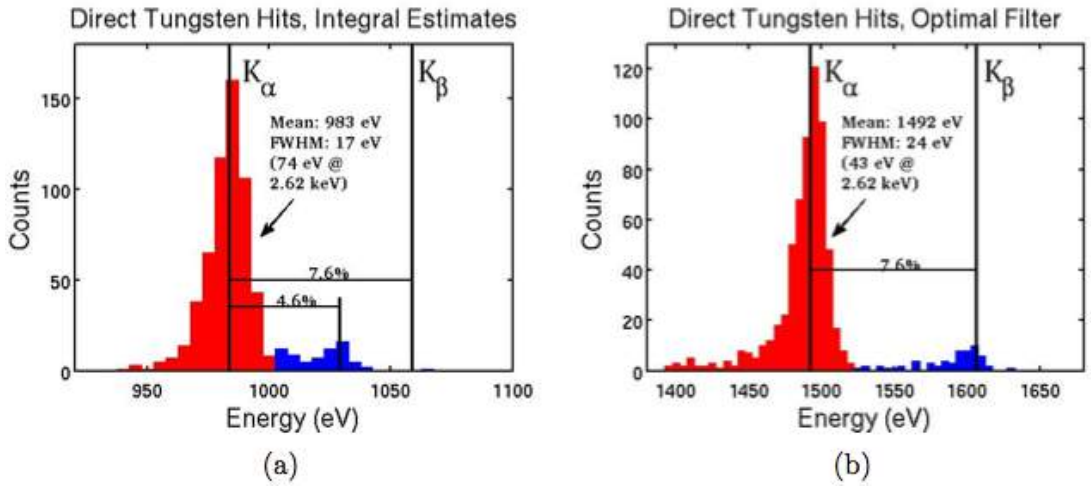

Figure 7.7: W-TES direct-hit histograms showing both Cl K_α(2.62 keV and K_β(2.82 keV lines. The plots shown here used the same dataset. (a Pulse integral method: Saturated event energies are suppressed using this method, and effect is non-linear. The observed separation of the K_α and K_β lines is 4.6 % rather than the correct 7.6 %. (b Template matching method: The K_α and K_β peaks show the proper 7.6 % energy separation.

For the data shown, a discrepancy of ~ 60 % in energy is evident for direct-hit events. For the non-saturated, small pulses the discrepancy is relatively small, $\sim 20\%$.

7.1.4 Energy Reconstruction with Different Temperatures and Voltage Biases

We performed a series of x-ray experiments on the same qp device but using different operating temperatures and W-TES voltage biases. We analyzed the data using a non-linear optimal filtering technique. Figure 7.9[left] shows the resulting energy distribution plot for one experiment performed at 43 mK, with the W-TESs voltage bias at -115 mV. Figure 7.9[right] shows the energy distribution plot for the same device operated at 56 mK, with a voltage bias at -125 mV. Notice the similarity of these two plots, particularly for W-TES direct-hit events, despite the different operating conditions (temperature and bias . It seems our model is robust and can

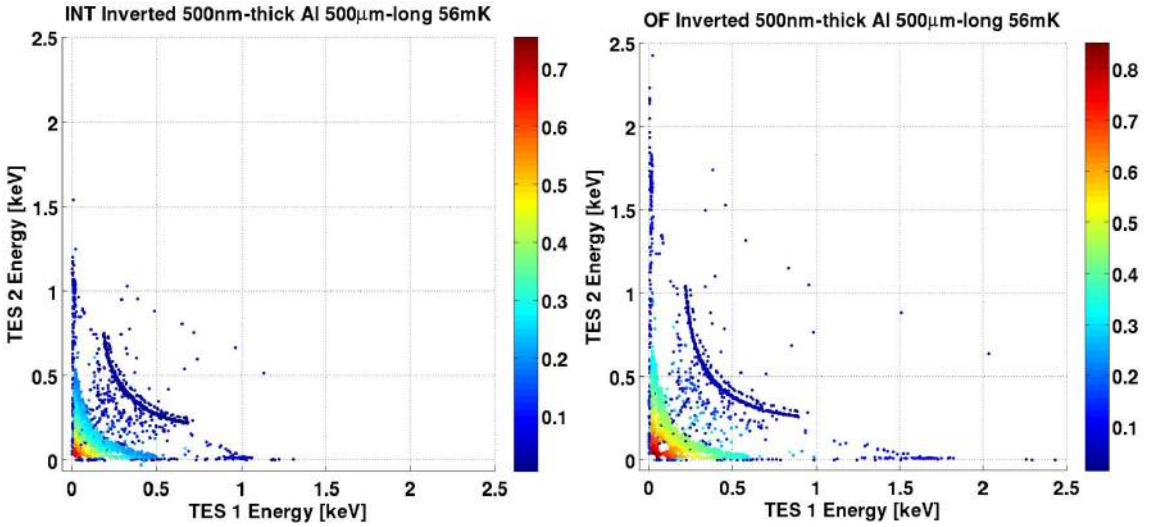

Figure 7.8: Energy distribution plots for an inverted geometry device (500 μm-long $\times$ 500 nm-thick Al film . *Left*: Pulse integral method. *Right*: Template matching method.

accurately reproduce event energies for a wide range of parameter space.

7.2 Al Film Diffusion

We have used two approaches to study the qp diffusion process in our Al films. The first involves a macroscopic 1-D diffusion equation with linear loss term, where we consider all qps to have an energy independent diffusivity, D, and we assume a single linear qp loss rate, $1/\tau$. This 1-D diffusion model has also been used by other groups [42]. Our second approach attempts to mimic effects caused by our sputtered Al film quality, incorporates qp decay rates into the diffusion process, and treats the diffusivity as a function of qp energy. In addition, we also incorporate a "percolation threshold",ϵ, into the diffusion model, whereby qps with energies below that threshold ($\Delta < \epsilon < 3\Delta$ do not diffuse, but rather lose their energy to the substrate. In terms of the energy down conversion process discussed in Chapter 3 (Figure 3.1 , our diffusion study assume a starting point at Stage III, where the qp energies are already below 3Δ.

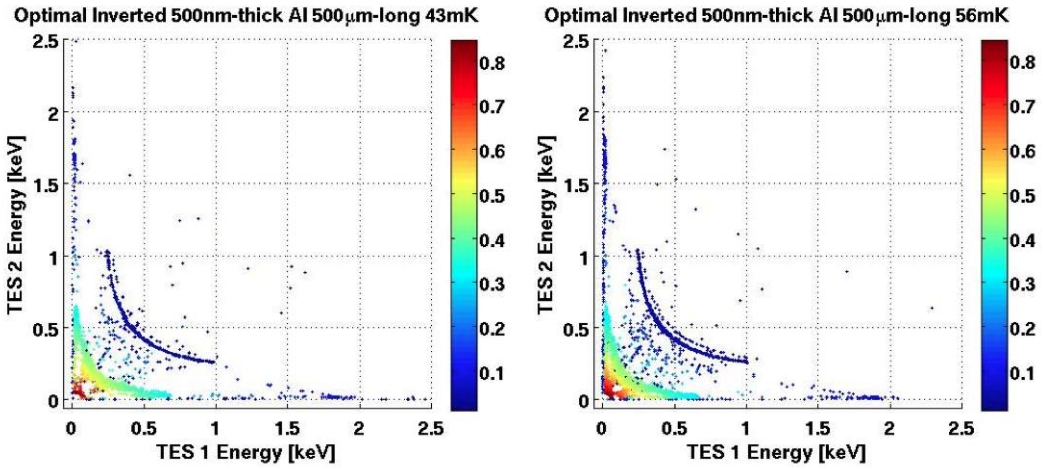

Figure 7.9: X-ray event energy distribution using optimal filter template matching technique. *Left*: Experiment performed at 43 mK with W-TES voltage bias at -115 mV. *Right*: Experiment performed at 56 mK with W-TES voltage bias at -125 mV.

7.2.1 1-D Diffusion Model

In our 1-D diffusion model, we consider the quasiparticle number density, $n = n(x, t$, to have a collective (finite life-time, τ. These qps are generated simultaneously in the Al film from a single point source at a rate of $s(x, t = n_0\ \delta(x - x_0\ \delta(t - t_0$. We can write the 1-D diffusion equation as:

$$\frac{dn(x,t}{dt} = D\nabla^2 n(x,t\ - \frac{n(x,t}{\tau} + s(x,t\ , \tag{7.9}$$

Since the qps eventually either get absorbed by a TES or are lost to the substrate, $n(x, t \to \pm\infty\ = 0$. We can integrate Equation 7.9 over time as follow:

$$\begin{aligned} \int_{-\infty}^{\infty} dt \frac{dn}{dt} = 0 &= D\nabla^2 \int_{-\infty}^{\infty} dt\ n - \frac{1}{\tau}\int_{-\infty}^{\infty} dt\ n + \int_{-\infty}^{\infty} dt\ s \\ 0 &= D\nabla^2\phi - \frac{\phi}{\tau} + \rho \end{aligned} \tag{7.10}$$

where we have defined:

$$\phi(x \equiv \int_{-\infty}^{\infty} dt\ n(x,t \tag{7.11}$$

$$\rho(x \equiv \int_{-\infty}^{\infty} dt\ s(x,t\ . \tag{7.12}$$

Equation 7.10 can thus be re-written as:

$$\left(\nabla^2 - \frac{1}{l_{\rm d}^2}\right)\phi(x\ = -\frac{\rho(x}{D} \tag{7.13}$$

where $l_{\rm d} = \sqrt{D\tau}$ is the qp diffusion length.

In addition, the current density of qps, $\mathbf{J}$, is proportional to the gradient of the number density:

$$\mathbf{J} = -D\nabla n \tag{7.14}$$

At the W/Al boundary, qps are either absorbed by the W-TES or reflected back into the Al film. This translates into the following boundary condition:

$$d\mathcal{A}\cdot J = -D\ d\mathcal{A}\cdot\nabla n = -|d\mathcal{A}|nv, \tag{7.15}$$

where $d\mathcal{A}$ has units of length in the 1-D case, and represents the "surface" where the qps can leave the Al film and enter the W-TES. The qp absorption coefficient, v, has units of velocity. In other words, we can define a characteristic absorption length, $l_{\rm a}$ as:

$$l_a = \frac{D}{v} \tag{7.16}$$

Equation 7.13 can be solved analytically [**?**]. Defining the fractional qp energy absorbed by the left (right TES as F_L (F_R :

$$F_L = \frac{\lambda_{\rm d}\left(\lambda_{\rm ar}\,\cosh\left(\frac{1-2\xi}{2\lambda_{\rm d}}\right)+\lambda_{\rm d}\,\sinh\left(\frac{1-2\xi}{2\lambda_{\rm d}}\right)\right)}{\lambda_{\rm d}\left(\lambda_{\rm al}+\lambda_{\rm ar}\,\cosh\left(\frac{1}{\lambda_{\rm d}}\right)+(\lambda_{\rm d}^2+\lambda_{\rm al}\lambda_{\rm ar}\,\sinh\left(\frac{1}{\lambda_{\rm d}}\right)\right.} \quad (7.17$$

$$F_R = \frac{\lambda_{\rm d}\left(\lambda_{\rm al}\,\cosh\left(\frac{1+2\xi}{2\lambda_{\rm d}}\right)+\lambda_{\rm d}\,\sinh\left(\frac{1+2\xi}{2\lambda_{\rm d}}\right)\right)}{\lambda_{\rm d}\left(\lambda_{\rm al}+\lambda_{\rm ar}\,\cosh\left(\frac{1}{\lambda_{\rm d}}\right)+(\lambda_{\rm d}^2+\lambda_{\rm al}\lambda_{\rm ar}\,\sinh\left(\frac{1}{\lambda_{\rm d}}\right)\right.} \quad (7.18$$

The dimensionless variables, ξ, $\lambda_{\rm d}$, $\lambda_{\rm al}$ and $\lambda_{\rm ar}$, are defined by:

$$\begin{aligned}\xi &= x_0/w\\ \lambda_{\rm d} &= l_{\rm d}/w\\ \lambda_{\rm al} &= l_{\rm al}/w\\ \lambda_{\rm ar} &= l_{\rm ar}/w\end{aligned}$$

where w is the length of the Al film (w = 250, 350 or 500 μm . The variable, x_0 specify the position of the initial energy deposition within the Al film ($x_0 = 0$ corresponds the center of the film, so $\xi = \pm 1/2$ corresponds to the two ends of the film . The characteristic absorption length values $l_{\rm al}$ and $l_{\rm ar}$ depend on the properties of the Al nearest the left and right W-TESs. A full derivation of this analytical solution can be found in R. Moffatt's thesis[16].

Figure 7.10 shows a maximum likelihood fit to x-ray data for a 350 μm-long Al film (non-inverted device geometry using this diffusion model. The fit yields estimates for two important parameters: the characteristic qp diffusion length, $l_{\rm d}$ and the qp absorption into each W-TES, $l_{\rm al}(l_{\rm ar}$. Applying Equation 7.9 to our data yields $l_{\rm d} \sim$ 130 μm for all three Al film lengths studied (250, 350 and 500 μm with non-inverted (W over Al devices. In addition, our data indicate $l_{\rm al} \approx l_{\rm ar} \sim 100$ μm. Summing the two W-TESs energies and reconstructing position yields the inset of Figure 7.10. As expected, the sum of the W-TESs signal energies is noticeable smaller than 2.62

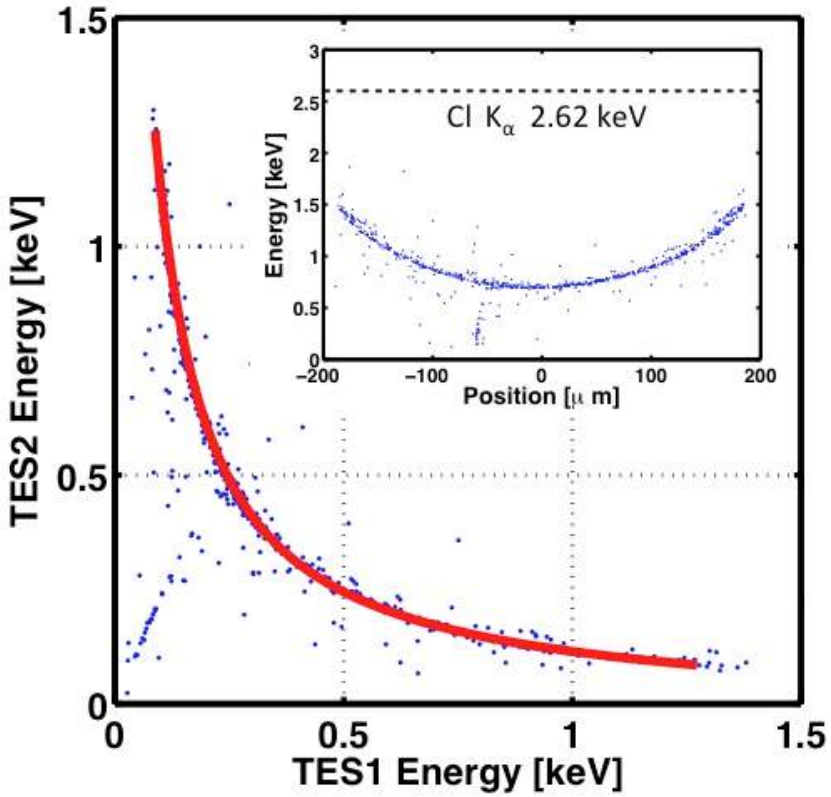

Figure 7.10: Raw energy collection distribution shown with a maximum likelihood fit (red . The banana-shaped cluster of points corresponds to direct-hit x-rays in the main Al film. (Inset : Collected x-ray energy vs. event location along the Al film. The energy loss (relative to the 2.62 keV x-rays can be attributed to a variety of factors as discussed in Chapter 3 and 6.

keV incident energy. We understand this discrepancy in terms of the energy loss mechanisms described in Chapter 3 and 6. Note that individual values of D and τ cannot be determined using Equation 7.9 alone.

A coordinate transformation can be performed on our energy distribution data (W-TES2 vs. W-TES1 to show event energy vs. event location along the Al film. X-ray events with the same energy generate a "banana" shape band, with larger event energies corresponding to bands further away from the origin as shown in Figure 7.11[left]. By defining an angle, θ, away from the x-axis (W-TES1 , we can transform each band (or population of events into a graph of event energy vs. event position

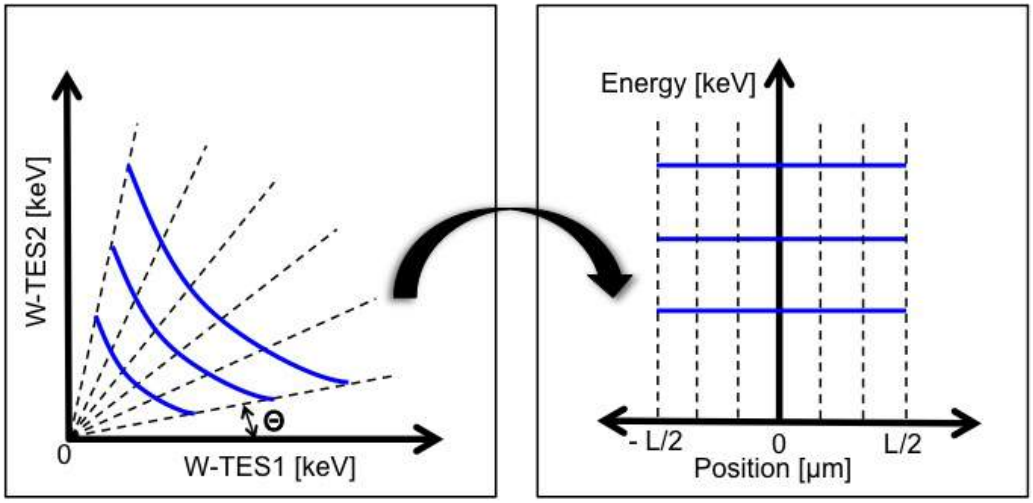

Figure 7.11: Coordinate transformation from raw energy distribution plot to energy vs. event position along the Al film. *Left*: Regular energy distribution plot where events with the same energy form a single "banana" band. Higher energy bands extend further away from the origin. Defining an angle θ away from the x-axis, we can transform each banana band into the energy vs. position plot shown on the right. The center of the Al film is defined to be at position zero. The film (length L extends to the W-TESs at the two ends of the Al film ($x = \pm L/2$.

as shown in Figure 7.11[right]. The Al film extends from $-L/2$ to $L/2$, where L is the length of the film (250, 350 or 500 μm .

Figure 7.12 shows the results after applying this transformation to the fitted data of Figure 7.10 (a 250 μm-long non-inverted device . Notice that the reconstructed energies for Cl Kα (2.62 keV and Kβ (2.82 keV are slightly smaller than the full x-ray energies due in part to energy loss to the substrate through phonon emission (see Section 3.1.4 Table 3.2 . These are the deposited energies before position-dependent qp trapping and sub-gap phonon losses have occurred, as will be addressed in the next section. One interesting feature seen in Figure 7.12[Left] is the cluster of events near $x = -50$ μm. These correspond to x-ray hitting the Al/W ground rail as indicated in the inset.

Another interesting feature seen in the reconstructed energy plot is shown in

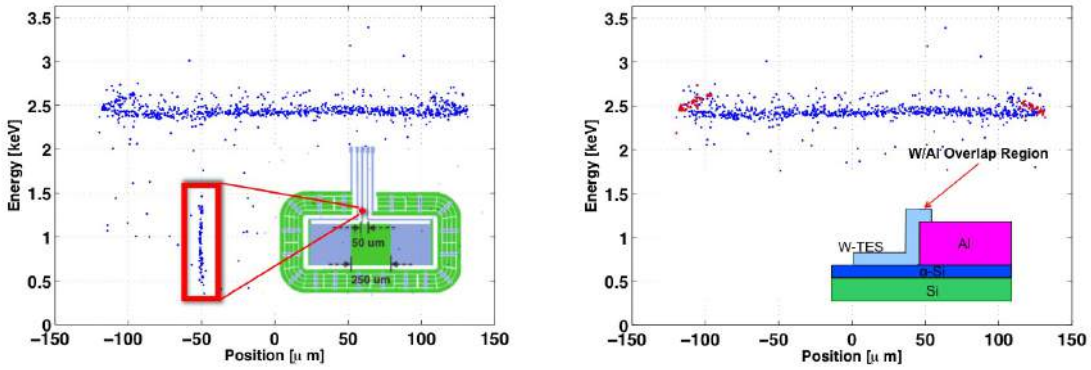

Figure 7.12: Reconstructed Cl Kα(2.62 keV and Cl Kβ(2.82 keV x-ray energies as a function of event position along Al film. The energy scale corresponds to the deposited energy after losing some phonon energies to the substrate but before position dependent qp trapping and sub-gap phonon losses have occurred, and therefore are smaller than 2.62 keV and 2.82 keV. *Left*: The spur seen in the red box (-50 μm consistent with events hitting directly in the Al/W ground rail. *Right*: Events in red are from x-ray directly hitting the W part of the W/Al overlap region.

Figure 7.12[right]. The population of events shown in red that form a "fold-back" band near $x = \pm 125$ μm are caused by 2.6 keV x-rays that directly hit the W film in the W/Al overlap region (shown in the inset .

For the non-inverted device, the W and Al has ~ 5 μm overlap region on each end of the Al film. The total event number in red compares with the total Al direct-hit events consistent with the ratio of the area of the W/Al overlap region to the total Al film area. These events show higher reconstructed energies because the "escaped" high energy phonons are captured by the Al film underneath. The situation is different for devices with the inverted geometry (see Figure 7.13[right] . There, x-ray events directly hitting this region of the W film have some phonon energy escape to the substrate, as usual. However, some of these escaped phonons can couple back into Al film and contribute signal to the opposite W-TES, also resulting in a fold-back effect (circled events in the Figure 7.13[right] . Figure 7.13[left] shows the non-inverted geometry re-plotted to show a direct comparison with the inverted device geometry.

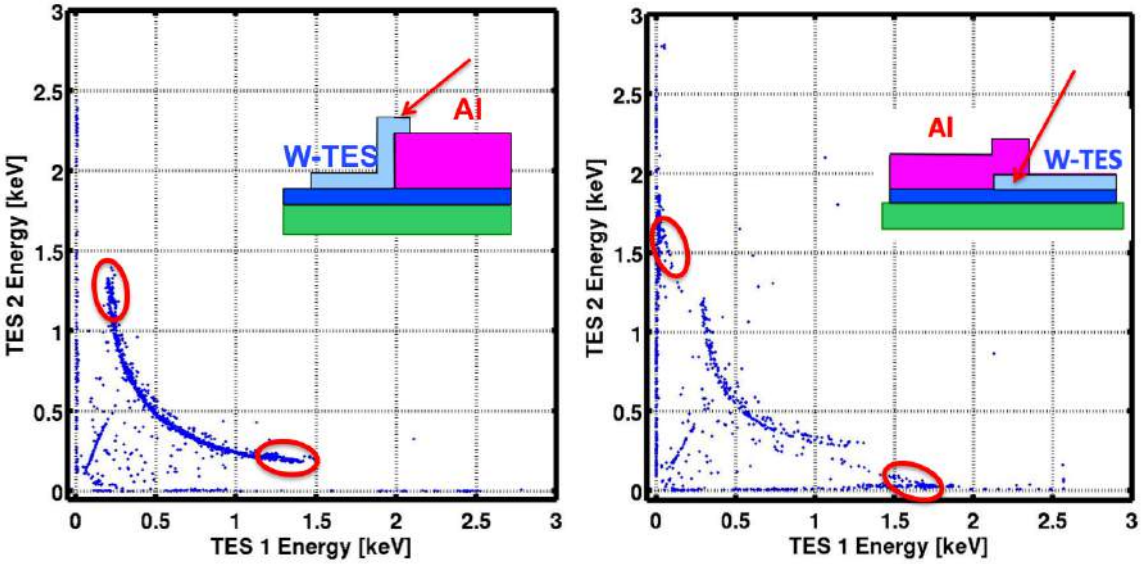

Figure 7.13: A fold-back effect for x-rays hitting the W/Al overlap region is evident for both the non-inverted[left] and inverted[right] devices.

Table 7.1 shows maximum likelihood fits for the nine inverted devices tested. In these fits, we used a fixed scaling factor, E_{sf}, for each film thickness, consistent with Table 3.2 (E_{sf} = 2.33, 2.45 and 2.52 keV for 300, 500 and 900 nm-thick Al films, respectively . The fits were not perfect, especially for the thicker Al films. But to get better maximum likelihood fits required non-physical values for E_{sf}. Table 7.2 shows the results of the position reconstruction for these nine inverted devices after performing the coordinate transformation described earlier.

The fitted values of the diffusion lengths and absorption lengths for these nine devices are shown in Table 7.3. The absorption lengths were found by averaging the values of l_a for W-TES1 and W-TES2. The diffusion length values, l_d, are comparable for devices with equal Al film thickness. On the other hand, for a fixed film length, l_d is greater for thicker films, indicating that the limiting factor for our qp diffusion is film thickness rather than intrinsic properties of the Al film. In addition, the absorption lengths for the same film thickness show comparable results and increase with thickness more dramatically than l_d. These trends are evident in the graphs shown in 7.14, where we plot l_a and l_d versus Al film thickness (z .

The diffusion length (in units of μm is plotted for each of nine devices in Figure 7.14[left]. Colors indicate data form devices with the same film length. The dashed-line is the best linear fit to all nine points plus an assumed data point at the origin. From this result we find:

$$l_{\mathrm{d}} = \sqrt{D\tau} \propto z \tag{7.19}$$

We know the diffusivity, D, is linearly proportional to the mean-free-path, Λ, and in the thickness-limited regime, $\Lambda \propto z$. Hence:

$$D \propto v_F \Lambda \propto z \tag{7.20}$$

Based on this result, we also find that the qp loss time $\tau \propto z$.

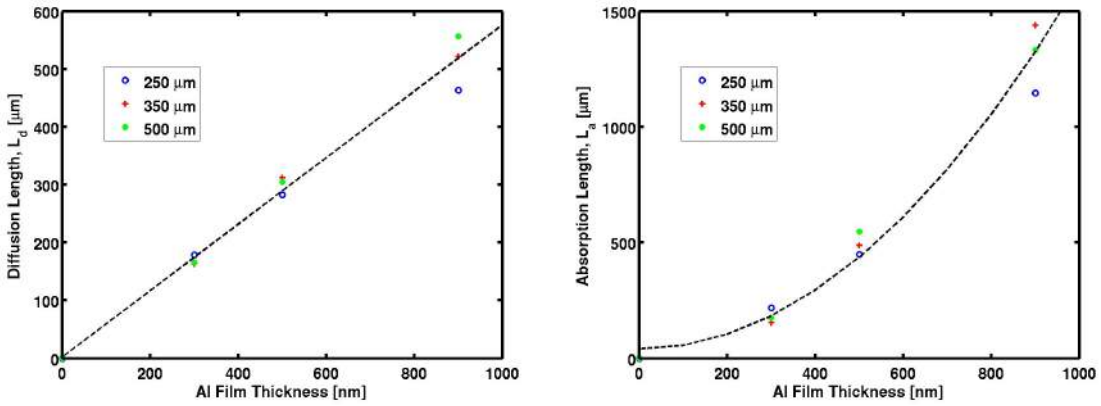

Figure 7.14: The colored data points correspond to the same film length. *Left*: Experimental values of the qp diffusion length for nine separate devices along with a linear fit (dashed line . *Right*: Experimental values of the qp absorption length for the same nine devices, with a quadratic fit (dashed-line .

In Figure 7.14[right], we plot the Al film qp absorption length for nine different test devices as function of the Al film thickness. Again, the colored data points correspond to the same film length. The dashed-line is a quadratic fit, which seems work well in this case. This indicates that:

$$l_{\mathrm{a}} \propto \frac{D}{v} \propto z^2 \tag{7.21}$$

so:

$$v \propto \frac{1}{z} \tag{7.22}$$

Physically,

$$v \propto < v_{qp} > p \tag{7.23}$$

where $< v_{qp} >$ is the average qp velocity, and p is the "effective" transmission probability for qps to move from the Al film into the W-TES. Thus, we can understand Equation 7.22 because the qp attempt frequency to go through the Al/W boundary decreases as the Al film thickness increases, assuming the same absolute transmission probability at the interface. The results shown in Figure 7.14[left] for the nine inverted qp devices with different lengths and film thicknesses indicate that the qp diffusion in our Al films is still thickness-limited even for $z = 900$ nm.

7.2.2 Microscopic Model: Percolation Threshold

To understand our Al quasiparticle diffusion process further, we consider an idealized microscopic model of qp decay. According to Kaplan, et. al. [63, 32, **?**], a qp's decay rate can be written as the sum of three terms: Γ_{emit}, Γ_{abs} and Γ_r:

$$\Gamma_{emit}(E = C\int_0^{E-\Delta} d\Omega\Omega^2\ \rho(E-\Omega\ \left(1-\frac{\Delta^2}{E(E-\Omega}\right)\times[n(\Omega\ +1][1-f(E-\Omega\ ] \tag{7.24}$$

$$\Gamma_{abs}(E = C\int_0^{\infty} d\Omega\Omega^2\ \rho(E+\Omega\ \left(1-\frac{\Delta^2}{E(E+\Omega}\right)\times n(\Omega\ [1-f(\Omega+E\ ] \tag{7.25}$$

$$\Gamma_r(E = C\int_{E+\Delta}^{\infty} d\Omega\Omega^2\ \rho(\Omega-E\ \left(1+\frac{\Delta^2}{E(\Omega-E}\right)\times[n(\Omega\ +1]f(\Omega-E \tag{7.26}$$

where

$$C = \frac{1}{\tau_0(k_bT_c\ ^3[1-f(E\ ]} \tag{7.27}$$

Γ_{emit} and Γ_{abs} correspond to qp rates for phonon emission and absorption, and Γ_r corresponds to qp-qp recombination. We used an accepted value from the literature to set $\tau_0 = 110$ ns. The term $f(E\ = 1/(e^{(E-E_F/k_bT}\ + 1$ is the Fermi function, the qp energy density $\rho(E\ = E/\sqrt{E^2-\Delta^2}$, and $n(\Omega$ is the number density of phonons per mode at energy Ω.

Detectable signals in our experiments correspond to Stage III of the down conversion model outlined in Figure 7.15. Here, we can assume the superconductor is near its thermodynamic equilibrium, and that both the quasiparticle and phonon number densities are in the dilute regime. At this stage (below the red dotted line in Figure 7.15 , both quasiparticle and phonon energies are small ($< 3\Delta$. Thus, these phonons can no longer break Cooper pairs, but instead are simply lost to the substrate. Hence, we can treat $\Gamma_{abs} \approx 0$. In addition, because the qp density is low in this regime, $\Gamma_r \approx 0$. The qp Fermi function, $f(E$, can be ignored since $T \ll T_c$,

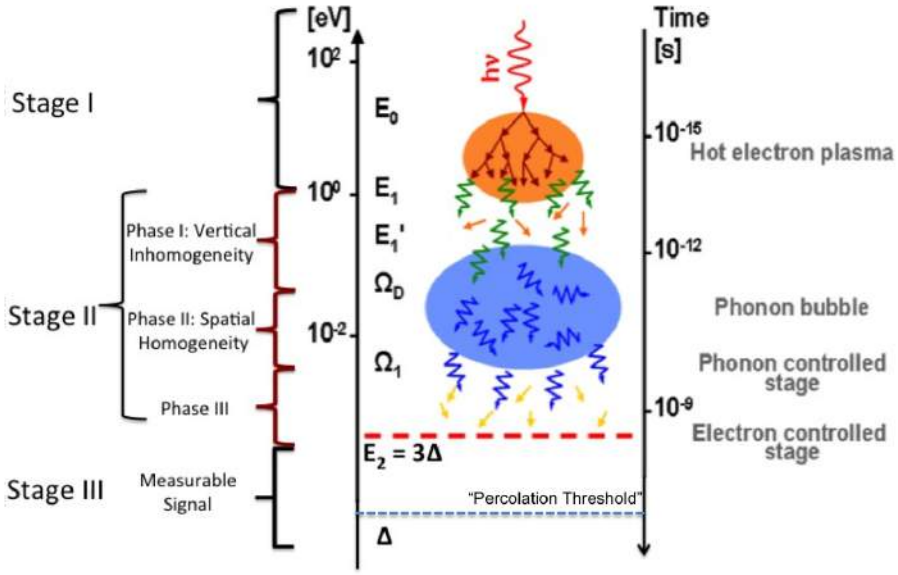

Figure 7.15: Energy down conversion process when a low energy x-ray is absorbed by a superconductor like Al. We added a new floating parameter (percolation threshold in between the energies Δ and 3Δ. Below this threshold, qps can get stuck in the film if they become trapped in local energy minima. Their energies eventually relax to the substrate and get loss.

and $n(\Omega \sim 0$ in the dilute limit. Changing into dimensionless quantities, $\tilde{E} \equiv E/\Delta$ and $\tilde{\Omega} \equiv \Omega/\Delta$, we can rewrite Equation 7.24 as:

$$\Gamma_{emit}(\tilde{E} = \frac{(1.76\ ^3}{\tau_0} \int_0^{\tilde{E}-1} d\tilde{\Omega}\tilde{\Omega}^2 \frac{\tilde{E}-\tilde{\Omega}}{\sqrt{(\tilde{E}-\tilde{\Omega}\ ^2-1}} \left(1 - \frac{1}{\tilde{E}(\tilde{E}-\tilde{\Omega}}\right) \qquad (7.28$$

We have used $\Delta = 1.76 k_b T_c$, and the integration over phonon energies, $\tilde{\Omega}$, goes from zero (no phonons emitted by qps to $\tilde{E} - 1$ (qps give all their energy to phonons . We can then calculate how fast the qps shed sub-gap phonons and lose their energy to the substrate before reaching a W-TESs at either end of the Al film. There is an additional energy loss mechanism that we describe via a floating fit parameter, ϵ, where Δ and 3Δ. We call ϵ the "percolation threshold". If qps decay to an energy below this threshold, they cease to propagate and get stuck in a local gap minimum. Thus, that energy is ultimately also lost to the substrate. To further complete the microscopic model, we allow the quasiparticle diffusion coefficient, D, to be energy dependent according to:

$$D(E \ = \frac{1}{3} v_{qp}(E \ \Lambda, \tag{7.29}$$

where the qp group velocity is given by:

$$v_{qp}(E \ = \frac{\partial E}{\partial p} = \frac{\partial \mathcal{E}}{\partial p}\frac{\mathcal{E}}{E} = v_F \sqrt{1 - \frac{\Delta^2}{E^2}} \tag{7.30}$$

and we have assumed a simple dispersion relation ($E_k^2 = \mathcal{E}_k^2 + \Delta^2$ to get $dE/d\mathcal{E} = \mathcal{E}/E$. Adding this percolation threshold to our microscopic model, we can thus compute Γ_{emit} (Equation 7.28 and use it to fit the experimental data as shown in Figure 7.16.

Next, using the same coordinate transformation as before (Section 7.2.1 , we generated the plots shown in Table 7.4 for Al direct hit events. The resulting fits (including the percolation threshold approach are comparable to those obtained with our simple 1-D diffusion equation. While the new fits are not noticeably better, the microscopic model does provide additional information in the form of two physics-related fit parameters: the percolation threshold (in units of Δ and the "effective" qp transmission probability at the Al/W interfaces. Values of these parameters are shown in Table 7.5 for the nine samples tested.

The percolation threshold is roughly constant for a given film thickness, but decreases for thicker films, where the qps can relax to lower energies before getting stuck at local gap variations. The "effective" transmission probabilities also decrease

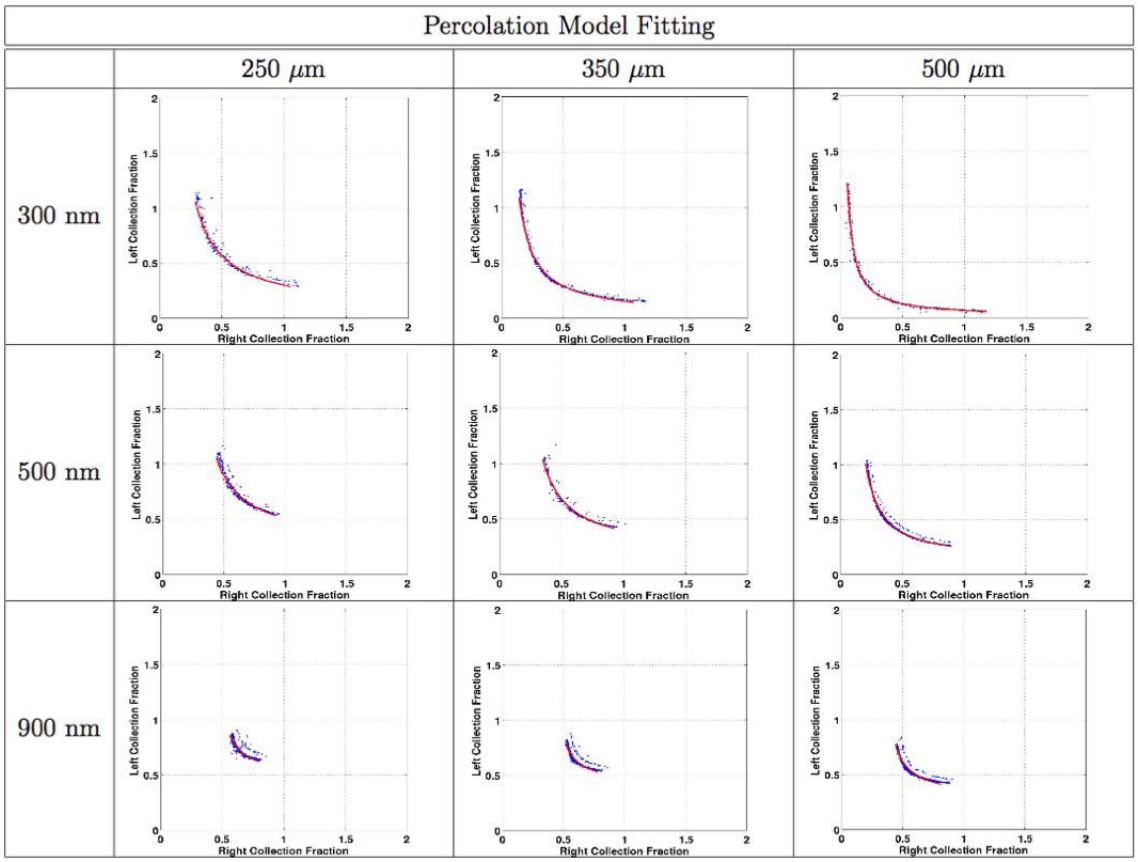

Figure 7.16: Maximum likelihood fit using the microscopic model with percolation threshold for nine of the inverted devices.

as the films get thicker, for the same reasons mentioned in Section 7.2.1. However, the effective qp transmission probability varies from sample to sample. We do not yet understand the origin of this variation.

Maximum likelihood fit with fixed E_{sf} using diffusion equation			
	250 μm	350 μm	500 μm
300 nm	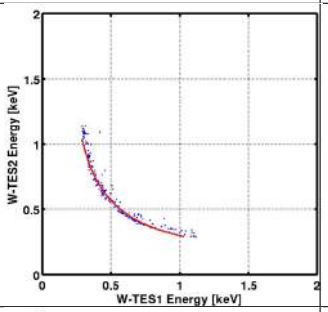	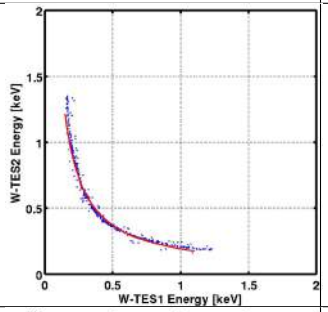	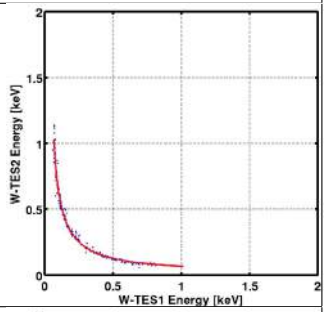
500 nm	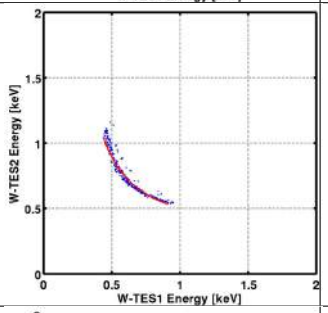	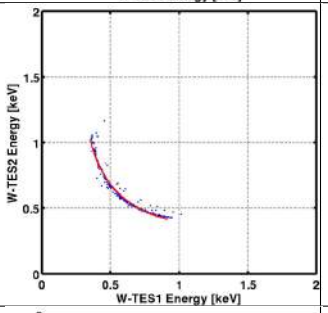	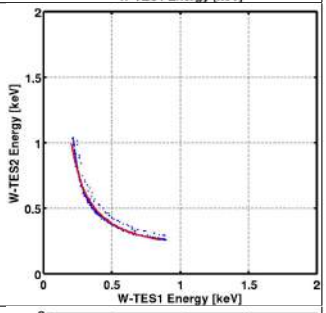
900 nm	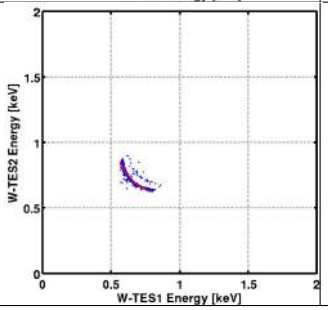	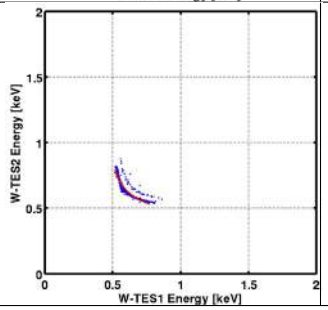	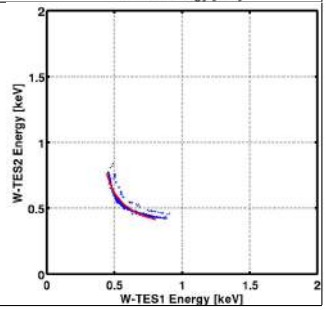

Table 7.1: Maximum likelihood fits for nine "inverted" test devices with various lengths (horizontal and thicknesses (vertical . Scaling factors, E_{sf}, were fixed, and only diffusion length, l_{d} and absorption length, l_{a} were fitted in these data.

Position reconstruction based on 1D diffusion equation			
	250 μm	350 μm	500 μm
300 nm	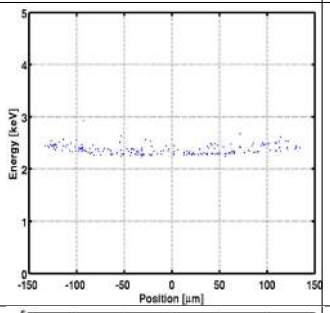	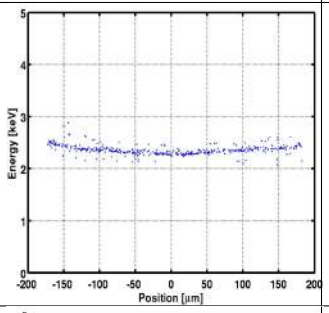	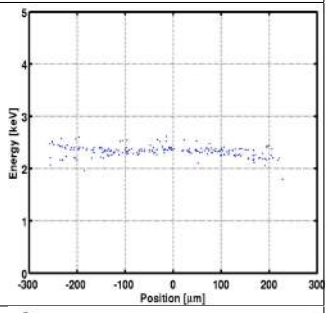
500 nm	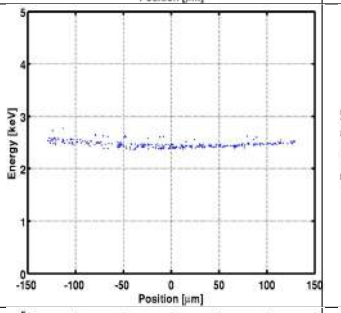	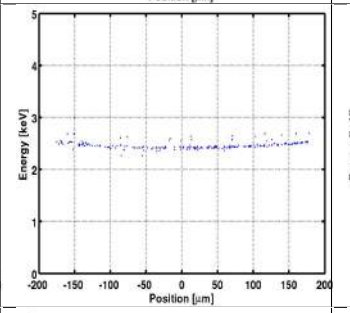	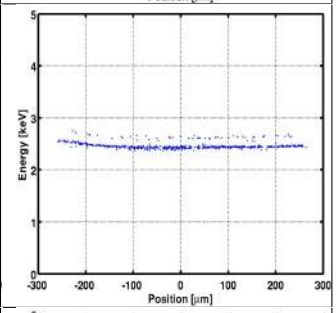
900 nm	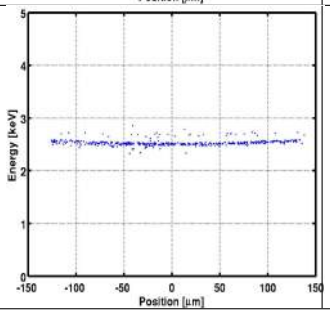	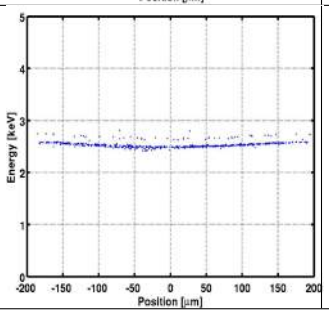	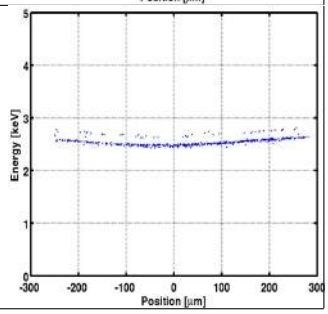

Table 7.2: The results of Cl K_α and K_β events position reconstruction for nine inverted test devices.

Diffusion Length l_d (μm			
	250 μm	350 μm	500 μm
300 nm	179	163	166
500 nm	283	312	305
900 nm	464	522	557

Absorption Length l_a (μm			
	250 μm	350 μm	500 μm
300 nm	216	150	154
500 nm	450	489	548
900 nm	1241	1440	1322

Table 7.3: *Left*: Fitted diffusion lengths for all nine inverted test devices. The diffusion length is roughly independent of the film length for a given film thickness, and increases with film length. *Right*: Fitted absorption length for all nine inverted test devices. The l_a values shown are averages for W-TES1 and W-TES2.

Position Reconstruction: Percolation Model			
	250 μm	350 μm	500 μm
300 nm	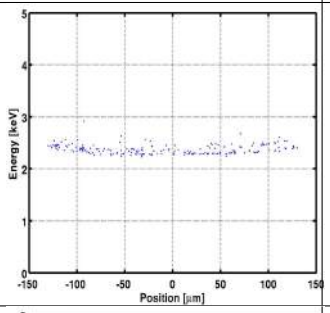	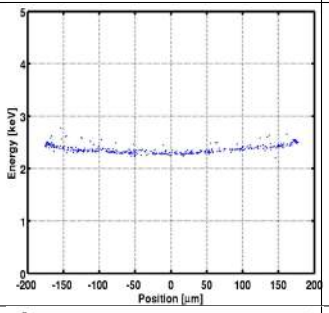	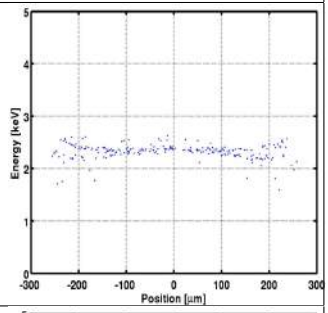
500 nm	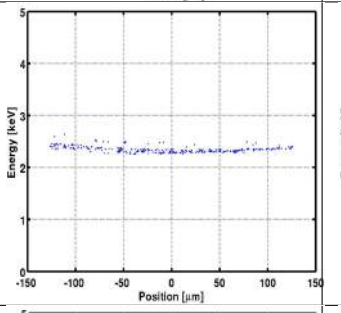	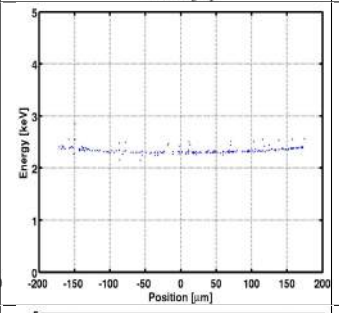	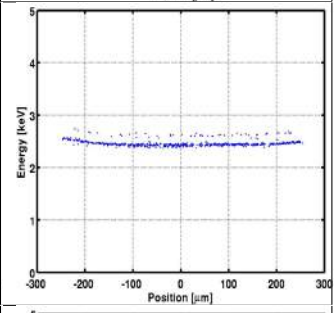
900 nm	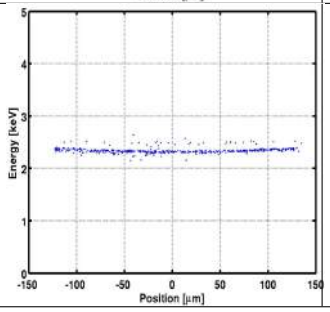	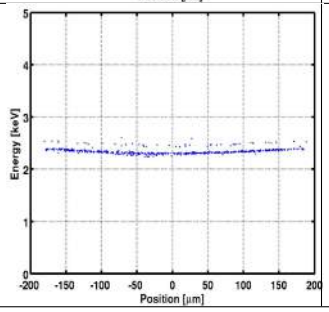	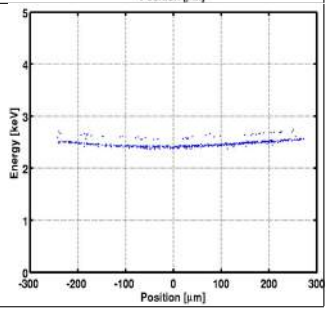

Table 7.4: Event position reconstruction using microscopic model. The results are similar to those shown in Table 7.2

Percolation Threshold (Δ			
	250 μm	350 μm	500 μm
300 nm	0.407	0.420	0.381
500 nm	0.330	0.298	0.268
900 nm	0.117	0.153	0.205

Effective Transmission Probabilities(%			
	250 μm	350 μm	500 μm
300 nm	0.077	0.073	0.067
500 nm	0.072	0.065	0.045
900 nm	0.014	0.018	0.036

Table 7.5: *Left*: Percolation threshold, ϵ, in units of Δ. The results are similar for vapors film lengths, but ϵ decreases for the thicker Al films. This indicates that in the thicker Al films, qps can relax to a lower energy state before getting stuck in a local gap minimum. *Right*: "Effective" transmission probability at the Al/W boundaries.

Chapter 8

Conclusion and Future Work

The next generation CDMS experiment detector design takes into account the results of quasiparticle transport studies described in this thesis. More specifically, the inverted (Al over W device design using J. M. Kreikebaum's fabrication recipe not only mitigates step coverage issues but also provides more freedom to increase Al film thickness and Al film length. This allows us to cover more detector surface area while keeping the W-TES film volume the same. In our studies, we showed that the quasiparticle diffusion in our 300 nm-thick films is thickness-limited, and the quasiparticle diffusion length is linearly proportional to film thickness. In addition, we found that the absorption length of quasiparticles at the Al/W overlap regions is proportional to Al film thickness squared. This is consistent with our predictions.

The Al/W "waterfall" model described in this thesis explains the observed W-TES pulse shapes. It accurately reproduces the two fall-times observed with our quasiparticle devices and even works for saturated W-TES events. The model also explains some anomalous double-peaked pulses that were first observed by our group in 1997. Combing the waterfall model with a non-linear template fitting technique, we can accurately reconstruct event energies. This model can appropriately be used for both the inverted and non-inverted devices. Collectively, our data indicate that the dominant bottleneck for quasiparticle transport at the Al/W interfaces is dominated by the Al/W overlap region. In the next year, we will further investigate the overlap region by fabricating and testing devices with different overlap widths (currently 5

μm . By doing so, we will be able to investigate superconducting proximity effects and learn how they influence W-TES energy collection in our devices. We will also re-investigate superconducting phase separation in W-TES. Appendix N shows the mask design for these studies.

The upcoming SuperCDMS SNOLAB experiment will focus on the direct detection of low mass WIMPs ($M_\chi \sim 3$ GeV/c^2 . We also hope to detect ^{8}B solar neutrinos. A modified version of our detectors is being developed to improve sensitivity to low mass WIMPs. Instead of relying equally on phonon and ionization signals to perform nuclear versus electron recoils event discrimination, the new "CDMS-HV" detectors will collect event energy after amplification via the Neganov-Luke effect. This should provide greatly enhanced energy sensitivity allowing single electron-hole detection. A set of small test devices (1 cm $\times$ 1cm $\times$ 4 mm has been designed (Appendix N . We hope to begin fabrication and testing of these devices soon.

Appendix A

Energy Down Conversion Calculations

Below are two scripts written by Blas and modified later by me for the energy down conversion in Al and W films.

A.1 Al Calculation:

```
% plot Al distribution for emitted phonons from Kozorezov & Bandler paper

tau_ph_e = 4.1e-12;       % Al Ohmega_D phonon scattering time in s with electron
c_s = 3.66e3;             % Al speed of sound in m/s before 6.42e3
tau_s = 0.025e-12;        % Al average time in s for electron to emitt Omega_D/2
eta_eff = 0.4;            % Al phonon escape combined for nu*p*(1-tsi_c /2
D = 0.019;               % Al diffusivity in m^2/s befoe 0.013 0.0042
t_dc = 0.4e-12;           % duration in sec of E_1* to Ohmega_D cascade

d = 300e-9;               % Al film thickness in meters
dz0 = d/100;
z0 = (-d/2 :dz0:(d/2 ;    % -d/2 < z0 , +z0/d is event location in film thickness

zeta = sqrt(pi^2*D*t_dc/2/d^2 ;
```

```
beta = tau_ph_e*c_s/d;
Z0 = 1.42;                % metal renormalization factor 1+lambda where lambda =

E_D_T = 428;              % Debye temperature in K
E_1_T = E_D_T*sqrt(tau_s/tau_ph_e ;                % temperature where tau_ee = t
h = 6.6e-34;              % Planck's constant in units of J-s
k = 1.38e-23;             % Boltzmann's constant in J/K
E_D_f = E_D_T*k/h;
E_1_f = E_1_T*k/h;

%% Phase 1 phonon loss calculation for beta << 1
m = 0:20;
mM = m'*ones(1,length(z0  ;
z0M = ones(length(m ,1 *z0;

Y_mbeta = (beta/3 *(1 - 3*m.^2*pi^2*beta^2 - 3*beta^3*(-1 .^m.*(2 - m.^2*pi^2 ...
    + 3*m.^3*pi^3*beta^3.*(atan(1./(m*pi*beta   + sinint(m*pi  - pi/2  ;

Y_mbetaM = Y_mbeta'*ones(1,length(z0  ;

kappa_mzeta = exp(-m.^2*zeta^2 .*sinh(m.^2*zeta^2 ./(m.^2*zeta^2 ; kappa_mzeta(1
kappa_mzetaM = kappa_mzeta'*ones(1,length(z0  ;

E_loss1_z0 = 8*eta_eff*sum(kappa_mzetaM.*cos(mM*pi.*(1/2 + z0M/d  .*Y_mbetaM ;
E_loss1 = mean(E_loss1_z0 ;

figure(1 ; plot(z0/d,E_loss1_z0*1e2
set(gca,'XTick', [-0.5:0.1:0.5],'linewidth',2,'fontsize',16
axis([-0.5 0.5 0 1.1*max(E_loss1_z0*1e2 ]
xlabel('Event Location [z_0/d]'
ylabel('Energy Loss Percentage'
%title(['Al (' num2str(d*1e9  ' nm  on Si Stage 1 Energy Loss']
%line(0.5*[-1 1],E_loss1*[1 1]*1e2,'color','r'

%% compute phonon energy distribution for stage 1 all very near Omega_D
x = E_D_T/E_1_T;              % ratio of Ohmega_D/Omega_1
```

```
dz = 0.001;
z = (1/x :dz:(1-dz ;

E1_sig = 0.05;
dE_1 = E_loss1*dz*exp(-(1-z .^2/(2*E1_sig^2  *sqrt(2/(pi*E1_sig^2  ;

%% Stage 2 phonon loss calculation
f_z = 1-z-(z/12 .*(z.^2.*(cos(sqrt(2 *log(z  -7*sqrt(2 *sin(sqrt(2 *log(z   -1 ;

dg = dz*(x./z .*f_z.*(expint(z*(x-1  -expint(1-z  ...
    +exp(z .*(expint(1  - expint(x*z   + log((x-1 /x./(1-z   ;

dE_2 = eta_eff*12*Z0/(11*Z0+3 *beta*dg;

E_loss2 = sum(dE_2 ;

figure(2
plot(z*E_D_f*1e-12,dE_1*(E_D_f*1e-12 /dz,'g'
set(gca,'linewidth',2,'fontsize',16
%{
title(['Al/Si Phonon loss; (E_1,E_2,E_{tot} /E = ' num2str(E_loss1,'%0.3f' ...
    ', ' num2str(E_loss2,'%0.3f'  ', ' num2str(E_loss1+E_loss2,'%0.3f' ...
    '; \Omega_1, \Omega_D = ' num2str(E_1_f*1e-12,'%0.2f' ...
    ', ' num2str(E_D_f*1e-12,'%0.2f'  ' THz']
%}
xlabel('Phonon Eneregy [THz]'
ylabel('Energy loss percentage per THz'

hold on; plot(z*E_D_f*1e-12,dE_2*(E_D_f*1e-12 /dz,'r' ; hold off
hold on; plot(z*E_D_f*1e-12,(dE_1+dE_2 *(E_D_f*1e-12 /dz,'b' ; hold off

ymax = max((dE_1+dE_2 *(E_D_f/1e12 /dz ;
%{
text(0.15*E_D_f/1e12,0.6*ymax,...
    {['\tau_{ph-e} = ' num2str(tau_ph_e*1e12  ' ps;'];
     ['c_s = ' num2str(c_s  ' m/s;'];
     ['\tau_s = ' num2str(tau_s*1e12  ' ps;'];
```

```
     ['\eta_{eff} = ' num2str(eta_eff  ';'];
     ['D = ' num2str(D  ' m^2/s;'];
     ['t_{dc} = ' num2str(t_dc*1e12  ' ps;'];
     ['Z(0  = ' num2str(Z0  ';'];
     ['d = ' num2str(d*1e9  ' nm;'];        % z_0/d = ' num2str(z0/d  ';'];
     ['\beta = ' num2str(beta,'%1.3f'  '; \zeta = ' num2str(zeta,'%1.3f'  ';'];
     ['E_D = ' num2str(E_D_T  ' K = ' num2str(E_D_f/1e12,'%1.2f'  ' THZ;'];
     ['E_1 = ' num2str(E_1_T,'%2.1f'  ' K = ' num2str(E_1_f/1e12,'%1.2f'  ' THZ;'
%}
legend('Phase 1 loss','Phase 2 loss','Total loss','location',[0.60 0.65 0.22 0.20

%% calculate the cumsum for z0=-d/2
figure(3 ;
z0=-d/2;
plot(m,1e2*cumsum(8*eta_eff*kappa_mzeta.*cos(m*pi.*(1/2 + z0/d  .*Y_mbeta ,'o'
axis([0 20 0 18]
xlabel('Number of m terms used in sum'
ylabel('Energy loss percentage for Stage 1'
title('Al/Si phonon loss for z_0 = -d/2'

text(5,8,...
    {['\tau_{ph-e} = ' num2str(tau_ph_e*1e12  ' ps;'];
     ['c_s = ' num2str(c_s  ' m/s;'];
     ['\tau_s = ' num2str(tau_s*1e12  ' ps;'];
     ['\eta_{eff} = ' num2str(eta_eff  ';'];
     ['D = ' num2str(D  ' m^2/s;'];
     ['t_{dc} = ' num2str(t_dc*1e12  ' ps;'];
     ['Z(0  = ' num2str(Z0  ';'];
     ['d = ' num2str(d*1e9  ' nm;'];        % z_0/d = ' num2str(z0/d  ';'];
     ['\beta = ' num2str(beta,'%1.3f'  '; \zeta = ' num2str(zeta,'%1.3f'  ';'];
     ['E_D = ' num2str(E_D_T  ' K = ' num2str(E_D_f/1e12,'%1.2f'  ' THZ;'];
     ['E_1 = ' num2str(E_1_T,'%2.1f'  ' K = ' num2str(E_1_f/1e12,'%1.2f'  ' THZ;'
```

A.2 W Calculation

```
%% plot W distribution for emitted phonons from Kozorezov & Bandler paper
```

```
tau_ph_e = 13.3e-12;      % W Ohmega_D phonon scattering time in s with electron
c_s = 3.18e3;             % W speed of sound in m/s
tau_s = 0.0125e-12;       % W average time in s for electron to emitt Omega_D/2 p
eta_eff = 0.043;          % W phonon escape combined for eta*p*(1-xi_c /2
D = 0.0035;               % W diffusivity in m^2/s
t_dc = 0.4e-12;           % duration in sec of E_1* to Ohmega_D cascade
Z0 = 1.26;                % metal renormalization factor 1+lambda where lambda =

d = 40e-9;                % W film thickness in meters
dz0 = d/100;
z0 = (-d/2 :dz0:(d/2 ;    % -d/2 < z0 , +z0/d is event location in film thickness

zeta = sqrt(pi^2*D*t_dc/2/d^2 ;
beta = tau_ph_e*c_s/d;

E_D_T = 380;              % Debye temperature in K
E_1_T = E_D_T*sqrt(tau_s/tau_ph_e ;              % temperature where tau_ee = t
h = 6.6e-34;              % Planck's constant in units of J-s
k = 1.38e-23;             % Boltzmann's constant in J/K
E_D_f = E_D_T*k/h;
E_1_f = E_1_T*k/h;

%% Phase 1 phonon loss calculation for beta << 1
m = 0:10;
mM = m'*ones(1,length(z0  ;
z0M = ones(length(m ,1 *z0;
if beta < 0.1
    Y_mbeta = (beta/3 *(1 - 3*m.^2*pi^2*beta^2 - 3*beta^3*(-1 .^m.*(2 - m.^2*pi^2
        + 3*m.^3*pi^3*beta^3.*(atan(1./(m*pi*beta   + sinint(m*pi  - pi/2  ;
else
    dx = 0.001; x = dx:dx:(1/beta ; xM = x'*ones(1,length(m  ; mxM = ones(length(
    Y_mbeta = beta^4*sum(dx*xM.^4.*(1 - (-1 .^mxM.*exp(-xM  ./(xM.^2 + mxM.^2*pi^
end
    Y_mbetaM = Y_mbeta'*ones(1,length(z0  ;
    kappa_mzeta = exp(-m.^2*zeta^2 .*sinh(m.^2*zeta^2 ./(m.^2*zeta^2 ; kappa_mzet
    kappa_mzetaM = kappa_mzeta'*ones(1,length(z0  ;
```

```
    E_loss1_z0 = 8*eta_eff*sum(kappa_mzetaM.*cos(mM*pi.*(1/2 + z0M/d  .*Y_mbetaM
    E_loss1 = mean(E_loss1_z0 ;

figure(1 ; plot(z0/d,E_loss1_z0*1e2
set(gca,'XTick', [-0.5:0.1:0.5],'linewidth',2,'fontsize',16
axis([-0.5 0.5 0 1.1*max(E_loss1_z0*1e2 ]
xlabel('Event Location [z_0/d]'
ylabel('Energy Loss Percentage'
%title(['W (' num2str(d*1e9  ' nm  on Si Phase 1 Energy Loss']
%line(0.5*[-1 1],E_loss1*[1 1]*1e2,'color','r'

%% compute phonon energy distribution for phase 1 all very near Omega_D
x = E_D_T/E_1_T;               % ratio of Ohmega_D/Omega_1

dz = 0.001;
z = (1/x :dz:(1-dz ;

E1_sig = 0.05;
dE_1 = E_loss1*dz*exp(-(1-z .^2/(2*E1_sig^2  *sqrt(2/(pi*E1_sig^2  ;

%% Phase 2 phonon loss calculation
f_z = 1-z-(z/12 .*(z.^2.*(cos(sqrt(2 *log(z  -7*sqrt(2 *sin(sqrt(2 *log(z   -1 ;

dg = dz*(x./z .*f_z.*(expint(z*(x-1  -expint(1-z  ...
    +exp(z .*(expint(1  - expint(x*z   + log((x-1 /x./(1-z   ;

dE_2 = eta_eff*12*Z0/(11*Z0+3 *beta*dg;

E_loss2 = sum(dE_2 ;

figure(2
plot(z*E_D_f*1e-12,dE_1*(E_D_f*1e-12 /dz,'g'
set(gca,'linewidth',2,'fontsize',16
%{
title(['W/Si Phonon loss; (E_1,E_2,E_{tot} /E = ' num2str(E_loss1,'%0.3f' ...
    ', ' num2str(E_loss2,'%0.3f'  ', ' num2str(E_loss1+E_loss2,'%0.3f' ...
    '; \Omega_1, \Omega_D = ' num2str(E_1_f*1e-12,'%0.2f' ...
```

```
    ', ' num2str(E_D_f*1e-12,'%0.2f'  ' THz']
%}
xlabel('Phonon Eneregy [THz]'
ylabel('Energy loss percentage per THz'

hold on; plot(z*E_D_f*1e-12,dE_2*(E_D_f*1e-12 /dz,'r' ; hold off
hold on; plot(z*E_D_f*1e-12,(dE_1+dE_2 *(E_D_f*1e-12 /dz,'b' ; hold off

ymax = max((dE_1+dE_2 *(E_D_f/1e12 /dz ;
%{
text(0.15*E_D_f/1e12,0.37*ymax,...
    {['\tau_{ph-e} = ' num2str(tau_ph_e*1e12  ' ps;'];
     ['c_s = ' num2str(c_s  ' m/s;'];
     ['\tau_s = ' num2str(tau_s*1e12  ' ps;'];
     ['\eta_{eff} = ' num2str(eta_eff  ';'];
     ['D = ' num2str(D  ' m^2/s;'];
     ['t_{dc} = ' num2str(t_dc*1e12  ' ps;'];
     ['Z(0  = ' num2str(Z0  ';'];
     ['d = ' num2str(d*1e9  ' nm;'];    % z_0/d = ' num2str(z0/d  ';'];
     ['\beta = ' num2str(beta,'%1.2f'  '; \zeta = ' num2str(zeta,'%1.2f'  ';'];
     ['E_D = ' num2str(E_D_T  ' K = ' num2str(E_D_f/1e12,'%1.2f'  ' THZ;'];
     ['E_1 = ' num2str(E_1_T,'%2.1f'  ' K = ' num2str(E_1_f/1e12,'%1.2f'  ' THZ;'
%}
legend('Phase 1 loss','Phase 2 loss','Total loss','location',[0.60 0.65 0.22 0.20
```

Appendix B

QP Mask Design

X-Ray Device Description

- X-Ray die has 6 devices
- TESs 180um square or 250um square
- The Al FIN lengths are 250um, 350um, 500um
- The Veto surrounding each device has 120um long by 10um wide TESs. The number of TESs varies with the size of the device. The width of the Veto is about 180um.

X-Ray Geometry

Al 180X250, W 180X180 um, Veto17 TESs 10X120 um

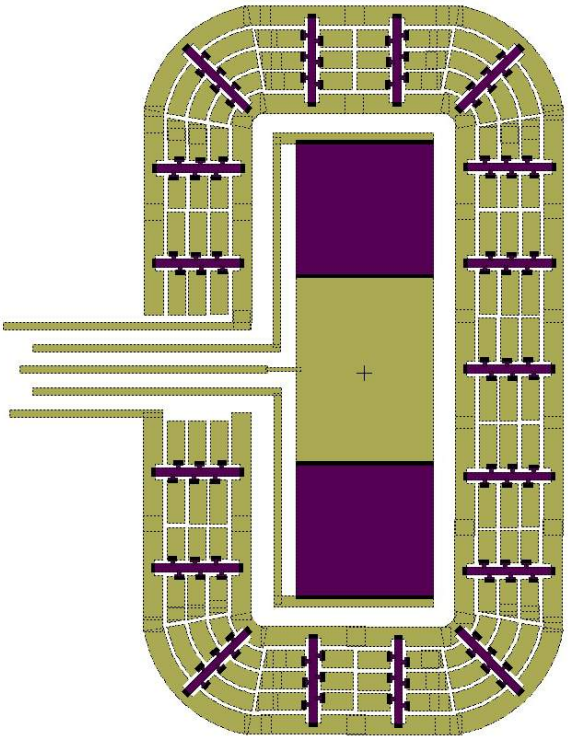

X-Ray Die layout (1.1cm X 1.1cm)

180X250X350X500

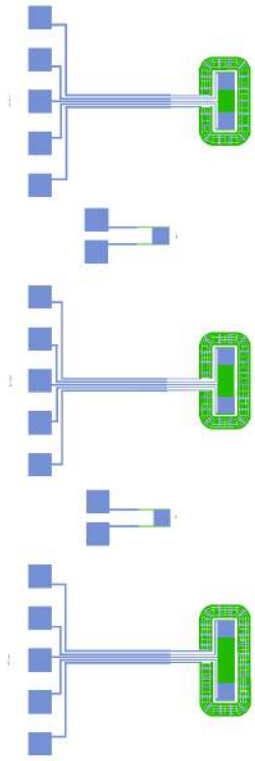

250X250X350X500

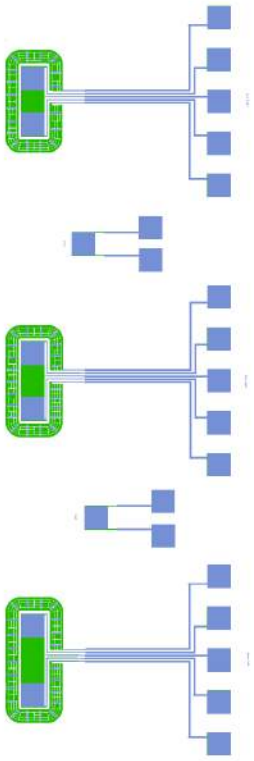

Appendix C

Inverted Fabrication Recipes

This is the detailed fabrication process made by John Mark Kreikebaum, and written by Matt Cherry. All the inverted qp study written in this thesis followed this recipe. Please also see Figure 4.4 as schematic reference.

- Step 1 - Diffusion clean of wafers 10' 5:1:1 H2O:Ammonium Hydroxide:Hydrogen Peroxide Dump Rinse 30" 50:1 HF Dip Dump Rinse 10' 5:1:1 H2O:Hydrochloric Acid:Hydrogen Peroxide Dump Rinse, Spin Dry
- Step 2 - αSi + W Bilayer Deposition Bury chamber and deposition platter with Al prior to wafer loading Load device substrates 15' RF Etch @ 3mT Ar, 100W 400A aSi @ 5.5mT Ar, 400W 400A W @ 3mT, 400W, with platter biased to -150V DC during deposition
- Step 3 - W TES Definition Singe 30', 150C, cool 10' Coat S1813 photoresist, 1.6um Pre-bake 35', 90C, cool 10' Align mask to wafer Expose W TES layer pattern 3.0s Develop MF319, 20s no agitation + 60s agitated Rinse, N2 blow dry Post-bake 35', 110C, cool 10' Etch W in fresh, unheated H2O2, 675s Dump Rinse, Spin Dry PR Strip PRS3000, 10' Dump Rinse, Spin Dry PR Strip PRS1000, 10' Dump Rinse, Spin Dry

- Step 4 - Al Deposition Bury chamber and deposition platter with Al prior to wafer loading Load device substrates 15' RF Etch @ 3mT Ar, 100W (Some devices incorporate a cooling step here 6000A Al (or desired thickness @ 2mT Ar, 700W

- Step 5 - Al Definition Singe 30', 150C, cool 10' Coat S1813 photoresist, 1.6um Pre-bake 35', 90C, cool 10' Align to previous layer Expose Al layer pattern 3.0s Develop MF319, 20s no agitation + 60s agitated Rinse, N2 blow dry Post-bake 35', 110C, cool 10' Etch Al in fresh unheated etchant (80:3:15 NP , 19 x 60s dips with DI quench in between Dump Rinse, Spin Dry PR Strip PRS3000, 10' Dump Rinse, Spin Dry PR Strip PRS1000, 10' Dump Rinse, Spin Dry

Following fabrication, the wafer is diced and specific dies are selected for testing.

Appendix D

Inverted Fabrication Recipes

This is the detailed fabrication process made by John Mark Kreikebaum, and written by Matt Cherry. All the inverted qp study written in this thesis followed this recipe. Please also see Figure 4.4 as schematic reference.

- Step 1 - Diffusion clean of wafers 10' 5:1:1 H2O:Ammonium Hydroxide:Hydrogen Peroxide Dump Rinse 30" 50:1 HF Dip Dump Rinse 10' 5:1:1 H2O:Hydrochloric Acid:Hydrogen Peroxide Dump Rinse, Spin Dry
- Step 2 - αSi + W Bilayer Deposition Bury chamber and deposition platter with Al prior to wafer loading Load device substrates 15' RF Etch @ 3mT Ar, 100W 400A aSi @ 5.5mT Ar, 400W 400A W @ 3mT, 400W, with platter biased to -150V DC during deposition
- Step 3 - W TES Definition Singe 30', 150C, cool 10' Coat S1813 photoresist, 1.6um Pre-bake 35', 90C, cool 10' Align mask to wafer Expose W TES layer pattern 3.0s Develop MF319, 20s no agitation + 60s agitated Rinse, N2 blow dry Post-bake 35', 110C, cool 10' Etch W in fresh, unheated H2O2, 675s Dump Rinse, Spin Dry PR Strip PRS3000, 10' Dump Rinse, Spin Dry PR Strip PRS1000, 10' Dump Rinse, Spin Dry

- Step 4 - Al Deposition Bury chamber and deposition platter with Al prior to wafer loading Load device substrates 15' RF Etch @ 3mT Ar, 100W (Some devices incorporate a cooling step here 6000A Al (or desired thickness @ 2mT Ar, 700W

- Step 5 - Al Definition Singe 30', 150C, cool 10' Coat S1813 photoresist, 1.6um Pre-bake 35', 90C, cool 10' Align to previous layer Expose Al layer pattern 3.0s Develop MF319, 20s no agitation + 60s agitated Rinse, N2 blow dry Post-bake 35', 110C, cool 10' Etch Al in fresh unheated etchant (80:3:15 NP , 19 x 60s dips with DI quench in between Dump Rinse, Spin Dry PR Strip PRS3000, 10' Dump Rinse, Spin Dry PR Strip PRS1000, 10' Dump Rinse, Spin Dry

Following fabrication, the wafer is diced and specific dies are selected for testing.

Appendix E

RRR Measurements

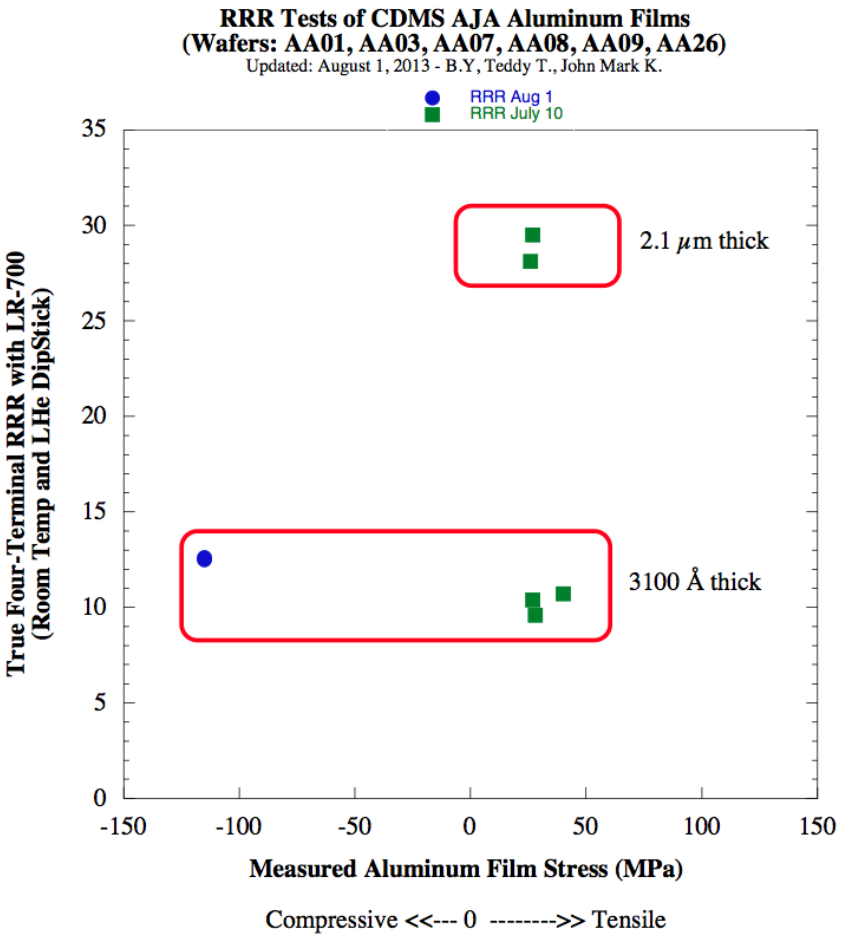

Appendix F

SQUIDResponse

02/03/08 W38D83 CQ

$R_{in} = 20.94k\Omega$ $R_{sa} = 4.60k\Omega$ $R_{FDBK} = 29.08k\Omega$

$I_{in} = \frac{9.8\,div \times 20\frac{mV}{div}}{9\,periods \times 10k\Omega} = 21.8\mu A$

$I_{max} = \frac{4div \times 50\frac{mV}{div} \times 0.3382}{1k\Omega} = 67.6\mu A$

$I_{FDBK} = \frac{9.1div \times 200\frac{mV}{div}}{8\,periods \times 1k\Omega} = 227.5\mu A$

$I_{min} = \frac{1.5div \times 50\frac{mV}{div} \times 0.3382}{1k\Omega} = 25.4\mu A$

$I_{RES} = \frac{157.4mV\,(0.3382)}{1k\Omega} = 53.2\mu A$

$R_{\mu} = \frac{\frac{1V}{200mV} \times 540\Omega}{.3382 \times 100} = 79.8\Omega$

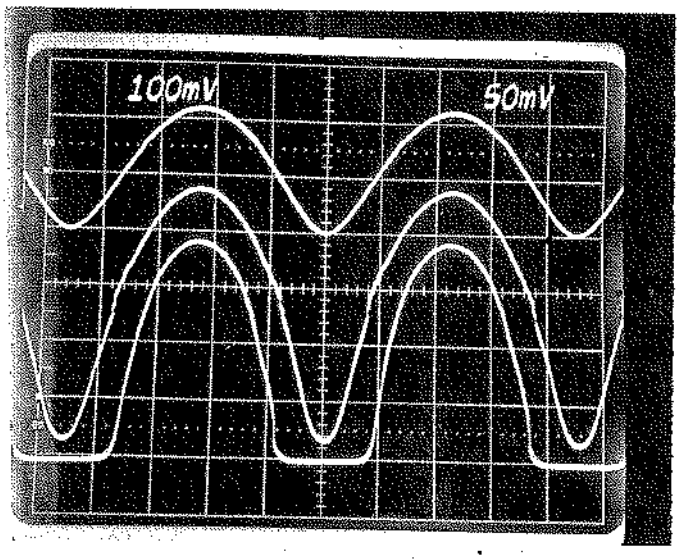

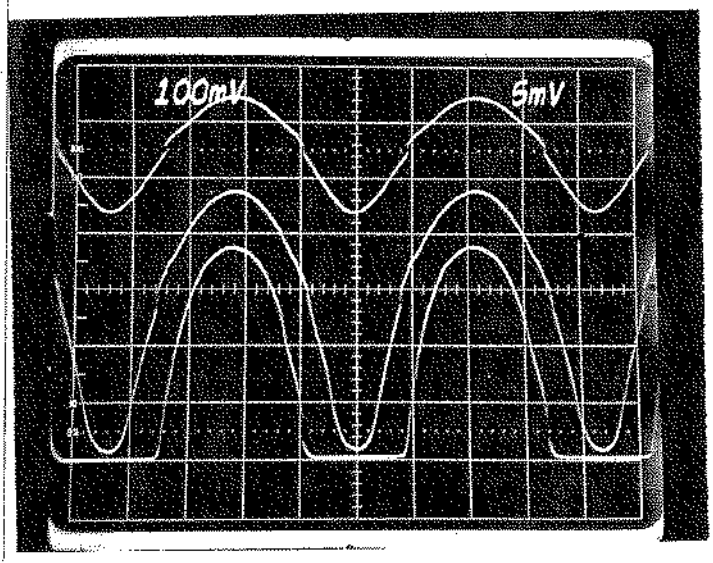

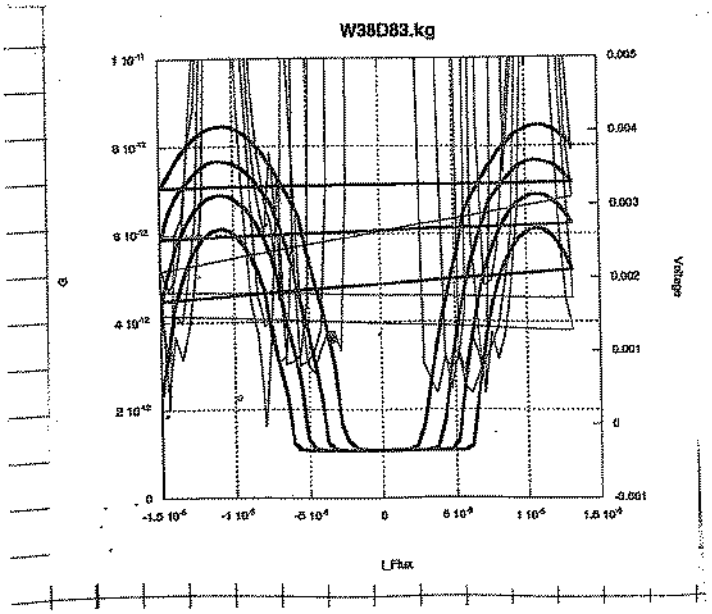

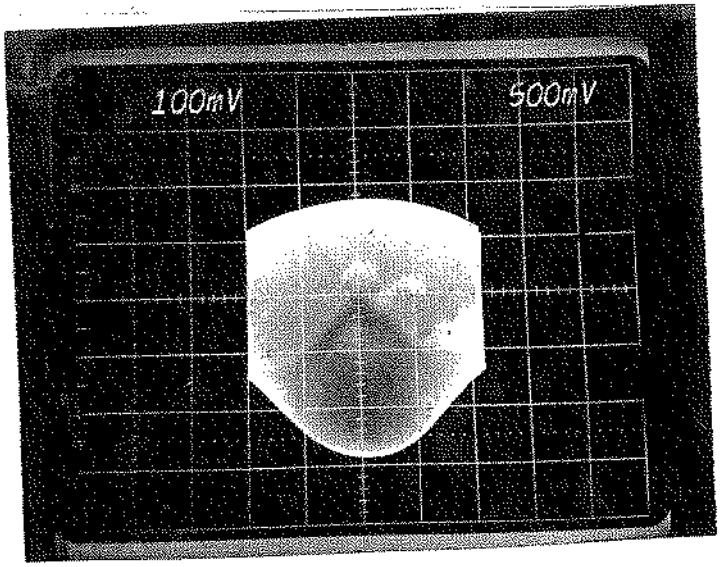

020605 W38D87 CD

$R_{in} = 18.69k\Omega$ $R_{SQ} = 4.20k\Omega$ $R_{FOBK} = 25.57k\Omega$

$I_{in}^{\phi} = \frac{9.8div \times 20\frac{mV}{div}}{9periods \times 1k\Omega} = 218\mu A$

$I_{max} = \frac{4.7div \times 50\frac{mV}{div} \times 0.3382}{1k\Omega} = 71.0\mu A$

$I_{FOBK}^{\phi} = \frac{9.1div \times 200\frac{mV}{div}}{8periods \times 1k\Omega} = 227.5\mu A$

$I_{min} = \frac{1.5div \times 50\frac{mV}{div} \times 0.3382}{1k\Omega} = 25.4\mu A$

$I_{RES} = \frac{16.79mV \times 0.3382}{1k\Omega} = 56.8\mu A$

$R_N = \frac{1V}{200mV} \times \frac{5\Omega}{0.3382 \times 100} = 77.5\Omega$

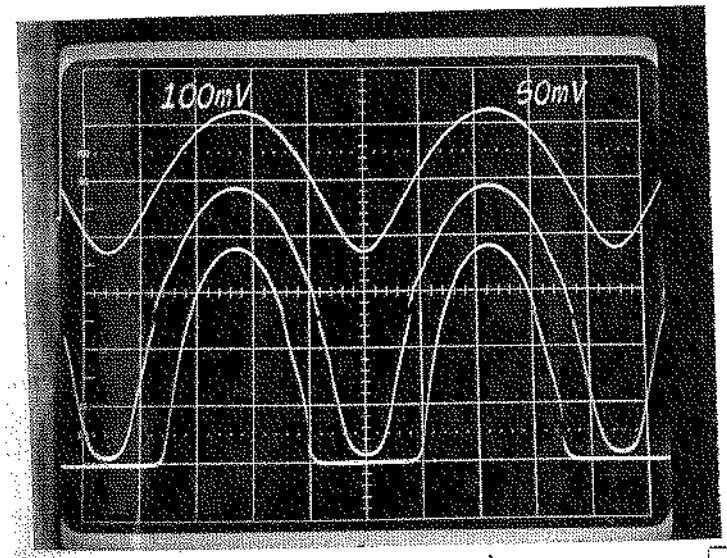

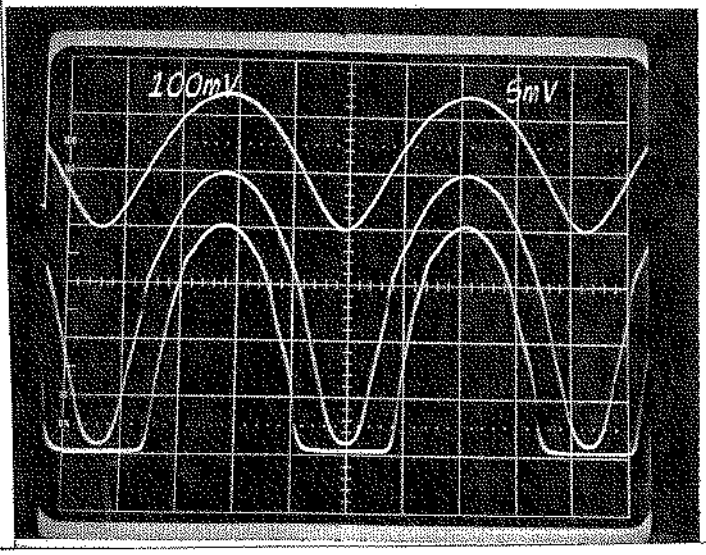

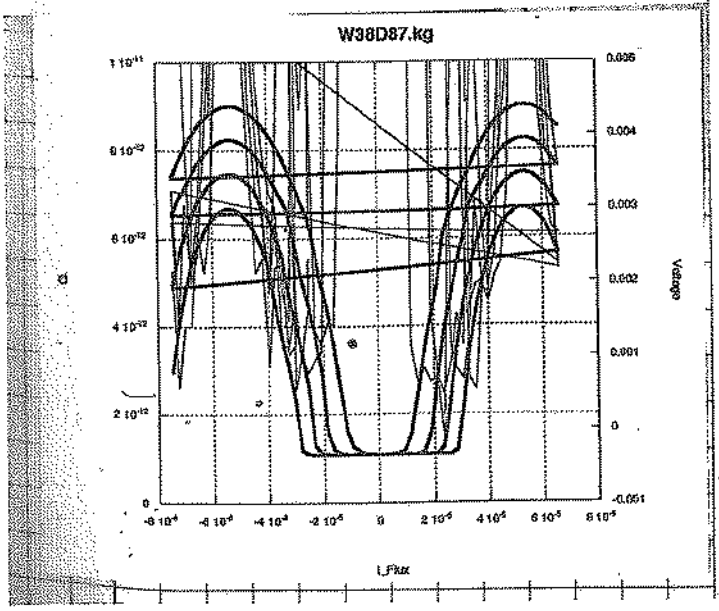

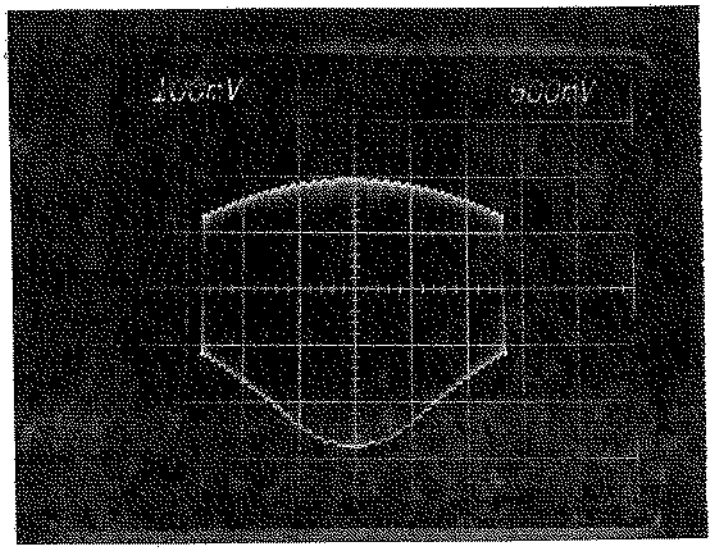

060712 W38DA6 BAG

$R_{IN} = 18.71\ K\Omega$ $R_{SA} = 4.28\ K\Omega$ $R_{FB} = 25.53\ K\Omega$

$I_{in}^{q} = \frac{(9.8\ dN)(20\ mV/dN)}{(9\ per)(1K\Omega)} = 21.8\ \mu A$

$I_{FB}^{q} = \frac{(10.2\ dN)(200mV/dN)}{(9\ per)(1K\Omega} = 226.7\ \mu A$

$I_{bias} = \frac{(157.1\ mV)(0.3382)}{1K\Omega} = 53.1\ \mu A$

$I_{max} = \frac{(3.8\ dN)(50\ mV/dN)(0.3382)}{1K\Omega} = 64.3\ \mu A$

$I_{min} = \frac{(1.3\ dN)(50\ mV/dN)(0.3382)}{1K\Omega} = 22.0\ \mu A$

$R_N = \frac{(1000\ mV_{pk}/200\ mV_{pk})}{(0.3382)(100)} \cdot 646\ \Omega = 95.5\ \Omega$

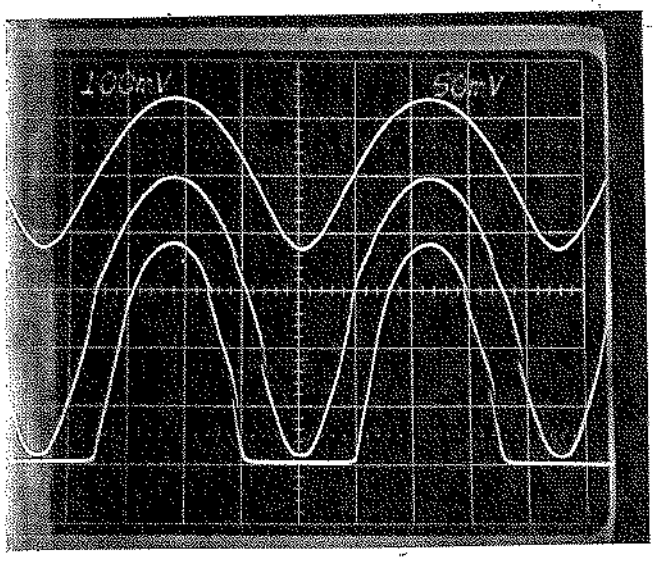

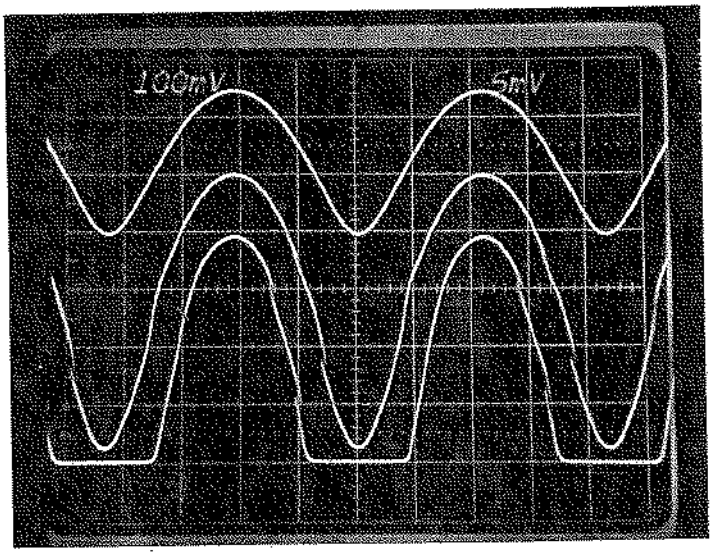

FB

IN

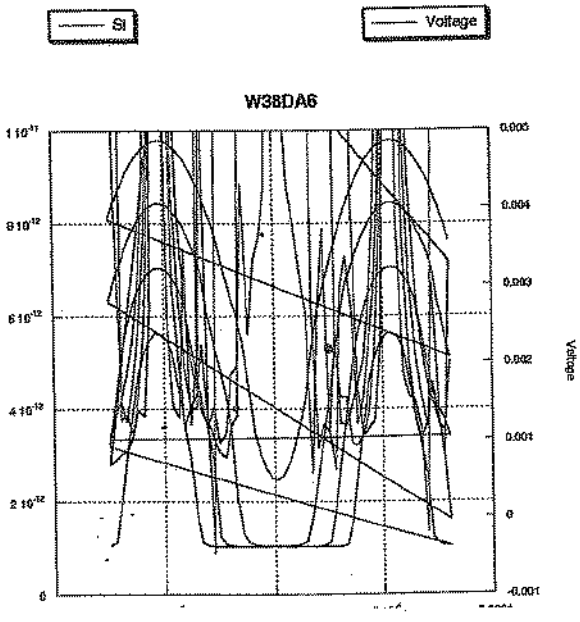

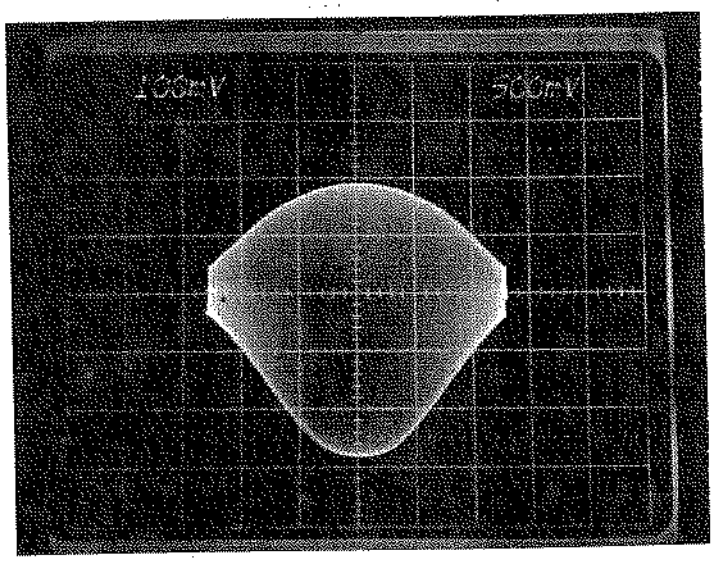

030826/030902 W38D B5 ADC/BND

$R_{th} = 19.94\ k\Omega$ $R_{sq.} = 4.58\ k\Omega$ $R_{PDBK} = 28.48\ k\Omega$

$I^{o}_{th} = \frac{(9.7\,div)(20\,\frac{mV}{div})}{(10\,per)(1\,k\Omega)} = 19.4\,\mu A$ $I_{max} = \frac{(9.8\,div)(50\,\frac{\mu V}{div})(0.3382)}{1\,k\Omega} = 64.3\,\mu A$

$I^{o}_{PDBK} = \frac{(9.1\,div)(200\,\frac{mV}{div})}{(9\,per)(1\,k\Omega)} = 202.2\,\mu A$ $I_{min} = \frac{(7.0\,div)(10\,\frac{mV}{div})(0.3382)}{1\,k\Omega} = 23.7\,\mu A$

$I_{Res} = \frac{(138.7\,mV)(0.3382)}{1\,k\Omega} = 46.9\,\mu A$ $R_N = \frac{(\frac{1000mV}{200mV})(659\,\Omega)}{(0.3382)(100)} = 97.4\,\Omega$

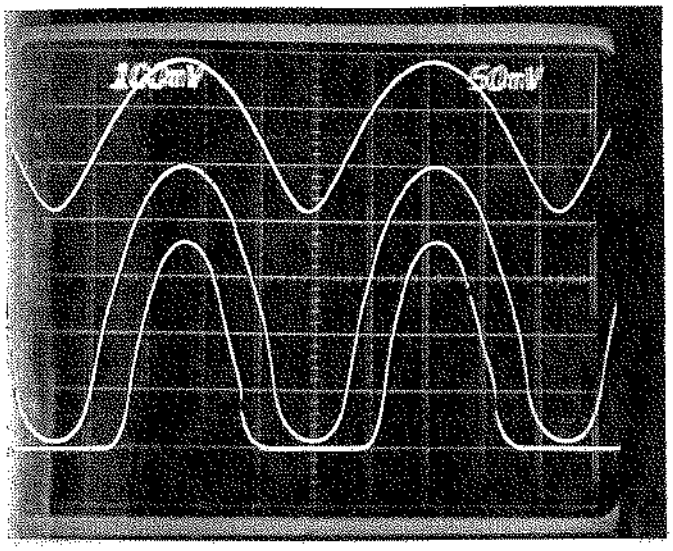

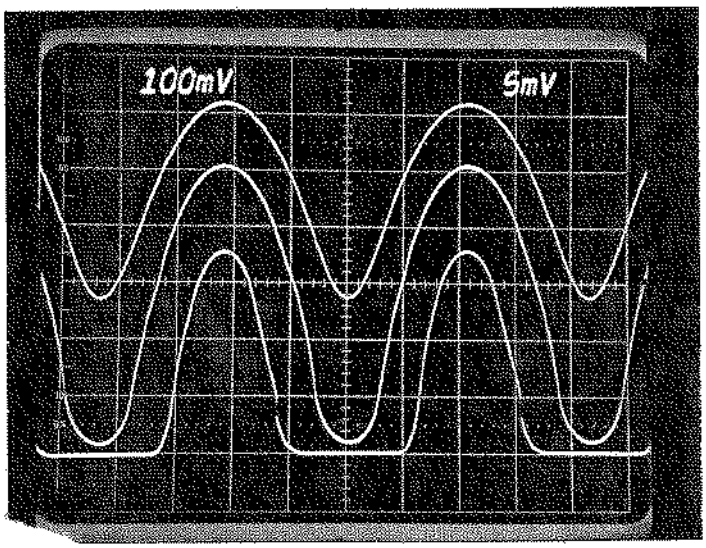

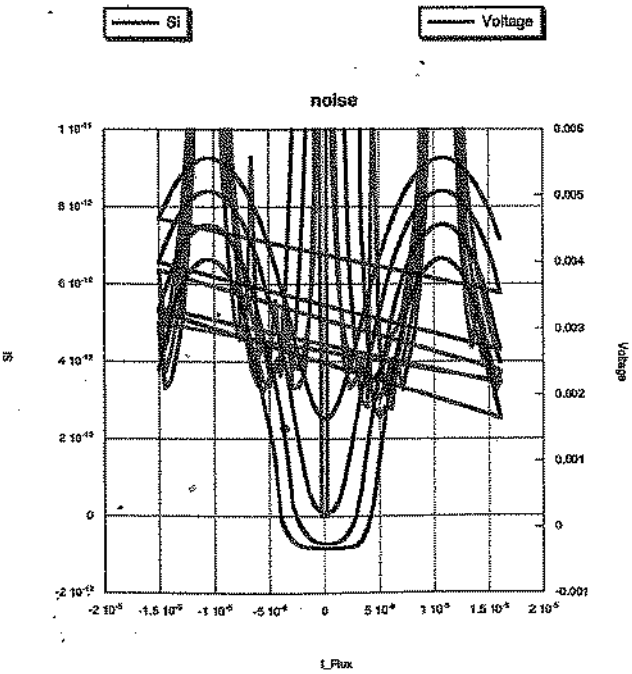

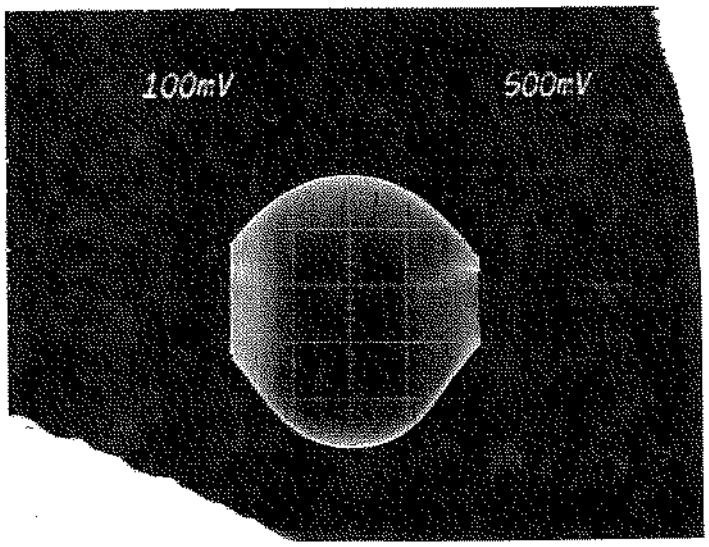

030903 W38DB8 AE/BND

$R_{in} = 9.01K\Omega$ $R_{sq.} = 4.47K\Omega$ $R_{FB} = 27.34k\Omega$

$I_\phi = \frac{(9.8div)(20mV)}{(10per)(1K\Omega)} \approx 19.6\,\mu A$

$I_{max} = \frac{(4.0div)(50\frac{mV}{div})(0.3382)}{1\,K\Omega} = 67.64\,\mu A$

$I_{peak} = \frac{(9div)(200mV/div)}{(9per)(1K\Omega)} \approx 202.2\,\mu A$

$I_{min} = \frac{(2.2div)(10\frac{mV}{div})(0.3382)}{1K\Omega} \approx 24.4\,\mu A$

$I_{res} \approx \frac{(193.3mV)(0.3382)}{(1K\Omega)} = 65.39\,\mu A$

$R_N = \frac{(\frac{1000}{20\Omega})(648\Omega)}{(0.3382)(100)} = 95.8\,\Omega$

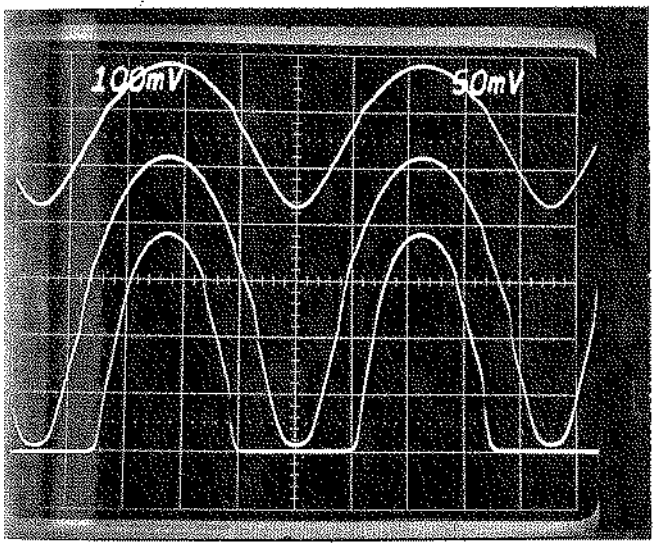

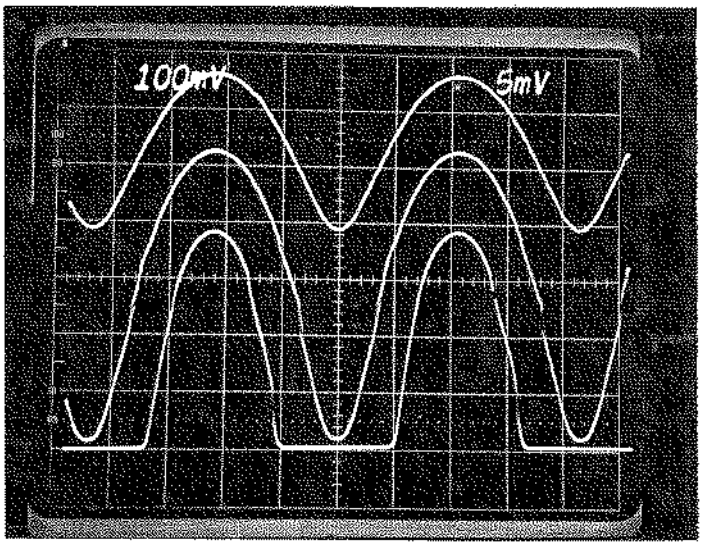

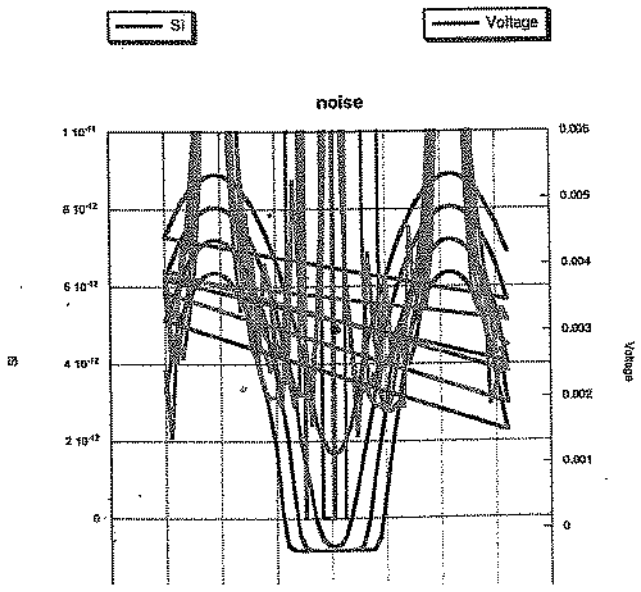

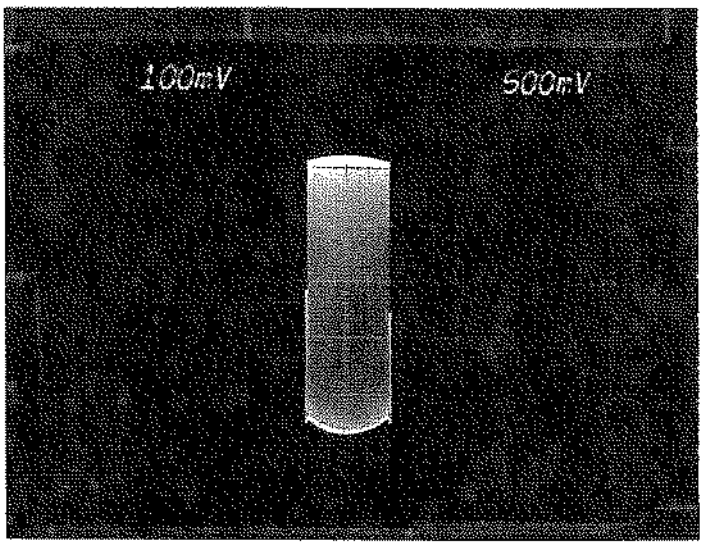

030919 W38DB9 (retest) AX

$R_{in} = 19.79\ k\Omega$ $R_{50} = 4.50\ k\Omega$ $R_{FDBK} = 28.24\ k\Omega$

$I_{in}^{\phi} = \frac{(9.9\,dw)(20\frac{mV}{dw})}{(9_{pcs})(1\,k\Omega)} = 22\ \mu A$ $I_{max} = \frac{(41\,dw)(50\frac{mV}{dw})(0.3382)}{1\,k\Omega} = 69.33\ \mu A$

$I_{FDBK}^{\phi} = \frac{(9.2\,dw)(200\frac{mV}{dw})}{(8_{pcs})(1\,k\Omega)} = 230\ \mu A$ $I_{min} = \frac{(4.0\,dw)(20\frac{mV}{dw})(0.3382)}{1\,k\Omega} = 27.06\ \mu A$

$I_{RES} = \frac{(138.2\,mV)(0.3382)}{(1\,k\Omega)} = 46.74\ \mu A$ $R_N = \frac{(\frac{1000\,mV}{200\,mV})(662\,\Omega)}{(0.3382)(100)} = 97.87\ \Omega$

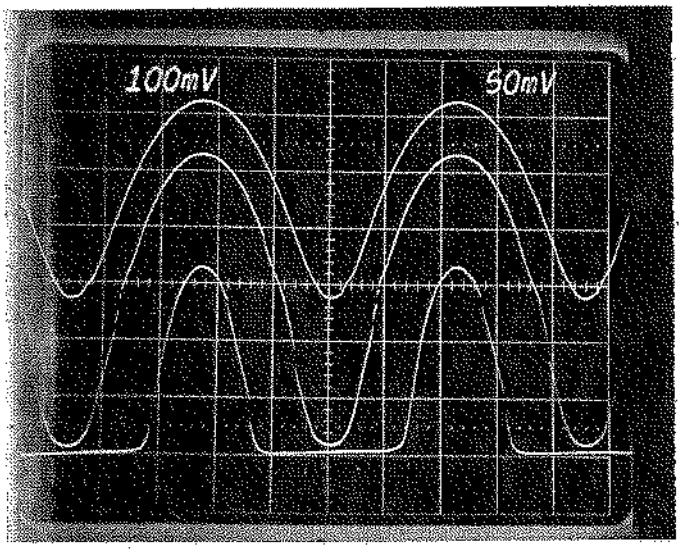

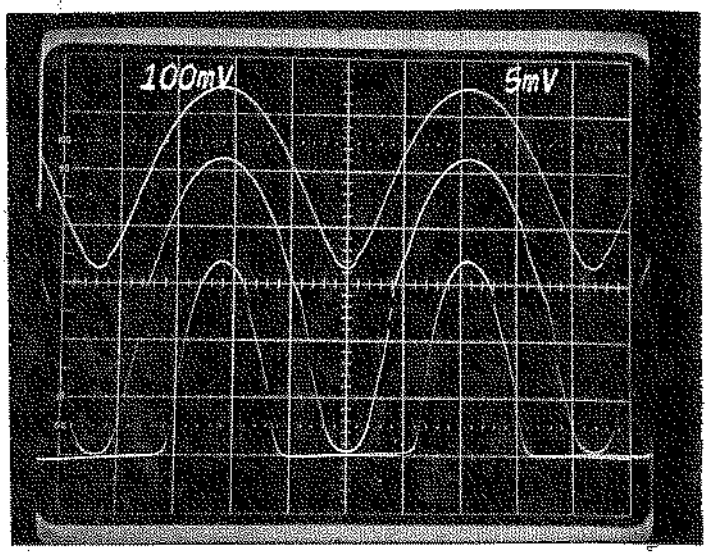

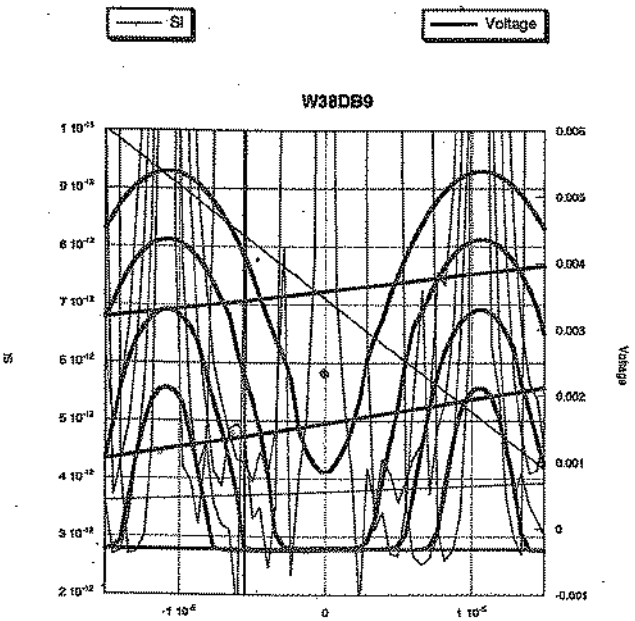

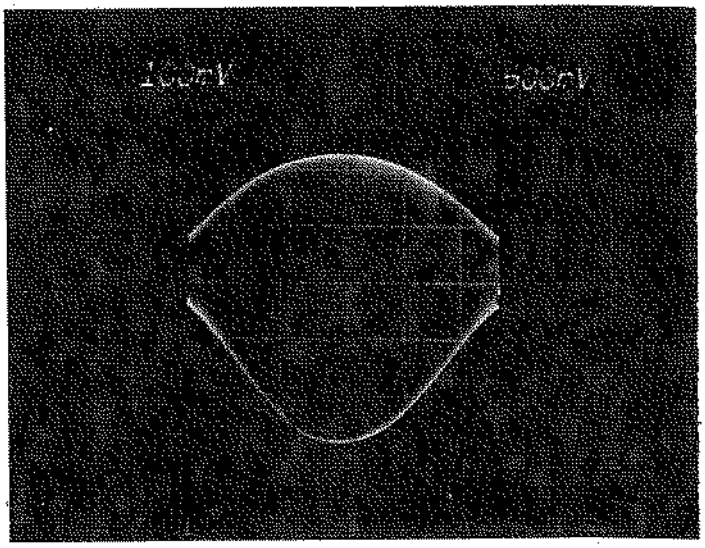

Appendix G

Source Calibration

Quick Summary of X-Ray Tests with Si(Li) and Mounted Fe-55 Source

July 21, 2012 - Betty and Jeff

****

We measured the energy spectrum of the 55Fe source mounted in its basic KO-15 gold-plated source collimator used for quasiparticle transport (QPT) experiments. The noise in the system was pretty awful. It appears to be environmental, dominated by 70 kHz (and 60 Hz harmonics). Earlier reported 30-40 MHz noise seems to be linked to a bad NIM power supply (which we threw away).

****

Basic Experiment with 55Fe source and Si wafer reflector and Si(Li) at 77 K.

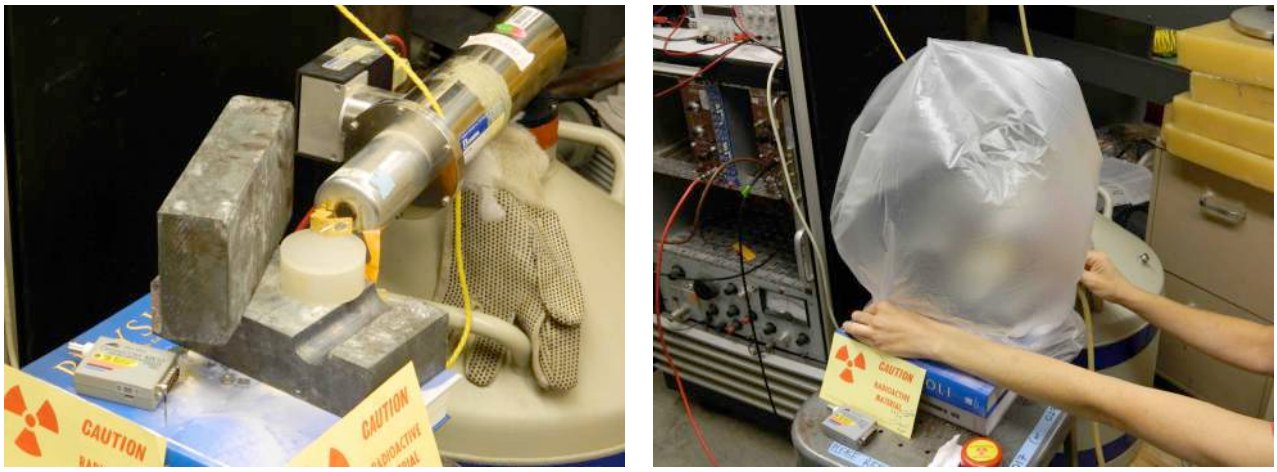

Figure 1. Setup used for 55Fe source and Si wafer fluorescence study. Our Si(Li) detector operates at 77K with a bias voltage of -1000 V (Ortec 428). Photos here show the test set-up without (left) and with (right) helium gas purge to effectively displace ambient argon. Canberra preamp power and raw signal amplification both provided by an Ortec 473.

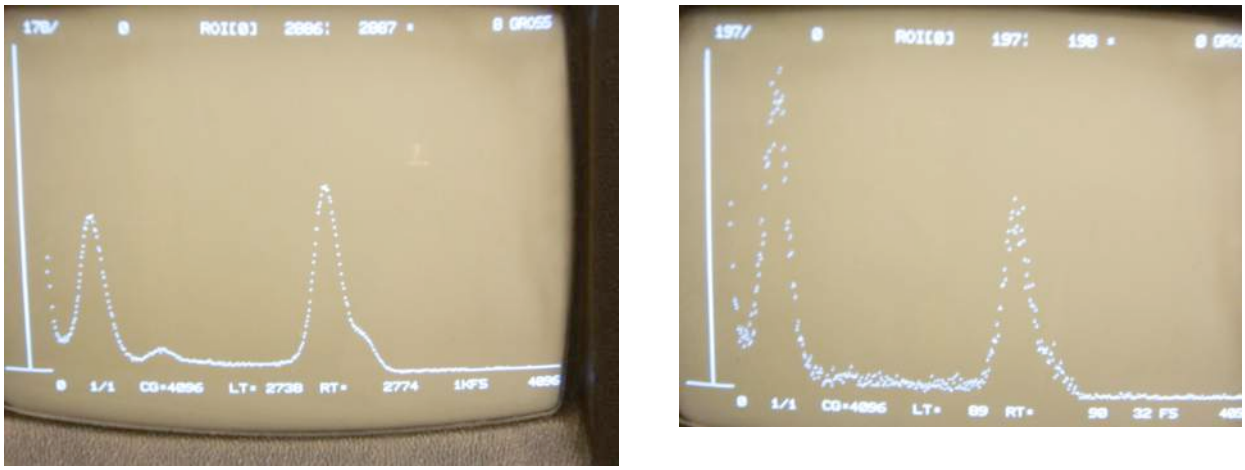

Figure 2. Photos of spectra obtained with Si reflector and 55Fe source. (See Fig. 1 for basic set-up.) Gaussian fits to the spectral peaks were done separately on a high statistic run (not shown), and rechecked. The data were used for energy and rate analyses. (Left): Spectrum (45 minutes) includes ambient Ar peak from air. (Right): Spectrum (90 seconds) obtained with the crude helium gas purge shown in Fig. 1. The two 55Fe (Mn) lines at 5.9 and 6.5 keV were resolved with appropriate fits. Note: The ≈ 50% increase in relative Si count rate (compared to the Fe lines) shown in Fig 2 was obtained by rotating the rigid source + reflector unit *in situ* by a few degrees with respect to the Si(Li) detector entrance window. The position was optimized on-the-fly before starting the purge and recording the spectrum shown on the right. A hint of the Ar peak is still evident after the crude purge was added, but the purge clearly worked for its intended purpose.

Discussion: Spectra from both high- and low-statistics runs (5 minutes - 45 minutes) were analyzed for peak positions, FWHM, integral count rates, etc. As shown in Fig. 3 the Tracor Northern MCA linearity (and zero) was found to be okay; it appears the system was configured properly before storage several years ago. The peak widths (≈ 200 bins FWHM for 4096 CG) are due to environmental noise at ≈ 70 kHz (as well as 60 Hz and its harmonics).

Basic settings used:

NIM rack plugged into wall power in Varian 017 lab, via SOLA transformer.
Ortec 428 Si(Li) detector bias = "-1000 V" (maxed out on Ch B)
Ortec 473 amp for signals and preamp power; gain ≈ x 500; (.25 μsec and 2 μsec)
Spectra recorded with Tracor Northern MCA.

Setup	**Si Peak** Bin (Integral Counts) 1.74 keV	**Ar Peak** Bin (Integral Counts) 2.96 keV	**Mn (55Fe)** Bin (Integral Counts) 5.90 keV, 6.50 keV
No purge	703 (126,000)	1193 (23,000)	2362 , 2603 (170,000)
Purge	708 (8,000)	---	2369, n/a (5,800)

Table 1. Summary table of Si(Li) detector response to 55Fe source with silicon reflector.

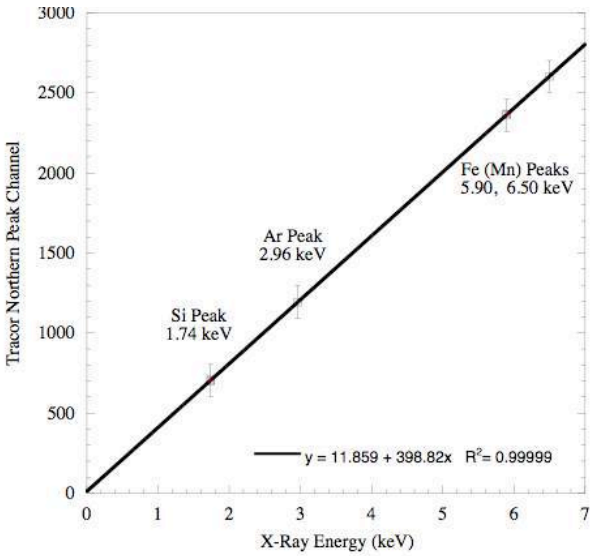

Figure 3. Reality check of the Tracor Northern MCA calibration. The argon peak was reduced a few orders of magnitude by purging the source-detector region with helium gas. (See Fig. 1) Error bars shown corrrespond to ± HWHW for each energy peak. The peak broadening was due to excessive 70 kHz (and harmonics) and 60 Hz (and harmonics) noise present in the system.

Brief Conclusions: (i) The Si fluorescence peak intensity depends on the Si surface angle-to-detector entrance window more than naively assumed. But our Si reflector is single crystal Si and not poly-Si, so that is likely the reason. **(ii)** The Si-fluorescence peak is clearly intense! We get more than enough 1.74 keV Si events for QPT studies, even after collimation. **(iii)** For QPT, we should definitely use a thinner Si reflector wafer to reduce the rate of coherently scattered Fe source (Mn) photons. **(iv)** The present Si(Li) system performance is stable and (even as-is) should provide a threshold sufficient to test NaCl reflectors. While the 1.04 keV and 1.07 keV lines of Na will be below threshold of the present Si(Li) electronics, the 2.62 keV and 2.81 keV lines for Cl should be easily visible (although unresolved from each other) if we purge the test set-up to remove ambient Ar. **(v)** We should use the Si(Li) system this week to rapidly evaluate source-reflector geometries and materials in preparation for more QPT experiments in the KO-15.

Si(Li) at 77K and Mounted Fe-55 Source With NaCl Reflector

July 23, 2012 - Betty and Jeff

****

We measured more energy spectra with the "30" mCi 55Fe lab source mounted in its basic KO-15 gold-plated source collimator used for quasiparticle transport (QPT) experiments. Today, we made a crude NaCl reflector from a supersaturated NaCl + water mixture deposited using a wooden Q-tip stick onto the backside of a Si dummy wafer remnant. We then leaned the NaCl reflector over the existing Si reflector used in the July 20th run (see previous write-up) and took pulse height data using the same Tracor Northern MCA and NIM electronics used last week. The noise in the system remains pretty awful; mostly 35 kHz -100 kHz (and 60 Hz harmonics).

Basic settings used:

NIM rack plugged into wall power in Varian 017 lab, via SOLA transformer (250 kVA).
Ortec 428 Si(Li) detector bias = "-1000 V" (maxed out on Ch B)
Ortec 473 amp for signals and preamp power; gain ≈ x 500; (.25 μsec and 2 μsec)
Spectra recorded with Tracor Northern MCA.

****

Figure 1. Photo of the simple NaCl reflector made by dabbing a supersaturated slurry of NaCl and H_2O onto a Si wafer piece (area ≈1 cm x 0.8 cm). The NaCl was taken from a 13 oz. container of un-ionized Diamond Crystal Kosher Salt purchased at Andronico's Market in ≈ 2009. (July 23, 2012)

Figure 2. Setup used for 55Fe source and NaCl fluorescence study. Our Si(Li) detector operates at 77K with a bias voltage of -1000 V (Ortec 428). Both the Canberra preamp power and raw signal amplification were provided by an Ortec 473.

Appendix H

Sample Holders

Scale: X4
Make two (2)
Material: OFHC Copper
Tolerances: +/- 0.001"

Jeffrey Yen
30 Nov 2011

Top View

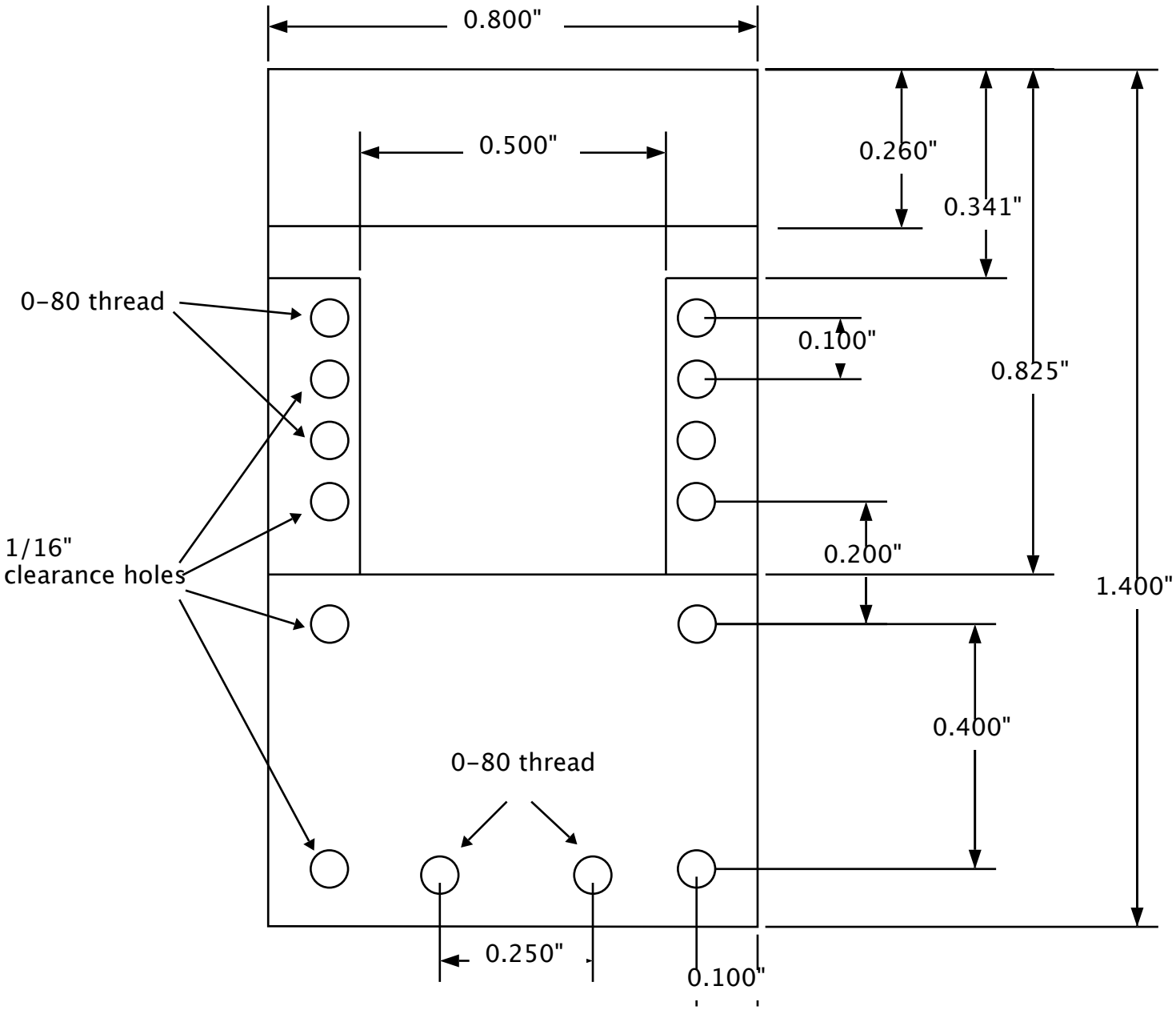

Side View

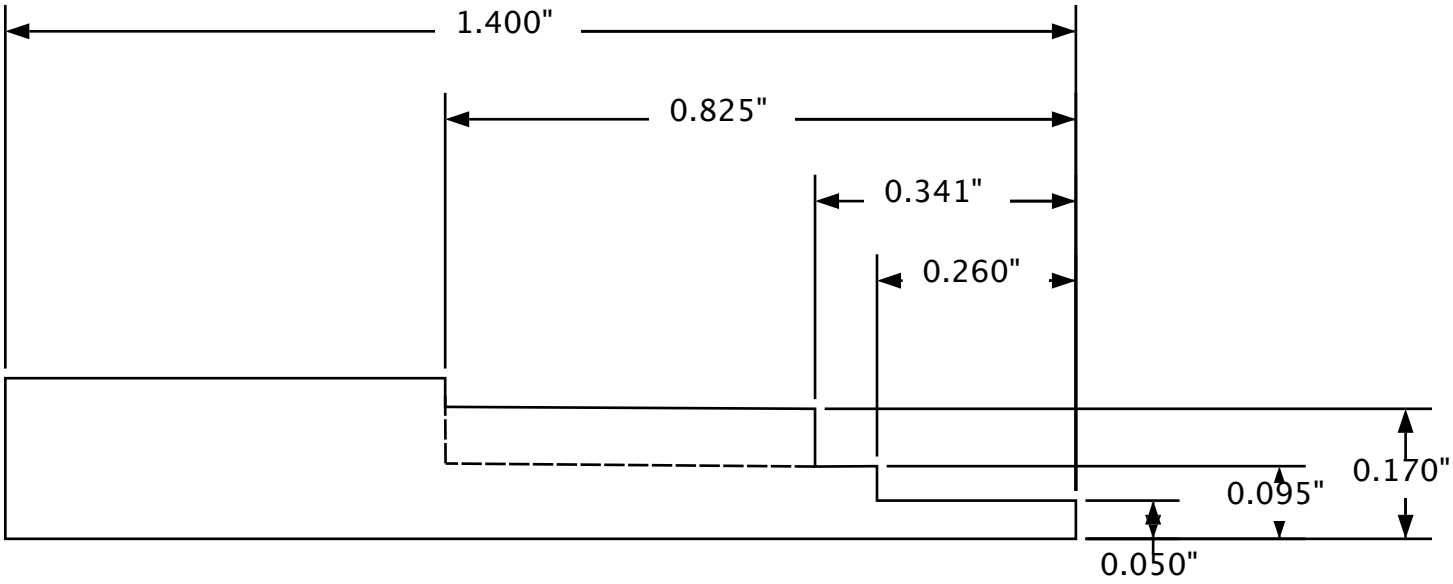

Front View

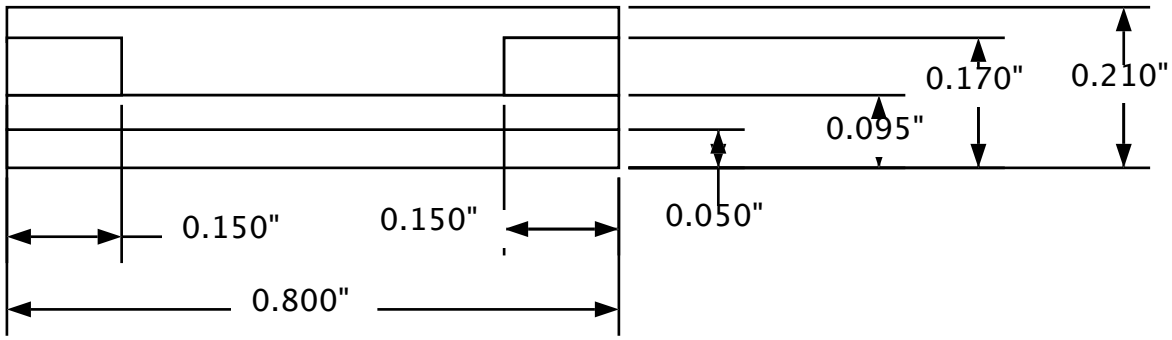

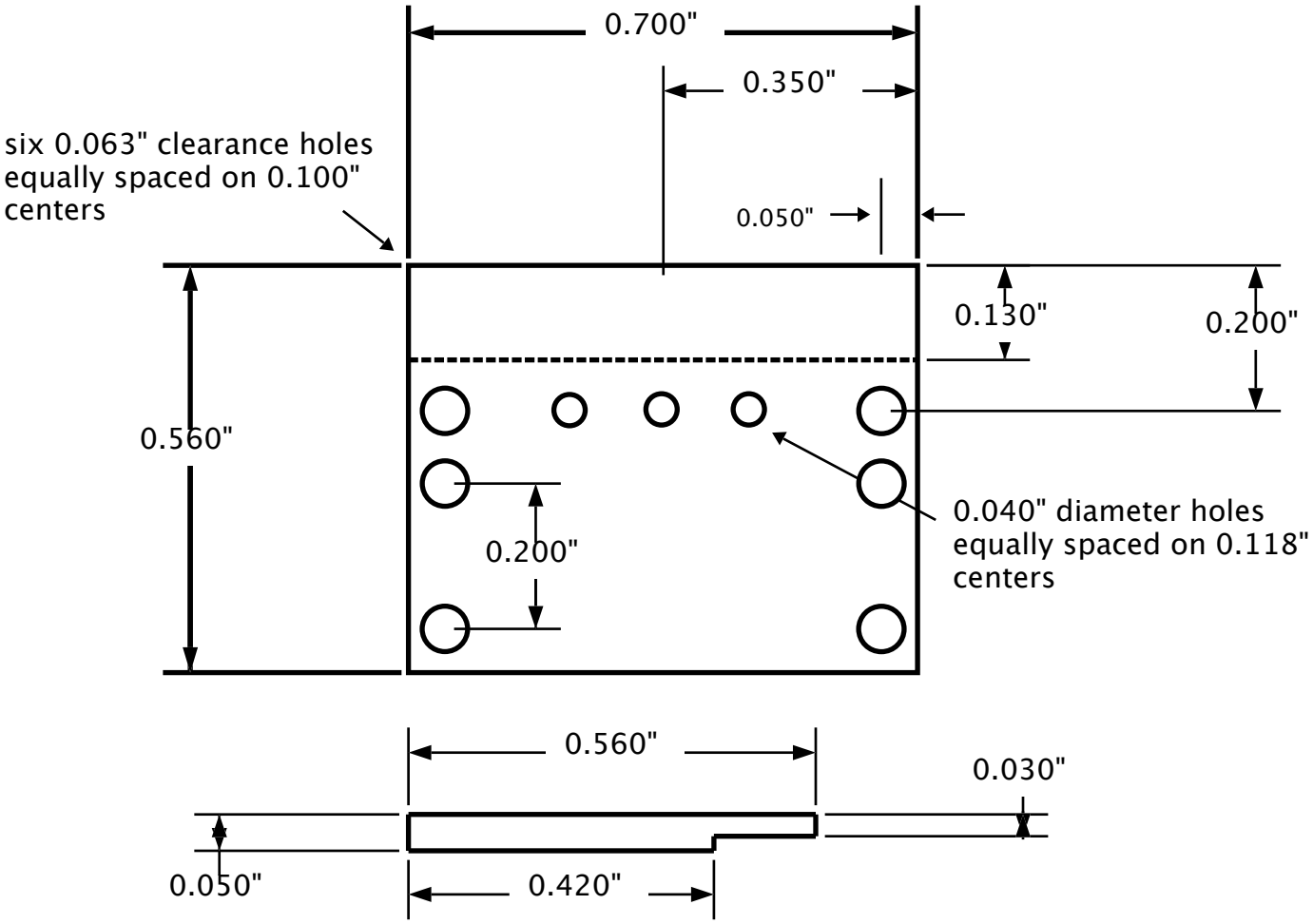

Scale: X2
Make three (3) 0.050" thick
Material: aluminum sheet
Tolerances: +/- 0.001"

Jeffrey Yen
28 Nov 2012

Appendix I

Optimal Filtering for Non-Linear Signals

This note is taken from Blas' talk at BALTIC in 2001

Summary of calculation

$$C\frac{dT}{dt} = I_s^2 R_W - \Sigma\left(T_e^5 - T_{ph}^5\right) + E_0\delta(t-t_0) + P_{nyq} + I_s V_{nyq}$$

$$R_s(I_b - I_s) + V_{nyq} + V_{R_s R_p nyq} = I_s(R_p + R_W) - L\frac{dI_s}{dt}$$

$$R_s(T, I_s) = \frac{R_n}{2}\left[1 + \tanh\left(\frac{T - T_{c0} + \left(I_s/A\right)^{\frac{2}{3}}}{\Delta T_c/(2\log 3)}\right)\right]$$

A = constant from GL theory

$$\left(V_{nyq}\right)_{rms} = \sqrt{4k_B RT/\Delta t}$$

$$\left(P_{nyq}\right)_{rms} = \sqrt{4k_B T^2 g/\Delta t};\quad g = \frac{dP}{dt} = 5\Sigma T^4$$

Covariance and weighting matrices

- Least squares analysis which is identical to optimal filter for stationary noise. For non-stationary noise simpler to work in time domain.

Deviation vector is signal minus average: $D^i = S^i - M^i$

Covariance matrix: $\mathrm{cov}\, M^{ij} = \left\langle D^i D^j \right\rangle$

Weighting matrix: $W^{ij} = inv\left(\mathrm{cov}\, M^{ij}\right)$

Least squares estimator:

$$\chi^2 = \left(S - M\right)^T \bullet \overline{\overline{W}} \bullet \left(S - M\right)$$

For this analysis, we calculate chi-squared for each of the 256 templates and histogram the minimum values in 256 bins

Covariance matrices

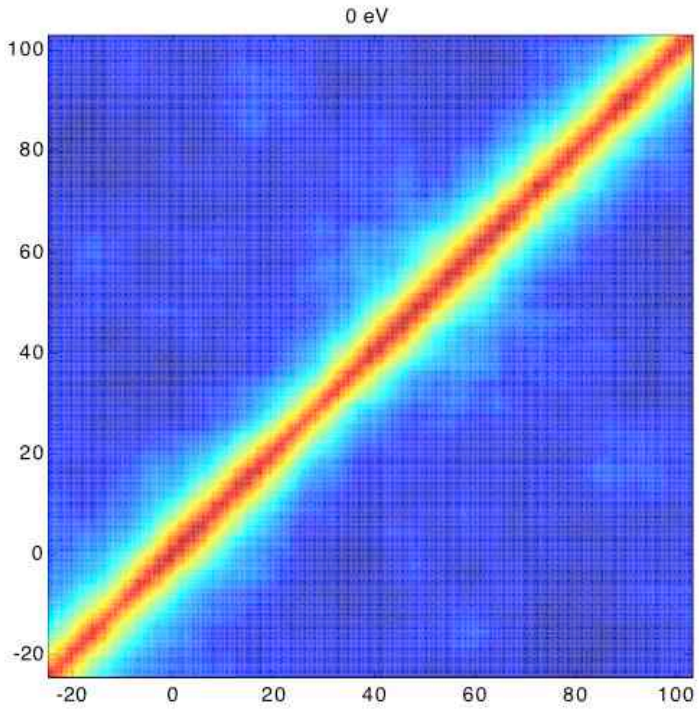

quiescent stationary noise

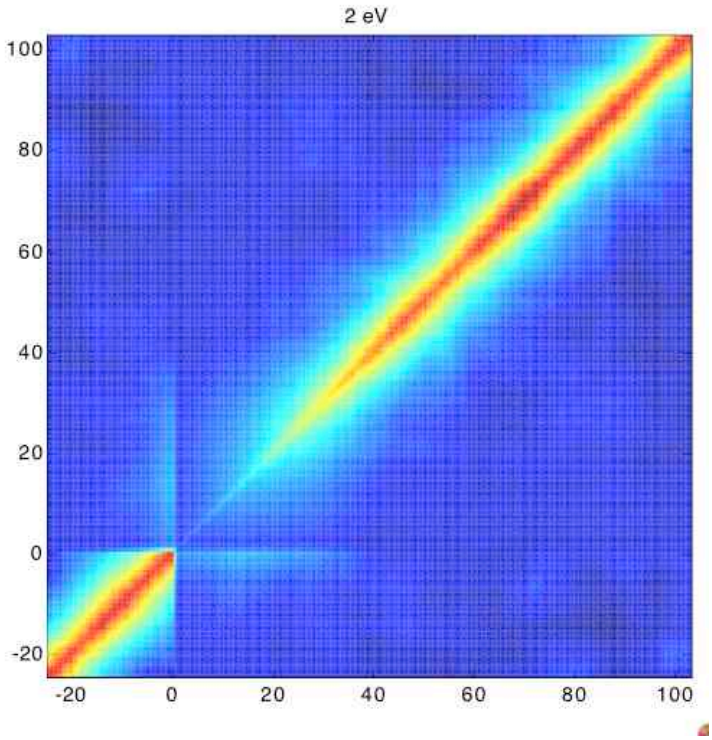

Non-stationary noise

Appendix J

Energy Down Conversion Calculations

Below are two scripts written by Blas and modified later by me for the energy down conversion in Al and W films.

J.1 Al Calculation:

```
% plot Al distribution for emitted phonons from Kozorezov & Bandler paper

tau_ph_e = 4.1e-12;       % Al Ohmega_D phonon scattering time in s with electron
c_s = 3.66e3;             % Al speed of sound in m/s before 6.42e3
tau_s = 0.025e-12;        % Al average time in s for electron to emitt Omega_D/2
eta_eff = 0.4;            % Al phonon escape combined for nu*p*(1-tsi_c /2
D = 0.019;               % Al diffusivity in m^2/s befoe 0.013 0.0042
t_dc = 0.4e-12;           % duration in sec of E_1* to Ohmega_D cascade

d = 300e-9;               % Al film thickness in meters
dz0 = d/100;
z0 = (-d/2 :dz0:(d/2 ;    % -d/2 < z0 , +z0/d is event location in film thickness

zeta = sqrt(pi^2*D*t_dc/2/d^2 ;
```

```
beta = tau_ph_e*c_s/d;
Z0 = 1.42;                % metal renormalization factor 1+lambda where lambda =

E_D_T = 428;              % Debye temperature in K
E_1_T = E_D_T*sqrt(tau_s/tau_ph_e ;                % temperature where tau_ee = t
h = 6.6e-34;              % Planck's constant in units of J-s
k = 1.38e-23;             % Boltzmann's constant in J/K
E_D_f = E_D_T*k/h;
E_1_f = E_1_T*k/h;

%% Phase 1 phonon loss calculation for beta << 1
m = 0:20;
mM = m'*ones(1,length(z0  ;
z0M = ones(length(m ,1 *z0;

Y_mbeta = (beta/3 *(1 - 3*m.^2*pi^2*beta^2 - 3*beta^3*(-1 .^m.*(2 - m.^2*pi^2 ...
    + 3*m.^3*pi^3*beta^3.*(atan(1./(m*pi*beta   + sinint(m*pi  - pi/2  ;

Y_mbetaM = Y_mbeta'*ones(1,length(z0  ;

kappa_mzeta = exp(-m.^2*zeta^2 .*sinh(m.^2*zeta^2 ./(m.^2*zeta^2 ; kappa_mzeta(1
kappa_mzetaM = kappa_mzeta'*ones(1,length(z0  ;

E_loss1_z0 = 8*eta_eff*sum(kappa_mzetaM.*cos(mM*pi.*(1/2 + z0M/d  .*Y_mbetaM ;
E_loss1 = mean(E_loss1_z0 ;

figure(1 ; plot(z0/d,E_loss1_z0*1e2
set(gca,'XTick', [-0.5:0.1:0.5],'linewidth',2,'fontsize',16
axis([-0.5 0.5 0 1.1*max(E_loss1_z0*1e2 ]
xlabel('Event Location [z_0/d]'
ylabel('Energy Loss Percentage'
%title(['Al (' num2str(d*1e9  ' nm  on Si Stage 1 Energy Loss']
%line(0.5*[-1 1],E_loss1*[1 1]*1e2,'color','r'

%% compute phonon energy distribution for stage 1 all very near Omega_D
x = E_D_T/E_1_T;              % ratio of Ohmega_D/Omega_1
```

```
dz = 0.001;
z = (1/x :dz:(1-dz ;

E1_sig = 0.05;
dE_1 = E_loss1*dz*exp(-(1-z .^2/(2*E1_sig^2  *sqrt(2/(pi*E1_sig^2  ;

%% Stage 2 phonon loss calculation
f_z = 1-z-(z/12 .*(z.^2.*(cos(sqrt(2 *log(z  -7*sqrt(2 *sin(sqrt(2 *log(z   -1 ;

dg = dz*(x./z .*f_z.*(expint(z*(x-1  -expint(1-z  ...
    +exp(z .*(expint(1  - expint(x*z   + log((x-1 /x./(1-z   ;

dE_2 = eta_eff*12*Z0/(11*Z0+3 *beta*dg;

E_loss2 = sum(dE_2 ;

figure(2
plot(z*E_D_f*1e-12,dE_1*(E_D_f*1e-12 /dz,'g'
set(gca,'linewidth',2,'fontsize',16
%{
title(['Al/Si Phonon loss; (E_1,E_2,E_{tot} /E = ' num2str(E_loss1,'%0.3f' ...
    ', ' num2str(E_loss2,'%0.3f'  ', ' num2str(E_loss1+E_loss2,'%0.3f' ...
    '; \Omega_1, \Omega_D = ' num2str(E_1_f*1e-12,'%0.2f' ...
    ', ' num2str(E_D_f*1e-12,'%0.2f'  ' THz']
%}
xlabel('Phonon Eneregy [THz]'
ylabel('Energy loss percentage per THz'

hold on; plot(z*E_D_f*1e-12,dE_2*(E_D_f*1e-12 /dz,'r' ; hold off
hold on; plot(z*E_D_f*1e-12,(dE_1+dE_2 *(E_D_f*1e-12 /dz,'b' ; hold off

ymax = max((dE_1+dE_2 *(E_D_f/1e12 /dz ;
%{
text(0.15*E_D_f/1e12,0.6*ymax,...
    {['\tau_{ph-e} = ' num2str(tau_ph_e*1e12  ' ps;'];
     ['c_s = ' num2str(c_s  ' m/s;'];
     ['\tau_s = ' num2str(tau_s*1e12  ' ps;'];
```

```
     ['\eta_{eff} = ' num2str(eta_eff  ';'];
     ['D = ' num2str(D  ' m^2/s;'];
     ['t_{dc} = ' num2str(t_dc*1e12  ' ps;'];
     ['Z(0  = ' num2str(Z0  ';'];
     ['d = ' num2str(d*1e9  ' nm;'];        % z_0/d = ' num2str(z0/d  ';'];
     ['\beta = ' num2str(beta,'%1.3f'  '; \zeta = ' num2str(zeta,'%1.3f'  ';'];
     ['E_D = ' num2str(E_D_T  ' K = ' num2str(E_D_f/1e12,'%1.2f'  ' THZ;'];
     ['E_1 = ' num2str(E_1_T,'%2.1f'  ' K = ' num2str(E_1_f/1e12,'%1.2f'  ' THZ;'
%}
legend('Phase 1 loss','Phase 2 loss','Total loss','location',[0.60 0.65 0.22 0.20

%% calculate the cumsum for z0=-d/2
figure(3 ;
z0=-d/2;
plot(m,1e2*cumsum(8*eta_eff*kappa_mzeta.*cos(m*pi.*(1/2 + z0/d  .*Y_mbeta ,'o'
axis([0 20 0 18]
xlabel('Number of m terms used in sum'
ylabel('Energy loss percentage for Stage 1'
title('Al/Si phonon loss for z_0 = -d/2'

text(5,8,...
    {['\tau_{ph-e} = ' num2str(tau_ph_e*1e12  ' ps;'];
     ['c_s = ' num2str(c_s  ' m/s;'];
     ['\tau_s = ' num2str(tau_s*1e12  ' ps;'];
     ['\eta_{eff} = ' num2str(eta_eff  ';'];
     ['D = ' num2str(D  ' m^2/s;'];
     ['t_{dc} = ' num2str(t_dc*1e12  ' ps;'];
     ['Z(0  = ' num2str(Z0  ';'];
     ['d = ' num2str(d*1e9  ' nm;'];        % z_0/d = ' num2str(z0/d  ';'];
     ['\beta = ' num2str(beta,'%1.3f'  '; \zeta = ' num2str(zeta,'%1.3f'  ';'];
     ['E_D = ' num2str(E_D_T  ' K = ' num2str(E_D_f/1e12,'%1.2f'  ' THZ;'];
     ['E_1 = ' num2str(E_1_T,'%2.1f'  ' K = ' num2str(E_1_f/1e12,'%1.2f'  ' THZ;'
```

J.2 W Calculation

```
%% plot W distribution for emitted phonons from Kozorezov & Bandler paper
```

```
tau_ph_e = 13.3e-12;      % W Ohmega_D phonon scattering time in s with electron
c_s = 3.18e3;             % W speed of sound in m/s
tau_s = 0.0125e-12;       % W average time in s for electron to emitt Omega_D/2 p
eta_eff = 0.043;          % W phonon escape combined for eta*p*(1-xi_c /2
D = 0.0035;               % W diffusivity in m^2/s
t_dc = 0.4e-12;           % duration in sec of E_1* to Ohmega_D cascade
Z0 = 1.26;                % metal renormalization factor 1+lambda where lambda =

d = 40e-9;                % W film thickness in meters
dz0 = d/100;
z0 = (-d/2 :dz0:(d/2 ;    % -d/2 < z0 , +z0/d is event location in film thickness

zeta = sqrt(pi^2*D*t_dc/2/d^2 ;
beta = tau_ph_e*c_s/d;

E_D_T = 380;              % Debye temperature in K
E_1_T = E_D_T*sqrt(tau_s/tau_ph_e ;              % temperature where tau_ee = t
h = 6.6e-34;              % Planck's constant in units of J-s
k = 1.38e-23;             % Boltzmann's constant in J/K
E_D_f = E_D_T*k/h;
E_1_f = E_1_T*k/h;

%% Phase 1 phonon loss calculation for beta << 1
m = 0:10;
mM = m'*ones(1,length(z0  ;
z0M = ones(length(m ,1 *z0;
if beta < 0.1
    Y_mbeta = (beta/3 *(1 - 3*m.^2*pi^2*beta^2 - 3*beta^3*(-1 .^m.*(2 - m.^2*pi^2
        + 3*m.^3*pi^3*beta^3.*(atan(1./(m*pi*beta   + sinint(m*pi  - pi/2  ;
else
    dx = 0.001; x = dx:dx:(1/beta ; xM = x'*ones(1,length(m  ; mxM = ones(length(
    Y_mbeta = beta^4*sum(dx*xM.^4.*(1 - (-1 .^mxM.*exp(-xM  ./(xM.^2 + mxM.^2*pi^
end
    Y_mbetaM = Y_mbeta'*ones(1,length(z0  ;
    kappa_mzeta = exp(-m.^2*zeta^2 .*sinh(m.^2*zeta^2 ./(m.^2*zeta^2 ; kappa_mzet
    kappa_mzetaM = kappa_mzeta'*ones(1,length(z0  ;
```

```
    E_loss1_z0 = 8*eta_eff*sum(kappa_mzetaM.*cos(mM*pi.*(1/2 + z0M/d  .*Y_mbetaM
    E_loss1 = mean(E_loss1_z0 ;

figure(1 ; plot(z0/d,E_loss1_z0*1e2
set(gca,'XTick', [-0.5:0.1:0.5],'linewidth',2,'fontsize',16
axis([-0.5 0.5 0 1.1*max(E_loss1_z0*1e2 ]
xlabel('Event Location [z_0/d]'
ylabel('Energy Loss Percentage'
%title(['W (' num2str(d*1e9  ' nm  on Si Phase 1 Energy Loss']
%line(0.5*[-1 1],E_loss1*[1 1]*1e2,'color','r'

%% compute phonon energy distribution for phase 1 all very near Omega_D
x = E_D_T/E_1_T;               % ratio of Ohmega_D/Omega_1

dz = 0.001;
z = (1/x :dz:(1-dz ;

E1_sig = 0.05;
dE_1 = E_loss1*dz*exp(-(1-z .^2/(2*E1_sig^2  *sqrt(2/(pi*E1_sig^2  ;

%% Phase 2 phonon loss calculation
f_z = 1-z-(z/12 .*(z.^2.*(cos(sqrt(2 *log(z  -7*sqrt(2 *sin(sqrt(2 *log(z   -1 ;

dg = dz*(x./z .*f_z.*(expint(z*(x-1  -expint(1-z  ...
    +exp(z .*(expint(1  - expint(x*z   + log((x-1 /x./(1-z   ;

dE_2 = eta_eff*12*Z0/(11*Z0+3 *beta*dg;

E_loss2 = sum(dE_2 ;

figure(2
plot(z*E_D_f*1e-12,dE_1*(E_D_f*1e-12 /dz,'g'
set(gca,'linewidth',2,'fontsize',16
%{
title(['W/Si Phonon loss; (E_1,E_2,E_{tot} /E = ' num2str(E_loss1,'%0.3f' ...
    ', ' num2str(E_loss2,'%0.3f'  ', ' num2str(E_loss1+E_loss2,'%0.3f' ...
    '; \Omega_1, \Omega_D = ' num2str(E_1_f*1e-12,'%0.2f' ...
```

```
    ', ' num2str(E_D_f*1e-12,'%0.2f'  ' THz']
%}
xlabel('Phonon Eneregy [THz]'
ylabel('Energy loss percentage per THz'

hold on; plot(z*E_D_f*1e-12,dE_2*(E_D_f*1e-12 /dz,'r' ; hold off
hold on; plot(z*E_D_f*1e-12,(dE_1+dE_2 *(E_D_f*1e-12 /dz,'b' ; hold off

ymax = max((dE_1+dE_2 *(E_D_f/1e12 /dz ;
%{
text(0.15*E_D_f/1e12,0.37*ymax,...
    {['\tau_{ph-e} = ' num2str(tau_ph_e*1e12  ' ps;'];
     ['c_s = ' num2str(c_s  ' m/s;'];
     ['\tau_s = ' num2str(tau_s*1e12  ' ps;'];
     ['\eta_{eff} = ' num2str(eta_eff  ';'];
     ['D = ' num2str(D  ' m^2/s;'];
     ['t_{dc} = ' num2str(t_dc*1e12  ' ps;'];
     ['Z(0  = ' num2str(Z0  ';'];
     ['d = ' num2str(d*1e9  ' nm;'];    % z_0/d = ' num2str(z0/d  ';'];
     ['\beta = ' num2str(beta,'%1.2f'  '; \zeta = ' num2str(zeta,'%1.2f'  ';'];
     ['E_D = ' num2str(E_D_T  ' K = ' num2str(E_D_f/1e12,'%1.2f'  ' THZ;'];
     ['E_1 = ' num2str(E_1_T,'%2.1f'  ' K = ' num2str(E_1_f/1e12,'%1.2f'  ' THZ;'
%}
legend('Phase 1 loss','Phase 2 loss','Total loss','location',[0.60 0.65 0.22 0.20
```

Appendix K

Thermal Modeling for KO-15

Electron-Phonon Coupling for QP Study

Jeffrey J. Yen & Robert Moffatt
April 9, 2015

Abstract. This note describes QP study thermal modeling.

1 Introduction

The thermal model for the W-TES system has many components shown in Figure 1. At equilibrium, we can write the power balance

$$\begin{aligned} P_{\mathrm{e-ph}} &= P_{\mathrm{x-e}} + P_J, \\ P_{\mathrm{s-MC}} &= P_{\mathrm{x-s}} + P_{\mathrm{e-ph}}, \\ P_{\mathrm{MC}} &= P_{\mathrm{x-MC}} + P_{\mathrm{s-MC}} + P_{\mathrm{L}}, \end{aligned}$$

where $\mathrm{P_J = V^2/R}$ is the Joule power in the W electron system. $\mathrm{P_{e-ph} \propto T^5}$ is electron phonon coupling in the W. $\mathrm{P_{s-MC} \propto T^4}$ is the thermal coupling from W phonon system to mixing chamber. $\mathrm{P_{MC} \propto T^2}$ is the cooling power from the fridge. P_L is any external heat load to the mixing chamber. $\mathrm{P_{x-e}}$, $\mathrm{P_{x-ph}}$ and $\mathrm{P_{x-MC}}$ are the power loading from the x-ray source onto electron system, phonon system and MC, respectively. If we ignore the x-ray power first, $\mathrm{P_{x-e}}$, $\mathrm{P_{x-ph}}$ and $\mathrm{P_{x-MC}}$ are all zero. At equilibrium, Joule hearing is equal to thermal power, therefore,

$$P_J = K\left(T_e^5 - T_{ph}^5\right) = K'\left(T_{ph}^4 - T_{MC}^4\right), \tag{1}$$

where K and K′ are electron-phonon coupling constant. Manipulate equation 1 we get

$$P_J = K\left[T_e^5 - \left(\frac{P_J}{K'} + T_{MC}^4\right)^{5/4}\right] \tag{2}$$

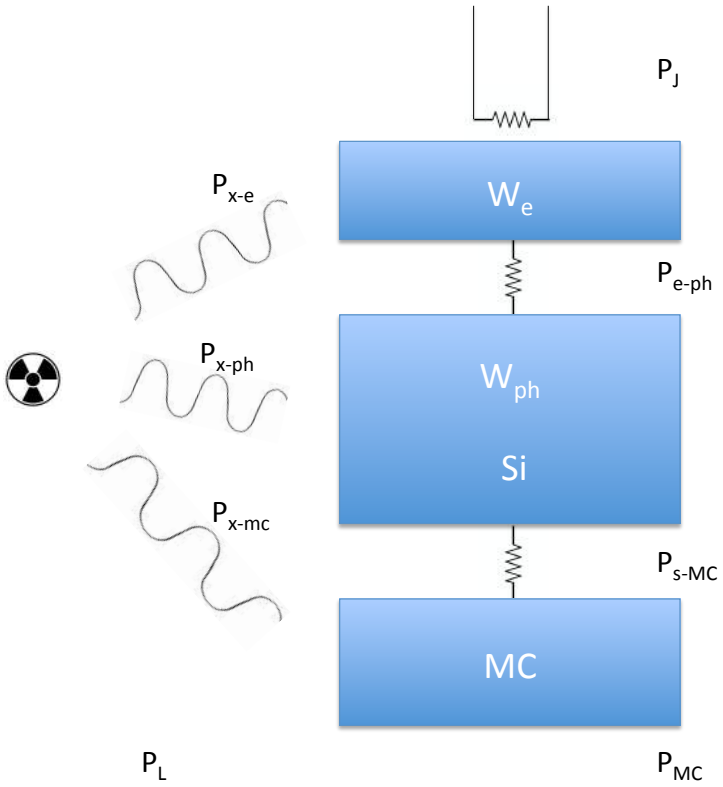

Figure 1. Thermal modeling for TES. $P_J = V^2/R$ is the Joule power in the W electron system. $P_{e-ph} \propto T^5$ is electron phonon coupling in the W. $P_{s-MC} \propto T^4$ is the thermal coupling from W phonon system to mixing chamber. $P_{MC} \propto T^2$ is the cooling power from the fridge. P_L is any external heat load to the mixing chamber. P_{x-e}, P_{x-ph} and P_{x-MC} are the power loading from the x-ray source onto electron system, phonon system and MC, respectively.

Appendix L

Simulation for TES Pulse

```
%% This script is used for simulating and fitting pulses.
%function Chi2 = benSimPulseV1_2bb_Run100(q
%close all
%clear all

p = [76.3432 1.0500 0.0418 1.6038];%46mK[75.4301 1.0007 0.0377 1.5946];%[ 76.047
Tc Tw WaterFrac Q L
q = [1.1350 1.6038 0.1271];%46mK[1.2414 1.5971 0.1859];%[ 1.0728 3.31 .1758];%42m
r = [3.71 0.096 2.67 1.875];
%TES Parameters
Tc = p(1 ;       %Critical Temp in mK
Tw = p(2 ;       %10-90% Width of Transition in mK
Rn = r(1 ;       %Normal Resistance in Ohms
Width = 250;    %Microns
Length = 250;   %Microns
Thick = 0.040;  %Microns
N = 10;         %Number of Strips to Model


%Waterfall Parameters
WaterFrac1 = p(3 ; %Fraction of Waterfall Which is Connected
WaterFracN = WaterFrac1;
```

```
LWater = 0.375;   %Length of Waterfall in Microns

%SQUID Parameters
Bias = r(2 ;     %Bias Voltage in Volts
Rl = 6930;        %Limiting Resistance in Ohms
Ib = Bias/Rl;     %Bias Current in Amps
Rs = 30*1e-3;        %Shunt Resistance in Ohms
Rp = r(3 *1e-3;       %Parasitic Resistance in Ohms
Gain = 1.e5;       %Effective KO15 gain in ohms

%OTHER Parameters
Q = 1e3*p(4 ;              %Incident Energy in eV
%Cl K-alpha:.531*2620eV=1391eV (Jeff measures 988 eV
Tb = 38.;       %Fridge Base Temp in mK
Thot = 1.4;      %1K Pot Temp in K
dt = 0.2e-6;           %Time Bin Size in sec
trace = 4096*dt;       %Trace Length in sec
IRFrac = 0;          %Fractional IR Absorption From 4.2 K
                       %Must Be Between 0 and 1

if Q > 1000
%%Run99
%Get Template Files
load('../INT/Run100/Run100_W_selected_38mK.mat' ;
Template = zeros(size(avg_W2,2 ,1 ;
Template(:,1  = avg_W2( ;
else
load('../INT/Run100/Run100_Al_selected_38mK.mat' ;
Template = zeros(size(data_combined,2 ,1 ;
Template(:,1  = data_combined(2,:,2 ;  % Pulse#, :, TES#      1 small 2 big 92 mi
end

Display = 1;

%%
%------------------------
%End of User-Set Parameters
```

```
%------------------------

t = dt:dt:trace;            %Time in sec

%Sig = 0.4606*0.32e-24;     %Electron-Phonon Coupling in W/mK^5/um^3 Run40=0.4606
K = r(4 *1e-22/N;%Sig * Width*Length*Thick / N;  %Electron-Phonon Coupling in W/m

SB = 5.67e-20;      %Stefan-Boltzmann Const in W/um^2/K^4
P_IR = SB*Width*Length*4.2^4 / N; %Blackbody IR absorption from 4.2 K bath
Pleak = IRFrac*P_IR;  %Estimated IR loading on TES in Joules

L = q(1 *2.44e-14;  %Lorenz Number from Weidemann-Franz Law, W*ohms/mK^2
JtoeV = 6.242e18;           %Convert Joules to eV
k = 1.38e-26;               % Boltzmann constant in J/mK
h_bar = 1.054e-34;          % Planck constant J-s/rad

%Functions For Normal And Superconducting Heat Capacity
Delta = 1.76*k*(Tc+Tw ;    %Superconducting Band Gap of Tungsten in Joules
C_norm = @(T  0.5*.00085 * Width*Length*Thick .* T / N;
%Goodstein: 2.43 -> 1.95 For Constant Voltage Bias
SuperConst = 2.43*C_norm(Tc+Tw *(Tc+Tw ^(3/2 *exp(1.76 ;%Heat Capacity of Superco
C_super = @(T  SuperConst .* T.^(-3/2  .* exp(-Delta./(k*T  ; % 1/N Incorporated
%C_super = @(T  .00085 * Width*Length*Thick .* T / N;
%Ginzberg-Landau Current-Coupling Constant
A = 3.52*sqrt(k*C_norm(Tc+Tw /h_bar/(Rn/N /(Tc+Tw /JtoeV /1.5;   % typical 1.5 in
AWater = A*WaterFrac1;

Qstart = 500;
QTime = q(2 *1e-6;   %SECONDS!  Time Constant of Short Tail

%Adjust Measured Parameters For Waterfall
WWater = WaterFrac1*Width;
RnWater = Rn * LWater/WWater;
if RnWater < Rn/2
    Rn = Rn - 2*RnWater;
else
    disp('Waterfall Resistance Exceeds Rn!!!'
```

```
end

%%
%Pre-Declare External Power Trace

Qext = zeros(1,length(t  ;


for i = Qstart:length(t  %Assemble Double Exponential Input Power
    Qext(i  = Q*dt/QTime*exp(-i/(QTime/dt  ;
end

if Q ~= 0
    Qext = Qext * Q / sum(Qext ;
end


%%
%------------------------
%BEGIN CALCULATIONS
%------------------------

%Pre-Declare Variables
Is = zeros(1,length(t  ;   %Source Current
T = zeros(N,length(t  ;    %TES Temperature
R = zeros(N,length(t  ;    %Observed TES Resistance
C = zeros(N,length(t  ;    %Heat Capacity of TES
P = zeros(1,length(t  ;    %Power Dissipated
TWater1 = zeros(1,length(t  ;
RWater1 = zeros(1,length(t  ;
TWaterN = zeros(1,length(t  ;
RWaterN = zeros(1,length(t  ;
Inoise = zeros(1,length(t  ; %Random Noise To Add To Is
SubSteps = zeros(1,length(t  ;%For Dynamic Step Size In DAQ Measurement
%%
%Equilibrium Calculation
Tnew = (Tc-Tw *ones(N,1 ;                  %Guess That TES Starts At Tc.
```

```
Rnew = Rn/2/N * ones(N,1 ;
Inew = Ib*Rs/(sum(Rnew +Rs+Rp ;
Cnew = C_norm(Tnew .*(N*Rnew/Rn  + C_super(Tnew .*(1-(N*Rnew/Rn  ;
TW1new = Tc-Tw;
RW1new = RnWater/2;
TWNnew = Tc-Tw;
RWNnew = RnWater/2;
PWater1 = K*Tc^5*RnWater/(Rn+2*RnWater ;
PWaterN = K*Tc^5*RnWater/(Rn+2*RnWater ;

dtEquil = min([C_norm(Tc *Rn/(N*L*Tc*JtoeV  dt] ;%C_norm(Tc *Tw/(4*abs(PWater
X = 100e-6/dtEquil;     %Run Equilibration For 100 uSec At A Time
TSave = zeros(N,1 ;
TW1Save = 0;
TWNSave = 0;
Beta = exp(-pi ;

while min(abs(Tnew-TSave   > 1e-10 || abs(TW1new-TW1Save  > 1e-10 || abs(TWNnew-T
%While T Is Still Settling
    TSave = Tnew;
    TW1Save = TW1new;
    TWNSave = TWNnew;
    for x = 1:X              %Let temp settle for 500 usec

        Told = Tnew;
        Rold = Rnew;
        Iold = Inew;
        Cold = Cnew;
        TW1old = TW1new;
        RW1old = RW1new;
        TWNold = TWNnew;
        RWNold = RWNnew;

        tempCond = L*Told./(Rn/N ;          %Temporary Conductance Matrix
        WaterCond1 = L*TW1old/RnWater;
        WaterCondN = L*TWNold/RnWater;
        Pcond = tempCond .* (circshift(Told,-1  - Told ; %Conduction Energy From
```

```
        Pcond(N  = 0; %No Conduction Off the End of the Strip
        PWater1 = Iold^2*RW1old;
        PWaterN = Iold^2*RWNold;

        Told(1  = Told(1  + dtEquil*PWater1*JtoeV/Cold(1 ;
        Told(N  = Told(N  + dtEquil*PWaterN*JtoeV/Cold(N ;
        Tnew = Told + dtEquil * (Pleak + Iold.^2.*Rold - K.*(Told.^5-Tb^5  + Pcon
        Rnew = rfn(Tnew,Iold,Rn/N,Tc,Tw,A ;
        %Massless Waterfall Instantly Adjusts To Change In Joule Heating
        TW1new = Tnew(1  + PWater1 / WaterCond1;
        RW1new = rfn(TW1new,Iold,RnWater,Tc,Tw,AWater ;
        TWNnew = Tnew(N  + PWaterN / WaterCondN;
        RWNnew = rfn(TWNnew,Iold,RnWater,Tc,Tw,AWater ;
        %Only Calculate New I_s Once Resistance of All Strips is Summed
        Inew = Ib * Rs/(sum(Rnew +RW1new+RWNnew+Rp+Rs ;
        Inew = (1-Beta *Inew + Beta*Iold;

        if mean(Tnew  < Tc-Tw/2 %Numerical Oscillation Suppression
            for i = 1:10
                Rnew = geomean([Rnew Rnew Rnew rfn(Tnew,Inew,Rn/N,Tc,Tw,A ],2 ;
                RW1new = geomean([RW1new RW1new RW1new rfn(TW1new,Inew,RnWater,Tc
                RWNnew = geomean([RWNnew RWNnew RWNnew rfn(TWNnew,Inew,RnWater,Tc
                Inew = Ib*Rs/(sum(Rnew +RW1new+RWNnew+Rp+Rs ;
                Inew = (1-Beta *Inew + Beta*Iold;
            end
        end %Oscillation Suppression

%         f_norm = 0.4*(N*Rnew/Rn .^3 + 0.3*(1+tanh((N*Rnew/Rn-0.25 /0.05  ;
        f_norm = N*Rnew/Rn;
        Cnew = C_norm(Tnew .*f_norm + C_super(Tnew .*(1-f_norm ;

    end   %T_equil loop
end   %While-Settling Loop
%%
T(:,1  = Tnew;              %Start in Equilibrium
Is(1 = Inew;
R(:,1  = rfn(T(:,1 ,Is(1 ,Rn/N,Tc,Tw,A ;
```

```
%disp(num2str(R(1,1
TWater1(1  = TW1new;
RWater1(1  = rfn(TWater1(1 ,Is(1 ,RnWater,Tc,Tw,AWater ;
TWaterN(1  = TWNnew;
RWaterN(1  = rfn(TWaterN(1 ,Is(1 ,RnWater,Tc,Tw,AWater ;
%disp(num2str(RWater1(1
Inoise(1  = sqrt(4*k*(sum(R(:,1  *mean(T(:,1   + RWater1(1 *TWater1(1  + RWaterN(
    + (Rs+Rp *Thot /dtEquil /(sum(R(:,1  +RWater1(1 +RWaterN(1 +Rp+Rs ;
C(:,1  = Cnew;
I0 = Inew;                    %Baseline Source Current
T0 = Tnew;                     %Baseline Temperature
%%
%THIS SECTION DOES NOT YET INCLUDE THE SECOND WATERFALL!!!
%Alpha = T/R * dR/dT at equilibrium
AlphaBob = (rfn(T0+1e-6,I0,Rn/N,Tc,Tw,A -rfn(T0-1e-6,I0,Rn/N,Tc,Tw,A  .*T0./(2e-6
BetaBob = (1 + Rs/(Rs+Rp+sum(R(:,1  +RWater1(1   .*...
    (rfn(T0,I0+1e-8,Rn/N,Tc,Tw,A -rfn(T0,I0-1e-8,Rn/N,Tc,Tw,A  .*I0./(2e-8*R(:,1
AlphaW = (rfn(TWater1(1 +1e-6,I0,RWater1(1 ,Tc,Tw,AWater -rfn(TWater1(1 -1e-6,I0,
    .*TWater1(1 ./(2e-6*RWater1(1  ;
BetaW = (rfn(TWater1(1 ,I0+1e-8,RWater1(1 ,Tc,Tw,AWater -rfn(TWater1(1 ,I0-1e-8,R
    .*I0./(2e-8*RWater1(1  ;
GammaBob = AlphaBob./(1+BetaBob ;
GammaW = AlphaW./(1+BetaW ;
LBob = (GammaBob/5 .*(1-(Tb./T0 .^5 ;
LW = (GammaW/5 .*(1-(Tb./TWater1(1  .^5 ;
fBob = (R(:,1 ./(Rp+RWater1(1 +sum(R(:,1    .*LBob./(LBob+1 ;
fW = (RWater1(1 /(Rp+RWater1(1 +sum(R(:,1    *LW./(LW+1 ;
E_est = Q*(sum(fBob +fW ;
%disp(num2str(E_est

%%
%Begin DAQ Measurement
for x = 1:length(t -1

    tempCond = L*T(:,x ./(Rn/N ;          %Temporary Conductance Matrix
    WaterCond1 = L*TWater1(x /RnWater;
    WaterCondN = L*TWaterN(x /RnWater;
```

```
Pcond = tempCond .* (circshift(T(:,x ,-1  - T(:,x  ; %Conduction Energy From
Pcond(N  = 0; %No Conduction Off the End of the Strip
PWater1 = Is(x ^2*RWater1(x ;
PWaterN = Is(x ^2*RWaterN(x ;

%How many quarter transition widths is the input energy OR how much does cros
SubSteps(x  = ceil(max([4*Qext(x /C(1,x /Tw 2*dt*max(tempCond./C(:,x  *JtoeV]
Beta = exp(-pi/SubSteps(x  ;

%Convert saved variables to unsaved interpolation variables
Tnew = T(:,x ;
Rnew = R(:,x ;
Inew = Is(x ;
Cnew = C(:,x ;
TW1new = TWater1(:,x ;
RW1new = RWater1(:,x ;
TWNnew = TWaterN(:,x ;
RWNnew = RWaterN(:,x ;

for s = 1:SubSteps(x  %Enter Sub-Bin Interpolation Loop

    Told = Tnew;
    Rold = Rnew;
    Iold = Inew;
    Cold = Cnew;
    TW1old = TW1new;
    RW1old = RW1new;
    TWNold = TWNnew;
    RWNold = RWNnew;

    tempCond = L*Told./(Rn/N ;          %Temporary Conductance Matrix
    WaterCond1 = L*TW1old/RnWater;
    WaterCondN = L*TWNold/RnWater;
    Pcond = tempCond .* (circshift(Told,-1  - Told ; %Conduction Energy From
    Pcond(N  = 0; %No Conduction Off the End of the Strip
    PWater1 = Iold^2*RW1old;
    PWaterN = Iold^2*RWNold;
```

```
        Told(1  = Told(1  + (dt*PWater1*JtoeV + Qext(x  /SubSteps(x /Cold(1 ;
%Dump Event Energy Into First Strip
        Told(N  = Told(N  + (dt*PWaterN*JtoeV /SubSteps(x /Cold(N ;  %Dump Waterf
        Tnew = Told + (dt/SubSteps(x   .* (Pleak + Iold.^2.*Rold - K.*(Told.^5-Tb
        Rnew = rfn(Tnew,Iold,Rn/N,Tc,Tw,A ;
        TW1new = Tnew(1  + PWater1 / WaterCond1;
        RW1new = rfn(TW1new,Iold,RnWater,Tc,Tw,AWater ;
        TWNnew = Tnew(N  + PWaterN / WaterCondN;
        RWNnew = rfn(TWNnew,Iold,RnWater,Tc,Tw,AWater ;
        %Only Calculate New I_s Once Resistance of All Strips is Summed
        Inew = Ib * Rs/(sum(Rnew +RW1new+RWNnew+Rp+Rs ;
        Inew = (1-Beta *Inew + Beta*Iold;


        if mean(Tnew  < Tc-Tw/2 %Numerical Oscillation Suppression
            for i = 1:10
                Rnew = geomean([Rnew Rnew Rnew rfn(Tnew,Inew,Rn/N,Tc,Tw,A ],2 ;
                RW1new = geomean([RW1new RW1new RW1new RW1new rfn(TW1new,Inew,RnW
                RWNnew = geomean([RWNnew RWNnew RWNnew RWNnew rfn(TWNnew,Inew,RnW
                Inew = Ib*Rs/(sum(Rnew +RW1new+RWNnew+Rp+Rs ;
                Inew = (1-Beta *Inew + Beta*Iold;
            end
        end %Oscillation Suppression

%         f_norm = 0.4*(N*Rnew/Rn .^3 + 0.3*(1+tanh((N*Rnew/Rn-0.25 /0.05  ;
        f_norm = N*Rnew/Rn;
        Cnew = C_norm(Tnew .*f_norm + C_super(Tnew .*(1-f_norm ;

    end %Sub-Bin Interpolation Loop

    %Put Variables From Last Sub-Bin Into Saved Matrices
    T(:,x+1  = Tnew;
    R(:,x+1  = Rnew;
    TWater1(x+1  = TW1new;
    RWater1(x+1  = RW1new;
    TWaterN(x+1  = TWNnew;
```

```
    RWaterN(x+1  = RWNnew;
    Inoise(x+1  = sqrt(4*k*(sum(R(:,x+1 .*T(:,x+1   + RWater1(x+1 *TWater1(x+1 ..
        + RWaterN(x+1 *TWaterN(x+1  + (Rs+Rp *Thot /dt /(sum(R(:,x+1  +RWater1(x+
    Is(x+1  = Inew;
    C(:,x+1  = Cnew;

end %DAQ Measurement

Chi2 = mean((Gain*(Is' - I0  - Template .^2./(Gain*Inoise' .^2 ;

%Calculate minimum observed current
Imin = Ib * Rs/(Rn+2*RnWater+Rp+Rs ;


%Calculate Energy Deposited
P0 = I0 * [(Ib-I0 *Rs - I0*Rp] * JtoeV;
P = P0 - Is .* [(Ib - Is *Rs - Is*Rp] * JtoeV;
Energy = trapz(t,P ;
%disp(num2str(Energy,7
%%
if Display
    figure(1
    hold off;clf;hold on
    plot(1e6*t,Template(:,1 ,'b-','linewidth',2 ;     %Template in Heavy Line
    plot(1e6*t,Gain*(Is-I0 ,'r-','linewidth',2 ;   %Simulation in Light Line
    plot(1e6*t,0,'k-','linewidth',1 ;
    set(gca,'linewidth',2,'fontsize',16 ;
    xlabel('Time (usec ','fontsize',16 ;
    ylabel('Output Voltage (Volts ','fontsize',16 ;
    title(['T_c=',num2str(Tc ,'mK, dT_c=',num2str(Tw ,'mK, R_n=',num2str(Rn+RnWat
    text(.3*1e6*trace, -Gain*I0(1 /10, ['E_{int} = ', num2str(Energy,4 , ' eV']
    text(.8*1e6*trace, -Gain*I0(1 /3, ['Chi2 = ', num2str(Chi2,3 ]
end
```

Appendix M

Optimal Filtering for Non-Linear Signals

This note is taken from Blas' talk at BALTIC in 2001

Summary of calculation

$$C\frac{dT}{dt} = I_s^2 R_W - \Sigma\left(T_e^5 - T_{ph}^5\right) + E_0\delta(t-t_0) + P_{nyq} + I_s V_{nyq}$$

$$R_s(I_b - I_s) + V_{nyq} + V_{R_s R_p nyq} = I_s(R_p + R_W) - L\frac{dI_s}{dt}$$

$$R_s(T, I_s) = \frac{R_n}{2}\left[1 + \tanh\left(\frac{T - T_{c0} + \left(I_s/A\right)^{\frac{2}{3}}}{\Delta T_c/(2\log 3)}\right)\right]$$

A = constant from GL theory

$$\left(V_{nyq}\right)_{rms} = \sqrt{4k_B RT/\Delta t}$$

$$\left(P_{nyq}\right)_{rms} = \sqrt{4k_B T^2 g/\Delta t};\quad g = \frac{dP}{dt} = 5\Sigma T^4$$

Covariance and weighting matrices

- Least squares analysis which is identical to optimal filter for stationary noise. For non-stationary noise simpler to work in time domain.

Deviation vector is signal minus average: $D^i = S^i - M^i$

Covariance matrix: $\mathrm{cov}\, M^{ij} = \left\langle D^i D^j \right\rangle$

Weighting matrix: $W^{ij} = inv\left(\mathrm{cov}\, M^{ij}\right)$

Least squares estimator:

$$\chi^2 = \left(S - M\right)^T \bullet \overline{\overline{W}} \bullet \left(S - M\right)$$

For this analysis, we calculate chi-squared for each of the 256 templates and histogram the minimum values in 256 bins

Covariance matrices

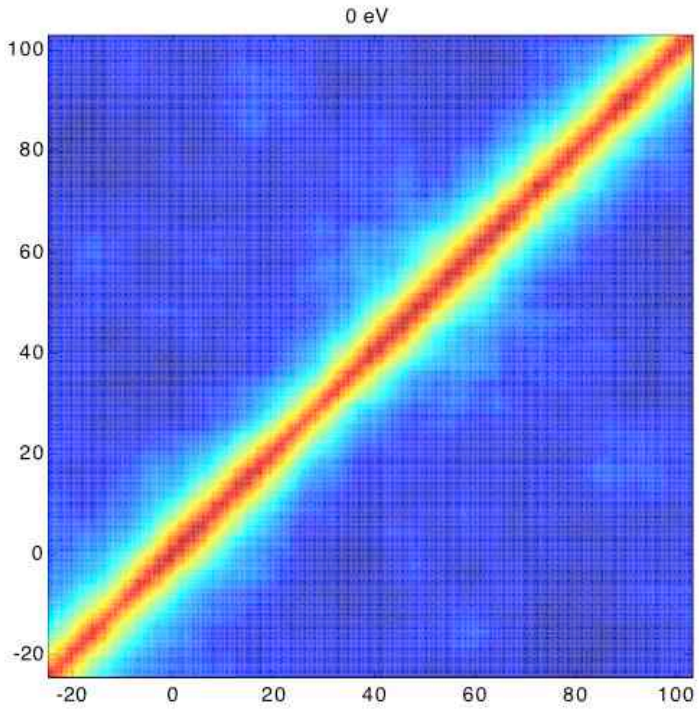

quiescent stationary noise

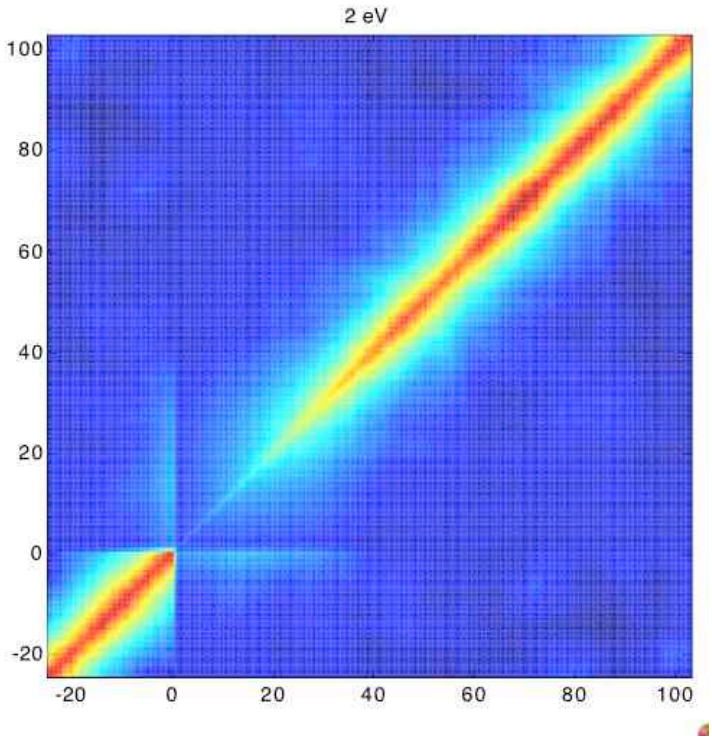

Non-stationary noise

Appendix N

Mask Documentation

Mask Documentation:

Overall Layout:

		PS2.5	P100	P100s	PS5		
	PS0	P50s	PS5	QP	P100	QP	
QP	P50	PS2.5	P100s	P50c	PS2.5	P100s	PS0
P50s	PS0	P100c	QP	PS0	P50s	PS5	P50
P50	PS5	P50s	PS2.5	PS5	P100	QP	P50s
PS5	P100c	PS0	P50	P100s	PS0	P50	PS2.5
	PS2.5	P100	QP	PS2.5	P50c	PS5	
		PS0	P100s	P100	QP		

There are 10 unique dice repeated in the 52 cells present on the chip. The quasiparticle and phase separation devices are each repeated 7 times while the circular phonon sensors are each repeated twice and the non-circular phonon sensors are repeated 5 times. They are arranged so each die type has an equal number of instances at each distance from the edge, so each die has an equal chance of being fabricated error free. Similarly, there is at least one copy of every die except the circular phonon sensors in each of the four quadrants of the mask. The blue squares on either side of the grid represent the alignment marks on the mask for orientation purposes.

- QP: Quasiparticle sensor
- PS0: Phase separation device, 0um tungsten outside overlap
- PS2.5: Phase separation device, 2.5um tungsten outside overlap
- PS5: Phase separation device, 5um tungsten outside overlap
- P100: Phonon sensor, 100um TES
- P50: Phonon sensor, 50um TES
- P100s: Phonon sensor, 100um TES, quarter size Al fins
- P50s: Phonon sensor, 50um TES, quarter size Al fins
- P50c: Phonon sensor, 50um TES, quarter size round Al fins
- P50c: Phonon sensor, 100um TES, quarter size round Al fins

Dice:

Quasiparticle sensor: This die contains 6 TESs surrounded by vetos, each with a 500um x 250um Al fin with 250um x 250um W squares bordering it on each end. The overlap between the Al and W is varied in each TES over the range: 10um, 15um, 20um, 30um, and 40um. The last device contains a full overlap of the 500um long Al fin. (This would be considered a 250um overlap using comparable terminology, but is labeled as FULL.) This allows testing of how the size of the overlap region affects quasiparticle trapping as the quasiparticles propagate from the Al to the W. This chip also contains four square TES of side length 250um, 100um, 50um, 25um, as well as two pads with a pure Al link and no TES. The pure Al link will allow us to test the parasitic resistance of the measurement circuit, since it will add no resistance of its own when it is superconducting.

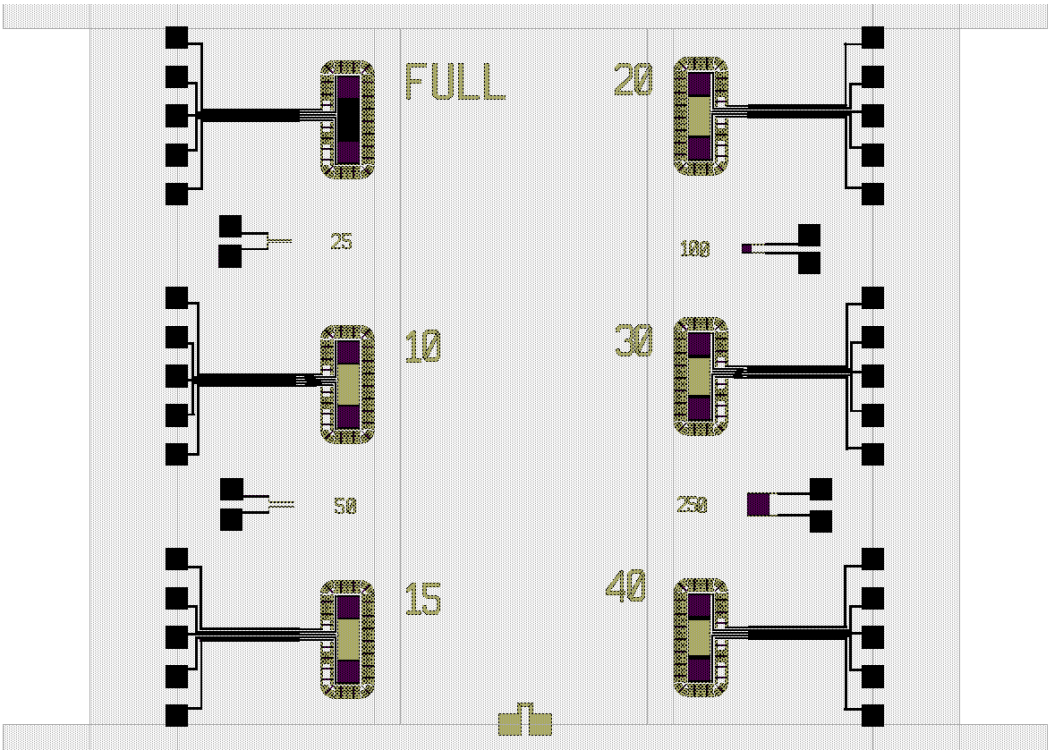

Fig. 1 The quasiparticle sensor die

Phase transition devices: There are three dice with phase transition devices, each containing 12 sensor arrays. The sensor arrays have 14 columns and 7 rows of TESs with rectangular Al fins, all wired in parallel and connected to two pads. On each die, the length of the TES and overlap between the W and the Al fins for each TES is varied. The left side of the die has arrays of 75um x 2um TESs, and the right side has arrays of 100um x 2um TESs. From top to bottom, the arrays contain TESs with overlap distances of: 5um, 10um, 15um, 20um, 30um, and 40um. The 100um TESs have 4 Al fins each while the 50um TESs have 3 fins. Between each of the three dice, the width of the tungsten outside the overlap with the Al fin is varied over the range: 0um, 2.5um, 5um. These devices will allow us to understand how the regions of overlap between Al and W affect the heat capacity of the TESs, as well as whether the improved T_c tungsten can avoid phase transition for longer (100um) TES sensors.

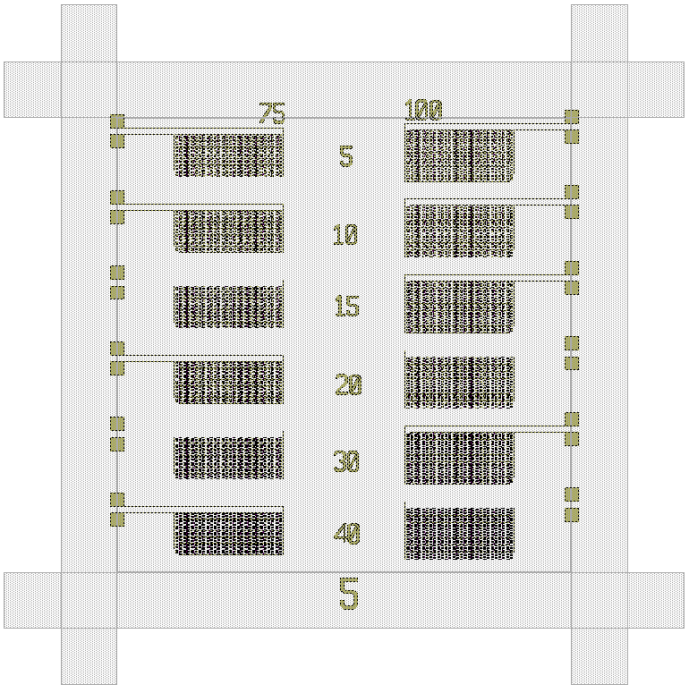

Fig. 2 The phase separation device chip, with 5um tungsten outside overlap

Phonon sensors: The four dice with phonon sensors contain a central 5x5 square of 1mm x 1mm TES chips surrounded by an 8x8 square ring of the same 1mm x 1mm TES chips. Both the central square and the outer ring are wired separately in parallel, and they each have approximately equal area, meaning there is approximately equal probability that an event will be registered in each. Each of the 1mm x 1mm chips contains a tungsten TES in the center surrounded by 6 large Al fins shaped like pie wedges separated at the polar angles of: 0^0, 45^0, 135^0, 180^0, 225^0, and 315^0. There is a 20um overlap between each Al fin and the tungsten, and the tungsten extends a further 2.5um outside the Al fin before reconnecting to the TES. The fins have 10um x 10um square holes spaced 100um apart to act as magnet field sinks, preventing magnetic field from trapping quasiparticles before they can propagate to the tungsten. Two of the four phonon sensor dice contain 100um tall by 4um wide TESs while the other two dice contain 50um tall by 2um wide TESs. Also, in two of the dice the Aluminum fins extend all the way to the edge making the sensor area ~1mm^2 while in the other, two, the fins only extend halfway to the edge giving an area of ~.25mm^2. These two variations lead to 4 unique combinations of TES length and fin area. Varying the size of the TESs in the phonon sensors allows us to examine how easily the TESs become saturated and better tune the balance between sensitivity and resiliency to saturation. Changing the Al fin area will allow us to see how efficient the various sizes are at collecting phonons and allow optimization of collection area versus quasiparticle loss within the fins.

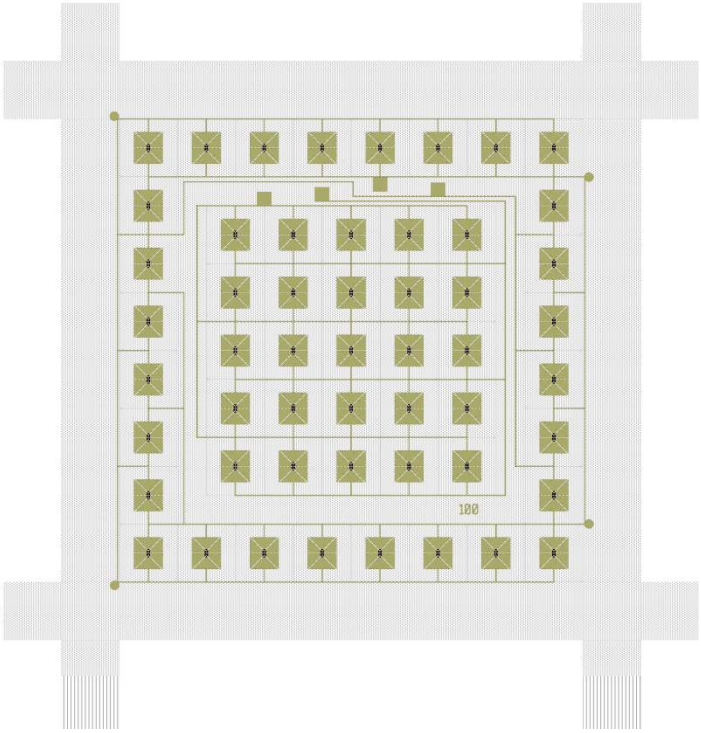

Fig 3. The phonon sensor die, with low area and 100um x 4um TESs

Bibliography

[1] A. C. C. Collaboration, **Combined Measurement of the Higgs Boson Mass in pp Collisions at $\sqrt{s}$ =7 and 8 TeV with the ATLAS and CMS Experiments**. *Physics Review Letter* **114**, 2015.

[2] P. Collaboration, **Planck 2013 results. I. Overview of products and scientific results**. *Astronomy & Astrophysics* **571**, 2014.

[3] E. Corbelli and P. Salucci, **The extended rotation curve and the dark matter halo of M33**. *Mon. Not. R. Astron. Soc.* **331**, 441–447 2000.

[4] D. J. Eisenstein, **Dark energy and cosmic sound**. *New Astronomy Reviews* **49**, 360–365 2005.

[5] D. Clowe *et al.*, **A direct empirical proof of the existence of dark matter**. *Astrophys. J. Lett.* **648**, L109 2006.

[6] E. A. Baltz, M. Battaglia, M. Peskin, and T. Wizansky, **Determination of dark matter properties at high energy colliders**. *Physical Review D* **74**, 103521 2006.

[7] S. C. Collaboration, **Improved WIMP-search reach of the CDMS II germanium data**. *Physical Review D* **92**, 072003 2015.

[8] L. Collaboration, **First results from the LUX dark matter experiment at the Sanford Underground Research Facility**. *Physical Review Letter* **112**, 091303 2014.

[9] C. Collaboration, **Results on light dark matter particles with a low-threshold CRESST-II detector**. *Eur. Phys. J. C* **in print**, in print 2015.

[10] C. Collaboration, **Silicon detector results from the first five-tower run of CDMS II**. *Physical Review D* **88**, 059901 2013.

[11] C. Collaboration, **Exclusion limits on the WIMP-nucleon cross section from the first run of the Cryogenic Dark Matter Search in the Soudan Underground Laboratory**. *Physical Review D* **72**, 052009 2005.

[12] C. Collaboration, **Improved WIMP-search reach of the CDMS II germanium data**. *Physical Review D* **92**, 072003 2015.

[13] N. E. Booth, **Quasiparticle Trapping and the Quasiparticle Multiplier**. *Applied Physics Letter* **50**, 293 1987.

[14] K. D. Irwin *et al.*, **A quasiparticle-trap-assisted transition-edge sensor for phonon-mediated particle detection**. *Review of Scientific Instruments* **66**, 5322–5326 November 1995.

[15] P. N. Luke, **Voltage-assisted Calorimetric Ionization Detector**. *Journal of Applied Physics* **64**, 6858–6860 1988.

[16] R. Moffatt, **Two-dimensional Spatial Imaging of Charge Transport in Germanium at Cryogenic Temperatures**. Ph.D. thesis, Stanford University, 2015.

[17] K. Schneck, **Search For Low-Mass Dark Matter With Supercdms Soudan And Study Of Shorted Electric Field Configurations In CDMS Detectors**. Ph.D. thesis, Stanford University, 2015.

[18] M. C. Pyle, **Optimizing The Design And Analysis Of Cryogenic Semiconductor Dark Matter Detectors For Maximum Sensitivity**. Ph.D. thesis, Stanford University, 2012.

[19] J. Filippini, **A Search for WIMP Dark Matter Using the First Five-Tower Run of the Cryogenic Dark Matter Search**. Ph.D. thesis, University of California, Berkeley, 2008.

[20] B. D. Josephson, **Possible New Effects in Superconductive Tunnelling** . *Physics Letters* **1**, 251–253 1962.

[21] S. Shapiro, **Josephson Currents in Superconducting Tunneling: The Effect of Microwaves and Other Observations**. *Physical Review Letters* **11**, 80 1963.

[22] M. Tinkham, *Introduction to Superconductivity* (Dover Publications, Inc., 31 East 2nd Street, Mineola, New York, 1996 .

[23] P. K. Day *et al.*, **A Broadband Superconducting Detector Suitable for Use in Large Arrays** . *Nature* **425**, 817–821 2003.

[24] D. G. McDonald, **Novel Superconducting Thermometer for Bolometric Applications**. *Applied Physics Letter* **50**, 775 1987.

[25] P. J. Shirron and M. J. DiPirro, **Concept for a high-resolution thermometer utilizing the temperature dependence of the magnetic penetration depth**. *IEEE Trans. Appl. Supercond.* **3**, 2140 1993.

[26] J. Bardeen, L. N. Cooper, and J. R. Schrieffer, **Theory of Superconductivity**. *Physical Review* **108**, 1175 1957.

[27] V. L. Ginzburg and L. D. Landau, **On the Theory of Superconductivity**. *Journal of Experimental and Theoretical Physics (Zh. Eksp. Teor. Fiz.* **20**, 1064–1082 1950.

[28] P. G. de Gennes, *Superconductivity of Metals and Alloys* (Addison-Wesley Publishing Company, 31 East 2nd Street, Mineola, New York, 1966 .

[29] L. N. Cooper, **Bound Electron Pairs in a Degenerate Fermi Gas**. *Physical Review* **104**, 1189–1190 1956.

[30] L. P. Gor'kov, **Microscopic Derivation of the Ginzburg-Landau Equations in the Theory of Superconductivity**. *Journal of Experimental and Theoretical Physics (Zh. Eksperim. i. Teor. Fiz.* **36**, 1918–1923 1959.

[31] W. Eisenmenger, *Non-equilibrium Superconductivity, Phonons, and Kapitza Boundaries* (Plenum Press, New York, 233 Spring Street, New York, NY 10013, YEAR .

[32] P. L. Brink, **Non-Equilibrium Superconductivity induced by X-ray Photons**. Ph.D. thesis, Magdalen College, Oxford, 1995.

[33] A. G. Kozorezov *et al.*, **Quasiparticle-phonon downconversion in nonequilibrium superconductors**. *Physical Review B* **61**, 2000.

[34] A. G. Kozorezov *et al.*, **Electron energy down-conversion in thin superconducting films**. *Physical Review B* **75**, 094513 2007.

[35] A. G. Kozorezov, **Energy Down-Conversion and Thermalization in Metal Absorbers**. *Journal of Low Temperature Physics* **167**, 473–484 2012.

[36] A. G. Kozorezov *et al.*, **Athermal energy loss from x-rays deposited in thin superconducting films on solid substrates**. *Physical Review B* **87**, 104504 2013.

[37] R. O. Lane and D. J. Zaffarano, **Transmission of 0-40 keV Electrons by Thin Films with Application to Beta-Ray Spectroscopy**. *Physical Review* **94**, 960 1954.

[38] A. Jaquier, P. Probst, R. Huguenin, and R. Stubi, **Temperature dependent electron scattering rates in aluminum from high precision RFSE measurements between 0.2 and 10K.**. *Physica B: Condensed Matter* **194-196**, 1177–1178 1994.

[39] D. N. Langenberg, . *Proceedings of the 14th International Conference on Low Temperature Physics* **V**, 223 1975.

[40] S. B. Kaplan, **Acoustic Matching of Superconducting Films to Substrates**. *Journal of Low Temperature Physics* **37**, 343 1979.

[41] J. Martin *et al.*, **Quasiparticle diffusion and loss processes in superconducting tunnel junctions**. *Nuclear Instrument and Methods A* **370**, 88–90 1996.

[42] M. Loidl *et al.*, **Quasiparticle diffusion over several mm in cryogenic detectors**. *Nuclear Instrument and Methods A* **465**, 440–446 2001.

[43] A. Tomada, **Quasi-Particles Test Designs**. Technical report, (unpublished , also available as `http://confluence.slac.stanford.edu/download/attachments/108696569/QP_TestDevices_QP1_111216.pdf?version=1&modificationDate=1328724842000`.

[44] J. M. Kreikebaum *et al.*, **Growth of α-β phase W thin films over steep Al topography in a confocal sputtering machine**. *Journal of Vacuum Science and Technology B* **33**, 011203 2015.

[45] A. E. Lita *et al.*, **Tuning of Tungsten Thin Film Superconducting Transition Temperature for Fabrication of Photon Number Resolving Detectors**. *IEEE Transactions on Applied Superconductivity* **15**, 3528 2005.

[46] G. Binnig, C. F. Quate, and C. Gerber, **Atomic Force Microscope**. *Physical Review Letters* **56**, 930 1986.

[47] Y. Martin, C. C. Williams, and H. K. Wickramasinghe, **Atomic force microscope-force mapping and profiling on a sub 100 $\AA$ scale**. *Journal of Applied Physics* **61**, 4723 1987.

[48] N. Ashcroft and N. Mermin, *Solid State Physics* (Brooks/Cole, Cengage Learning, 10 Davis Drive, Belmont, CA 94002, 1976 .

[49] J. Wilks and D. S. Betts, **An Introduction to Liquid Helium, 2nd edn.**. *Clarendon, Oxford* 1987.

[50] C. Enss and S. Hunklinger, *Low Temperature Physics* (Springer, New York, 2005 .

[51] H. Marshak, **Nuclear Orientation Thermometry**. *Journal of Research of the National Bureau of Standards* **88**, 1983.

[52] B. A. Hines, K. M. Sundqvist, D. N. Seitz, and M. E. Huber, **Flux-Coupled Direct Feedback in a SQUID Amplifier**. *IEEE Transactions on Applied Superconductivity* **21**, 262–266 2011.

[53] M. E. Huber *et al.*, **DC SQUID Series Array Amplifiers With 120 MHz Bandwidth**. *IEEE Transactions on Applied Superconductivity* **11**, 4048–4053 2001.

[54] K. M. Sundqvist, **Carrier Transport and Related Effects in Detectors of the Cryogenic Dark Matter Search**. Ph.D. thesis, University of California at Berkeley, 2012.

[55] S. W. Leman, **Development of Phonon-Mediated Transition-Edge-Sensor X-Ray Detectors for use in Astronomy**. Ph.D. thesis, Stanford University, 2006.

[56] half life, **Half-Life**. Technical report, (unpublished , also available as `http://archive.is/ie.lbl.gov/toi/perchart.htm`.

[57] NIST, **Mass Attenuation**. Technical report, (unpublished , also available as `http://physics.nist.gov/PhysRefData/XrayMassCoef/`.

[58] S. J. Hart *et al.*, **Phase Separation in Tungsten Transition Edge Sensors**. *AIP Conference Proceedings* **215**, 1185 2009.

[59] B. Shank *et al.*, **Nonlinear Optimal Filter Technique For Analyzing Energy Depositions In TES Sensors Driven Into Saturation**. *AIP Advances* **4**, 117106 2014.

[60] M. Pyle, **Quasiparticle propagation in aluminum fins and tungsten TES dynamics in the CDMS ZIP detector**. *NIM A: 11th International Workshop on Low Temperature Detectors* **559**, 405–407 2006.

[61] A. Sommerfeld, . *Naturwissenschaft* **15**, 825 1927.

[62] B. Shank, **TESTING AND CHARACTERIZATION OF SUPERCDMS DARK MATTER DETECTORS**. Ph.D. thesis, Stanford University, 2014.

[63] S. B. Kaplan *et al.*, **Quasiparticle and phonon lifetimes in superconductors**. *Physical Review B* **14**, 1976.